NANYANG
TECHNOLOGICAL
UNIVERSITY
SINGAPORE

ADDITIVE MANUFACTURING OF ALLOY AND MULTI-METAL OXIDE COATED ELECTRODES FOR ELECTROLYSIS OF WATER

CHIDANAND HEGDE (G1600348B)

SCHOOL OF MECHANICAL AND AEROSPACE ENGINEERING

2020

ADDITIVE MANUFACTURING OF ALLOY AND MULTI-METAL OXIDE COATED ELECTRODES FOR ELECTROLYSIS OF WATER

CHIDANAND HEGDE (G1600348B)

School of Mechanical and Aerospace Engineering

A thesis submitted to Nanyang Technological University
in partial fulfillment of the requirements for
the degree of Doctor of Philosophy

2020

Statement of Originality

I hereby certify that the work embodied in this thesis is the result of original research, is free of plagiarised materials, and has not been submitted for a higher degree to any other University or Institution.

12th October 2020

....

Date

....

Chidanand Hegde

Supervisor Declaration Statement

I have reviewed the content and presentation style of this thesis and declare it is free of plagiarism and of sufficient grammatical clarity to be examined. To the best of my knowledge, the research and writing are those of the candidate except as acknowledged in the Author Attribution Statement. I confirm that the investigations were conducted in accord with the ethics policies and integrity standards of Nanyang Technological University and that the research data are presented honestly and without prejudice.

12th October 2020	
. . . .	. . . .
Date	Hua Li

Authorship Attribution Statement

This thesis contains material from **two** papers published in the following peer-reviewed journals in which I am listed as an author.

Chapter 3 is published as **C. Hegde**, X. Sun, K. N. Dinh, A. Huang, H. Ren, B. Li, R. Dangol, C. Liu, Z. Wang, Q. Yan, and H. Li. Cu and Fe Co-Doped Ni Porous Networks as an Active Electrocatalyst for Hydrogen Evolution in Alkaline Medium. *ACS Applied Materials and Interfaces* **12**, 2380-2389 (2020). DOI: 10.1021/acsami.9b17273.

The contributions of the co-authors are as follows:

- Prof Qingyu Yan and A/Prof Hua Li guided throughout this work and reviewed the manuscript.
- I and Dr. Xiaoli Sun wrote the manuscript.
- I conducted experimental work at the Singapore Centre for 3D Printing and School of Materials Science and Engineering.
- I conducted XRD, and FESEM tests at FACTS NTU.
- Dr. Xiaoli Sun and Aijian Huang under the guidance of A/Prof Zhiguo Wang conducted DFT calculations and wrote the manuscript concerning the DFT calculations. Dr. Xiaoli Sun is also the co-first author of the manuscript. However, the DFT calculations are included in this thesis to better explain the experimental results.
- Dr. Hao Ren conducted Transmission electron microscopy imaging.
- Dr. Raksha Dangol and Khang Ngoc Dinh helped in BET surface area measurement.
- Dr. Bing Li and Dr. Chuntai Liu collected X-ray photoelectron spectroscopy data.

Chapter 4 is published as **C. Hegde**, X. Sun, H. Ren, A. Huang, D. Liu, B. Li, R. Dangol, C. Liu, S. Li, H. Li, Q. Yan, NiAg0. 4 3D porous nanoclusters with epitaxial interfaces exhibiting Pt like activity towards hydrogen evolution in alkaline medium. *Nanoscale* (2020). DOI: 10.1039/D0NR00993H.

The contributions of the co-authors are as follows:

- Prof Qingyu Yan and A/Prof Hua Li guided throughout this work and reviewed the manuscript.
- I and Dr. Xiaoli Sun wrote the manuscript.
- I conducted experimental work at the Singapore Centre for 3D Printing and School of Materials Science and Engineering.
- I conducted XRD, and FESEM tests at FACTS NTU.
- Dr. Xiaoli Sun and Aijian Huang under the guidance of A/Prof Shuiqing Li performed density functional theory calculations and wrote the manuscript concerning the DFT calculations. Dr. Xiaoli Sun is also the co-first author of the manuscript. However, the DFT calculations are included in this thesis to better explain the experimental results.
- Dr. Hao Ren conducted Transmission electron microscopy imaging.
- Dr. Raksha Dangol conducted BET surface area measurement.
- Dr. Daobin Liu conducted ICP-OES tests.
- Dr. Bing Li and Dr. Chuntai Liu collected X-ray photoelectron spectroscopy data.

12th October 2020

....

Date   Chidanand Hegde

Acknowledgments

Firstly, I would like to heartily thank my supervisor Associate Professor Li Hua for giving me the opportunity to pursue this Ph.D. research under his supervision. He was always there to help in giving his insightful comments and guide me throughout this journey. I also would like to express my immense gratitude to my co-supervisor Professor Alex Yan Qingyu whose insightful comments, suggestions and weekly guidance helped me to refine my level of understanding and research. I am extremely grateful for the degree of freedom which he gave me in exploring various research directions during my Ph.D., and for being extremely patient and supportive in the process of mentoring me throughout this journey. I am also very grateful for accepting as his student in my second year of Ph.D. Thanks for seeing the potential in me despite not having a relevant scientific background.

Besides my supervisors, I would like to thank the rest of my thesis committee, Associate Professor Liu Erjia and Assistant Professor Qian Shunzhi for their suggestions and comments to improve this work.

My sincere thanks go to Dr. Dinh Ngoc Khang for training me in the experimental methods and characterization techniques in my beginning days. I also would like to thank Dr. Ren Hao and Dr. Tan Hui Teng for their help in TEM testing, Dr. Daobin Liu for his help in ICP-OES and XPS tests. My sincere thanks to Dr. Li Bing for assisting me with XPS studies. My sincere thanks also go to Dr. Xiaoli Sun for her patience and collaborative work for theoretical computational studies. I am also grateful to Dr. Raksha Dangol for her help in my experiments and also for answering my innumerable queries. My sincere thanks to Dr. Wenjing Huang and Dr. Chade Liu for their constant help during this Ph.D. My sincere thanks to Mr. Lim Joel for being a constant companion during my experiments and for endless discussions about science and life. I am also extremely grateful to the most professional and knowledgeable research staff

at FACTS who truly are best at their job. They deserve the credit for keeping FACTS equipment always ready and open for the researchers.

I am also very grateful to my mother, brother, and my in-laws who took care of everything at home during my overseas stay. Special gratitude to my late father, who always wanted me to pursue post-graduation and put education above everything. Many thanks to my beloved wife for digital illustrations and also being there for me always during this tough phase. Last but not least I thank all family members and friends who have been moral support for me always.

Table of Contents

List of Figures

List of Tables

List of Symbols and Abbreviations

3D	Three dimensional
CNT	Carbon nanotube
LSV	Linear sweep voltammetry
CV	Cyclic voltammetry
HER	Hydrogen evolution reaction
OER	Oxygen evolution reaction
FESEM	Field emission scanning electron microscopy
TEM	Transmission electron microscopy
HRTEM	High resolution transmission electron microscopy
HAADF	High angle annular dark-field
STEM-EDX	Scanning transmission electron microscope energy dispersive X-ray spectroscopy
XRD	X-ray diffraction
EDS/EDX	Energy-dispersive X-ray spectroscopy
XPS	X-ray photoelectron spectroscopy
η	Overpotential
η_{10}	Overpotential at geometric current density of 10 mA cm^{-2}
η_{100}	Overpotential at geometric current density of 100 mA cm^{-2}
C_{dl}	Double-layer capacitance
ECSA	Electrochemical active surface area
TOF	Turn over frequency
LDH	Layered double hydroxide
EIS	Electron impedance spectroscopy
PAS	Positron annihilation spectroscopy
DFT	Density functional theory
CVD	Chemical vapor deposition
Gt	Gigaton
GC	Glassy carbon
AM	Additive manufacturing
Fs	Femtosecond
FsLDW	Femtosecond laser direct writing

AJP	Aerosol jet printing
3DPNC	3-dimensional porous nanoclusters
PNW	Porous networks
HEA	High entropy alloy
SS	Stainless steel
CFP	Carbon fiber paper
BET	Brunauer–Emmett–Teller
FTIR	Fourier transform infrared spectroscopy
SAED	Selected area diffraction

Abstract

Rapid economic growth and industrialization to serve human needs have caused catastrophic damage to the environment. As a result, there is an urgent need to transition to carbon-neutral and renewable energy sources. While the renewable energy generation from solar and wind has been instrumental in this energy transition, the relevance of these is limited due to the humongous capacity of batteries needed to store all the generated energy. As an alternative, the harvested renewable energy could be stored in fuels like hydrogen. However, renewable hydrogen production is limited by (a) insufficient production of renewable energy, and (b) inefficient electrolysis of water. The primary objective of this thesis is to address the problem of inefficient electrolysis, by advancing the catalyst design and synthesis methods.

The past decade has seen significant advancement in the design and synthesis of active catalysts for water splitting. Based on the experimental results, the catalysts are mapped into a volcano plot, which illustrates the relationship between reaction kinetics and the Gibbs energy of adsorption of reaction intermediates. In particular, a few of the experimental and computational results point towards a possible improvement in the catalytic activity of Ni by alloying. Inspired by this we investigated two catalyst systems for their activity for hydrogen evolution reaction (HER).

In the first part, the effect of doping of Cu and Fe on the catalytic activity of Ni for HER is investigated. Cu and Fe co-doped Ni porous networks were prepared by thermal annealing of hydrothermally synthesized Cu, Fe co-doped nickel hydroxide. Experimental and computational results showed that doping of Cu and Fe enhanced the activity of Ni. Among various doping combinations, the $NiCu_{0.05}Fe_{0.025}$ alloy with 5% Cu and 2.5% Fe exhibited the best activity with a low overpotential of 60 mV at 10 mA cm^{-2} and specific activity of 0.1 mA $cm^{-2}{}_{(ECSA)}$ at 117 mV overpotential. The density functional theory calculations revealed that co-

doping of Fe and Cu into the Ni lattice shifted the d-bands of Ni to lower energy levels and hence reduced the hydrogen adsorption energy to -0.131 eV from -0.258 eV. When $NiCu_{0.05}Fe_{0.025}(OH)_2$ nanowire catalyst was used as an oxygen evolution reaction (OER) catalyst and was coupled with $NiCu_{0.05}Fe_{0.025}$ porous networks for overall water splitting, the $NiCu_{0.05}Fe_{0.025}$|| $NiCu_{0.05}Fe_{0.025}(OH)_2$ catalyst couple achieved a current density of 10 mA cm^{-2} at 1.491 V, similar to that of the Pt/C||RuO_2 couple and offered a negligible loss in the performance when operated at 20 mA cm^{-2} for 30 hours.

In the second part, $NiAg_{0.4}$ heterogeneous alloy which exhibited Pt/C-like activity for HER is reported. $NiAg_{0.4}$ 3D porous nanoclusters (3DPNC) were synthesized by thermal reduction of hydrothermally synthesized $Ag@Ni(OH)_2.2/3H_2O$. The synthesized $NiAg_{0.4}$ 3D porous nanoclusters comprised of nanoparticles of lateral dimension ~50 nm forming a 3D porous network with pores of 10 nm – 80 nm. High-resolution transmission electron microscopy images revealed the epitaxial growth of Ag (200) on the Ni (111) plane leading to the creation of abundant interfaces between the Ni and Ag lattices. $NiAg_{0.4}$ 3DPNC showed remarkable activity by achieving 10 mA cm^{-2} at 40 mV overpotential at a Tafel slope of 39.1 mV dec^{-1} in 1 M KOH solution. Further, the specific activity of $NiAg_{0.4}$ 3DPNC (0.1 mA $cm^{-2}{}_{(ECSA)}@\eta$ = 45 mV) closely matched with state-of-the-art Pt/C catalyst (0.1 mA $cm^{-2}@\eta$ = 26 mV). DFT calculations revealed low hydrogen adsorption energy of -0.04 eV at the Ni-Ag interface. The activity of the NiAg heterogeneous alloys for various Ni/Ag ratios directly correlated with the interface area, further confirming the role of the Ni-Ag interface for hydrogen evolution. $NiAg_{0.4}$ 3DPNC also exhibited exceptional stability and durability when tested for 5000 CV cycles and 80 hours chronoamperometry test.

Despite great progress in catalyst design, one of the primary challenges in the fabrication of electrodes for electrocatalysis is in integrating the catalyst powder to a conductive substrate. Herein, we have developed a single-step femtosecond laser direct writing process to fabricate

binder-free electrodes coated with metal alloys and oxides. A novel ink formulation consisting of metal salt solution, binder, reducing agent, and a surfactant was formulated to realize the laser synthesis of metal oxides and alloys. Ink is dried on the conductive substrate, which is followed by the femtosecond laser direct writing process. The metal precursor in the ink is transformed into multi-metal oxides or alloys depending on the ink formulation and laser parameters. A large family of 57 metal oxides and alloys were synthesized through this approach. In-depth material characterization based on XRD, FESEM, TEM, and XPS tests confirmed the formation of multi-metal oxides and alloys. SS@$NiCoCuFeCr_{0.5}$ electrode prepared by this method showed exceptional activity for oxygen evolution reaction by furnishing 10 mA cm^{-2} at 213 mV overpotential and showed no degradation of activity when operated for 50 hours. To take a step further, a hybrid additive manufacturing (AM) process combining aerosol jet printing and laser direct writing was developed to form thin film metal oxides and alloys. The metal precursor ink was printed via aerosol jet printing, which was later irradiated with a femtosecond laser to fabricate multi-material micro-components of any complex 2D shapes. As a proof of concept, a sensor with Ag current collector and multi-metal oxide sensing element was fabricated in just two steps. The hybrid AM process is versatile and is conducive to the rapid fabrication of multi-material devices.

In summary, works done as a part of this Ph.D. study have demonstrated two key hypotheses: (a) Alloying Nickel with metals with a contrasting tendency towards hydrogen adsorption (positive ΔG_H) produced alloys with enhanced catalytic activity for HER. (b) Through femtosecond laser, direct writing, and aerosol jet printing, highly active and durable electrodes coated with metal oxides/alloys can be fabricated with low energy and resource footprint.

Chapter 1 Introduction

This chapter serves as a bird's eye view of this entire thesis. Firstly, a broader problem statement of the thesis is elucidated. Secondly, a brief description of the scope and objectives of this thesis is made. In the later section, a very succinct summary of the thesis is outlined. In the final section, the key findings and outcomes of this thesis are listed.

1.1 Problem Statement

Since the advent of the industrial revolution and from the time man started using machines to perform the simple tasks to most complex and herculean functions one thing that has become an absolute necessity for humanity is the energy that runs it “THE FUEL”. Over the last couple of centuries, we have used mainly coal and petroleum as the primary source of fuel for transportation, industries, electricity, and other energy needs. According to a survey by the international energy agency, the global demand for energy in 2013 was 18 TW which is expected to increase to 26 TW in 2040, increasing the CO_2 emissions to 44 Gt a year.[1] To meet the energy demands without damaging the environment alternative sources of energy that are carbon neutral and renewable are necessary. On the bright side, countries across the world have made rapid progress in the transition to renewable energy by increased harvesting of solar and wind energy in the past decade. However, the complete transition to renewable energy is limited by the intermittent nature of these renewable sources and the need for an enormous quantity of battery storage for energy storage. Alternatively, electricity generated from renewable energy can be stored in chemical bonds. In this regard, hydrogen is one of the promising energy carriers, as hydrogen can be renewably generated from the electrolysis of water.

In this context, the most important challenge is to produce hydrogen by electrolysis of water efficiently. The current method of hydrogen production is energy-intensive and also inefficient. Further, the catalysts used in electrolyzers are typically precious metals like Platinum, Ruthenium, Rhodium, and Iridium, etc., which are expensive. Therefore, the key to energy-efficient and cost-effective renewable hydrogen production is (1) availability of cheaper renewable electricity, (2) cheaper and energy-efficient electrolyzers with electrodes made from earth-abundant elements. The focus of this thesis is to achieve the second objective. And we attempt to do it by (1) Research and development of Ni-based electrocatalysts for water splitting, (2) Developing an energy-efficient and rapid one-step additive manufacturing process to fabricate the electrodes. In the following section, a brief overview of the scope and objectives of this thesis is elucidated.

1.2 Objectives and Scope

Alkaline electrolysis is one of the renewable routes to hydrogen production. From our literature survey, we find that among the earth-abundant elements Ni has one of the most favorable hydrogen adsorption energies to promote hydrogen evolution. Also, previous reports imply a plausible boost in HER activity of Ni through alloying with metals that have positive Gibbs energy of hydrogen adsorption. Inspired by this, we propose to investigate the effect of alloying of Cu, Fe, and Ag on the HER activity of Ni. Furthermore, conventional methods of catalyst synthesis and application involve the synthesis of catalysts in the powder form. This further entails the use of electrically conductive additives such as carbon black and binders to hold the catalyst to the current collector. However, if the catalyst could be directly synthesized on the conductive substrate it will reduce the number of steps, energy, and time required for the entire process. Herein, we propose a combination of laser-based sintering method and aerosol jet printing to synthesize metal nanostructures directly on the conductive substrate.

In particular, the objectives of the thesis comprise the following:

1. To investigate the effect of doping of Fe and Cu on the catalytic activity of Ni
    - ❈ Prepare Cu and Fe co-doped Ni porous networks by thermal reduction of Cu and Fe co-doped Ni hydroxide.
    - ❈ Investigate the morphology, phase, and surface electronic characteristics of Cu and Fe co-doped Ni porous networks.
    - ❈ Investigate the effect of the doping concentration of Cu and Fe on the electrocatalytic activity, and optimizing the doping concentration for the best activity.

- ❈ Estimating the Gibbs energy of hydrogen adsorption (ΔG_H) for pristine and doped Ni through density functional theory (DFT) calculations.

2. Interface engineering at Ni-Ag heterogeneous alloy to achieve Pt/C-like activity for HER
   - ❈ Synthesize NiAg 3D porous networks with epitaxial interfaces through hydrothermal method, followed by the thermal reduction in the hydrogen atmosphere.
   - ❈ Investigating the morphology, phase, crystal growth, and surface electronic properties of the synthesized products.
   - ❈ To study the effect of variation of Ag alloying concentration on the electrocatalytic activity for hydrogen evolution.
   - ❈ To investigate the correlation between the interface area and catalytic activity of NiAg alloy.
   - ❈ Estimating the ΔG_H at the Ni-Ag interface by DFT calculations.
3. To develop a novel process for in-situ synthesis and coating of metal alloy and metal oxide nanostructures through Femtosecond laser direct writing
   - ❈ To develop an ink formulation from the commercially available industrial chemicals to develop a thin film suitable for laser processing.
   - ❈ Investigate the effect of laser parameters namely, the laser power and laser writing speed on the nature of the products formed.
   - ❈ To investigate the effect of salt and polymer concentration of the ink on the nature of the products formed through laser writing.
   - ❈ To investigate the catalytic activity of the synthesized catalysts by laser direct writing.
4. To develop a hybrid additive manufacturing process through a combination of aerosol jet printing and laser direct writing

- Optimizing the printing parameters to successfully print metal precursor ink through aerosol jet printing.
- To investigate the nature of the product formed through XRD and FESEM study.
- To fabricate a multi-material sensor by hybrid AM as a proof of concept for multi-material microfabrication.

1.3 Thesis outline

The thesis is divided into 7 chapters and the following is the brief content of each section:
Chapter 1 is a summary of the entire thesis. The chapter begins with a problem statement, followed by the scope and objectives of this thesis. Later, the original contributions from the thesis are listed.

Chapter 2 deliberates elaborately on the past scientific studies related to electrocatalysis and synthesis methods. In the beginning, the fundamentals of electrocatalysis are understood based on the reaction mechanism, volcano plot, and the thermodynamic aspects of electrolysis. Later, various catalyst design techniques reported in the past are deliberated. Further, the shortcomings associated with the conventional electrode fabrication method are scrutinized and an alternate approach is suggested. In the end, key research gaps in the research field of electrocatalysis are highlighted and our hypothesis for catalyst design and additive manufacturing approach to electrode fabrication is proposed.

Chapter 3 reports the enhancement in the activity of Ni for HER achieved by co-doping of Cu and Fe. Firstly, the rationale behind choosing Ni as the host and Cu and Fe as the dopant atoms is delineated. Secondly, the synthesis method and characterization of Cu, Fe co-doped Ni nanoclusters are explained. The catalytic activity of the material is characterized using experimental methods and theoretical simulations and the positive impact of doping of Cu and Fe on its activity is established. The durability of the catalyst is tested for electrolysis and the activity of the catalyst is compared with state-of-the-art Pt/C catalyst.

Chapter 4 reports Pt/C like activity exhibited by $NiAg_{0.4}$ heterogeneous alloy for hydrogen evolution reaction. The alloy is synthesized to furnish abundant epitaxial interfaces between Ni and Ag. The XRD, XPS, TEM, and SEM and characterizations are employed to investigate the constituents, phase, and morphology of the material. From theoretical calculations and experimental results, the origin of the activity of $NiAg_{0.4}$ is established to be arising from the epitaxial interface of Ni-Ag heterogeneous alloy. The specific activity of the $NiAg_{0.4}$ approaches the Pt/C catalyst and the catalyst shows excellent durability.

Chapter 5 demonstrates the fabrication of binder-free electrodes coated with multi-metal oxide and alloys through femtosecond laser direct writing. Firstly, the rationale behind choosing the femtosecond laser writing process is enunciated. Secondly, the ink formulation necessary to achieve this process is synthesized. The formation of multi-metal oxides and high entropy alloy is ascertained through XRD, FESEM, TEM, ICP-OES test results. One of the fabricated electrodes showed exceptional activity and stability for the OER. The activity of the Cu, Fe co-doped Ni and $NiAg_{0.4}$ catalysts synthesized through this method showed similar specific activity as the conventionally synthesized samples. In the end, the extent of micro-fabrication that can be achieved through this process is delineated and recommendations for future work are proposed.

Chapter 6 demonstrates a novel hybrid additive manufacturing process developed to synthesize metal oxide and alloy thin films. Metal precursors ink is printed using an aerosol jet printer, which is sintered using the femtosecond laser. The formation of metal oxide and alloy thin films is confirmed from XRD, FESEM tests. A proof of concept sensor is designed using the hybrid additive manufacturing process to show the multi-material fabrication that can be achieved. In the end, future recommendations are suggested for using this method for the rapid fabrication of sensors.

Chapter 7 gives a summary of the scientific contributions of this thesis. In the end, future research recommendations based on our current work are advised.

1.4 Findings and Outcomes/Original contributions of this thesis

In the pursuit of attaining the objectives of the dissertation, this Ph.D. study produced several findings. The following are the original contributions:

1. Co-doping of Fe and Cu atoms to Ni lattice shifted the d-bands of Ni to lower energy levels and reduced the ΔG_{H} from -0.258 eV to -0.131 eV. The doping concentrations of Cu and Fe do influence HER activity as observed from the experimental results. Upon optimization, the Ni nanoclusters with 2.5% Fe and 5% Cu doping concentration showed the best HER activity. The specific activity $\mathrm{NiCu_{0.05}Fe_{0.025}}$ was ~4 times that of the pristine Ni.
2. The interface of Ni and Ag exhibited remarkable activity for HER, similar to the state-of-the-art Pt/C catalyst. The interface of Ni and Ag exhibited exceedingly low hydrogen adsorption energy of -0.04 eV as revealed from the DFT calculations. The specific activity of $\mathrm{NiAg_{0.4}}$ 3DPNC (0.1 mA cm^{-2}@ 45 mV(η)) approached that of Pt/C (0.1 mA cm^{-2}@ 26 mV (η)) and was exceptionally superior to pristine Ni (0.1 mA cm^{-2}@ 177 mV(η)) and pristine Ag (0.1 mA cm^{-2}@ 313 mV(η)). Deeper investigation into the variation of activity of different Ni-Ag alloys for varying Ni : Ag ratios revealed the role of Ni-Ag epitaxial interface for its HER activity. Furthermore, $\mathrm{NiAg_{0.4}}$ 3DPNC showed excellent durability and stability for HER.
3. Enhanced HER activity of Ni through co-doping of Cu and Fe and interface engineering by Ag confirms our hypothesis of catalyst design through the mixing of elements with a contrasting tendency for hydrogen adsorption based on the volcano plots. Thus, the

same catalyst design strategy could be implemented to design better catalysts with desired catalytic activity.

4. A novel additive manufacturing process to fabricate electrodes coated with high entropy alloy and multi-metal oxide nanoparticles is developed. We formulated ink based on metal salt solution, comprising citric acid as a surfactant-cum-reducing agent and carboxymethyl cellulose as a binder. The ink can be dried on various substrates such as glass, metal, and carbon fiber paper. The dried ink is processed using a femtosecond laser to transform the ink into multi-metal oxide or high entropy alloy nanoparticles depending on the composition of the ink. The versatile process was used to prepare a large family of 57 multi-metal oxides and alloys. The formation of multi-metal oxides and alloys is confirmed through XRD, XPS, FESEM, TEM and ICP-OES tests. Furthermore, Femtosecond laser writing method is rapid, conducted at room temperature and in open atmosphere, and consumes substantially low quantity of solvents. The fabricated electrodes exhibited excellent activity and durability for alkaline electrolysis.
5. A hybrid additive manufacturing process is developed combining the aerosol jet printing and Femtosecond laser writing. The desired patterns are printed using an Aerosol jet printer to form a uniform thin film of dried ink. The printed patterns are processed using a femtosecond laser to transform the dried ink into metal oxide or metal alloy thin films. The aerosol jet printing and laser writing parameters can be suitably tuned to fabricate desired thin film thickness in the range of 1 µm to 10 µm.

Chapter 2 Literature Review

In this chapter, we will discuss the fundamental science behind the electrolysis of water. In the beginning, we will elaborate on the reaction mechanism and volcano plot and its implication on approach to catalyst design. Later, various catalyst design approaches and synthesis methods which have been successfully demonstrated in the past will be elaborated. Towards the end, we will briefly explain the research gaps that are present, and the research opportunities, which are available to explore in the field of electrocatalysis and additive manufacturing of electrodes.

2.1 Introduction

The energy demand of the world is rapidly inflating owing to increased industrialization and economic development across the world. While the standard of living has improved, thanks to the advancement in science and technology, on the downside, the environmental pollution that has accompanied is also causing an unprecedented ramification on the quality of air, water, and land which are an integral part of human existence. Therefore, there is a dire need for the world to transition into pollution-free and renewable sources of energy. There has been a positive development in the transition to renewable energy generation from solar and wind in the past few years and the electrification of cars, trains, and other industrial processes. Hydrogen aptly complements the energy needs of the world in areas where electricity is not a feasible solution, viz. in shipping, heavy transport vehicles, aircraft, and power plants. Therefore, hydrogen is a potential renewable energy carrier for the future. Unfortunately, according to the International Renewable Energy Agency report of 2018, more than 95% of the hydrogen produced today is from fossil fuels i.e., coal and natural gas which is not sustainable. The primary cause of this is the cost of hydrogen. The green hydrogen (produced from renewable sources) is at least twice as expensive as the blue hydrogen (produced from fossil fuels with carbon capture). The cost of the green hydrogen is mainly determined by the following two factors (a) the cost of renewable electricity, (b) the efficiency of the electrolysis process. While the cost of renewable electricity is determined by various factors such as locations, availability of sunlight and wind, government policies, etc., the efficiency of the electrolysis process is mainly determined by the activity of the catalyst used. Owing to this there has been increasing study in the scientific community to develop efficient electrolysis methods and developing novel catalysts to accomplish the same.

In this light, it is imperative to review and understand the research progress made in the past, to assess the pros and cons of various techniques, and build on those ideas to make further progress. In this chapter, we shall discuss the fundamentals of water splitting and the critical parameters that decide the performance of the catalyst. Furthermore, we shall examine various strategies employed by the researchers to enhance the performance of the catalyst. In the later sections, we will examine various synthesis methods employed in the past for catalyst synthesis and suggest an alternative process based on additive manufacturing. The following section describes the basics of electrocatalysis of water.

2.2 Fundamentals of water splitting

Renewable hydrogen production is primarily accomplished by using renewable electricity to split the water molecule into hydrogen and oxygen according to the following equation:

$$2\ H_2O \rightarrow 2\ H_2 + O_2 \qquad (2.1)$$

Hydrogen is oxidized, and oxygen is reduced and the reaction occurs on the surface of an electrocatalyst. The reaction can be accomplished in different types of electrolyzers with each type having inherent advantages and disadvantages as illustrated in Figure 2.1. The debate on the advantages and limitations of these electrolyzers is not a subject of this thesis, as each of them has suitable applications depending on the needs and constraints of the industry. In this thesis, we mainly focus on catalyst development for alkaline electrolyzers. Going back to the equation 2.1, the standard free energy required to convert one mole of water to oxygen and hydrogen is +237.2 kJ/mol, and the corresponding thermodynamic electrode potential to achieve this is 1.23 V.[2] However due to sluggish kinetics and complexity of the bubble release mechanism the actual voltage needed for a reasonable rate of production is more than 1.23 V. This difference in theoretical thermodynamic electrode potential and the actual potential required is known as overpotential (η) as shown in Figure 2.2. As we can see from Figure 2.2, the current density (rate of H_2 production) depends on the overpotential. For this reason, reducing the overpotential is crucial to achieving efficient electrolysis. Further, the overpotential needed to achieve a specific current density depends on the catalyst used. Therefore, η is a critical parameter that can be used to assess the activity of the catalyst.

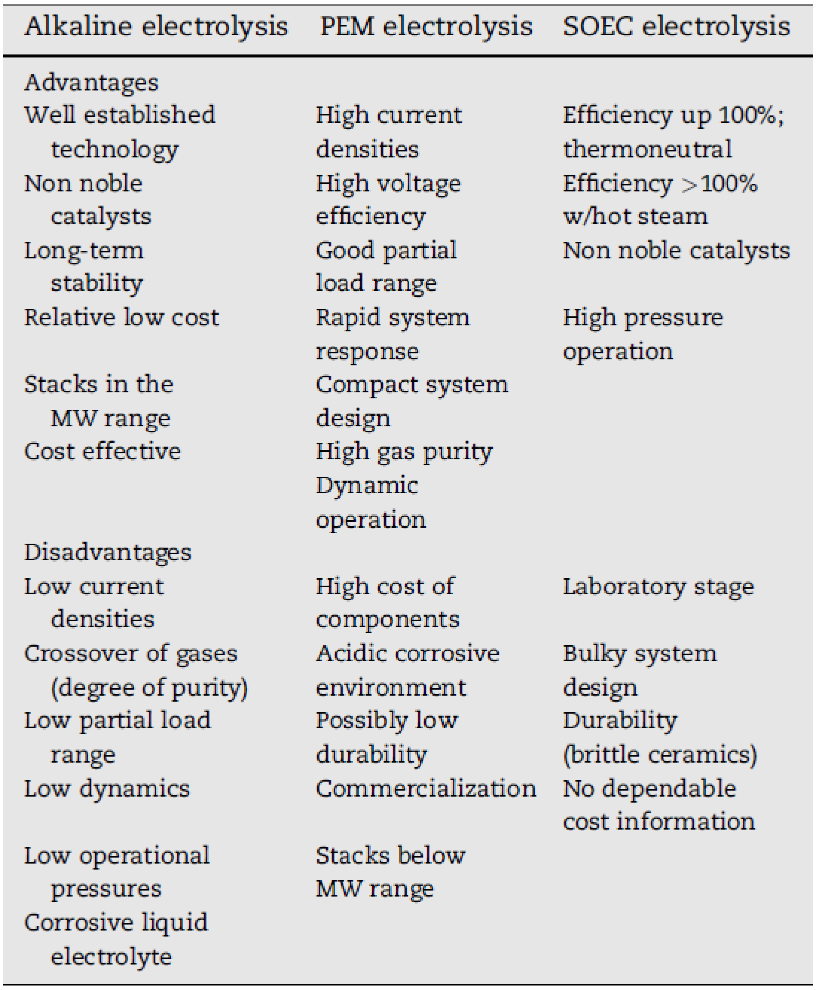

Alkaline electrolysis	PEM electrolysis	SOEC electrolysis
Advantages		
Well established technology	High current densities	Efficiency up 100%; thermoneutral
Non noble catalysts	High voltage efficiency	Efficiency >100% w/hot steam
Long-term stability	Good partial load range	Non noble catalysts
Relative low cost	Rapid system response	High pressure operation
Stacks in the MW range	Compact system design	
Cost effective	High gas purity	
	Dynamic operation	
Disadvantages		
Low current densities	High cost of components	Laboratory stage
Crossover of gases (degree of purity)	Acidic corrosive environment	Bulky system design
Low partial load range	Possibly low durability	Durability (brittle ceramics)
Low dynamics	Commercialization	No dependable cost information
Low operational pressures	Stacks below MW range	
Corrosive liquid electrolyte		

Figure 2.1 Comparison of advantages and disadvantages of different electrolysis methods.[3]

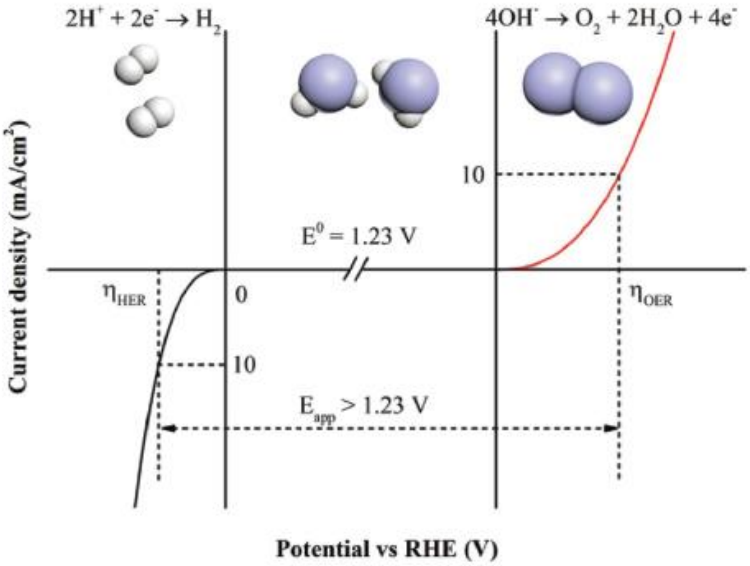

Figure 2.2 Schematic illustration of overpotential for the half-reactions of water electrolysis.[4]

To get a deeper insight into the overpotential, comprehensive understanding of electrode kinetics and the reaction mechanism is fundamental. In the following section, we shall deliberate on the reaction kinetics which is best described by the Nernst equation.

2.2.1 Nernst equation

The Nernst equation has the following mathematical form:

$$E = \mathrm{E}^0 + (\mathrm{R}T/n\mathrm{F}) \ln(C_0/C_R) \tag{2.2}$$

Where E is the electrode potential, E^0 is the standard electrode potential, n is the number of electrons involved in the reaction, F is Faraday's constant, T is temperature, R is the universal gas constant, and C_0 and C_R represent the concentration of oxidized and reduced species. Arguably, the potential required for electrolysis is primarily dependent on the standard electrode potential (E^0) which is fixed for every reaction. Apart from E^0, the potential is also dependent on the concentration of reactants and products at the electrode, the number of electrons involved, and the temperature. Favorably, these parameters can be appropriately tuned to achieve electrolysis at a lower voltage. With further mathematical treatment, the relationship between current density and voltage can be deduced as per the Butler-Volmer[5] equation:

$$j = j_0[\exp(-\alpha f\eta) - \exp((1 - \alpha)f\eta)] \tag{2.3}$$

where j is the current density in mA cm^{-2}, α is the transfer coefficient, f is defined as F/RT, η is the overpotential, and j_0 is the current density at zero overpotential known as exchange current density. Current density determines the rate of chemical conversions at the electrode i.e., hydrogen production in the case of water splitting. Therefore, a higher current density is desired for faster chemical reactions. From Equation (2.3), it follows that the exchange current density directly influences the current density. Based on this equation a graph of current density vs. overpotential is plotted in Figure 2.3 to compare the variation in current density for different j_0. Evidently, to achieve a certain current density, the catalyst with higher j_0 requires a low overpotential, i.e., it is more energy-efficient. In electrolyzers, a typical current density used is in the range of 0.5 to 1 A cm^{-2}. For such a high current density, a slight change in j_0 can severely impact the overpotential required, and consequently, the energy consumed. In conclusion, we can accomplish energy-efficient and faster electrochemical conversion with higher j_0. The j_0 closely correlates with the adsorption energy of the reaction intermediate on the catalyst surface. To understand these aspects let us first look into the reaction mechanism of the water splitting.

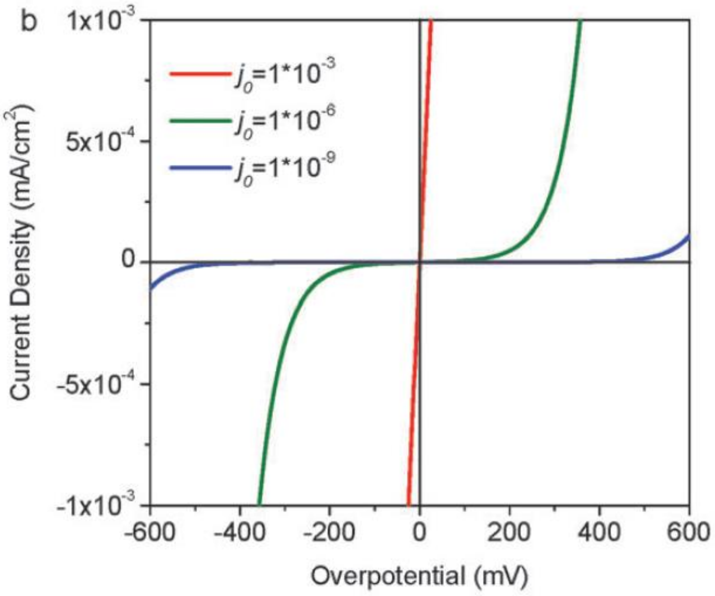

Figure 2.3 Influence of j_0 on the current density at various overpotentials.[5]

2.2.2 Reaction mechanism

The water-splitting reaction involves the breaking of the bond between oxygen and hydrogen and the formation of bonds of the same elements, i.e., H-H and O-O bonds. The overall reaction involves four electrons, due to which the charge transfer occurs in multiple steps. The mechanism is complicated involving multiple reactants and reaction intermediates in contact with the catalyst surface. The following reactions mechanisms are widely accepted for water splitting in the acidic and basic medium.

Hydrogen evolution reaction (HER):

HER is a cathodic half-reaction in which hydrogen is produced by the reduction of the water molecule. The following steps describe the overall chemical reaction.

Volmer step:

$$M + H_2O + e^- \rightarrow M\text{-}H_{ads} + OH^- \ (\sim 120 \text{ mV decade}^{-1}) \tag{2.4}$$

Heyrovsky step:

$$M\text{-}H_{ads} + H_2O + e^- \rightarrow M + H_2 + OH^- \ (\sim 40 \text{ mV decade}^{-1}) \tag{2.5}$$

Tafel step:

$$M\text{–}H_{ads} + M\text{–}H_{ads} \rightarrow 2\,M + H_2\ (\sim 30\ \text{mV dec}^{-1}) \qquad (2.6)$$

M in the above steps denotes the active center in the catalyst which is the site of chemical conversion. The values in the brackets are known as the Tafel slope, which is a measure of the kinetics of the reaction. Tafel slope and its relevance will be discussed elaborately in the later sections. The first step in HER is always the Volmer step where H^+ ions from water are reduced to H atoms which adsorb on the active sites. Following the Volmer step, the reaction can either proceed through the Tafel step or the Heyrovsky step. Thus, HER is a two-step reaction involving two electrons. Owing to the simple mechanism the overpotential associated with HER is relatively lesser compared to OER.

At the anode, oxygen is produced by water oxidation,[6] as depicted by the following reactions:

Oxygen evolution reaction (OER):

OER in acidic electrolyte:

$$M + H_2O \rightarrow OH\text{-}M + H^+ + e^- \qquad (2.7)$$
$$OH\text{-}M \rightarrow O\text{-}M + H^+ + e^- \qquad (2.8)$$
$$O\text{-}M + H_2O \rightarrow OOH^* + H^+ + e^- \qquad (2.9)$$
$$OOH\text{-}M \rightarrow M + O_2 + H^+ + e^- \qquad (2.10)$$

OER in basic electrolyte:

$$M + OH^- \rightarrow OH\text{-}M + e^- \qquad (2.11)$$
$$OH\text{-}M + OH^- \rightarrow O\text{-}M + H_2O + e^- \qquad (2.12)$$
$$O\text{-}M + OH^- \rightarrow OOH\text{-}M + e^- \qquad (2.13)$$
$$OOH\text{-}M + OH^- \rightarrow M + O_2 + H_2O + e^- \qquad (2.14)$$

Unlike HER, the OER progresses in three steps and involves the transfer of 4 electrons. Because of this reason, the activation energy for the formation and transformation of each of the reaction intermediate is high, leading to a slower reaction. As a consequence, the overpotential for OER is generally higher than HER. Furthermore, the pH of the electrolyte influences the reaction kinetics. For HER the acidic pH is more favorable than the basic, while for the OER basic pH is more favorable. Because of this reason the electrolysis is often conducted in basic medium. The overpotential of a reaction is primarily determined by the adsorption energy of the reaction intermediates during the chemical reaction. In the following section, we shall discuss about the Gibbs energy of reaction, which provides a quantitative estimation of activation energy that should be supplied for a chemical reaction.

2.2.3 Gibbs energy change for the reaction pathway

A chemical reaction on an electrocatalyst can be described in a very simplistic way in the following steps (a) The reactant adsorbs on the active site of the catalyst, (b) there is an exchange of charges at the catalyst surface leading formation of a new reaction intermediate or the final product, and finally (c) the product formed is desorbed from the catalyst surface. For the process like water splitting, the reaction pathway involves the formation of several reaction intermediates. Consequently, the adsorption energy of each of these reaction intermediates collectively determines the overall Gibbs energy of the process. Notably, the energy of adsorption and desorption is different for each catalyst, which makes one catalyst perform better than the other. Figure 2.4 illustrates the Gibbs energy change for the reaction path of HER and OER. According to thermodynamics, lesser Gibbs energy change for a reaction implies lower energy consumption for the process. Therefore, the best catalyst takes the reaction through a pathway that consumes the least amount of energy, i.e., near to the zero energy. This concept is best explained by the Sabatier's principle which closely describes characteristics of an ideal catalyst. It states "ideal catalyst binds the reaction intermediates not too weakly or too strongly so that the overall maximum free energy difference can be lowered and the reaction kinetics can be faster by mediating the strength of adsorption of reaction intermediates".[7]

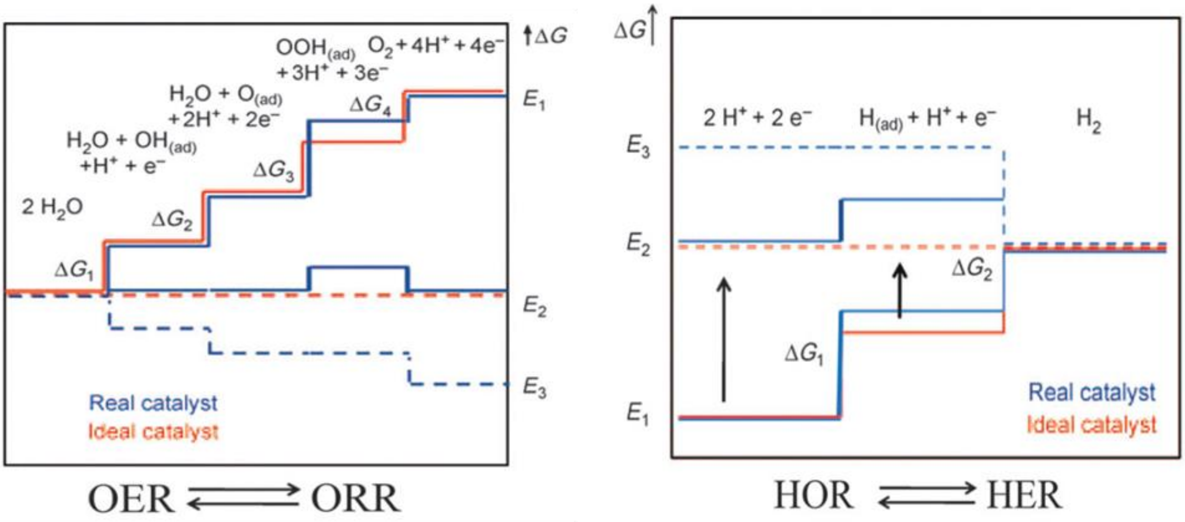

Figure 2.4 Gibbs energy diagram for different steps in OER and HER.[5]

The reason is obvious: if an intermediate is strongly adsorbed to the catalyst, it will stop the further chemical reactions, in contrast, weak adsorption may lead to desorption or ineffective charge transfer. Hence the optimum energy of adsorption (Gibbs energy near to zero) prompts easy adsorption and desorption that boosts the reaction kinetics. Sabatier's principle is illustrated in Figure 2.5 (a).

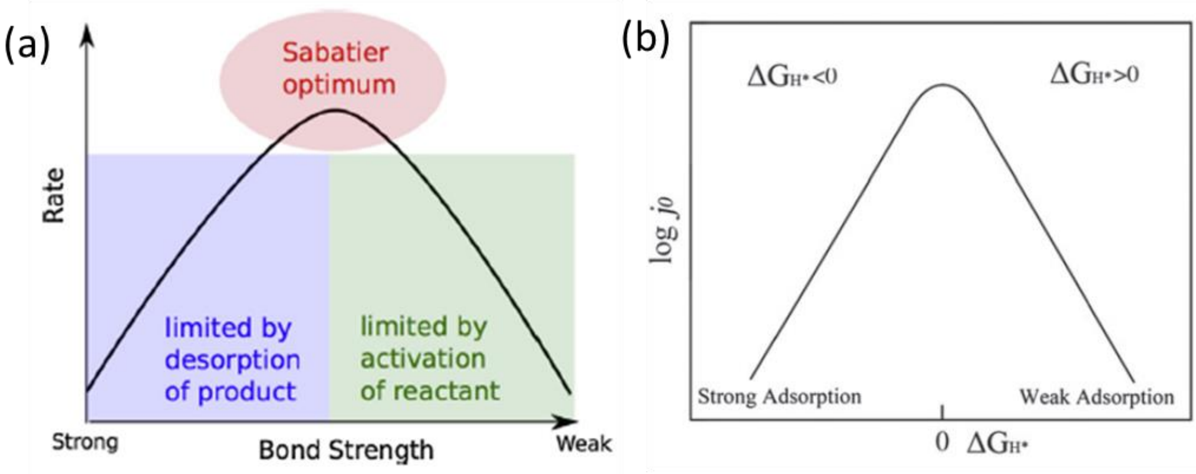

Figure 2.5 (a) Schematic illustration of Sabatier's principle[7], (b) A typical volcano plot for HER.[5]

2.2.4 Volcano plot

The Gibbs energy of adsorption can be determined by DFT calculations and verified through experiments. Since the exchange current density signifies the reaction kinetics, a graph of j_0 vs. ΔG is plotted to map the activity of various catalysts. The plot is known as a volcano plot akin to its shape as shown in Figure 2.5 (b). The elements and compounds at the top of the volcano plot have the lower Gibbs energy of adsorption and higher exchange current densities, which is indicative of superior reaction kinetics. The materials on the left of the peak of the volcano plot strongly adsorb the reactants, while materials on the right adsorb weakly. Evidently, both strong and weak adsorption results in slower reaction kinetics. Therefore, the position of a catalyst on the volcano plot gives a fair idea about its catalytic activity. The volcano plots for HER and OER catalysts are shown in Figure 2.6.

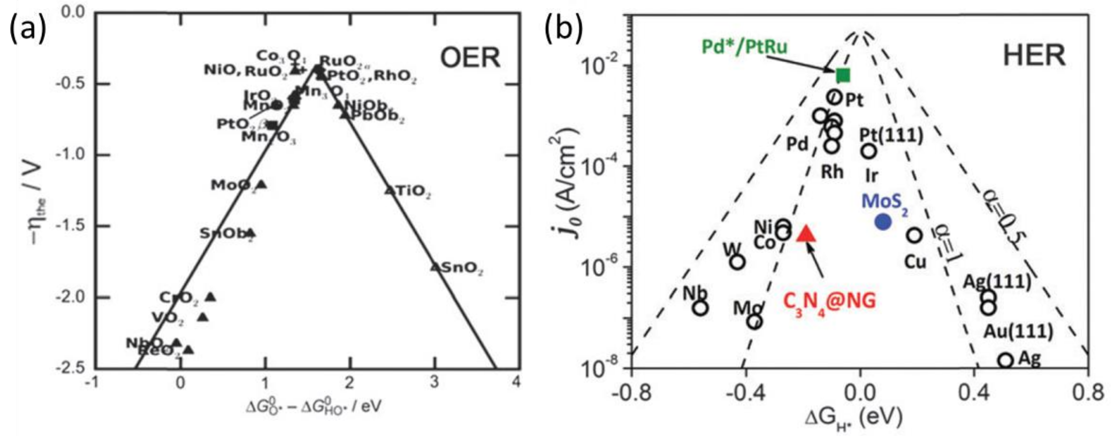

Figure 2.6 Volcano plots for HER and OER.[5]

As seen from the plots, catalysts with ΔG_H values closer to zero exhibit high activity. For OER the difference in adsorption energy of OH^* and O^* reaction intermediates (ΔG_O- ΔG_{OH}) should be near zero for better activity. Potentially, the volcano plot can be used to predict the performance of the composite system of elements. For instance, in the case of HER, the elements with negative ΔG adsorb the catalyst too strongly, whereas the ones with positive ΔG adsorb weakly. Thus, by synthesizing composite systems such as alloys and multi-metal compounds, we can expect to synthesize catalysts with tuned ΔG_H values. In conclusion, the Gibbs energy of the adsorption of reaction intermediates determines the activity of the catalyst. Therefore, the focus of the catalyst design should be to tune the electronic structure of the catalyst surface to facilitate optimized ΔG of adsorption of reaction intermediates. In the following section, we shall discuss various techniques that have been employed in the past to achieve this.

2.3 Strategies to improve the catalyst performance

Broadly, there are two strategies to improve catalytic activity[1]:

1. Increasing the number of active sites per unit weight of the catalyst: Active site of catalyst is the location on the catalyst where the reaction intermediates are adsorbed and are converted to products. Therefore, by increasing the number of active sites the number of molecules undergoing chemical reaction per second increases. Active sites can be increased by increasing the mass loading of the catalyst on the electrode. This approach however consumes a large amount of catalyst, hence is not economically viable. Alternatively, by careful design of the catalyst network more active sites can be exposed resulting in higher activity. Typically, in this approach, the catalyst is synthesized in the shape of nanosheets, nanowires, or nanoparticles with very large surface area per mass. Consequently, a larger number of active sites are exposed when compared to bulk materials. Figure 2.6 illustrates several strategies to achieve this.
2. Increasing the intrinsic activity of each catalytic site:

   In this strategy, the activity of the individual active site is improved by tuning the ΔG of adsorption of reaction intermediates and by enhancing the charge transfer at each active site. Notably, this approach is remarkably superior to the first approach. Firstly, the enhancement in the performance of the catalyst can be more than ten orders of magnitude,[1] in contrast to the first strategy where the increase in the performance can't be more than three orders of magnitude. Secondly, owing to the high activity, a lesser quantity of catalyst is sufficient. Consequently, there is a substantial cost reduction.

Nonetheless, in practice, both of these approaches are used complementary to each other to design and synthesize active catalysts.

In the following subsections, we shall discuss some of the strategies that have been adopted by the researchers in the past. While most of the strategies focus on improving intrinsic activity, some of them do incorporate both the strategies. We wish to bring to the reader's notice that research in the field of electrocatalysis is highly competitive. As a result, we observe a high volume of journal papers in this area throughout the year. Therefore, in the interest of the length of the thesis, we can only discuss a limited number of reported works, because of which the list is not exhaustive. Nonetheless, we believe the following strategies encapsulate the most general methods of catalyst design.

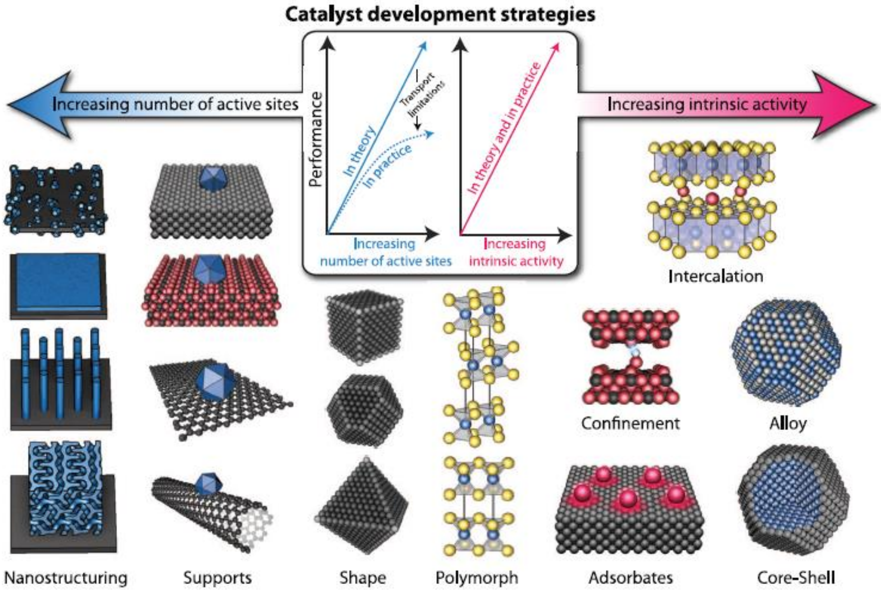

Figure 2.7 Illustration on ways of improving the performance of a catalyst.[1]

The various strategies are as follows:

2.3.1 Doping/multi-metal systems

Studies have shown that the catalytic activity is remarkably improved by elemental doping. The synergistic effect of the multiple elements outperforms the catalysts containing single element systems. A striking example of this is the outstanding performance of nickel-based catalysts by Fe doping. Ni-Fe LDH catalysts[8-12] have shown exceptional performance for OER and are potential candidates to replace the RuO_2 based catalysts. Furthermore, incorporation of vanadium[13] into NiFe LDH improved the performance elucidating the impact of doping and the synergistic effect in the multi-element system.

Zhang *et al*. synthesized the FeCoW nanoalloy system using the sol-gel process. The catalyst exhibited an overpotential of 191 mV on gold foam and 223 mV on the GC electrode.[14] Through DFT calculations, they proved that the FeCoW surface has the optimum energy for OH^- adsorption which is a critical step in the oxygen evolution mechanism. Further investigation revealed that $W_{0.5}Co_{0.4}Fe_{0.1}$ performed the best because the optimal ratio of W, Co and Fe inhibited the oxidation of Co^4 and promoted electron transfer from Co to Fe. The catalyst needed only 310 mV overpotential to attain 100 mA cm^{-2} and showed a low Tafel slope of 32 mV dec^{-1}.

Shen *et al*. synthesized Ni-Cu alloy[15] encapsulated in graphitic carbon shells using the sol-gel process followed by methane reduction. They observed shifts in the Raman spectra by varying the reduction time that validated the interaction of carbon shell and nickel core. This interaction is believed to be responsible for stability in harsh conditions and better performance. DFT calculations showed that $Ni_{43}Cu_{12}$ clusters encapsulated in single layer graphene afforded low ΔG_{H^*} of -0.03 eV which is very close to the ideal value of 0 eV according to Sabatier's principle. Also, calculations showed that increasing the thickness of the carbon degraded the performance.

Kuang *et al*. synthesized CoCu nanoalloy embedded in nitrogen-doped carbon framework[16] which was a suitable catalyst for ORR and HER reactions. They attribute the performance to nitrogen doping, high mass transfer, and synergistic coupling between copper and cobalt atoms. The catalyst could reach a current density of 10 mA cm^{-2} at 145 mV in an alkaline medium. The performance surpassed the cobalt embedded nitrogen-doped CNTs[17] reported by Zou *et al*. It follows that the synergistic effect of cobalt and copper could be the primary factor for superior performance.

Zhang *et al*. studied the effect of copper incorporation into the nickel oxide lattice by synthesizing nickel-copper oxide nanowires[18] with different ratios of Ni to Cu. They found that the insertion of copper reduces the bandgap from 3.20 eV to 2.96 eV and reduces the resistance. Also, the small difference in the atomic radius of two elements helped the easy formation of nanowires with different proportions. The copper-based catalysts for HER and OER are less studied. Therefore, it would be interesting to investigate the copper doping in other transition metal-based catalysts.

Studies from Xue's group showed the enhancement of HER activity in CoS_2 by copper incorporation[19] in the lattice. Doping of copper reduced the hydrogen adsorption energy, as well as aroused the inert S sites for catalytic action which were otherwise inactive. The EIS studies showed that charge transfer resistance for copper doped CoS_2 was much lesser and the electrochemical active surface area of doped samples were higher indicating an increased number of active sites with doping. With a mere 7% addition of copper, the catalyst showed incredible performance with only 52 mV η and a low Tafel slope of 42 mV dec^{-1}. The presence of multiple metals tunes the electronic structure of the material suitable for water splitting. Therefore, further research in this direction is encouraged.

2.3.2 Defect engineering

Introducing defects in the crystal structure alters the electronic structure of the material, which facilitates an improved catalytic action. For instance, Wang *et al*. showed through the DFT calculations that the introduction of oxygen vacancies[20] in Co_3O_4 could enhance the catalytic activity. Vacancies created new defect states in the bandgap, and the two electrons in the defect could easily get excited leading to better conductivity. Further studies by Xu *et al*. showed that plasma engraved Co_3O_4[21] showed better performance compared to pristine Co_3O_4. XPS studies revealed that some of the Co^{+3} reduced to Co^{+2} due to plasma engraving, resulting in a higher Co^{+2}/Co^{+3} ratio compared to the non-engraved samples. They believe this change in the electronic structure improved catalytic performance. The catalytic performance of the defect engineered Co_3O_4 nanosheets were ten times better than the pristine Co_3O_4 nanosheets proving the role of defects in catalysis. A similar study was done on $NiCo_2O_4$ by Bao *et al*. by creating oxygen vacancies[22] in $NiCo_2O_4$ nanosheets. Through DFT calculations they found that the oxygen vacancies reduced the water adsorption on the active sites which is crucial to oxygen evolution. Also, EIS studies showed a better charge transfer characteristic in defect induced samples.

Similar to anion vacancies, the studies by Liu *et al*. showed that even cation vacancies[23] in $CoSe_2$ nanosheets improved catalytic performance. They used DETA and ultrasound to exfoliate the nanosheets from the bulk samples. The PAS and XAFS studies revealed the cation vacancies in the nanosheets. According to their explanation, DETA pulls the cations from the nanosheets during the ultrasound treatment leading to the defects. Series of DFT calculations revealed that cation vacancies enhanced the water adsorption energies favoring the catalytic action. As a result, the performance was superior to the bulk samples. Qiao’s group synthesized NiO nanorods rich with oxygen vacancies[24] via the ion exchange route in the gas phase. Through DFT calculations they proved that the anion vacancies optimized the chemical and electronic properties to best suit the HER. The catalyst exhibited η_{10} of 110 mV and outperformed Pt catalyst at high overpotentials.

2.3.3 Encapsulation

Often, the nanoalloys synthesized for catalytic applications undergo corrosion which leads to their instability. Encapsulation is one of the strategies which protects the catalyst from the harsh environment. It is known that when a 2D crystal is coated on a metal surface, it will affect the Fermi energy states and surface work function which might promote adsorption of reactants[25] on the coated 2D element rather than the metal. The charge transfer from the metal can happen through the 2D crystal while it is being protected from the harsh environment. Usually, carbon is used for coating metal substrates. As previously discussed this strategy was used to encapsulate[15-16] NiCu and CoCu based nanoalloys. Similar studies carried out by Cui *et al*. showed that single-layer graphene encapsulated FeNi alloy[26] showed an outstanding OER performance. Through DFT calculations and experiments they found that single-layer graphene encapsulating the alloy promoted the electron transfer with ease, while the metal atoms inside altered the electronic structure of graphene that promotes oxygen evolution reaction.

2.3.4 Reduction of charge transfer resistance

The conductivity of the catalyst is an important parameter which makes the charge transfer between the reactants and the catalyst easier. A significant energy loss can be reduced through this approach. In general, transition metal oxides are poor conductors[4] of electricity because of which the catalytic performance is affected. So, researchers have sought to work on transition metal sulfides,[27-29] selenides,[30] nitrides,[31-32] and phosphides[33] which have a partial metallic character which is also proved using DFT calculations. Zeng's group synthesized Ni-Fe disulfide@oxyhydroxide[34] core-shell material which had highly conductive Ni-Fe disulfide core while the oxyhydroxide shell, that catalyzed the OER with a small η_{10} of 230 mV.

Typically, catalysts are synthesized in the powder form, and their application requires mixing them with conductive carbon and binder. This method increases the charge transfer resistance due to the presence of a binder and inhomogeneous mixing of carbon and the catalyst. One of the ways to minimize this is to directly grow the catalysts on the conductive substrates like nickel foam,[10] carbon cloth,[35-37], etc. Directly growing the catalyst on the conductive substrate has several advantages. Firstly, the catalyst doesn't need a binder to be attached to the electrode, and secondly the charge transfer resistance between the electrode and the catalyst is reduced. Zhang *et al*. synthesized $Cu(OH)_2$ nanowires on Cu foam by chemical reaction with ammonium persulfate and sodium hydroxide. The as-formed nanowires were coated with NiCo LDH[38] through electrodeposition and were directly used as a supercapacitor. There have also been reports where the catalyst is anchored on graphene, carbon black,[39] or CNTs[40] which makes the charge transfer easier.

2.3.5 Hierarchical structures

Zhou *et al*. synthesized $Ni@Ni_3S_2$ nanorods via the one-step hydrothermal process. The catalyst exhibited an extremely low overpotential of 157 mV.[41] Typically, nickel foam shows an anodic oxidation peak which destabilizes the catalytic performance. The $Ni@Ni_3S_2$ showed no such peaks indicating better activity compared to typical nickel-based catalysts. However, the Tafel slope for the catalyst was not impressive which they attribute to the complex reaction mechanism for charge transfer of nickel foam and Ni_3S_2 nanorods. They concluded that the synergistic effect between Ni_3S_2 nanorods, nickel oxide, and nickel foam could be the reason for superior performance. Nsanzimana *et al*. synthesized Fe-Co-2.3Ni-B nanoparticles using $NaBH_4$ as both the reducing agent and boron source.[42] The catalyst had Tafel slope of 38 mV dec^{-1} and η_{10} of 274 mV for OER. The XPS analysis showed a binding energy shift in the B 1s spectrum, indicating electron deficiency in boron making the metal electron-rich. The author believes that this could facilitate the sluggish OER process. Also, the incorporation of Fe into

Co-Ni-B brought about improved performance. The ECSA analysis showed the trimetallic boride had a higher electrochemical active surface area as compared to monometallic borides. Also, bimetallic/trimetallic systems are believed to reduce the thermodynamic barrier needed for O-O bond formation[43] leading to enhanced catalytic activity. Thus, the synergistic effect between the different transition metal is of great interest when compared to monometallic systems.

Xing *et al*. synthesized $Ni(OH)_2$@Ni/CC via a two-step electrodeposition method which showed remarkable performance[44] both for HER and OER. Through DFT calculations they confirmed that the synergistic effect between Ni and $Ni(OH)_2$ gives rise to such an improved performance where only 190 mV overpotential is needed to achieve 100 mA cm^{-2} for HER and 458 mV for OER. Yu *et al*. synthesized $Ni_{0.7}Fe_{0.3}S_2$ hierarchical flower-like structures on nickel foam[45] with excellent performance for both OER and HER. The performance was better than the NiFe LDH catalysts and NiS_2. They attribute the performance to change in the morphology from nanowalls to hierarchical flower-like structures, due to Fe doping which increased the exposed active sites. Also, Fe addition is believed to alter the electronic structure within NiS_2 making it more suitable for catalytic activity.

Xu *et al*. synthesized NiSe@CoP core-shell nanowire by a 2-step solvothermal method which showed remarkable HER performance[46] with only 91 mV in the alkaline medium. They attribute the performance to a large number of active sites, the synergistic effect between CoP shell and NiSe core, and fast electron transport. Gao *et al*. synthesized hierarchical $NiCo_2O_4$ microtubes[47] through the solvothermal process using PEG-200 as the solvent. The microtube was an assembly of $NiCo_2O_4$ nanowires leading to a mesoporous structure throughout the hollow cuboid. The catalyst had a very high BET surface area of 69.6 m^2/g with a pore size of 17.43 nm. Such morphology greatly facilitates active site exposure owing to its large surface area. Synthesis pathways like this open the door to designing similar complex structures in the same family of compounds like hydroxides, sulfides, and phosphides.

Dutta *et al*. synthesized NiSe@NiFeLDH/Ni foam[10] via a two-step hydrothermal method. The catalyst showed excellent performance with a low η_{100} of only 240 mV for OER and η_{100} of 276 mV for HER. The post-test XPS analysis revealed the formation of oxyhydroxides which are responsible for the performance. Also, they found the strong synergistic interaction between NiSe and NiFe LDH enhanced the performance. Ma *et al*. synthesized CuNiN catalyst[48] on nickel foam which showed excellent performance for HER both in alkaline and acidic environment. The current density reached as high as 100 mA cm^{-2} at η of 110 mV. Previous studies by the same author showed the poor stability of pure nickel nitrides, but in this case, CuNiN was found very stable in the acidic environment because of copper insertion. Through DFT calculations they could see that Ni was the active center while Cu acted as a promoter and enhanced catalytic stability. Thus, hierarchical structures can furnish interesting combination of materials that are active for catalysis and better charge transfer between electrode and the catalyst to achieve high rate of electrolysis.

2.3.6 Exfoliation and nanostructuring

Numerous studies have indicated that few atomic layer sheets perform much better compared to the bulk samples. Xie's group exfoliated ultrathin Fe_7S_8 nanosheets[49] from the bulk samples and found that the OER performance was approximately five times the bulk samples and revealed that even Fe could be an active center for OER. The catalyst exhibited η_{10} of 270 mV. The DFT calculations showed that overlap of d-orbitals of Fe^{+2} and Fe^{+3} in the ultrathin Fe_7S_8 renders the catalyst highly active for OER. Furthermore, another study on exfoliation of $NiPS_3$[50] also shows enhanced activity for OER compared to the bulk material.

So far, we discussed various techniques used to design and synthesize active catalysts for water splitting. In this work, we mainly focus on the alloying technique to tune the electronic structure of the host metal. In this regard the high throughput computational study by Norskov's group is noteworthy. They investigated the ΔG_H of a group of 256 surface alloys through DFT calculations and predicted the anticipated electrocatalytic activity from those results. As seen from Figure 2.8b the yellow and green color circles represent alloy systems that may exhibit high activity. All these are also closely related to the Volcano plot (Figure 2.8a). The left side of the volcano plot is filled with metals with negative ΔG_H (stronger H adsorption) while the right side has the metals with positive ΔG_H (weaker H adsorption). Intuitively, mixing these metals by alloying could bring about tuning of ΔG_H to near-zero values. However, the computational results are only suggestive of the anticipated activity of the alloys. For this reason, an investigation into the actual activity of catalysts through experiments is necessary to verify the theoretical predictions. Since we wish to synthesize earth-abundant catalysts we chose Ni as the host metal as it already possesses favorable ΔG_H closer to zero and a higher j_0 as seen from Figure 2.8a. To our knowledge, a detailed investigation into the catalytic activity of Ni through doping or alloying is not been done. The computational study shows Co, Cu, Fe, Rh, Pd, Ru, Ag, Ir, Cd, and Pt as the suitable solute elements which might produce active catalysts (Figure 2.8b). However, Ru, Rh, Pd, Ir, and Pt are expensive and Cd is extremely toxic. Consequently, we chose Cu, Fe, and Ag as a solute element in the synthesis of Ni-based alloys.

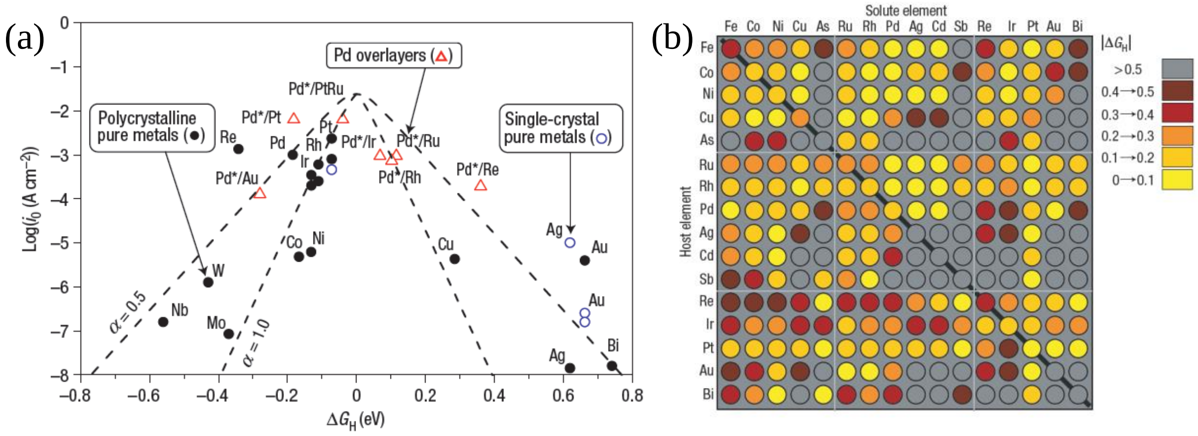

Figure 2.8 (a) Volcano plot for hydrogen evolution reaction, (b) computed ΔG_H for surface alloys of 256 alloy combinations.[51]

In the following section, we will briefly look at the parameters that hold key to assessing the activity of the catalysts for water splitting.

2.4 Parameters for catalyst characterization

In practice, the following parameters are measured to investigate the performance of a catalyst.

a. Overpotential to reach 10 mA cm^{-2} (η_{10}): According to theoretical calculations, the reduction of H$^+$ to hydrogen occurs at 0 V and the oxidation of oxygen at 1.23 V. However, due to slow kinetics and poor charge transfer the actual voltage at which the electrolysis starts is much higher than the theoretical voltage. This excess potential is known as overpotential as previously discussed. Also, since the framework of the electro-catalysis is to power the catalyst from the electricity generated from solar energy or other renewable sources of energy, 10 mA cm^{-2} current density[52] is chosen as a reference, which is the typical current density observed in the conversion of solar energy to electricity with 10% efficiency. Experimentally the overpotential is determined by carrying linear sweep voltammetry (LSV) test and measuring the overpotential necessary to reach 10 mA cm^{-2} in an electrolytic cell.

b. Tafel slope: Tafel slope is a measure of the rate of change of current density with the applied potential. Tafel slope is calculated from the Tafel equation: $\eta = A \log(j/j_0)$, where A is the Tafel slope. Experimentally this is calculated by plotting a graph between over-potential and log of current density, where the slope of the graph gives the Tafel slope. Tafel slope is a critical parameter that decides the intrinsic catalytic activity of the catalyst. Reaction mechanisms can be predicted to form the Tafel slope value.

c. Exchange current density (j_0): j_0 is the current density at the electrode under the equilibrium conditions, i.e., at zero overpotential. At zero overpotential, the energy is just sufficient to carry out a chemical conversion. As a result, the current density at this voltage is decisive to its intrinsic activity. Exchange current density is a measure of intrinsic rates of electron transfer between the electrode and electrolyte, providing an insight into the nature of bonding between the electrode and the reacting species. j_0 can be calculated from the Tafel plot.

d. Faradaic efficiency: Faradaic efficiency is the ratio of the actual quantity of gas produced during the electrolysis to the expected quantity calculated from the electrochemical equation.

e. Stability: The long-term stability of the catalyst is a significant parameter for the commercial application. Typically, one of the following[2] methods is used to estimate stability:

    1. Chronoamperometry (constant current) or chronopotentiometry (constant potential): Constant potential is applied corresponding to a current density slightly higher than 10 mA cm^{-2} for a long time, and the variation of current with time is measured to assess the stability. Alternatively, a constant current density of 10 mA cm^{-2} is applied for long durations and the voltage variation

with time is measured. A stable catalyst shows a constant voltage or current with time.

2. Cyclic voltammetry method: In the CV method, the cyclic voltammetry is carried out at high scan speeds (e.g. 100 mV s^{-1}) for more than 1000 cycles. Later, the LSV performance after the CV is compared with the LSV curves before the CV measurement. A stable catalyst shows the least change in the LSV plots.

f. Electrocatalytic surface area (ECSA): ECSA is a measure of surface area that is active for catalysis. Larger surface area for a given mass of the catalyst indicates the highly porous structure of the catalyst. The larger surface area exposes more active sites enhancing the performance. ECSA is measured by running a CV at different scan rates. From the data, the difference in current density (Δj) is plotted against scan rates. The double-layer capacitance C_{dl} is computed by dividing the slope of the graph by two. The ECSA is calculated by dividing C_{dl} by the specific capacitance of the material in the catalyst.

g. Specific activity: The ECSA can be further used to estimate the specific activity of the catalyst which is the activity of the catalyst when the effect of the surface area is normalized. In other words, specific activity is the current density offered by the catalyst whose surface is perfectly flat. In practice, specific activity is calculated by dividing the geometric current density by the ECSA.

So far, we elaborated on techniques of intelligent catalyst design and means to characterize them. The design of a highly active catalyst is certainly one of the significant steps in the fabrication of electrolyzers. In addition, the synthesis methods to fabricate the actual electrode for electrolyzers also substantially influence the cost and efficiency of the electrolyzer. In the following section, we will briefly touch upon the various methods used for catalyst synthesis and the challenges associated with them. In the final section, we will suggest an alternate method of electrode fabrication based on additive manufacturing which combines the synthesis of the catalyst and the assembly of the electrode in a single step.

2.5 Catalyst synthesis methods

The following are a few of the frequently used synthesis methods for catalyst synthesis.

1. Hydrothermal process: Metal salts along with other precursors that are soluble in solvents like water, ethanol, ethylene glycol, etc., are subjected to high temperature (100℃ to 200˚C) and high pressure. Under high pressure and temperature, metal salts are transformed into hydroxides, alloys, oxides, sulfides, selenides, etc., depending on the precursors used.
2. Solvothermal method/Oil phase synthesis: Used typically where precursors are soluble in organic solvents like DMF, oleylamine, dodecathethiol, etc. The reaction is often conducted under inert gas flow and high temperature (100℃ to 400˚C).
3. Solid-state synthesis: The precursor metal salts or metals are ground and loaded into a glass tube and sealed under vacuum. The glass tube is annealed at high temperature (300℃ to 1500℃) in a box furnace to transform the precursors to desired products.
4. Precipitation method: Often used to synthesize metal hydroxides. The pH of the metal salt solution is appropriately changed to precipitate metal hydroxides.
5. Ball milling: Used generally to mix multiple materials by shear mixing. The ball milling process leads to alloying through high energy shear mixing.
6. Chemical vapor deposition: Conducted in a tube furnace in the flow of gases such as CO_2, Argon, H_2, N_2, NH_3, etc. Metal salt precursors are heated at elevated temperatures to transform to desired products like oxides, alloys, sulfides, carbides, selenides, phosphides.

7. Pulsed laser deposition: target metal is irradiated with a laser that vaporizes the target material. The vapors are deposited on the desired target to form a thin film coating of desired materials.

The above processes have some commonalities that are worth the attention. In most cases, the chemical reaction is conducted at a high temperature at an extended period. Furthermore, the processes use a large quantity of solvent during synthesis and later during washing and drying of the synthesized products. Also, processes like CVD, sputtering, and PLD required controlled atmosphere viz. vacuum, or gases like CO_2, Argon, H_2, N_2, NH_3, etc. Suffice to say, all these processes are energy and resource-intensive and often use toxic solvents and chemicals. Furthermore, the actual fabrication of electrodes for electrocatalysis involves a few more steps. The synthesized catalyst powder is mixed with conductive filler and a binder in a solvent to form a slurry. The slurry is later coated on a conductive substrate like stainless steel, carbon cloth, carbon fiber paper, or metal foils and dried to finally form the electrode. Unfortunately, all the steps involved are tedious, energy-intensive, and also consume excess quantities of solvent. Also, the bonding of the catalyst to the electrode is not strong, and therefore, the durability of the fabricated electrodes is not good. In this connection, alternative synthesis methods that can solve these problems are desired.

2.6 Additive manufacturing route to catalyst synthesis

Other than the synthesis methods mentioned previously, researchers have attempted to follow some unconventional routes to material synthesis. In the following paragraphs, we will touch upon some of the recent reports that use additive manufacturing to fabricate electrodes. Wang *et al.* coated Cu-BTC MOF on 3D printed ABS framework which was used for removal of methylene blue.[53] The coating was done by step by step in-situ growth process. The catalyst could remove methylene blue within 10 minutes with 93.3% and 98.3% efficiency for a solution with 10 mg/L and 5 mg/L concentration respectively. They could also remove the Cu-BTC from the ABS framework to be reused for other applications. Michorczyk *et al*. synthesized Mn and Na_2WO_4 containing monoliths[54] by using 3D printed molds. The catalyst exhibited 23-25 % methane conversion, with high selectivity of 67-70 % towards C_2-C_3 hydrocarbons. Ambrosi *et al*. 3D printed helical shaped steel electrodes and subsequently electrodeposited IrO_2 on these electrodes. The catalyst showed good performance for OER reaction and also pH sensing. The author demonstrated that 3D printing could be used to fabricate custom shaped electrodes for specific applications [55]. Shah's group has printed various metal and metal oxide-based inks [56-57] such as Fe, Co, Ni, and Cu based oxides. Also, their ink formula is versatile and can be applied to any metal-based and metal oxide-based inks. The 3D printed Fe electrodes, which was used as an electrode for a metal-air battery. They also demonstrated 3D printing of Ni-Mn-Ga shape memory alloy by sintering the 3D printed ink containing these metallic powders. After sintering, the precursor formed a uniformly mixed alloy, and structures as fine as 300 µm diameters could be achieved. The printed part showed credible magnetic properties.[58] Sha *et al*. synthesized highly porous graphene foams with a mixture of nickel powder and sucrose.[59] By using a commercial CO_2 laser, the powder was sintered, and later the nickel was leached away to get the porous graphene foams. The foams showed a large porosity of 99.3%. The foams had a conductivity of 8.7 S cm^{-1}, owing to multilayered graphene structures formed during the synthesis. Heng *et al*. synthesized MoS_2/carbon hybrids[60] for hydrogen evolution reaction using a laser. The laser was used to transform the metal precursors to MoS_2 in a single step. Jin *et al*. synthesized metal alloy nanoparticles in solution by laser irradiation[61] of metal powder suspension. Lauren *et al*. patterned a large family of metal oxides using laser induced[62] thermal voxels. Cody *et al*. synthesized mixed metal oxides[63] by direct laser writing of aqueous precursors. Ruquan *et al*. synthesized metal oxides nanoparticles embedded in graphene nanosheets[64] by laser irradiation of modified PI tapes. Thus, usage of laser for nanomaterial synthesis is an interesting and effective approach and needs further exploration.

From these examples, we observe that the additive manufacturing process can be effectively used to synthesize nanomaterials. In particular, the laser-based material synthesis is an interesting approach as the process is often conducted under ambient pressure and room temperature. However, in most of the reported methods of laser synthesis the final product formed is nano/microparticles in the solution. The synthesized powder should be separated from the solution to be later used for electrode fabrication. However, the problems with the slurry formation and lack of strong bonding persist. In the case of methods that directly deposit metal oxides and alloys onto the substrate,[62-63] there is a need for post-processing to remove the solution precursor followed by washing and drying of the substrate. Therefore, there is a lack of an effective laser writing process in which a variety of materials can be directly deposited on a conductive substrate in a single step without the need for any post-processing steps. Developing such an additive manufacturing process could revolutionize the way electrodes are manufactured for electrolyzers. In this work, we have developed a method that particularly solves these problems. The details of the process shall be discussed in chapter 5 of this thesis.

2.7 Research gap and hypothesis

In the previous sections, we discussed elaborately on the latest advances in the field of catalyst design for water splitting. We also reviewed various conventional processes of nanomaterial synthesis and deliberated on the opportunity for additive manufacturing in the synthesis of nanomaterials and thin films. Based on this review we identified the following research gaps:

2.7.1 Enhancing the catalytic activity of Ni through alloying

The research advancement in the past few decades has resulted in the design and synthesis of active catalysts through a variety of approaches as discussed in the previous section. The relationship between the ΔG_H and activity of the catalyst is well established and there is a consensus among researchers about the relevance of volcano plot in the catalyst design. However, a systematic study on the effect of doping/alloying of different metals into Ni lattice is been lacking and there is a tremendous opportunity to further explore in that direction. Nickel has negative ΔG_H of approximately -0.28 eV, and we hypothesize that, by alloying/doping Ni with metals with positive ΔG_H, we could bring about alloys with ΔG_H near to zero. However, there is a need for a detailed investigation into the alloying concentration of dopants and their effect on the intrinsic activity. Inspired by this, we propose to synthesize Ni-based alloys and investigate the effect of doping/alloying concentration on the catalytic activity, charge transfer kinetics, ECSA. Further, we also propose to estimate the ΔG_H of the synthesized alloys through computational methods based on density functional theory.

2.7.2 Opportunity for laser-based AM in electrode fabrication

Conventional methods of electrocatalyst preparation include nanomaterial synthesis through processes such as hydrothermal, solid-state reaction, CVD, ball milling, etc. These processes are often carried out at high temperatures, often required a controlled atmosphere, hence are energy-intensive and time-consuming. Further, as these nanomaterials are in the powder form, the electrode preparation necessitates the formulation of catalyst slurry with binders and conductive fillers, which is coated on the conductive substrate. The process is tedious and does not produce robust electrodes. Because of all these reasons, it would be advantageous to have a synthesis process which could incorporate both the synthesis and fabrication of catalyst in a single step. Binder free electrode synthesis through processes like the hydrothermal method, CVD, sputtering, etc. have been successful in the past to realize this. However, they are still limited by the number of compatible substrates and the variety materials that can be synthesized. Inspired by this we propose to develop a laser-based synthesis method that can combine the synthesis and fabrication of electrode in a single step for a large family of metal alloys and oxides. Although various reports in the past have shown metal oxide and alloy synthesis, they often require added steps for electrode fabrication. The bottleneck in those methods is the lack of ink which can be dried over a substrate and later processed by laser for single-step fabrication. In this work, we propose to formulate a new ink formulation that can be dried over a variety of substrates and later processed using a high-power femtosecond laser to transform the ink into metal oxides or alloys. By using aqueous-based ink formulations that consist of dissolved metal salts we hope to exploit the exceptional degree of customization that can be achieved. Furthermore, by using a high-power femtosecond laser we hope to achieve the processing of metal salt-based inks which is difficult in continuous lasers.

2.8 Summary

In the beginning, we discussed the fundamental science of water splitting based on thermodynamics and reaction kinetics. Next, key concepts that are fundamental to designing active catalysts were elaborated. Later, we deliberated on various reported catalyst design approaches and synthesis methods. Finally, we pointed out the key research gaps present in the area of electrocatalysis as well as electrode fabrication methods. In the next chapter, we will report the results of our investigation of the effect of doping Cu and Fe on the catalytic activity of Ni towards hydrogen evolution reaction.

Chapter 3 Cu and Fe co-Doping of Ni Porous Network to Enhance its Activity for Hydrogen Evolution

In this chapter, we describe the synthesis, characterization, and catalytic activity of doped Ni porous network for water splitting. Initially, the rationale behind choosing Ni as the host and the choice of dopants is described. The subsequent section of this chapter deliberates on the synthesis, detailed material characterization of the Cu and Fe co-doped Ni porous network. Electrochemical characterizations to evaluate the catalytic activity of the catalysts are carried out to arrive at an optimized doping concentration of Cu and Fe. In the next part, density functional theory calculations are conducted to investigate the effect of doping on the electronic structure of Ni. Finally, the durability of the catalyst is investigated by chronopotentiometry test, followed by the characterization of the catalyst after the long-term durability test.

3.1 Introduction

The previous chapter deliberated deeply into the fundamentals of water splitting and the various techniques employed to design and synthesize highly active electrocatalysts. In this chapter, we will discuss the impact of doping of Cu and Fe atoms into Ni lattice on the electrocatalytic activity of nickel.

To accomplish compatible integration of the catalysts and for efficient overall water splitting, the coupling of the HER and OER catalysts in a common electrolyte is essential.[65] Lack of stability of catalysts in acidic medium coupled with sluggish OER kinetics causes the acid electrolysis lesser favorable than the alkaline electrolysis.[66] Advancements in the past decade have resulted in the synthesis of earth-abundant catalysts demonstrating modest stability and activity for OER in the alkaline medium.[4, 8, 67-68] However, since alkaline electrolysis is not favorable to HER, the activity of the reported catalysts is not appealing in the alkaline medium. For instance, the activity of the state of the art Pt/C catalyst in the basic medium is two orders of magnitude lesser than its activity in the acidic medium.[69] Many of the active catalysts reported for HER in alkali constitute expensive and scarce elements like Pt,[70-72] Rh,[73], and Ru.[66]

In view of this, the fundamental understanding of the reaction mechanism is crucial. HER is a two-electron process, which involves adsorption of hydrogen on the catalyst surface. The Gibbs energy of hydrogen adsorption determines the catalytic activity of the surface, which in the case of HER should be near to zero for superior activity.[51] The adsorption energy is solely dependent on the electronic structure catalyst, which can be engineered to promote reaction pathways with lower energy barriers by doping of suitable elements.[74-76] Doping of more than one element shown to be effective in tuning the adsorption energies of catalysts for HER.[70, 73] Furthermore, the efficiency of the catalyst depends on both the quantity of the active sites and the intrinsic activity of the individual active site.[77] Therefore, the choice of dopants and the concentration of the dopants will play a decisive role in designing the catalyst for HER.

In this context, Ni is one of the suitable metals among the earth-abundant elements to be the host for doping, owing to its suitable Gibbs energy of hydrogen adsorption ($\Delta G_H \approx -0.28$ eV)[78] on (111) plane.. In this context, computational studies by Greeley *et al*. suggest the plausible boost in the HER performance of nickel by doping of atoms with positive adsorption energies such as copper, silver, and bismuth.[51] Also, NiFe based catalysts have been reported to exhibit good activity towards HER.[13, 45, 79] Inspired by these findings, we chose earth-abundant copper and iron as dopants to tune the catalytic activity of nickel. The following section describes the synthesis and characterization methods which were employed for this work.

3.2 Materials and methods

3.2.1 Chemicals

Nickel (II) sulfate hexahydrate ($NiSO_4.6H_2O$, Sigma Aldrich), copper (II) sulfate pentahydrate ($CuSO_4.5H_2O$, Sigma Aldrich), iron (III) nitrate nonahydrate ($Fe(NO_3)_3.9H_2O$), nickel (II) nitrate hexahydrate ($Ni(NO_3)_2.6H_2O$, Sigma Aldrich). silver nitrate ($AgNO_3$, 0.1 M, Sigma Aldrich), urea (NH_2CONH_2, Sigma Aldrich), ethylene glycol (Sigma Aldrich), Pt/C 20% wt. (Fuel cell research) and Nafion (5% solution, Sigma Aldrich) were used without further treatment.

3.2.2 Synthesis of Cu and Fe co-doped Ni porous networks

Cu, Fe co-doped $Ni(OH)_2$ nanowires were synthesized by a typical hydrothermal method. Firstly, 0.526 g (2 mmol) of $NiSO_4.6H_2O$ was dissolved in 25 ml deionized (DI) water. Later, $CuSO_4.5H_2O$ and $Fe(NO_3)_3.9H_2O$ were added corresponding to the doping concentrations of Cu and Fe. To the above solution, 0.601 g (10 mmol) of urea was added and dissolved under magnetic stirring for 15 minutes. Finally, DI water was added to the above solution to make the final solution volume to 30 ml and was transferred to a 45 ml stainless-steel Teflon-lined autoclave and heated in an electric oven at 120 ^{0}C for 12 hours. Later, the samples were washed with DI water and ethanol thrice and dried in the oven at 60 ºC for 12 hours. Cu, Fe co-doped $Ni(OH)_2$ nanowires powder was transferred to an alumina boat and annealed in a tube furnace with hydrogen gas. The thermal reduction of hydroxides was done at 400 ºC for 2 hours with a ramping rate of 3 ºC per minute.

3.2.3 Sample characterization

The phase of the synthesized samples was determined using Shimadzu XRD-6000 with Cu-K_α radiation ($\lambda = 1.5406$ Å) operated at 40 kV and 30 mA. The synthesized samples were dispersed in ethanol and were drop-cast on a glass slide and used for the measurement. JEOL field emission scanning electron microscope (JSM-7600F, JEOL Ltd. Tokyo, Japan) was used to image the nanostructures. High-resolution imaging, elemental mapping, EDX analysis, and high angle annular dark-field scanning transmission electron microscopy (HAADF-STEM) were performed by TEM (JEOL JEM 2100, 200 kV). The surface composition of the samples was studied by X-ray photoelectron spectroscopy from Theta Probe electron spectrometer. The composition of the sample was estimated using an Inductively coupled plasma-optical emission spectrometer (PerkinElmer Optima 8000) in which the average of three measurements was considered for the estimation of the concentration of each element. Brunauer-Emmett-Teller (BET) surface area was measured by N_2 adsorption-desorption isotherms at 77 K using Tri-star II 3020 model.

3.2.4 Electrochemical measurements

Electrochemical measurements were done using Solartron analytical equipment (Model 1470E). For the powder samples, 5 mg of powder was dispersed in 950 ul of isopropanol (IPA) and 50 µl of Nafion solution and ultra-sonicated for 1 hour. 5-40 µl of this uniform dispersed slurry was drop cast on a glassy carbon electrode (GCE-3mm) and allowed to dry. The tests for HER performance were conducted using a typical 3 electrode cell with Hg/HgO as the reference electrode, Pt mesh as the counter electrode for OER, graphite electrode as counter electrode for HER, and 1 M KOH as the electrolyte. The HER performance was measured by linear sweep voltammetry (LSV) from -0.7 V to -1.7 V vs Hg/HgO at a scan rate of 2 mV per second, and OER performance was measured from 0 V to 1 V vs the reference electrode at a scan rate of 1 mV per second. The measured potential was converted to potential vs. reversible hydrogen electrode (RHE) by using the relation $E_{vsRHE} = E_{vsHg/HgO} + 0.098 + 0.059^{*}$ pH. The durability tests for $NiCu_{0.05}Fe_{0.025}$ PNW were carried out by chronopotentiometry test by applying a constant current density of 20 mA cm^{-2} for 30 hours and measuring the voltage during the process for overall water splitting and applying a constant current density of 10 mA cm^{-2} for 20 hours for HER. The durability of the $NiAg_{0.4}$ 3DPNC catalyst was tested by chronoamperometry test by applying a constant voltage of -76 mV vs RHE for 80 hours and measuring the current during the process. Furthermore, 5000 cyclic voltammetry sweeps between -0.9 V to -1.7 V versus Hg/HgO reference electrode were conducted to investigate the durability of the catalyst. For X-ray diffraction (XRD) and scanning electron microscopy (SEM) characterization of post-stability test samples, the catalyst slurry was coated on carbon cloth and the chronopotentiometry test was repeated as described above. To estimate the electrochemical active surface area (ECSA) of the samples, cyclic voltammetry (CV) scans were performed between 0.674 V to 0.774 V vs. reference hydrogen electrode at various scan rates from 2 mV s^{-1} to 12 mV s^{-1} The difference between the current densities at 0.724 V during the forward and reverse scan ($j_{anodic} – j_{cathodic}$) was plotted against the scan rate. The slope of the plot equals twice the double layer capacitance C_{dl}. The roughness factor was calculated by dividing the C_{dl} by the specific capacitance (40 uF cm^{-2}), which was later used for ECSA normalization.[80] Electron impedance spectroscopy (EIS) measurements were done in Autolab PGSTAT302 (Eco Chemie, Netherlands) potentiostat by varying the frequency from 100 kHz to 0.1 Hz with an amplitude of 10 mV. The solution resistance R_s was estimated from the x-intercept of the plot of -Z” vs Z’ in the high-frequency range, which was later used for the iR correction.

3.2.5 Computational methods

All the calculations were adopted by density functional theory (DFT) methods and implemented in the Vienna Ab initio Simulation Package (VASP)[81] code. The electron-ion interaction was described by using the projector augmented wave (PAW) method.[82] The exchange-correlation was calculated by the generalized gradient approximation (GGA) functional as parametrized by Perdew-Burke-Ernzerhof (PBE). For valence electron calculation, a 400 eV cutoff energy for the plane-wave basis set was used. Self-consistent field (SCF) calculations were performed with the force convergence criterion and energy of 0.02 eV $Å^{-1}$ and 10^{-6} eV, respectively. The Brillouin zone was sampled by using a 6×6×1 Monkhorst-Pack k-point mesh in the structure optimization. A vacuum thickness of 20 Å selected to prevent the interactions between two adjacent periodic structures along the perpendicular direction. In all cases, spin-polarized considerations were taken into account.

The Gibbs free energy (ΔG_H) of hydrogen atoms adsorption on metal-doped Ni (111) surfaces were calculated by:

$$\Delta G_{\mathrm{H}} = \Delta E_{\mathrm{nH}} + \Delta E_{\mathrm{ZPE}} - T\Delta S_{\mathrm{H}} \tag{3.1}$$

where ΔE_{ZPE} is the difference in zero point energy, and ΔS_{H} is the entropy difference between the gas phase and the adsorbed state, respectively. ΔE_{nH} is the chemisorption energy of the n^{th} H atoms, which was given by:

$$\Delta E_{\mathrm{nH}} = E_{\mathrm{M+nH}} - E_{\mathrm{M+(n-1)H}} - \frac{1}{2}E_{\mathrm{H_2}} \tag{3.2}$$

where $E_{\mathrm{M+nH}}$ and $E_{\mathrm{M+(n-1)H}}$ are the total energy of metal-doped Ni (111) surfaces with n*th* and (n-1)*th* H atoms adsorption. And E_{H2} is the total energy of molecule hydrogen in the gas phase. The computed frequencies of H_2 gas are 42 cm^{-1}, 58 cm^{-1}, and 4345 cm^{-1} which agree well with previous studies.[83-84] While the ΔZPE was calculated to be 0.04 eV for H atom adsorption on Ni (111) surfaces, which do not differ notably with the adsorption sites and the doping of different metal atoms. The hydrogen adsorption entropy is give by $\Delta S_H = \frac{1}{2} S_{H2}$, in which S_{H2} is the entropy of hydrogen molecule in the gas phase at 300 K and 1 bar presure.[85] The value of ΔE_{ZPE}-$T\Delta S_H$ was equal to 0.245 eV.

3.3 Results and Discussion

3.3.1 Characterization of Cu and Fe co-doped Ni porous networks

The hydrothermal process was used to synthesize Cu, Fe doped $Ni(OH)_2$ nanowires. Later, the synthesized hydroxide nanowires were annealed in a tube furnace with hydrogen gas flow at 400 ºC to transform to porous networks (see Experimental Section for details). To study the effect of doping of Cu and Fe separately on activity for HER, a series of samples were synthesized with varying doping compositions. Firstly, the Cu doping concentration was varied from 1% to 10% to find the optimum doping concentration. Later, the Cu doping concentration was fixed at 5% and Fe doping concentration was varied from 1% to 5%. X-ray diffraction measurements were carried to investigate the phase and crystallinity of the synthesized powder. The diffraction peaks of all the samples as shown in Figure 3.1a-b located at 44.48º, 51.83º, and 76.35º are assigned to (111), (200), and (220) planes of nickel (PDF no. #040032941). Identical peaks in all the samples reveal the homogeneous distribution of dopant atoms (Cu and Fe) in the nickel lattice. Furthermore, the lattice parameters (Table 3.2) of the doped samples were computed from the XRD spectra. Evidently, the doping of Cu and Fe increased the lattice parameter of the doped samples revealing expansion of the Ni lattice on doping with Cu and Fe. The inductively coupled plasma-optical emission spectroscopy test (ICP-OES) on the $NiCu_{0.05}Fe_{0.025}$ PNW sample confirms the formation of alloy with a composition very close to the expected composition from synthesis as shown in Table 3.1. X-ray photoelectron spectroscopy (XPS) studies were carried out to investigate the surface chemical composition and the chemical states of the constituent elements for $NiCu_{0.05}Fe_{0.025}$ PNW and pristine Ni PNW. XPS survey spectrum for $NiCu_{0.05}Fe_{0.025}$ PNW (Figure 3.2a) reveals characteristic peaks of Ni, Cu, Fe, and oxygen.

Table 3.1 ICP-OES test results for $NiCu_{0.05}Fe_{0.025}$ PNW.

Element	Concentration in mg/L (average of 3 readings)	Atomic percentage (%)	Expected concentration from the synthesis (%)
Ni	66.43	92.24 ± 0.02	93
Fe	1.924	2.73 ± 0.04	2.32
Cu	4.024	5.03 ±0.04	4.65

The core-level XPS spectra of $NiCu_{0.05}Fe_{0.025}$ PNW in the Ni 2p, Cu 2p, and Fe 2p region are shown in Figure 3.2(b-f). For the Ni 2p spectrum two distinct sets of peaks can be observed corresponding to distinct oxidation states of nickel. The peaks at 852.6 eV and 870.3 eV correspond to Ni (0) oxidation state.[86] The Ni $2p_{3/2}$ peak at 855.7 eV along with Ni $2p_{1/2}$ peak at 873.3 eV with spin-orbital splitting energy of 17.6 eV and characteristic satellite peaks at 861.2 eV and 879.8 eV indicate the existence of Ni in the Ni^{2+} oxidation state.[87]

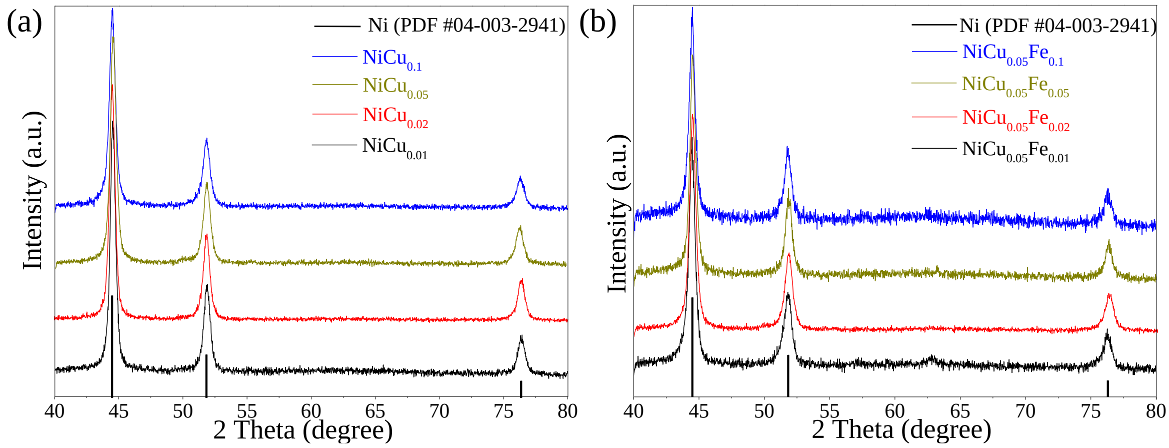

Figure 3.1 XRD patterns of (a) Cu doped Ni PNW with different Cu concentrations, and (b) Cu, Fe co-doped Ni PNW with different Fe concentrations.

Table 3.2 Computed lattice parameters of the Cu and Fe co-doped Ni from the XRD spectra.

Alloy system	Computed lattice parameter from XRD spectra (Å)	Alloy system	Computed lattice parameter from XRD spectra (Å)
FCC Ni	3.5250	$NiCu_{0.10}$	3.5315
FCC Cu	3.6149	$NiCu_{0.05}Fe_{0.01}$	3.5265
FCC Fe	3.5710	$NiCu_{0.05}Fe_{0.025}$	3.5289
$NiCu_{0.01}$	3.5251	$NiCu_{0.05}Fe_{0.05}$	3.5326
$NiCu_{0.02}$	3.5258	$NiCu_{0.05}Fe_{0.025}$ post HER	3.5280
$NiCu_{0.05}$	3.5261		

In contrast, the Ni $2p_{3/2}$ and Ni $2p_{1/2}$ peaks of the Ni (0) state of the pristine Ni PNW are located at 852.25 eV and 869.58 eV (Figure 3.2(c-d)). Thus, the electron binding energy is shifted to higher energies in $NiCu_{0.05}Fe_{0.025}$ PNW owing to the doping of Cu and Fe. This is further seen from the negative shift of Ni^{2+} $2p_{3/2}$ peak at 855.26 eV and Ni^{2+} $2p_{1/2}$ peak at 872.86 eV for the

Ni PNW. The core-level XPS spectrum of $NiCu_{0.05}Fe_{0.025}$ PNW in the Cu 2p region is shown in Figure 3.2e.

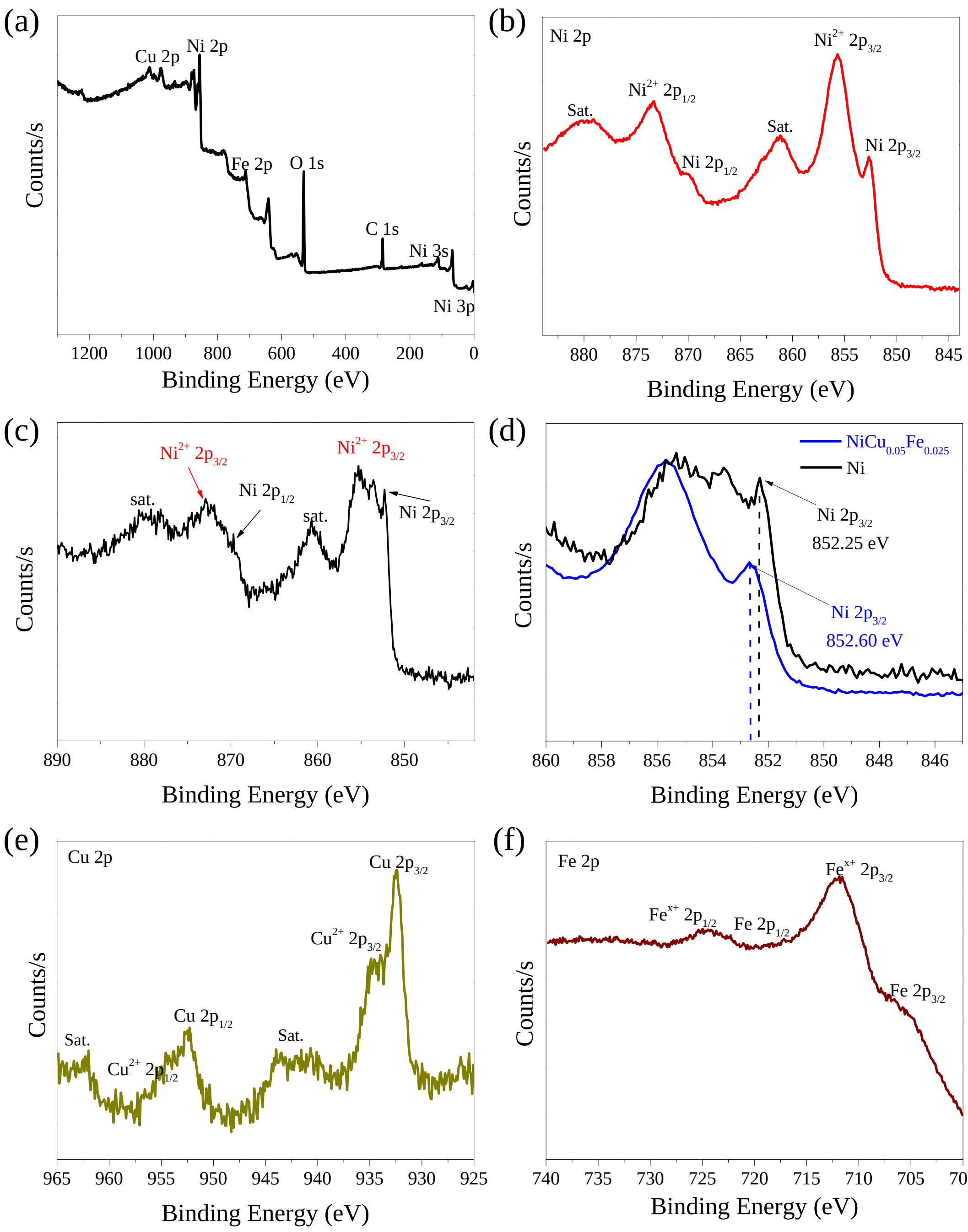

Figure 3.2 (a) XPS survey spectrum of $NiCu_{0.05}Fe_{0.025}$ PNW. Core level XPS spectra of (b) $NiCu_{0.05}Fe_{0.025}$ PNW in Ni 2p region, (c) pristine Ni in the Ni 2p region, and core level XPS spectra of $NiCu_{0.05}Fe_{0.025}$ PNW in (d) Cu 2p region, and (d) Fe 2p region.

Peaks at 932.7 eV and 952.3 eV in the Cu 2p spectrum correspond to Cu (0) oxidation state. The smaller peaks at 934.6 eV and 954.5 eV along with satellite peaks at 941.3 eV and 944.3 eV indicate the existence of Cu^{2+}.[88] Furthermore, the Fe 2p spectrum (Figure 3.2f) reveals a small peak at 706.8 eV corresponding to Fe (0) state[86] and larger peaks at 711.6 eV and 724.3 eV confirm the presence of oxidized Fe species. Thus, the surface composition of $NiCu_{0.05}Fe_{0.025}$ PNW reveals the partial oxidation of the metallic surface and confirms the presence of all three metals Ni, Fe, and Cu on the catalyst surface.

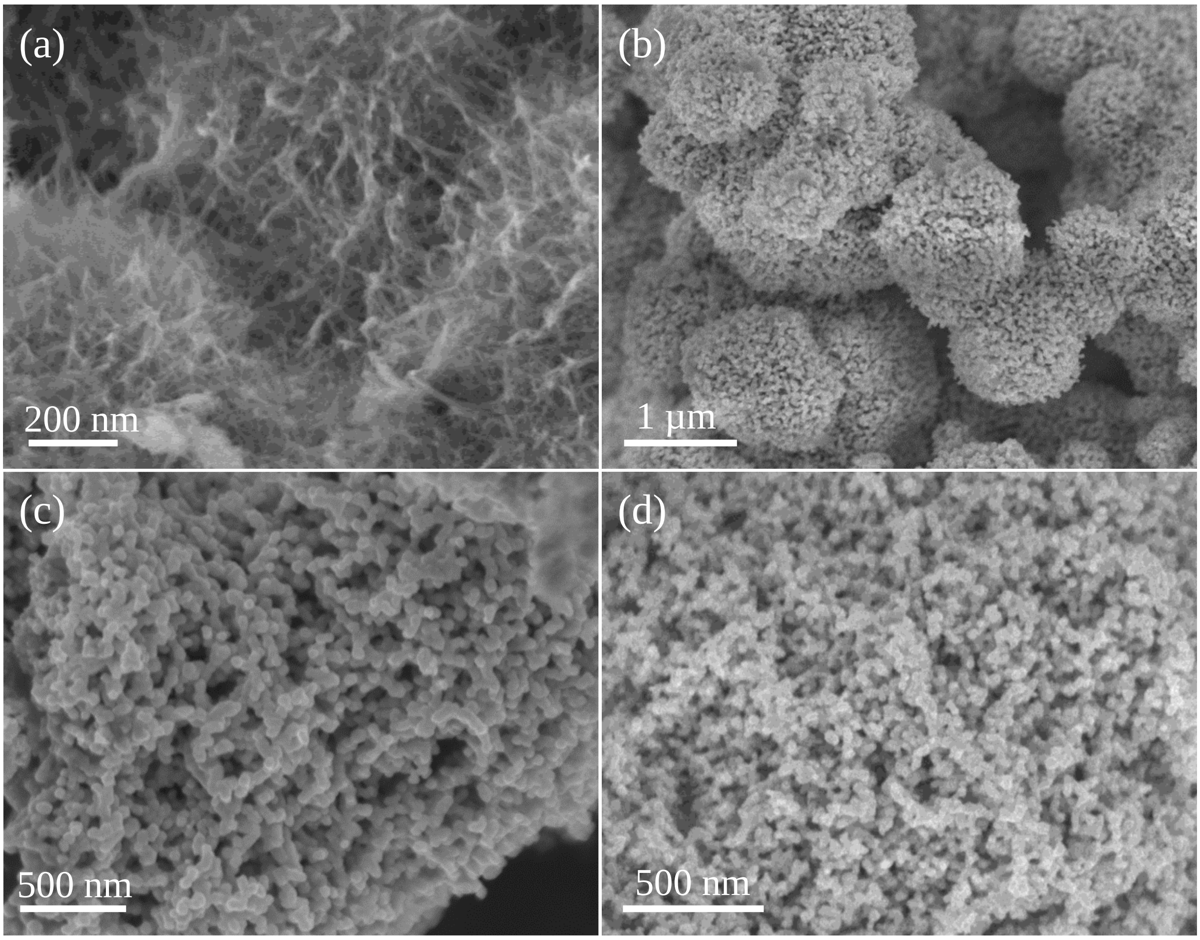

Figure 3.3 FESEM image of (a) $NiCu_{0.05}Fe_{0.025}(OH)_2$ nanowire precursor, (b-c) $NiCu_{0.05}Fe_{0.025}$ PNW, and (d) Ni PNW.

The morphology of the synthesized samples was investigated from FESEM imaging. The FESEM image of Cu, Fe co-doped $Ni(OH)_2$ reveals the formation of thin nanowires as depicted in Figure 3.3a. After the reduction in the tube furnace with hydrogen flow, the nanowires were transformed into highly porous network clusters of ~ 1 µm comprising numerous nanoparticles of ~ 80 nm as shown in Figure 3.3(b-c). The morphology of the pristine Ni PNW is similar to that of $NiCu_{0.05}Fe_{0.025}$ PNW as seen from Figure 3.3d. The TEM images shown in Figure 3.4a illustrates the porous network morphology with abundant pores throughout the structure with the dimensions between 10 nm and 100 nm. The porous network morphology is suitable for catalytic activity owing to high surface area and enhanced diffusion of electrolyte for better charge transfer and greater exposure of active sites. The HRTEM image (Figure 3.4c) for the $NiCu_{0.05}Fe_{0.025}$ PNW reveals the interplanar spacing of 0.203 nm corresponding to the exposed (111) plane of nickel (PDF #04-003-2941). Further, the selected area electron diffraction pattern (SAED) reveals the polycrystalline nature of the material with multiple bright spots and rings corresponding to (111), (200), and (220) planes of Ni (Figure 3.4b). The HAADF image and STEM-EDX elemental mapping images as shown in Figure 3.4(d-g) confirm the homogeneous distribution of Ni, Fe, and Cu atoms throughout the nanocluster.

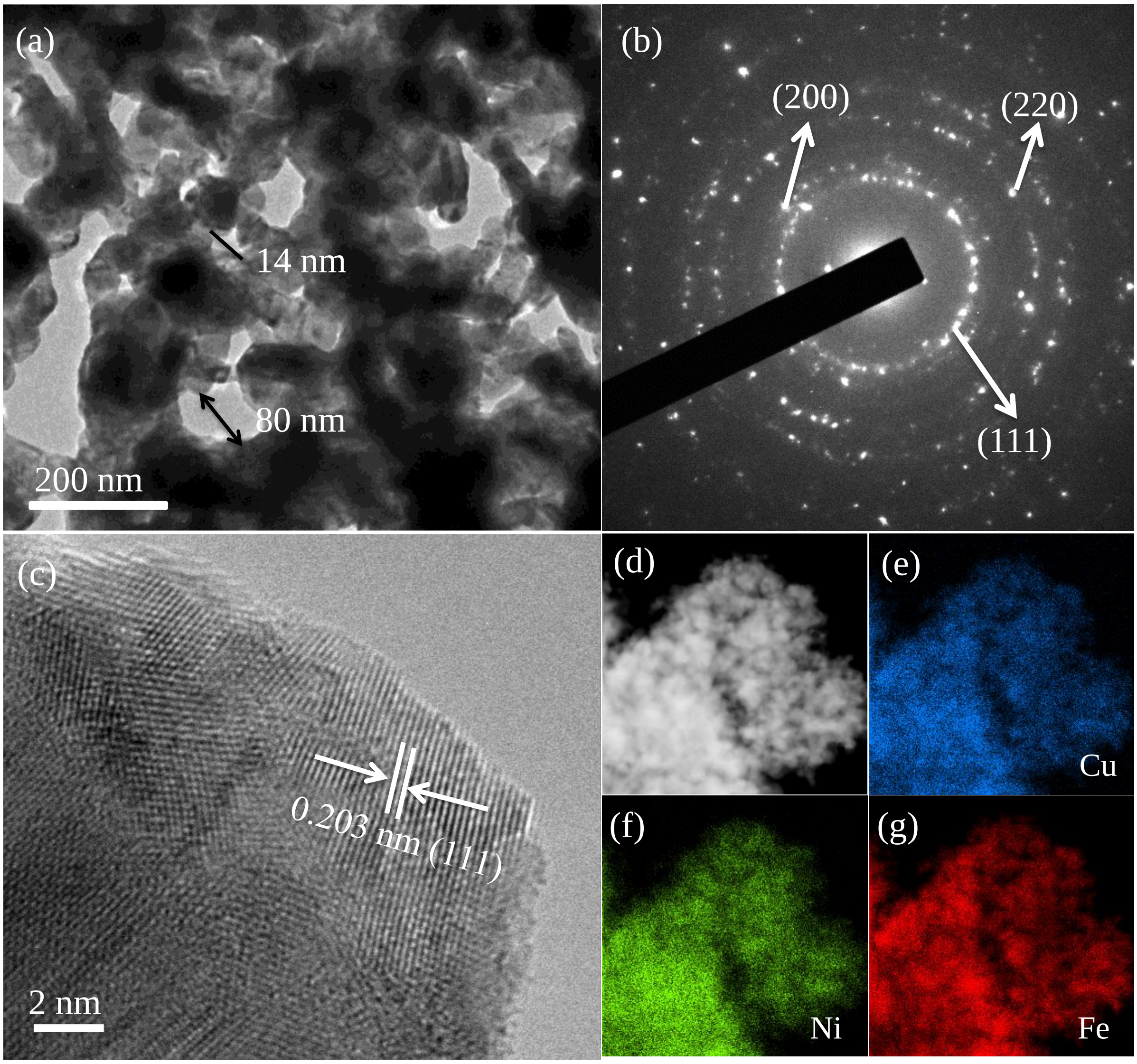

Figure 3.4 (a) Transmission electron microscopy image, (b) SAED pattern, (c) HRTEM image, (d) HAADF-STEM image, and (e-g) corresponding STEM-EDX elemental mapping images of $NiCu_{0.05}Fe_{0.025}$ PNW.

3.3.2 HER activity of Cu and Fe co-doped Ni porous networks

To investigate the effect of Cu doping concentration on the performance of catalyst for HER, four different samples were synthesized with Cu doping concentrations of 1%, 2%, 5%, and 10%. The catalytic performance was measured in 1 M KOH solution in a typical three-electrode cell with Hg/HgO as the reference electrode and graphite counter electrode and catalyst loaded glassy carbon electrode as the working electrode. To minimize the capacitive current during the tests, a low scan rate of 2 mV s^{-1} was used. To investigate the effect of mass loading on the catalytic performance, the overpotential at 10 mA cm^{-2} for various mass loadings was measured. All the overpotentials reported here are with respect to the reference hydrogen electrode. Figure 3.5 illustrates the variation of overpotential for HER with mass loading for Ni PNW, $NiCu_{0.05}Fe_{0.025}$ PNW, and Pt/C catalysts. Based on the results the mass loading corresponding to the saturation region in the plot was used for further studies viz. 2.4 mg cm^{-2} for Cu, Fe co-doped Ni PNW and Ni PNW, and 0.4 mg cm^{-2} for Pt/C catalyst.

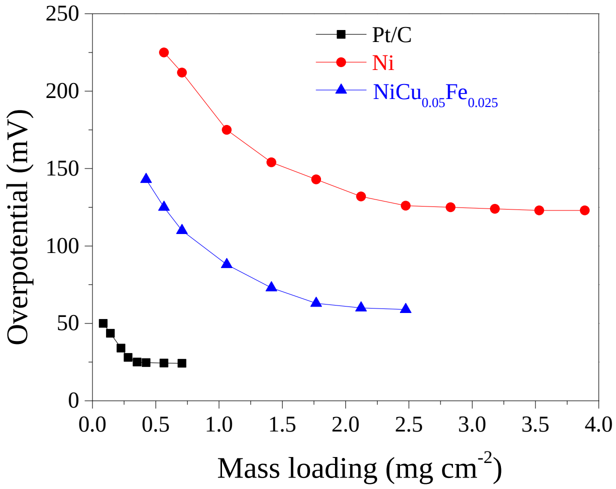

Figure 3.5 Variation of overpotential at 10 mA cm^{-2} with mass loading for various catalysts for hydrogen evolution reaction.

Figure 3.6a depicts the linear sweep voltammetry (LSV) curves for HER with iR correction. Catalysts with 1% ($NiCu_{0.01}$) and 2% ($NiCu_{0.02}$) Cu doping concentrations exhibit η_{10} of 90 mV and 86 mV, respectively, exhibiting enhanced activity compared to the pristine nickel PNW, which has a larger overpotential of 123 mV. On further increasing the doping concentration to 5% ($NiCu_{0.05}$), an active HER catalyst was obtained with a low overpotential of 74 mV (Figure 3.6b). However, further increasing the doping concentration to 10% ($NiCu_{0.1}$) did not improve the HER activity, as seen from the increased η_{10} of 87 mV for the $NiCu_{0.1}$ PNW.

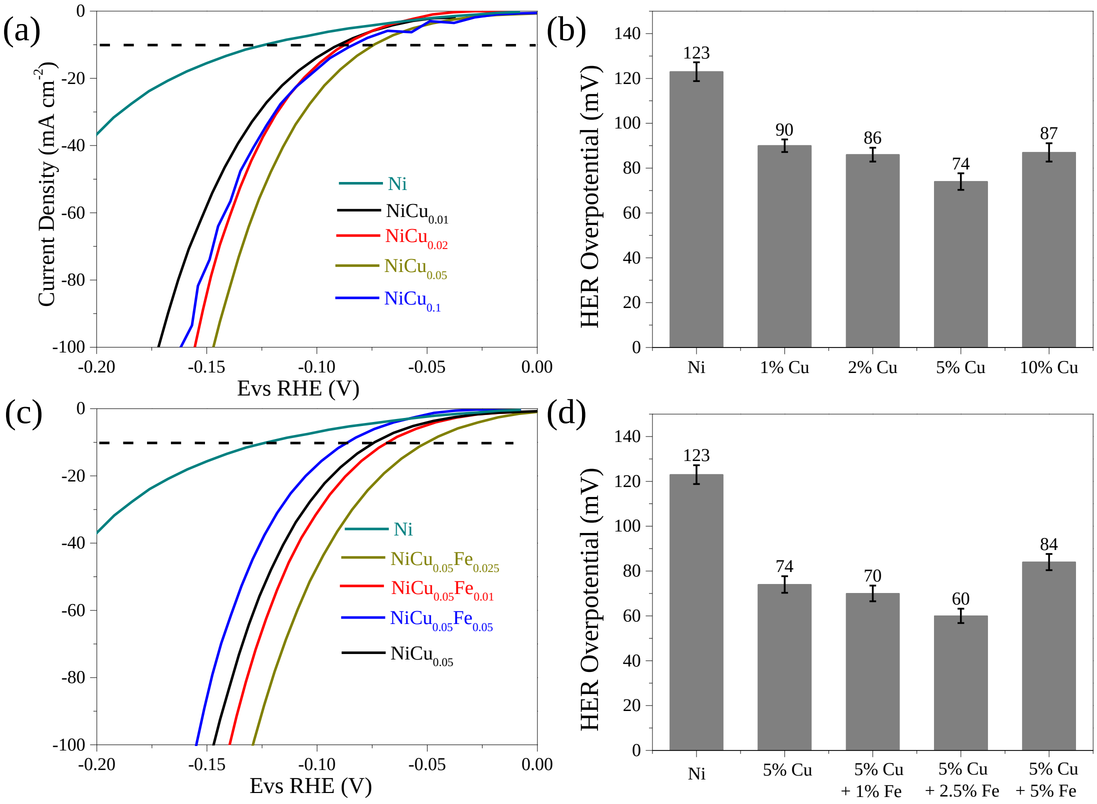

Figure 3.6 HER polarization curves of (a) Cu doped Ni PNW for different Cu doping concentration, (c) Cu, Fe co-doped Ni PNW for different Fe doping concentration, and plot of the variation of overpotential at 10 mA cm^{-2} for varying (b) Cu doping concentration, and (d) Fe doping concentration in 5% Cu doped samples.

Also, the Tafel slope of NiCu$_{0.05}$ PNW (61.6 mV dec^{-1}) is significantly lower than the Tafel slope of Ni PNW (137.45 mV dec^{-1}) revealing the enhanced reaction kinetics in the doped samples. Thus NiCu$_{0.05}$ PNW with 5% Cu doping exhibited the best HER activity (Figure 3.6a-b) among various Cu doped samples. Further, to investigate the effect of Fe doping on the catalytic activity, Fe doping concentration was varied from 1% to 5%, while maintaining a fixed Cu doping concentration of 5%. The HER LSV curves depicted in Figure 3.6c reveal that NiCu$_{0.05}$Fe$_{0.01}$ (1% Fe doping) and NiCu$_{0.05}$Fe$_{0.025}$ (2.5% Fe doping) catalysts showed excellent HER activity with low η_{10} of 70 mV and 60 mV, respectively. However, on the further increase of Fe doping concentration, the HER performance was slightly reduced, as revealed from the higher overpotential of 84 mV for $NiCu_{0.05}Fe_{0.05}$ PNW. Thus, among the Cu, Fe co-doped PNW, $NiCu_{0.05}Fe_{0.025}$ PNW exhibited the best HER activity with a low η_{10} of 60 mV outperforming both pristine Ni PNW and Cu-doped PNW (Figure 3.7a-b). The activity of the $NiCu_{0.05}Fe_{0.025}$ PNW is slightly inferior to that of Pt/C (20% wt. loading) catalyst, which showed low η_{10} of 30 mV. Tafel slope of $NiCu_{0.05}Fe_{0.05}$ PNW (60.8 mV dec^{-1}), is lower than both pristine Ni PNW (137.45 mV dec^{-1}) and $NiCu_{0.05}$ PNW (61.8 mV dec^{-1}), but larger than that of Pt/C (32 mV dec^{-1}). A modest Tafel slope of 60.8 mV dec^{-1} indicates the Volmer reaction as the rate-determining step ($E_{cat} + H_2O \rightarrow E_{cat}H_{ads} + OH^-$). The Nyquist plots (Figure 3.7c) also revealed large charge transfer resistance for Ni PNW, which in contrast is significantly lower in the doped samples. Thus, enhanced charge transfer kinetics was observed in the doped samples. Furthermore, $NiCu_{0.05}Fe_{0.025}$ PNW reached a high current density of 100 mA cm^{-2} at a low overpotential of 130 mV surpassing the activity of the noble metal Pt/C (20% wt.) catalyst revealing good mass transfer kinetics at higher potentials. The activity of $NiCu_{0.05}Fe_{0.025}$ PNW is impressive when compared to recently reported earth-abundant catalysts as shown in Table 3.2. Also, a very low voltage increase (6 mV increase) was observed when $NiCu_{0.05}Fe_{0.025}$ PNW was operated at a constant current density of 10 mA cm^{-2} for 20 hours (Figure 3.7d) revealing excellent stability of the catalyst. The porous network morphology was preserved even after the long-term electrolysis as observed from the FESEM image (Figure 3.8a). Also, the phase of the catalyst remained the same as that of the synthesized sample as evidenced by the XRD pattern (Figure 3.8b).

Table 3.3 HER activity of the $NiCu_{0.05}Fe_{0.025}$ PNW in comparison with other reported catalysts with good performance.

Catalyst	HER overpotential (mV @ mA cm^{-2})	Tafel slope (mV dec^{-1})	Electrolyte	Stability	Relative Cost	Ref.
$CoS_2/CoSe_2$ hybrid	80 mV @ 10 mA cm^{-2}	33.6	0.5 M H_2SO_4	3000 CV cycles	Medium	89
$Ni_{20}Fe_{20}Mo_{10}Co_{35}Cr_{15}$ high entropy alloy	172 mV @ 10 mA cm^{-2}	41	1 M KOH	8 hours	Medium	90
Pt_3Ni_3 NWs	70 mV @ 19.8 mA cm^{-2}	NA	1 M KOH	3 hours	High	71
Micro-nano MoS_2 spheres	214 mV @ 10 mA cm^{-2}	74	0.5 M H_2SO_4	24 hours	Medium	91
Phosphate doped FeP nanosheets	95 mV @ 10 mA cm^{-2}	41	0.5 M H_2SO_4	24 hours	Low	92
np-CoP_3 on Ti mesh	76 mV @ 10 mA cm^{-2}	50	1 M KOH	60 hours	Medium	93
PtCo–Co/TiM	70 mV @ 46.5 mA cm^{-2}	35	1 M KOH	50 hours	High	94
$Fe_{1.89}Mo_{4.11}O_7/MoO_2$	197 mV @10 mA cm^{-2}	79	1 M KOH	1000 CV cycles	Medium	95
$Ni(OH)_2$–CoS_2/CC	99 mV @ 20 mA cm^{-2}	118	1 M KOH	30 hours	Medium	96
CrO_x/Ni–Cu	48 mV @ 10 mA cm^{-2}	64	KH_2PO_4 + K_2HPO_4 buffer	24 hours	Low	97
FeP nanoparticles	154 mV @ 10 mA cm^{-2}	65	0.5 M H_2SO_4	1.66 hours	Low	98
Ni doped FeP/C hollow nanorods	117 mV @ 10 mA cm^{-2}	54	1 M KOH	12 hours	Low	99
$NiCu_{0.05}Fe_{0.025}$ PNW	**60 mV @ 10 mA cm^{-2}**	**60.8**	**1 M KOH**	**20 hours**	**Low**	**This work**

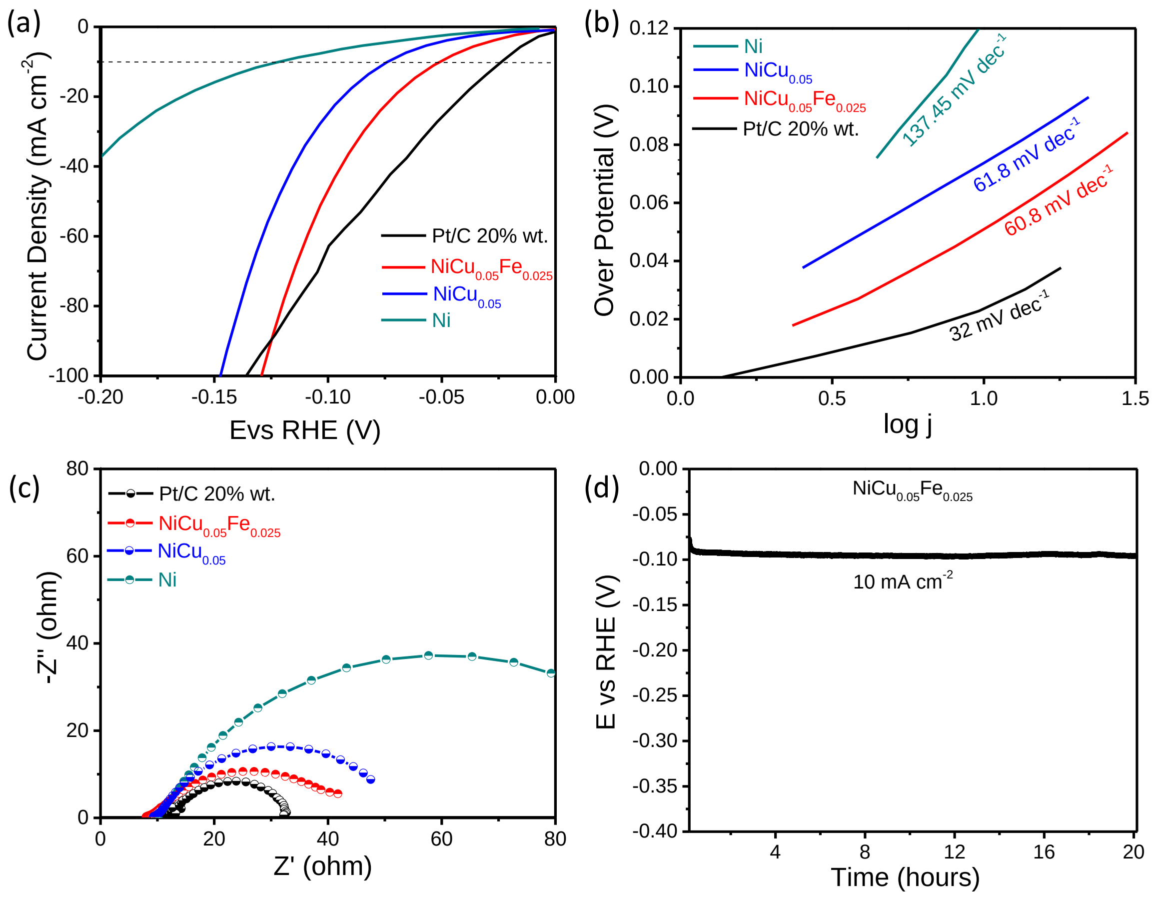

Figure 3.7 (a) HER polarization curves for $NiCu_{0.05}Fe_{0.025}$ PNW, $NiCu_{0.05}$ PNW, Ni PNW and Pt/C catalysts in 1 M KOH solution and their corresponding (b) Tafel slopes, (c) Nyquist plots at -76 mV overpotential. (d) Chronopotentiometry test for $NiCu_{0.05}Fe_{0.025}$ PNW at constant current density of 10 mA cm^{-2} for 20 hours.

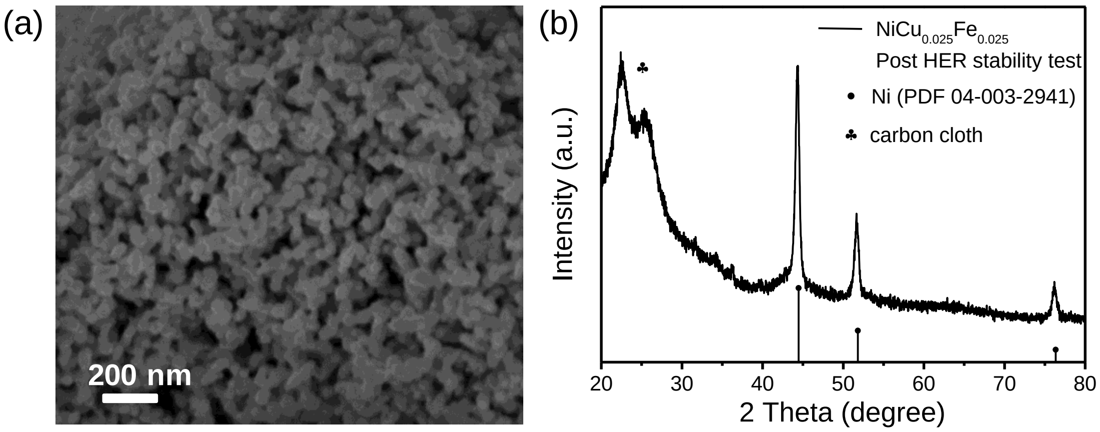

Figure 3.8 (a) FESEM images of $NiCu_{0.05}Fe_{0.025}$ PNW after HER stability test for 20 hours, (b) XRD plot of $NiCu_{0.05}Fe_{0.025}$ PNW catalyst on carbon cloth after long term stability test for hydrogen evolution reaction for 20 hours.

To get further insight into the origin of the activity of the catalyst, the specific activity of the pristine Ni PNW and $NiCu_{0.05}Fe_{0.025}$ PNW were estimated by computing the normalized current density with respect to the electrochemical active surface area (ECSA) of the catalysts. The ECSA was estimated from the cyclic voltammetry curves (see Experimental section for details) as shown in Figure 3.9(a-b). The same catalyst loading (2.4 mg cm^{-2}) was used across all samples. The plot of ECSA normalized current vs. overpotential is illustrated in Figure 3.9d. The $NiCu_{0.05}Fe_{0.025}$ PNW showed a high specific activity of 0.1 mA $cm^{-2}{}_{(ECSA)}$ at a very low overpotential of 117 mV whereas the Ni PNW required an overpotential of 220 mV to reach the same activity. Interestingly, the double-layer capacitance (C_{dl}) of 23.55 mF cm^{-2} for $NiCu_{0.05}Fe_{0.025}$ PNW was only slightly larger than C_{dl} of 20.35 mF cm^{-2} for Ni PNW (Figure 3.9c) revealing a minimal increase in the electrochemical active surface area by doping. Also, the BET surface area measured from N_2 adsorption-desorption isotherms revealed similar surface areas of 3.6 m^2/g for Ni PNW and 3.175 m^2/g for $NiCu_{0.05}Fe_{0.025}$ PNW (Figure 3.10(a-b)). Hence, we infer that the surface area had an inconsequential role in the enhanced HER performance of the NiCu$_{0.05}$Fe$_{0.025}$ PNW. Therefore, we presume that the improvement in the catalytic activity of the doped NiCu$_{0.05}$Fe$_{0.025}$ PNW may be primarily due to enhanced intrinsic activity of the active sites achieved via co-doping of Cu and Fe.

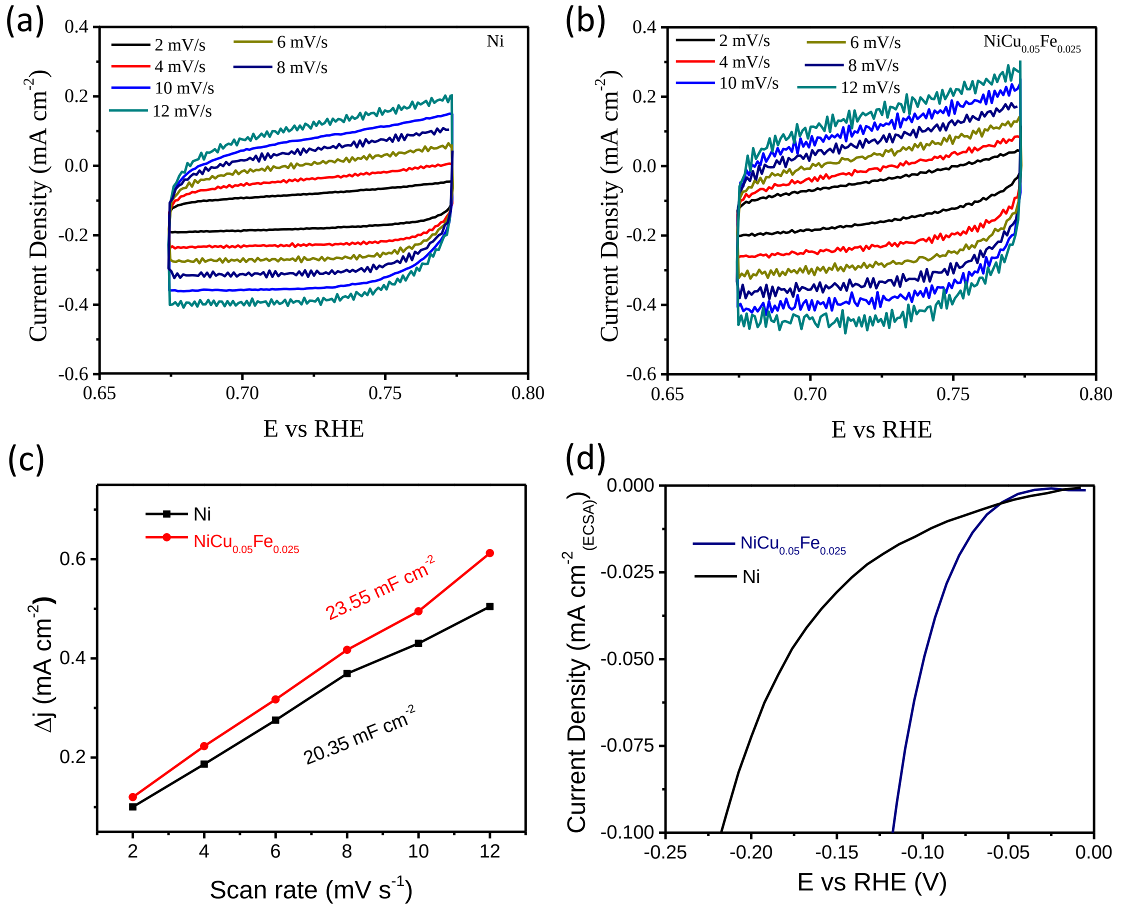

Figure 3.9 (a) Cyclic voltagram curves for (a) Ni PNW, (b) NiCu$_{0.05}$Fe$_{0.025}$ PNW, (c) plot of variation of capacitive current (j_{anodic} - $j_{cathodic}$) at 0.724 V (vs RHE) with varying scan rates (2 mV/s to 12 mV/s) for Ni PNW and NiCu$_{0.05}$Fe$_{0.025}$ PNW, and (d) polarization curves of Ni PNW and NiCu$_{0.05}$Fe$_{0.025}$ PNW catalysts after ECSA normalization for hydrogen evolution reaction.

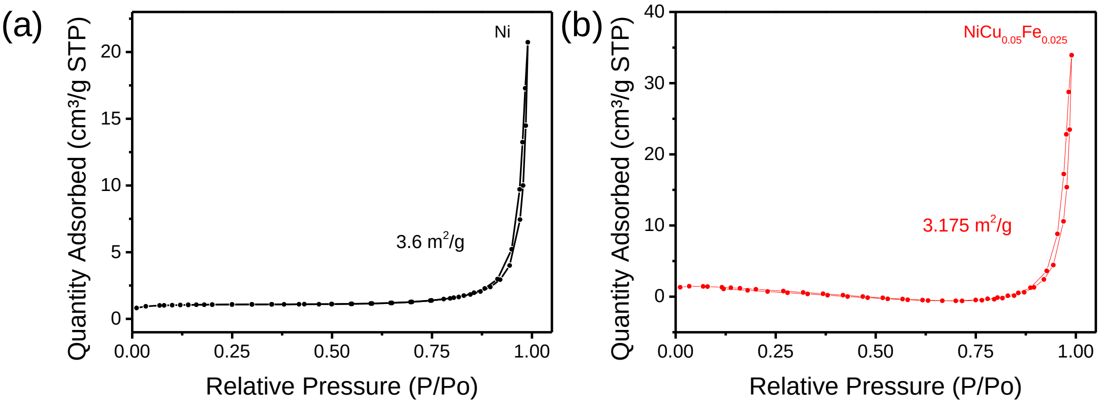

Figure 3.10 N_2 adsorption-desorption isotherms for (a) Ni PNW, and (b) $NiCu_{0.05}Fe_{0.025}$ PNW.

3.3.3 Computation of Gibbs Energy of hydrogen adsorption

DFT calculations were employed to estimate the ΔG_H on the pristine and doped Ni surface. The sites and the corresponding ΔG_H plots are shown in Figure 3.11(a-d). The numerical ΔG_H values are listed in Table 3.3. The values of ΔG_H increased from -0.258 eV for H adsorbed on pristine Ni to -0.208 eV and -0.190 eV for Fe- and Cu- Ni alloy, respectively. The calculated ΔG_H values became closer to the optimum value (0 eV) with the doping of Fe and Cu, which is also observed from the experimental results. Remarkably, the ΔG_H for Cu, Fe co-doped Ni alloy is -0.131 eV, which showed excellent electrocatalytic performance better than pristine Ni and other single metal-doped alloys. The result also shows that the doped metal enhanced the HER performance of the adjacent regions and did not affect the remoter regions, as the ΔG_H for S5 and S6 sites remain ~0.32 eV. Further, it is worth to note that the active sites (sites with reduced ΔG_H) for the HER in the doped samples are sites S2 and S3, which are nickel sites. In contrast, the adsorption energies for Cu site (S1; $\Delta G_H = 0.405$ eV) and Fe site (S4; $\Delta G_H = 0.253$ eV) in the Cu, Fe co-doped Ni PNW are higher, hence not active for hydrogen evolution. Thus, an appropriate concentration of Cu and Fe atoms the Ni (111) surface would contribute to enhanced hydrogen evolution. In contrast, a very large concentration of Cu and Fe atoms would lead to decreased activity owing to the increased density of inactive sites. This explains the reduced HER activity of the Cu-doped Ni PNW beyond 5% doping concentration, and the reduced activity of Cu, Fe co-doped Ni PNW beyond 2.5% Fe doping concentration.

Table 3.4 The calculated Gibbs free energy (ΔG_H) for pristine, Fe-, Cu-, Cu, Fe doped Ni nanosheets. (S1- the top of the doping metal atoms, S2 - Ni fcc sites, S3 - Ni hcp sites, S4 - the top Ni near the doping metal atoms, S5 and S6 - the amphiposition top Ni atoms)

ΔG_H (eV)	S1	S2	S3	S4	S5	S6
Pure Ni	0.325	-0.258	-0.248			
Fe doped Ni	0.576	-0.208	-0.199	0.206	0.319	0.311
Cu doped Ni	0.729	-0.190	-0.182	0.308	0.317	0.318
Cu, Fe co-doped Ni	0.405	-0.131	-0.116	0.253	0.296	0.317

According to the *d*-band theory,[100] the binding of adsorbates with metals can be determined by the antibonding state occupancy, which is formed between the valence state of adsorbates and *d* state of transition metal. Thus, the *d*-band center can be used to indicate the reactivity of metal catalysts from their electronic properties, i.e., the closer the *d*-band center is to the transition metal *d* state's Fermi energy level, the higher is the metal reactivity.[101] In this study, for H atoms adsorbed on the Ni (111) surface, the Ni atoms 3*d* orbital directly participates in the binding with H atoms. The *d*-band center of pristine and doped Ni surface was calculated from their projected density of states using the equation (4):

$$\varepsilon_d = \frac{\int_{-\infty}^{+\infty} x\rho(x)dx}{\int_{-\infty}^{+\infty} \rho(x)dx} \tag{3.3}$$

where, $\rho(x)$ is the PDOS at the energy of x, which is shown in Figure 3.12(a-d). The integral domain was set to be -2 eV to 0 eV of Ni 3*d*-orbital states, representing the closest region near the Fermi energy. And the bonding energy $\Delta\varepsilon$ of H atoms on the Ni surface was calculated by[102-103]:

$$\Delta\varepsilon \propto -\frac{V^2}{|\varepsilon_d - \varepsilon_s|} \tag{3.4}$$

V is the coupling matrix element, which can be assumed as a constant value; ε_s is the adsorbate states energy level and can be set to 0 eV. Thus, it can be concluded that the initial bonding energy increases with the decrease in $|\varepsilon_d - \varepsilon_s|$ value.

The *d* band centers are in the range of -1.19 eV to -1.250 eV for spin-on and -1.138 eV to -1.268 eV for spin down, respectively (Figure 3.12(a-d)). The calculated ε_d (denoted as yellow lines for spin-on and green lines for spin down) shifted to lower energy levels for the Cu-, Fe-, and Cu, Fe- doped samples, thus demonstrating a weaker binding of the metal surface with adsorbates. Figure 3.12(e-f) shows the nearly linear relationship between Gibbs free energy (ΔG_H) and the d band center of the pristine Ni and the doped samples. As the d-band center shifted to lower energy levels the Gibbs energy of hydrogen adsorption changed to lesser negative energies near to zero. Thus, the shift of d-bands closely relates to the ΔG_H, i.e., the hydrogen adsorption energy is reduced as the d-bands shifted to lower energy levels. In conclusion, in contrast to the pristine nickel, which offers a very strong binding for hydrogen (ΔG_H = -0.258 eV), the doping of Cu and Fe reduces the binding energy (ΔG_H = -0.131 eV) to facilitate enhanced hydrogen evolution.

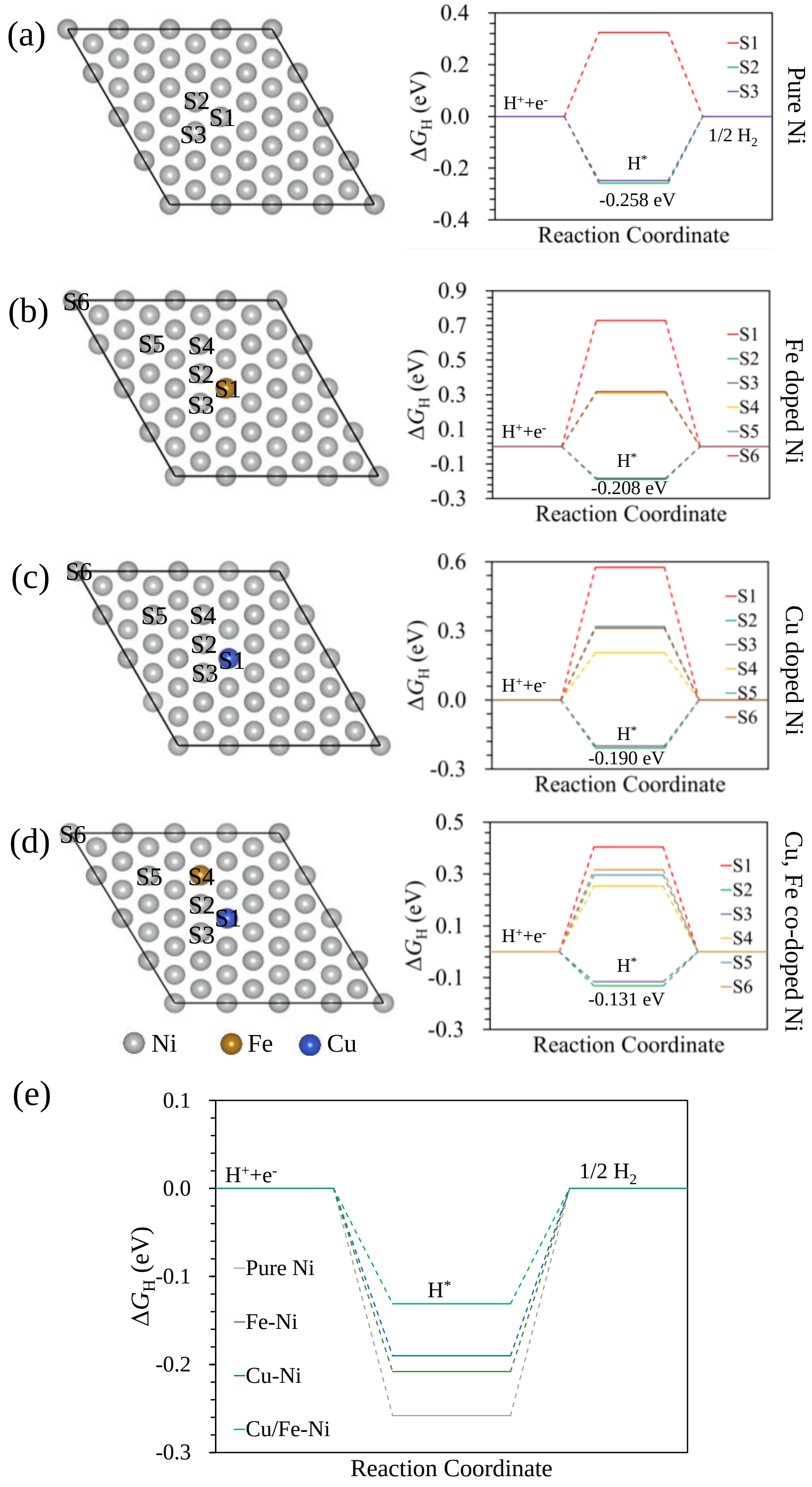

Figure 3.11 The free energy diagram for H atoms adsorbed on (a) pristine, (b) Fe-, (c) Cu-, (d) Cu, Fe doped Ni nanosheets. The top view and adsorption sites are listed on the left. (e) The Gibbs Free energy for H adsorbed at active site for pristine Ni and Fe-, Cu-, Cu/Fe-doped Ni alloy.

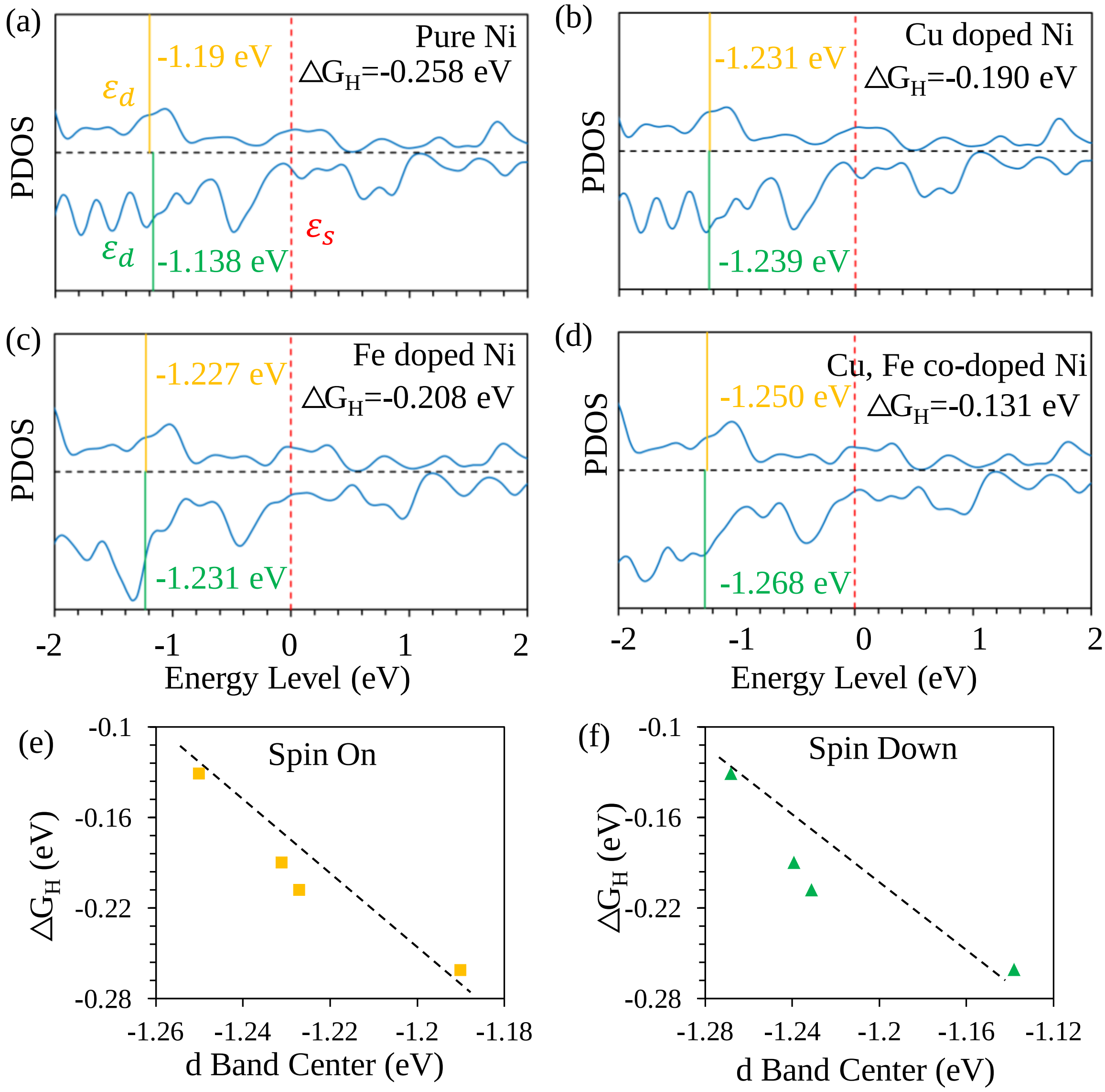

Figure 3.12 The Projected 3d-orbital density of states of Ni atoms (S2 sites) for (a) pristine, (b) Cu-, (c) Fe-, (d) Cu, Fe- doped Ni nanosheets. The red dotted lines correspond to Ɛs. Spin-polarization was considered as the yellow lines represent the Ɛd for spin on while the green lines show the Ɛd for spin down. (e-f) The relationship between d-band center and Gibbs free energy (ΔG_H) for both spin on and spin down.

It is well known that NiFe based hydroxides are active for OER in alkaline medium.[8, 104] Therefore, we tested the OER performance of precursor $NiCu_{0.05}Fe_{0.025}(OH)_2$ nanowires OER. The $NiCu_{0.05}Fe_{0025}(OH)_2$ nanowires exhibited reasonable oxygen evolution activity, with a low η_{10} of only 270 mV. Encouraged by this, the overall water splitting cell was constructed using these two active catalysts. Figure 3.13a depicts the performance of the synthesized catalysts in comparison with state-of-the-art Pt/C and RuO_2 catalysts. The $NiCu_{0.05}Fe_{0.025}$ || $NiCu_{0.05}Fe_{0.025}(OH)_2$ cell reached 10 mA cm^{-2} at 1.491 V showing activity similar to that of Pt/C || RuO_2 couple. Furthermore, $NiCu_{0.05}Fe_{0.025}$ || $NiCu_{0.05}Fe_{0.025}(OH)_2$ cell achieved high current density of 100 mA cm^{-2} at extremely low voltage of 1.528 V while the Pt/C || RuO_2 couple required 1.59 V for the same. In comparison with many of the reported bifunctional catalysts, $NiCu_{0.05}Fe_{0.025}$ || $NiCu_{0.05}Fe_{0.025}(OH)_2$ catalyst couple exhibited excellent overall water splitting performance as seen from Table 3.4. Furthermore, chronopotentiometry test at 20 mA cm^{-2} for 30 hours for $NiCu_{0.05}Fe_{0.025}$ || $NiCu_{0.05}Fe_{0.025}(OH)_2$ cell showed minimal loss (13 mV increase in voltage) of activity (Figure 3.11b) indicating the modest stability of the catalysts for overall water splitting. Since, both HER and OER catalysts in our design contain the same elements (Ni, Cu, and Fe) fabrication of electrolyzers can be significantly simplified,[2] subsequently reducing the production and maintenance cost required for the commercial application. Thus, through optimized doping of Fe and Cu into Ni, earth-abundant catalyst couple $NiCu_{0.05}Fe_{0.025}$ || $NiCu_{0.05}Fe_{0.025}(OH)_2$ with a catalyst performance better than the state of the art (Pt/C || RuO_2) catalyst was achieved.

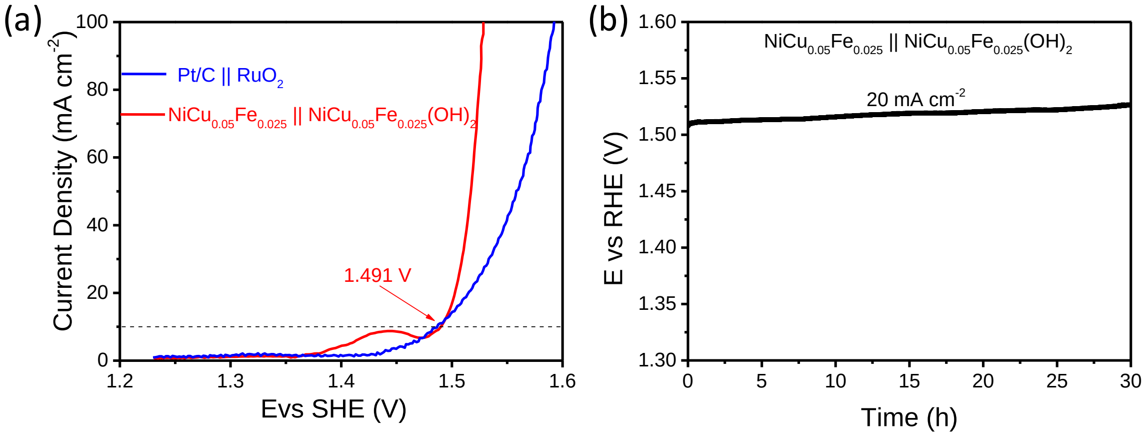

Figure 3.13 (a) Overall water splitting performance of $NiCu_{0.05}Fe_{0.025}$ || $NiCu_{0.05}Fe_{0.025}(OH)_2$ cell in comparison with Pt/C || RuO_2 cell, (b) Chronopotentiometry test for the overall water splitting by using $NiCu_{0.05}Fe_{0.025}$ || $NiCu_{0.05}Fe_{0.025}(OH)_2$ cell.

Table 3.5 Comparison of overall water splitting performance of reported catalysts with $NiCu_{0.05}Fe_{0.025}$ PNW || $NiCu_{0.05}Fe_{0.025}(OH)_2$.

Catalyst	Voltage @ 10 mA cm^{-2}	Electrolyte	Reference
Ternary nickel–iron sulfide micro flowers	1.625 V	1 M KOH	45
CoS nanoparticles	1.77 V	1 M KOH	105
Iron and dinickel phosphides on nickel foams	1.42 V	1 M KOH	106
Ni_3S_2 nanoporous thin films on nickel foil	1.611 V	1 M KOH	107
Iron fluoride-oxide nanoporous thin films on Fe foil	1.58 V	1 M KOH	108
Self-supported NiMo-based nanowire arrays on Ni foam	1.507 V	1 M KOH	109
3D $Co(OH)_2$@NCNTs@NF	1.72 V	1 M KOH	110
$NiCu_{0.05}Fe_{0.025}$ PNW || $NiCu_{0.05}Fe_{0.025}(OH)_2$ nanowires	**1.491 V**	**1 M KOH**	**This work**

3.4 Conclusions

In conclusion, we achieved a significant improvement in the catalytic activity of Ni by doping of Cu and Fe atoms into Ni lattice. In-depth characterization by, FESEM, TEM, XRD, and XPS reveal successful doping of Cu and Fe into Ni lattice. Electrochemical tests and DFT calculations reveal the improvement in the catalytic activity of Ni by doping of Cu and Fe and much higher activity for Cu and Fe co-doped Ni. This work confirms our hypothesis that when metal with negative ΔG_H (Ni), is doped/alloyed with metals with positive ΔG_H (Cu, Fe) the d-band center is tuned in such a way that ΔG_H approaches closer to zero, thus promoting optimum hydrogen adsorption suitable for efficient catalysis. Furthermore, the synthesized catalyst also shows decent durability when tested for 30 hours. To conclude, this work can be a good model for the future design of active catalysts for hydrogen evolution.

3.5 Outlook to next chapter

The research findings from this chapter have reasonably corroborated our hypothesis of catalyst design based on the volcano plots. The doping of Cu and Fe into Ni improved its activity for HER. In the next chapter, we will explore another catalyst system that is designed based on the interface engineering of metals with contrasting hydrogen adsorption energy. We will explore NiAg heterogeneous alloy system and probe the correlation between the Ni-Ag interface area and the electrocatalytic activity based on experimental results and DFT calculations.

Chapter 4 Interface Engineering at Ni-Ag Epitaxial Interface to Achieve Pt/C Like Activity for Hydrogen Evolution

In this chapter, we describe the synthesis, characterization, and catalytic activity of NiAg 3D porous nanoclusters for water splitting. Initially, we deliberate briefly on the advantages of alkaline electrolysis and the challenges associated with it. Later, we discuss the rationale behind the synthesis of Ni-Ag heterogeneous alloy comprising epitaxial interfaces. Next, the experimental process to synthesize and characterize the samples is elaborated. Electrochemical characterizations to evaluate the catalytic activity NiAg alloys are conducted out to arrive at an optimized alloying concentration of Ni and Ag. In the next part, DFT calculations are conducted to estimate the hydrogen adsorption energy at the Ni-Ag interface. Furthermore, the correlation between interface area and catalytic activity is established from the electrochemical test results. Finally, the durability of the catalyst is investigated by chronoamperometry and cyclic voltammetry tests, followed by the characterization of the catalyst after the long-term durability test.

4.1 Introduction

In the previous chapter, we discussed the synthesis of Cu and Fe co-doped Ni catalyst and how doping of Cu and Fe improved the electrocatalytic activity of Ni. The work served as an initial confirmation of our hypothesis on catalyst design through mixing metals with a contrasting tendency for hydrogen adsorption. Going forward in this chapter, we explore an alternative approach to the mixing of two metals, i.e., interface engineering in a heterogeneous alloy system. Ni-Ag heterogeneous alloy with epitaxial interfaces shows Pt/C like electrocatalytic activity as revealed from theoretical calculations and experimental results. To better explain the motivation for this work, we will briefly revisit the advantages of alkaline electrolysis and later explain the rationale behind interface engineering of Ni and Ag in the following paragraphs.

The activity and efficiency of the catalysts are pH-dependent. Although numerous studies of acid electrolysis have been reported, the high cost of proton exchange membrane and sluggish electron-transfer kinetics of the OER in acidic medium hinder its feasible application.[66] Further, reported earth-abundant catalysts for OER are unstable in the acidic medium[111] compared to alkaline medium, which is an important criterion for the real-life application. Besides, the alkaline electrolysis is favorable owing to broad reactant availability and product purity.[112] Further, the hydrogen evolution reaction in alkaline medium involves water dissociation step ($H_2O + e^{-1} \leftrightarrow H_{ads} + OH^{-1}$) unlike the discharge of protons in acid ($H^+ + e^{-1} \leftrightarrow H_{ads}$) due to which the HER activity in alkaline medium is 2-3 orders of magnitude lesser than activity in the acid medium.[113] This is evident from the lower activity of Pt in alkaline electrolytes.[69] Although Pt and its alloys[70-71] have shown remarkable catalytic activity, the high cost, low abundance, and sensitivity to poisoning for sulfides and chlorine limits it's wide-scale application.[69] In the past, alloy catalysts such as boron-doped RhFe alloy,[73] NiMo alloy in holey graphene,[114] Pt_3Co nanoparticles,[72] IrAg nanotubes,[115] PtNiCo ternary alloy nano frame crystals,[70, 116] are reported to exhibit remarkable activity for HER. However, these catalysts are active in acid medium and few of the reported catalysts in the basic medium,[116-117] are less active compared to Pt. Also, the long-term stability of these catalysts is a concern to be addressed for commercial applications.

In the case of metals, coupling between the adsorbate valence states and the d states of the metal influences the adsorption energy which determines the activity of the catalyst.[118] The position of the d states relative to Fermi energy determines the coupling, where the element with d state nearer to Fermi energy exhibiting stronger interaction with the adsorbate.[75] For HER, ΔG_H should be near to zero for best catalytic performance according to Sabatier's principle, which is evident from the high activity of Pt ($\Delta G_{ads} \approx -0.1$ eV).[78] As revealed from previous studies elements such as nickel, cobalt, molybdenum, tungsten have negative adsorption energies (stronger adsorption) while copper, silver, and bismuth have positive energy of adsorption (weaker adsorption).[51] In the case of metals mixing two or more metals can alter the d band center leading to the tuning of the adsorption energies to promote the catalytic activity.[119-121] Among the earth-abundant metals, the nickel-based catalyst is a preferred choice. Nickel has Gibbs energy of hydrogen adsorption near to -0.28 eV[78] which is one of the best among earth-abundant metals. In this study, we chose Ag as the alloying element which has positive energy of adsorption ($\Delta G \approx 0.5$ eV). However, Ni and Ag are thermally immiscible in the bulk.[122] Therefore, the NiAg alloy nanoparticle synthesis through general routes is not easily achieved. Furthermore, the HER activity of the previously reported NiAg alloy[117] is not impressive (η_{10} ~ 300 mV). As an alternative, interface engineering of nanostructures is widely regarded as one of the ways to enhance the catalytic activity of nanostructures.[71, 76, 120] Inspired this, we chose to synthesize $NiAg_{0.4}$ 3D porous nanoclusters with epitaxial interfaces between Ni and Ag.

4.2 Materials and methods

4.2.1 Chemicals

Nickel (II) nitrate hexahydrate ($Ni(NO_3)_2.6H_2O$, Sigma Aldrich). Silver nitrate ($AgNO_3$, 0.1 M, Sigma Aldrich), urea (NH_2CONH_2, Sigma Aldrich), ethylene glycol (Sigma Aldrich), Pt/C 20% wt. (Fuel cell research) and Nafion (5% solution, Sigma Aldrich) were used without further treatment.

4.2.2 Synthesis of $NiAg_x$ 3D porous nanoclusters

$NiAg_x$ ($0 < x < 4.5$) 3D porous nanoclusters were synthesized through the hydrothermal process. In the first step, 1 mmol $Ni(NO_3)_2.6H_2O$ and 5 mmol urea were dissolved in 10 ml DI water. To this solution, various volumes of 0.1 M $AgNO_3$ were added ranging from 1 ml to 8 ml corresponding to Ni to Ag molar ratios from 10:1 to 10:8. For the synthesis of $NiAg_{2.75}$ and $NiAg_{4.42}$ nanoclusters, 0.5 mmol of $Ni(NO_3)_2$ and 2.5 mmol urea were mixed in 5 ml DI water with 10 ml and 15 ml of 0.1 M $AgNO_3$ solution respectively. To this solution, 10 ml of ethylene glycol and was added and further with DI water to make the overall solution to 30 ml. This solution was transferred to a 45 ml Teflon coated stainless steel autoclave and heated in an electric oven at 120 ^{0}C for 9 hours. The formed black colored product was washed 3 times with DI water and ethanol through centrifugation and dried in an electric oven at 60 ^{0}C for 12 hours. The synthesized powder was later transferred to a quartz boat and annealed in a tube furnace with hydrogen gas flow with a ramping rate of 3 °C per minute to 400 °C for 2 hours. The pristine Ni nanoclusters were synthesized with a similar process but without the addition of $AgNO_3$ and pristine Ag nanoparticles were synthesized without the addition of $Ni(NO_3)_2.6H_2O$.

4.2.3 Sample characterization

The phase of the synthesized samples was determined using Shimadzu XRD-6000 with Cu-K_α radiation ($\lambda = 1.5406$ Å) operated at 40 kV and 30 mA. The synthesized samples were dispersed in ethanol and were drop-cast on a glass slide and used for the measurement. JEOL field emission scanning electron microscope (JSM-7600F, JEOL Ltd. Tokyo, Japan) was used to image the nanostructures. High-resolution imaging, elemental mapping, EDX analysis, and HAADF-STEM imaging were performed by TEM (JEOL JEM 2100, 200 kV). The surface composition of the samples was studied by X-ray photoelectron spectroscopy from Theta Probe electron spectrometer. The composition of the sample was estimated using an Inductively coupled plasma-optical emission spectrometer (PerkinElmer Optima 8000) in which the average of three measurements was considered for the estimation of the concentration of each element. BET surface area was measured by N_2 adsorption-desorption isotherms at 77 K using Tri-star II 3020 model.

4.2.4 Electrochemical measurements

Electrochemical measurements were done using Solartron analytical equipment (Model 1470E). For the powder samples, 5 mg of powder was dispersed in 950 ul of isopropanol (IPA) and 50 µl of Nafion solution and ultra-sonicated for 1 hour. 5-40 µl of this uniform dispersed slurry was drop cast on a glassy carbon electrode (GCE-3mm) and allowed to dry. The tests for HER performance were conducted using a typical 3 electrode cell with Hg/HgO as the reference electrode, graphite electrode as counter electrode, and 1 M KOH as the electrolyte. The HER performance was measured by linear sweep voltammetry (LSV) from -0.7 V to -1.7 V vs Hg/HgO at a scan rate of 2 mV per second. The measured potential was converted to potential vs. reversible hydrogen electrode (RHE) by using the relation $E_{\mathrm{vsRHE}} = E_{\mathrm{vsHg/HgO}} + 0.098 + 0.059 * \mathrm{pH}$. The durability of the $NiAg_{0.4}$ 3DPNC catalyst was tested by chronoamperometry test by applying a constant voltage of -76 mV vs RHE for 80 hours and measuring the current during the process. Furthermore, 5000 cyclic voltammetry sweeps between -0.9 V to -1.7 V versus Hg/HgO reference electrode were conducted to investigate the durability of the catalyst. For X-ray diffraction (XRD) and scanning electron microscopy

(SEM) characterization of post-stability test samples, the catalyst slurry was coated on carbon cloth and the chronopotentiometry test was repeated as described above. To estimate the electrochemical active surface area (ECSA) of the samples, cyclic voltammetry (CV) scans were performed between 0.674 V to 0.774 V vs. reference hydrogen electrode at various scan rates from 10 mV s^{-1} to 50 mV s^{-1} The difference between the current densities at 0.724 V during the forward and reverse scan ($j_{\mathrm{anodic}} - j_{\mathrm{cathodic}}$) was plotted against the scan rate. The slope of the plot equals twice the double layer capacitance C_{dl}. The roughness factor was calculated by dividing the C_{dl} by the specific capacitance (40 uF cm^{-2}), which was later used for ECSA normalization.[80] Electron impedance spectroscopy (EIS) measurements were done in Autolab PGSTAT302 (Eco Chemie, Netherlands) potentiostat by varying the frequency from 100 kHz to 0.1 Hz with an amplitude of 10 mV. The solution resistance R_s was estimated from the x-intercept of the plot of -Z” vs Z’ in the high-frequency range, which was later used for the iR correction.

4.2.5 Computational methods

All of the computations were done using the spin-polarized density functional theory (DFT) methods based on the Vienna Ab initio Simulation Package (VASP).[81] The electron-ion interaction was described using the projector augmented wave (PAW) method. Perdew-Burke-Ernzerhof exchange-correlation functional within a generalized gradient approximation (GGA) was employed. For the valence electrons a 400 eV cutoff energy for the plane-wave basis set was used. Self-consistent field (SCF) computations were done with a force and energy convergence criterion of 0.02 eV $Å^{-1}$ and 10^{-6} eV, respectively. The Brillouin zone was sampled using the 6×6×1 Monkhorst-Pack k-point mesh in structure optimization for Ni and Ag. The vacuum thickness was set at ~20 Å to prevent the interactions between two adjacent periodic images. In all cases, spin-polarized considerations were taken into account.

The Gibbs free energy (ΔG_H) of hydrogen adsorption on metal-doped Ni (111) surfaces was given by

$$\Delta G_{\mathrm{H}} = \Delta E_{\mathrm{nH}} + \Delta E_{\mathrm{ZPE}} - T\Delta S_{\mathrm{H}} \tag{4.1}$$

where ΔE_{ZPE} is the difference in zero-point energy, and ΔS_{H} is the entropy difference of the gas phase and the adsorbed state, respectively. ΔE_{nH} is the chemisorption energy of the nth H atom, which was calculated from:

$$\Delta E_{\mathrm{nH}} = E_{\mathrm{M+nH}} - E_{\mathrm{M+(n-1)H}} - \frac{1}{2} E_{\mathrm{H_2}} \tag{4.2}$$

where $E_{\mathrm{M+nH}}$ and $E_{\mathrm{M+(n-1)H}}$ are the total energy of metal-doped Ni (111) /Ag (111) surfaces with n-*th* and n-1-*th* H atoms adsorption, respectively. E_{H2} is the total energy of molecule hydrogen in the gas phase. The computed frequencies of H_2 gas are 42 cm^{-1}, 58 cm^{-1}, and 4345 cm^{-1} which agrees well with previous studies.[83-84] The ΔE_{ZPE} is calculated to be 0.04 eV for H adsorption on surfaces, which do not differ notably with the adsorption sites and the adatom. The entropy of hydrogen adsorption is given by $\Delta S_H = \frac{1}{2} S_{H2}$, where S_{H2} is the entropy of molecule hydrogen in the gas phase at 300 K and 1 bar.[85] To sum up, the value of ΔE_{ZPE}-$T\Delta S_H$ is equal to 0.245 eV.

4.3 Results and Discussion

4.3.1 Characterization of $\mathrm{NiAg_x}$ 3D porous nanoclusters

Samples with varying Ni/Ag ratios were synthesized by controlling the precursor ratios from 10:1 to 1:3. ICP-OES test results listed in Table 4.1 reveals the concentration of Ni and Ag in different samples. Based on the ICP-OES results we name our samples as follows: Ni 3DPNC, $\mathrm{NiAg_{0.13}}$ 3DPNC, $\mathrm{NiAg_{0.25}}$ 3DPNC, $\mathrm{NiAg_{0.34}}$ 3DPNC, $\mathrm{NiAg_{0.40}}$ 3DPNC, $\mathrm{NiAg_{0.44}}$ 3DPNC, $\mathrm{NiAg_{0.6}}$ 3DPNC, $\mathrm{NiAg_{0.95}}$ 3DPNC, $\mathrm{NiAg_{2.75}}$ 3DPNC, $\mathrm{NiAg_{4.42}}$ 3DPNC, and Ag NPs corresponding to the respective Ni/Ag ratios. Here, 3DPNC refers to 3D porous nanoclusters and NPs refer to nanoparticles.

Table 4.1 ICP-OES results for the synthesized samples with different Ni/Ag ratios.

Ni : Ag ratio in the precursor solution	Expected molar concentration from synthesis	Measured molar concentration from ICP-OES	Expected molar concentration from synthesis	Measured molar concentration from ICP-OES	Name of the sample in the report
	Ni (%)	Ni (%)	Ag (%)	Ag (%)	
1 : 0.1	90.9	88.43019	9.1	11.56981	$NiAg_{0.13}$ 3DPNC
1 : 0.2	83	80.20356	17	19.79644	$NiAg_{0.25}$ 3DPNC
1 : 0.3	76.9	74.63433	23.1	25.36567	$NiAg_{0.34}$ 3DPNC
1 : 0.4	71.5	71.89	28.5	28.11	$NiAg_{0.4}$ 3DPNC
1 : 0.5	66.67	69.57572	33.33	30.42428	$NiAg_{0.44}$ 3DPNC
1 : 0.6	62.5	62.55256	37.5	37.44744	$NiAg_{0.6}$ 3DPNC
1 : 0.8	55.55	51.37111	44.45	48.62889	$NiAg_{0.95}$ 3DPNC
1 : 2	33.33	26.63245	66.67	73.36755	$NiAg_{2.75}$ 3DPNC
1 : 3	25	18.4579	75	81.5421	$NiAg_{4.42}$ 3DPNC

The phase of the synthesized samples was investigated by XRD analysis. For the black powder obtained from the hydrothermal synthesis, the XRD peaks at 38.2°, 44.4°, 64.6°, and 77.6° are assigned to (111), (200), (202), and (311) planes of cubic silver (PDF no. #01-087-0720), respectively, as shown in Figure 4.1a. Smaller peaks at 23.9°, 33.63°, 41.30°, 59.8°, and 98.9° correspond to (002), (110), (103), (300), and (410) planes of hexagonal $Ni(OH)_2.2/3H_2O$ (PDF no. #00-022-0444), respectively. Thus, the sample from hydrothermal synthesis consists of Ag and $Ni(OH)_2.2/3H_2O$ as observed from the XRD studies.

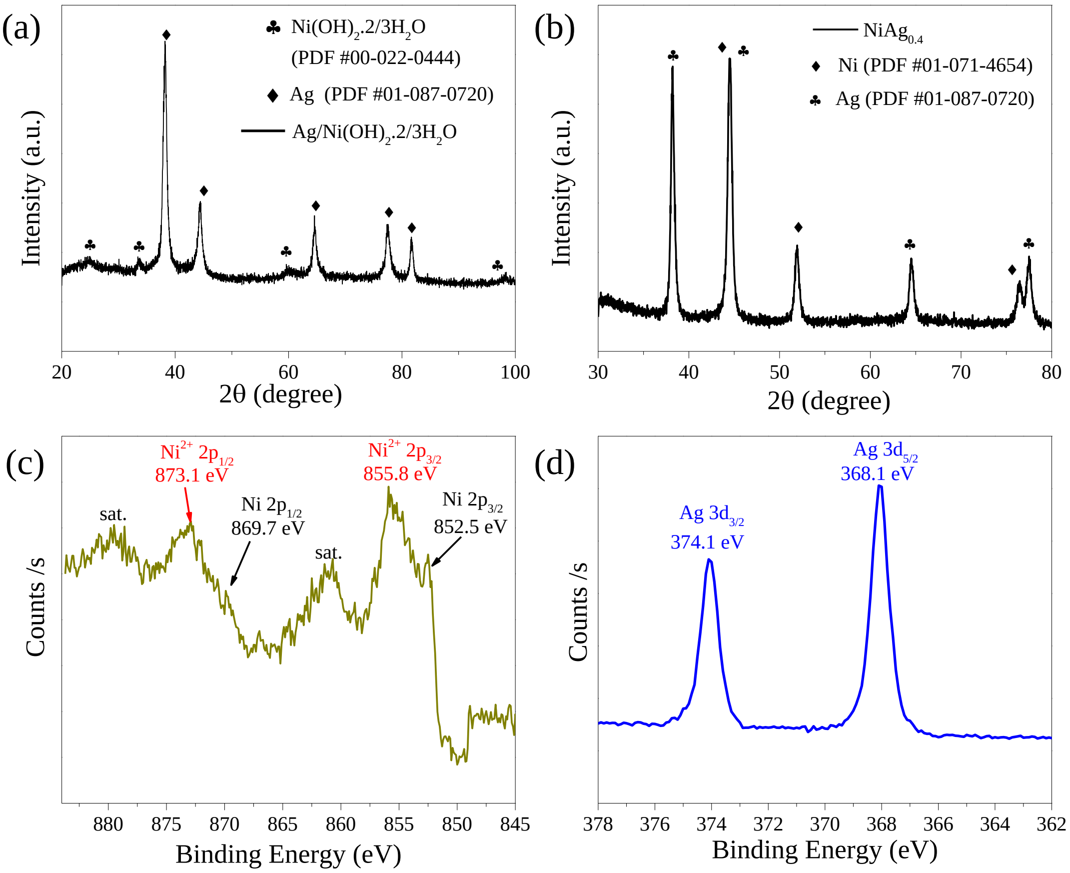

Figure 4.1 XRD spectra of (a) $Ag/Ni(OH)_2.2/3H_2O$ precursor, (b) $NiAg_{0.4}$ 3DPNC, and high resolution XPS spectra of $NiAg_{0.4}$ 3DPNC in the (c) Ni 2p region, (d) Ag 3d region.

The $Ag/Ni(OH)_2.2/3H_2O$ sample was then processed by the thermal reduction in the flow of hydrogen at 400 °C in the tube furnace. The XRD peaks of the thermally reduced $NiAg_{0.40}$ 3DPNC at 44.5°, 52°, and 76.5° (Figure 4.1b) are assigned to (111), (200), and (220) planes of cubic nickel (PDF no. #01-071-4654), which confirms the conversion of nickel hydroxide to nickel. The intensity of XRD peaks corresponding to Ag increased with an increase in the concentration of Ag in the samples as illustrated in Figure 4.2(a-b). We also computed the lattice parameters of Ni and Ag from the XRD spectra (Table 4.2). Evidently, there is no significant change in the lattice parameters of Ni or Ag which indicate that Ag and Ni are not inserted in the crystal lattice of each other. This probably arises from large difference in atomic sizes of Ni and Ag. In this report, the chemical state and morphology of the $NiAg_{0.40}$ 3DPNC are primarily discussed due to its best electrocatalytic activity. The XPS core-level spectrum in the Ni 2p region (Figure 4.1c) reveals the peaks at 852.5 eV (Ni $2p_{3/2}$) and 869.7 eV (Ni $2p_{1/2}$) corresponding to the Ni (0) state.[86] Besides, the peaks at 855.8 eV (Ni^{2+} $2p_{3/2}$) and 873.1 eV (Ni^{2+} $2p_{1/2}$) alongside the satellite peaks at 860.9 eV and 879.3 eV are the characteristic peaks of the Ni^{2+}.[87] This indicates the partial oxidation of the surface nickel atoms. Further, the Ag 3d spectrum (Figure 4.1d) reveals peaks at 368.1 eV and 374.1 eV corresponding to Ag $3d_{5/2}$ and Ag $3d_{3/2}$ with a spin-orbital splitting of 6 eV revealing the Ag (0) oxidation state of silver[123] in the $NiAg_{0.4}$ 3DPNC.

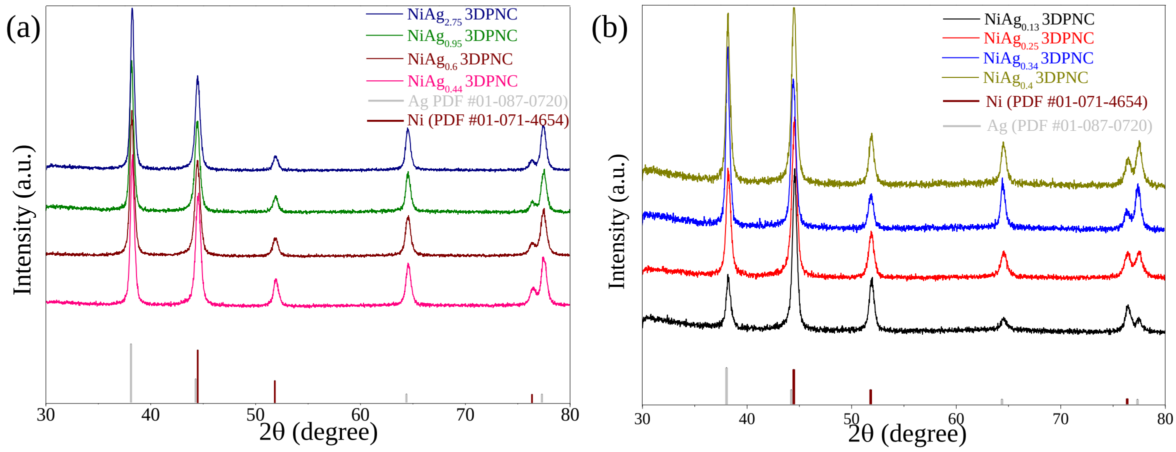

Figure 4.2 XRD patterns of (a) $NiAg_{0.13}$ 3DPNC, $NiAg_{0.25}$ 3DPNC, $NiAg_{0.34}$ 3DPNC, and $NiAg_{0.4}$ 3DPNC, and (b) $NiAg_{0.44}$ 3DPNC, $NiAg_{0.6}$ 3DPNC, $NiAg_{0.95}$ 3DPNC, and $NiAg_{2.75}$ 3DPNC.

The FESEM image (Figure 4.3a) of the $Ag/Ni(OH)_2.2/3H_2O$ before thermal reduction shows nanoparticles attached to the nanosheets, which is also distinctly seen from the transmission electron microscope image (Figure 4.3b). The HRTEM image of the nanoparticle (Figure 4.3c) reveals the d spacing of 0.235 nm and 0.204 nm corresponding to the (111) and (200) planes of cubic Ag (PDF no. #01-087-0720). Further, the HRTEM image of the nanosheets reveals the d spacing of 0.231 nm (Figure 4.4a) ascribed to (200) planes of hexagonal $Ni(OH)_2.2/3H_2O$ (PDF no. #00-022-0444). Thus, the unique structure of $Ag/Ni(OH)_2.2/3H_2O$ in which Ag nanoparticles are attached to $Ni(OH)_2.2/3H_2O$ nanosheets is revealed from HRTEM images. After the thermal reduction in hydrogen gas at 400 °C, hexagonal $Ni(OH)_2.2/3H_2O$ transforms to cubic Ni, which leads to a change in morphology of the samples to 3D porous nanoclusters as shown in Figure 4.3(d-e). The 3D porous nanocluster comprises nanoparticles of ~50 nm (lateral dimension) and pores of nearly 10 nm to 80 nm as seen from HAADF-STEM (Figure 4.3g) and FESEM image (Figure 4.3d). Pristine Ag forms nanoparticles (Ag NPs) as shown in Figure 4.5a, while nickel exhibits 3D porous nanocluster morphology similar to $NiAg_{0.4}$ 3DPNC (Figure 4.5b).

Table 4.2 Calculated lattice parameter values of Ni and Ag from XRD spectra.

Alloy system	Lattice parameter for Ni	Lattice Parameter for Ag
$NiAg_{0.13}$	3.51942	4.075916
$NiAg_{0.25}$	3.521636	4.075263
$NiAg_{0.34}$	3.520331	4.077883
$NiAg_{0.40}$	3.519652	4.076312
$NiAg_{0.44}$	3.517344	4.072512
$NiAg_{0.6}$	3.5195	4.073881
$NiAg_{0.95}$	3.5195	4.073881
$NiAg_{2.75}$	3.520234	4.07505

Further, the HRTEM image of $NiAg_{0.4}$ 3DPNC (Figure 4.3f) reveals the exposed (111) and (200) planes of Ag (PDF no. #01-087-0720) corresponding to the d spacing of 0.235 nm and 0.204 nm, respectively. The measured angle between (111) and (200) plane is 54.30°, which is close to the theoretical angle of 54.74°. Also, the adjacent region reveals d-spacing of 0.204

nm and 0.180 nm, corresponding to (111) and (200) planes of Ni (PDF no. #01-071-4654), respectively, with an angle of 54.54° between them. A closer examination of Fast Fourier Transform (FFT) images (Figure 4.4b) reveals epitaxial growth of Ag (200) on the Ni (111) surface leading to the generation of abundant epitaxial interfaces between Ag and Ni lattice in the nanostructure. It is worth noting that the lattice parameter of Ag (200) and Ni (111) are very close viz. 0.204 nm for Ag (111) and 0.2035 for Ni (111).

Also, as revealed from the HRTEM image (Figure 4.3f) the growth of Ag (200) on Ni (111) is continuous and no abrupt distortions are observed in the lattice. The SAED pattern (Figure 4.3j) exhibits rings corresponding to both Ni and Ag. The innermost ring is assigned to Ag (111) (PDF #01-087-0720), while the second ring from the center can be ascribed to either Ni (111) or Ag (200). The third ring corresponds to Ni (200) (PDF #01-071-4654), thus confirming the co-existence of Ni and Ag in the nanoclusters. Also, the HAADF-STEM image and STEM-EDX elemental mapping images (Figure 4.3(g-i)) reveal the homogeneous distribution of Ni and Ag in the nanocluster.

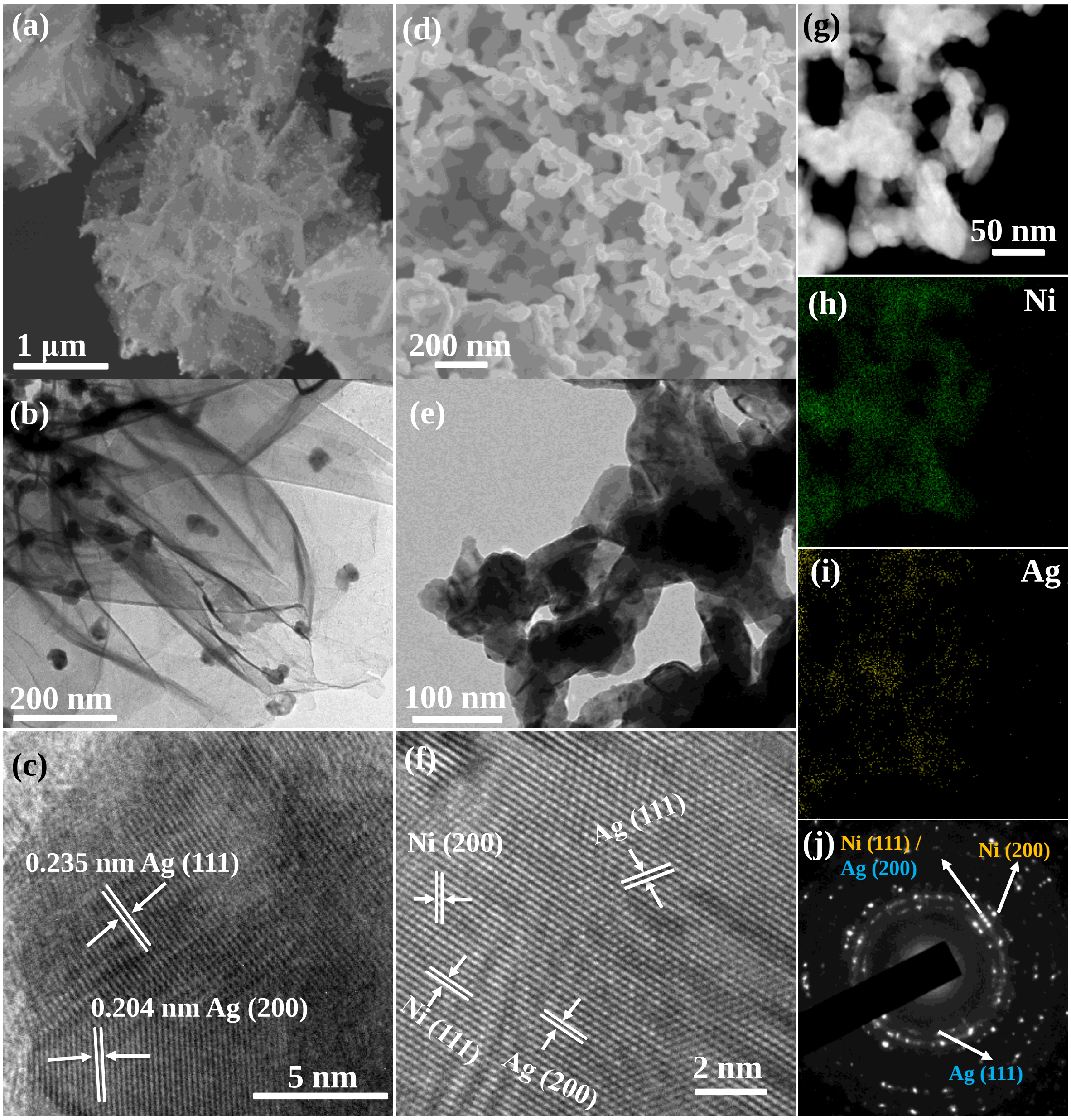

Figure 4.3 (a) FESEM image, (b) TEM image, (c) HRTEM image of the Ag nanoparticles attached to $Ni(OH)_2.2/3H_2O$ nanosheets. (d) FESEM image, I TEM image, (f) HRTEM image of $NiAg_{0.4}$ 3DPNC, and (g) HAADF-STEM image and corresponding (h-i) STEM-EDX elemental mapping images for Ni and Ag, respectively, and (j) SAED pattern of $NiAg_{0.4}$ 3DPNC.

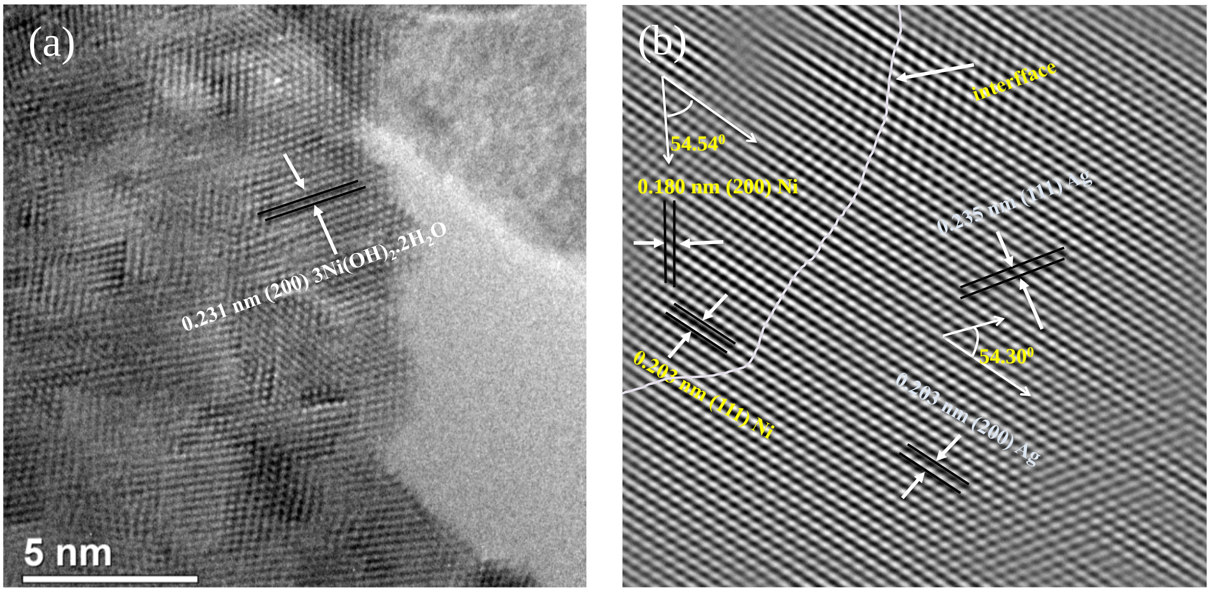

Figure 4.4 (a) HRTEM image of $Ag/Ni(OH)_2.2/3H_2O$ precursor, (b) fast Fourier transform analyzed image of $NiAg_{0.4}$ 3DPNC.

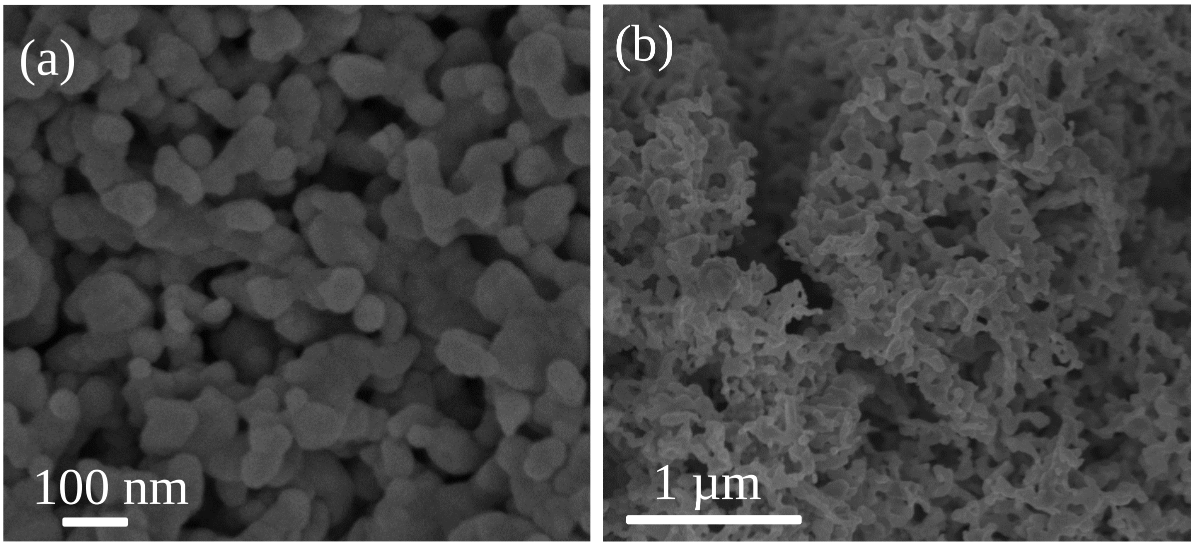

Figure 4.5 FESEM images of (a) Ag NPs, (b) Ni 3DPNC.

4.3.2 HER activity of $NiAg_{0.4}$ 3D porous nanoclusters

The electrochemical hydrogen evolution activity of the synthesized catalysts was tested in a three-electrode cell consisting of Hg/HgO as the reference electrode, graphite electrode as the counter electrode and catalyst loaded glassy carbon electrode as the working electrode. The electrolyte is 1 M KOH solution for all the experiments. The current densities reported in the following section are based on the geometric surface area of the electrodes. In the later sections, the specific activity based on the electrochemical active surface area is also discussed. Mass loading of the catalyst drastically affects the current density and can contribute to errors in the estimation of overpotential (η) across different samples.[52] Therefore, we measured the variation of overpotential @ 10 mA cm^{-2} (η_{10}) with different mass loadings for synthesized samples and commercial Pt/C (20% wt.). As observed from Figure 4.6a, for synthesized catalysts, the η_{10} gradually decreased with an increase in the mass loading up to 2.5 mg cm^{-2}. Thereafter, η_{10} remained constant. In contrast, in the case of the commercial Pt/C, the decrease in η_{10} was not observed for mass loadings above 0.5 mg cm^{-2}. Based on these outcomes, we used the mass loading of 2.5 mg cm^{-2} for all the samples to evaluate HER performance. Figure 4.6b illustrates the HER polarization curves (without iR correction) for various synthesized samples. The η_{10} for $NiAg_{0.13}$ 3DPNC (11.57% molar percentage of Ag) is 60 mV, which is lower than both pristine Ni 3DPNC (η_{10} =132 mV) and Ag NPs (η_{10} = 280 mV) as depicted in Figure 4.7a. On increasing the Ag concentration from 11.57% to 28.11%, the η_{10} gradually drops to 52 mV and 50 mV for $NiAg_{0.25}$ 3DPNC and $NiAg_{0.34}$ 3DPNC and reaches the lowest value of 45 mV for $NiAg_{0.4}$ 3DPNC.

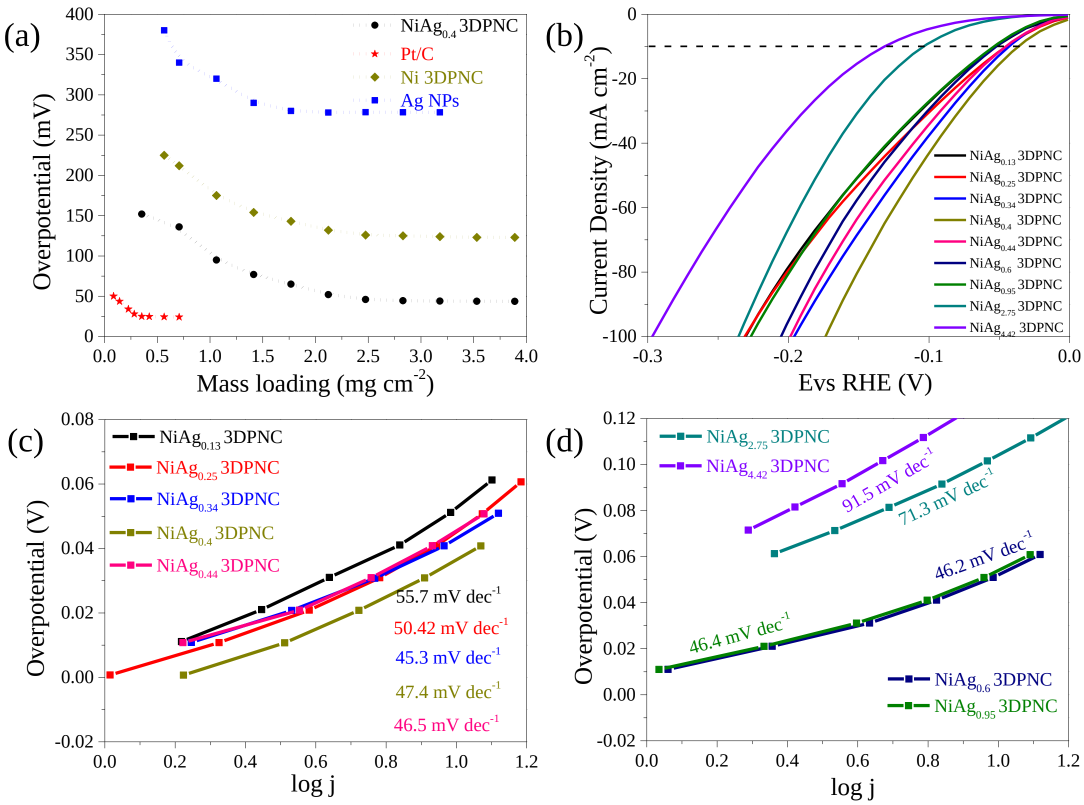

Figure 4.6 Variation of overpotential with catalyst loading for Ni 3DPNC, Ag NPs, NiAg$_{0.4}$ 3DPNC, and Pt/C catalysts. (b) HER polarization curves of NiAg$_x$ 3DPNC with varying Ni to Ag ratios without iR correction and their corresponding (c-d) Tafel plots.

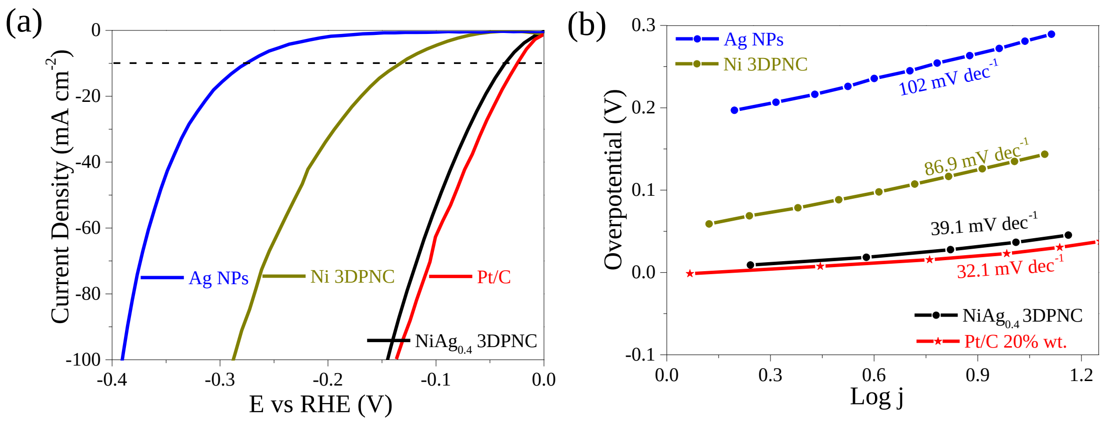

Figure 4.7 (a) HER polarization curves of Pt/C, Ni 3DPNC, Ag NPs, and NiAg$_{0.4}$ 3DPNC samples in 1 M KOH solution after iR correction, and their corresponding (b) Tafel plots.

However, on further increasing the Ag content, η_{10} increases to 51 mV, 61 mV, 69 mV, 110 mV, and 140 mV for NiAg$_{0.44}$ 3DPNC, NiAg$_{0.6}$ 3DPNC, NiAg$_{0.95}$ 3DPNC, NiAg$_{2.75}$ 3DPNC, and NiAg$_{4.42}$ 3DPNC, respectively (Figure 4.8a). Thus, from the above results, we infer that the Ag content in the porous nanoclusters influences the catalytic activity and the NiAg$_{0.4}$ 3DPNC (28.11% Ag) shows the best activity. Furthermore, Figure 4.7(a-b) shows HER activity of NiAg$_{0.4}$ 3DPNC (with iR correction) in comparison with the state-of-the-art Pt/C, pristine Ni 3DPNC, and Ag NPs. NiAg$_{0.4}$ 3DPNC exhibits low η_{10} equal to 40 mV, which is very close to Pt/C ($\eta_{10} = 28$ mV) and significantly lower than that of pristine Ni 3DPNC ($\eta_{10} = 132$ mV) and Ag NPs ($\eta_{10} = 280$ mV). Furthermore, the Tafel slope of NiAg0.4 3DPNC equals 39.1 mV dec^{-1} similar to that of Pt/C (32.1 mV dec^{-1}). The Tafel slope value of 39.1 mV dec^{-1} for NiAg$_{0.4}$ 3DPNC suggests that HER occurs through Volmer-Heyrovsky mechanism, in which electrochemical desorption is the rate-determining step.[5, 124] In contrast, the Tafel slopes of pristine Ni 3DPNC (86.9 mV dec^{-1}) and Ag NPs (102 mV dec^{-1}) are relatively high, which is indicative of their lower reaction kinetics. Encouraged by this, we also tested the HER activity of NiAg$_{0.4}$ 3DPNC in 0.5 M H_2SO_4 solution. However, unlike its activity in alkaline solution,

$NiAg_{0.4}$ 3DPNC shows a higher η_{10} equal to 178 mV significantly larger than Pt/C (η_{10} = 22 mV) as observed from the polarization curves illustrated in Figure 4.9. This could be attributed to the high susceptibility of Ni to corrosion in the acidic environment.[33]

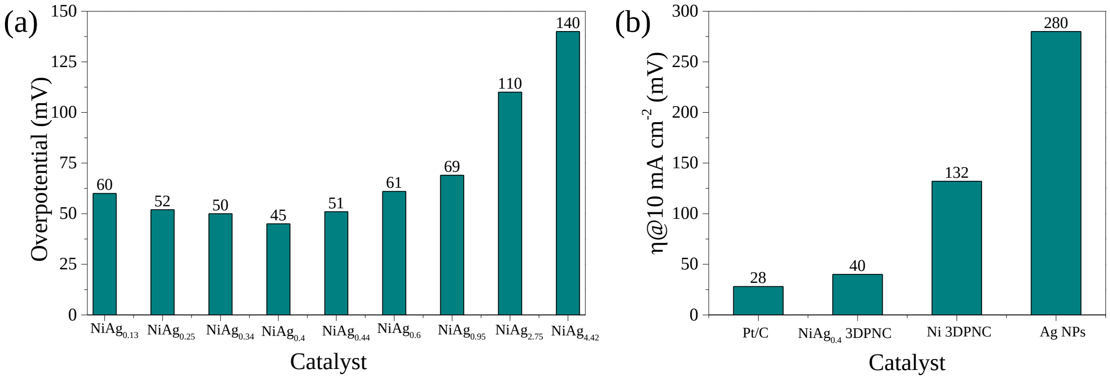

Figure 4.8 Variation of overpotential at 10 mA cm^{-2} for (a) synthesized catalysts with varying Ag composition, (b) Pt/C, $NiAg_{0.4}$ 3DPNC, Ni 3DPNC and Ag NPs.

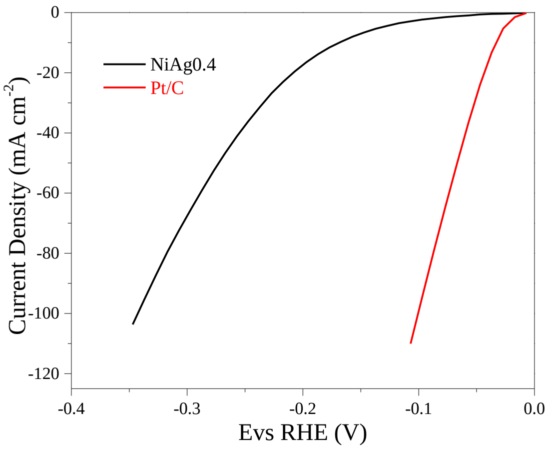

Figure 4.9 HER polarization curves for $NiAg_{0.4}$ 3DPNC and Pt/C in 0.5 M H_2SO_4.

The activity of the catalyst primarily depends on two factors; firstly, the activity of the individual active site, and secondly the number of active sites. The activity of the individual catalytic sites gives a profound insight into the intrinsic activity of the catalyst. The intrinsic activity of the catalyst can be reasonably estimated from specific activity,[125] which is computed by normalizing the geometric current density based on the electrochemical active surface area (ECSA). Herein, we evaluated the ECSA for synthesized samples from double-layer capacitance. CV scans were conducted between -0.15 V to -0.25 V vs Hg/HgO reference electrode with scan rates of 5, 10, 20, 30, 40, 50, and 60 mV s^{-1} (Figure 4.10(a-c)). The plot of capacitive current ($j_{anodic} - j_{cathodic}$) vs. the scan rate (Figure 4.11a) was used to estimate the double-layer capacitance (C_{dl}), which gives a good estimate of ECSA. The roughness factor, which was computed by dividing the C_{dl} by the specific capacitance (40 µF cm^{-2}), was used to calculate the ECSA normalized current for each sample.[80]

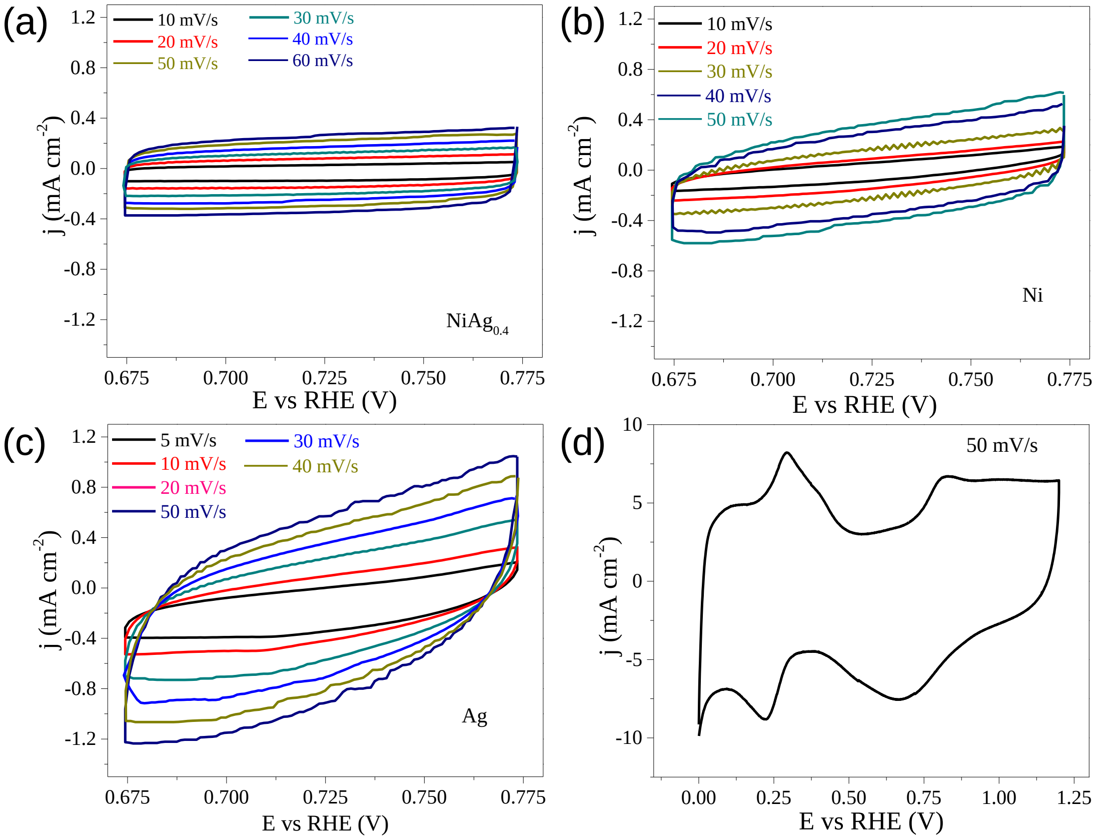

Figure 4.10 Cyclic voltagram (CV) curves for (a) $NiAg_{0.4}$ 3DPNC, (b) Ni 3DPNC, (c) Ag NPs, and (d) CV curve for underpotential deposition for Pt/C 20% wt. catalyst.

For the Pt/C catalyst, the hydrogen underpotential deposition method was used to estimate the roughness factor (Figure 4.10d). The hydrogen underpotential deposition method is more reliable and widely used for estimation of ECSA of Pt as it eliminates the contribution of capacitance arising from the carbon in Pt/C.[126] The calculated C_{dl} and roughness factor values of all the samples are listed in Table 4.2. As revealed from Figure 4.11(c-d) the η @ 0.1 mA $cm^{-2}_{(ECSA)}$ for $NiAg_{0.4}$ 3DPNC is 45 mV, which is very close to the η for Pt/C (26 mV @ 0.1 mA $cm^{-2}_{(ECSA)}$). In contrast, pristine Ni 3DPNC and Ag NPs require higher η viz. 177 mV and 313 mV (Figure 4.11(c-d)), respectively, to achieve 0.1 mA $cm^{-2}_{(ECSA)}$. Thus, the specific activity of $NiAg_{0.4}$ 3DPNC approaches Pt/C and is superior to pristine Ni 3DPNC and Ag NPs. Furthermore, electron impedance spectroscopy (EIS) test was carried out to investigate the charge transfer resistance of the synthesized samples. The Nyquist plots (Figure 4.11b) at -1 V vs Hg/HgO reveal charge transfer resistances in the following order: 29.6 Ω for Pt/C < 33.9 Ω for $NiAg_{0.4}$ 3DPNC < 114.5 Ω for Ni 3DPNC < 149.1 Ω for Ag NPs. Thus, $NiAg_{0.4}$ 3DPNC and Pt/C offer better charge transfer kinetics compared to pristine Ni 3DPNC and Ag NPs. The above results strongly indicate that the enhanced activity of $NiAg_{0.4}$ 3DPNC may be arising from the synergistic effect of both Ni and Ag in the nanoclusters. Epitaxial Interfaces may promote optimized hydrogen adsorption as reported previously for $NiPS_3/Ni_2P$ heterojunction.[76]. To obtain further insight into the mechanism of the catalysis, DFT calculations were done to determine the ΔG_H at the Ni-Ag interface. The following section elucidates the results from the DFT study.

Table 4.3 Roughness factor values for different catalysts that were evaluated from the double-layer capacitance.

Catalyst	C_{dl} (mF cm^{-2})	Roughness factor (cm^2 per cm$^2_{(geometric)}$)
Ni 3DPNC	7	175
Ag NPs	12.8	320
Pt/C	20.4738 mC cm^{-2}	97.5
NiAg$_{0.4}$ 3DPNC	4.9	125

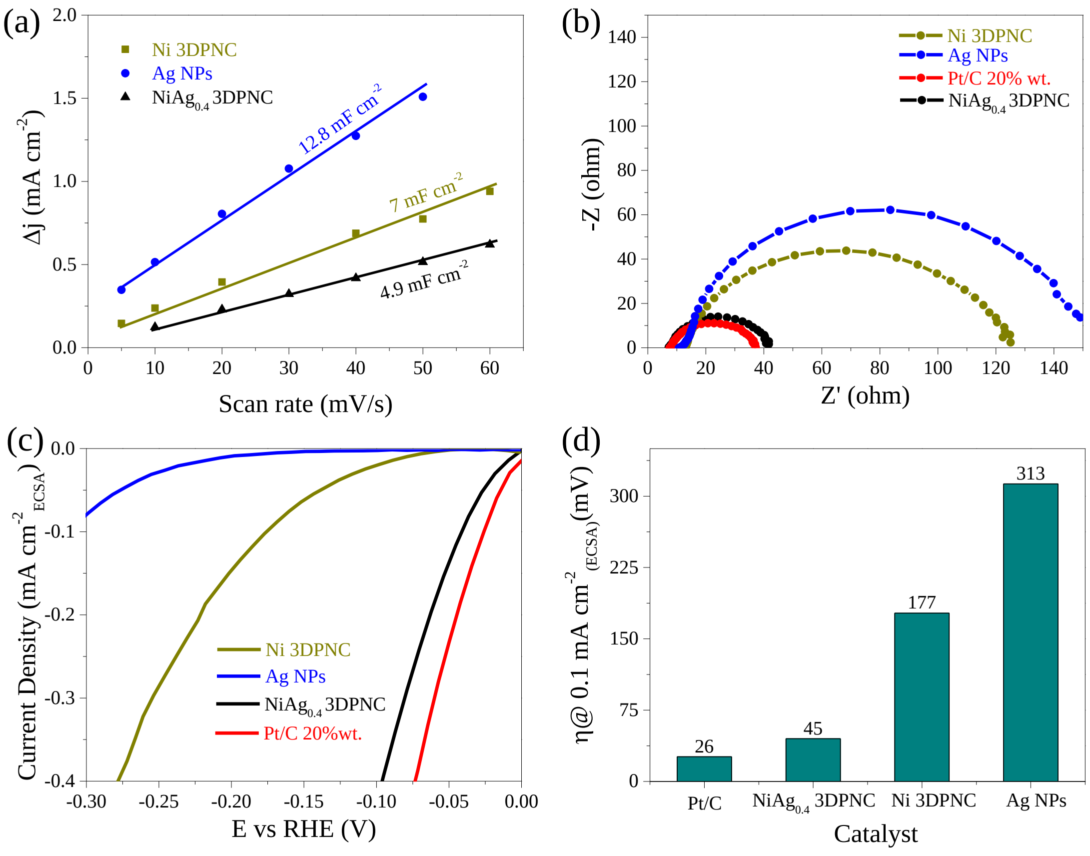

Figure 4.11 (a) The plot of capacitive current ($j_{anodic} - j_{cathodic}$) (at 0.724 V vs RHE) vs. scan rate for Ni 3DPNC, Ag NPs, and NiAg$_{0.4}$ 3DPNC. (b) Nyquist plot at -1 V vs Hg/HgO for Ni 3DPNC, Ag NPs, NiAg$_{0.4}$ 3DPNC, and Pt/C. (c) The plot of ECSA normalized current density vs. E_{vsRHE} for the above samples. (d) Comparison of overpotential at specific activity of 0.1 mA cm$^{-2}_{(ECSA)}$ for the above samples.

4.3.3 Determination of hydrogen adsorption energy at Ni-Ag interface

According to the thermodynamics, Gibbs free energy (ΔG_H) of hydrogen adsorption could be a useful in estimating the catalytic activity. For an active catalyst, the ΔG_H should be near to zero. The HER free energy diagram for pristine Ni is illustrated in Figure 4.12b. The ΔG_H are 0.325 eV (S1), -0.258 eV (S2), and -0.248 eV (S3) for pristine Ni (111), which are very far from near zero ΔG_H necessary for an advanced HER catalyst. The HER free energy diagrams for Ag/Ni (111) interface are illustrated in Figure 4.12d. Due to the change of symmetry of surface geometry, the ΔG_H for nine active sites is calculated (Figure 4.12c).

The calculated ΔG_H for the S2 site is -0.04 eV, which is close to the optimum value (0 eV). The ΔG_H for S3 and S6 sites are -0.20 eV and -0.21 eV, respectively, indicating a small change in the ΔG_H for these sites. In contrast, ΔG_H for S7 and S8 sites remain ~ 0.26 eV. Interestingly, $\triangle G_H$ for Ag site is 1.11 eV, which is larger than $\triangle G_H$ of all the sites. In summary, the adsorption of Ag on Ni (111) alters the $\triangle G_H$ of the adjacent S2 site close to zero, while the remoter sites (S3, S6, S7, and S8) are minimally affected. The H adsorption on S1, S4, and S5 sites is not stable and H moves to S6, S7, and S8 sites after relaxation.

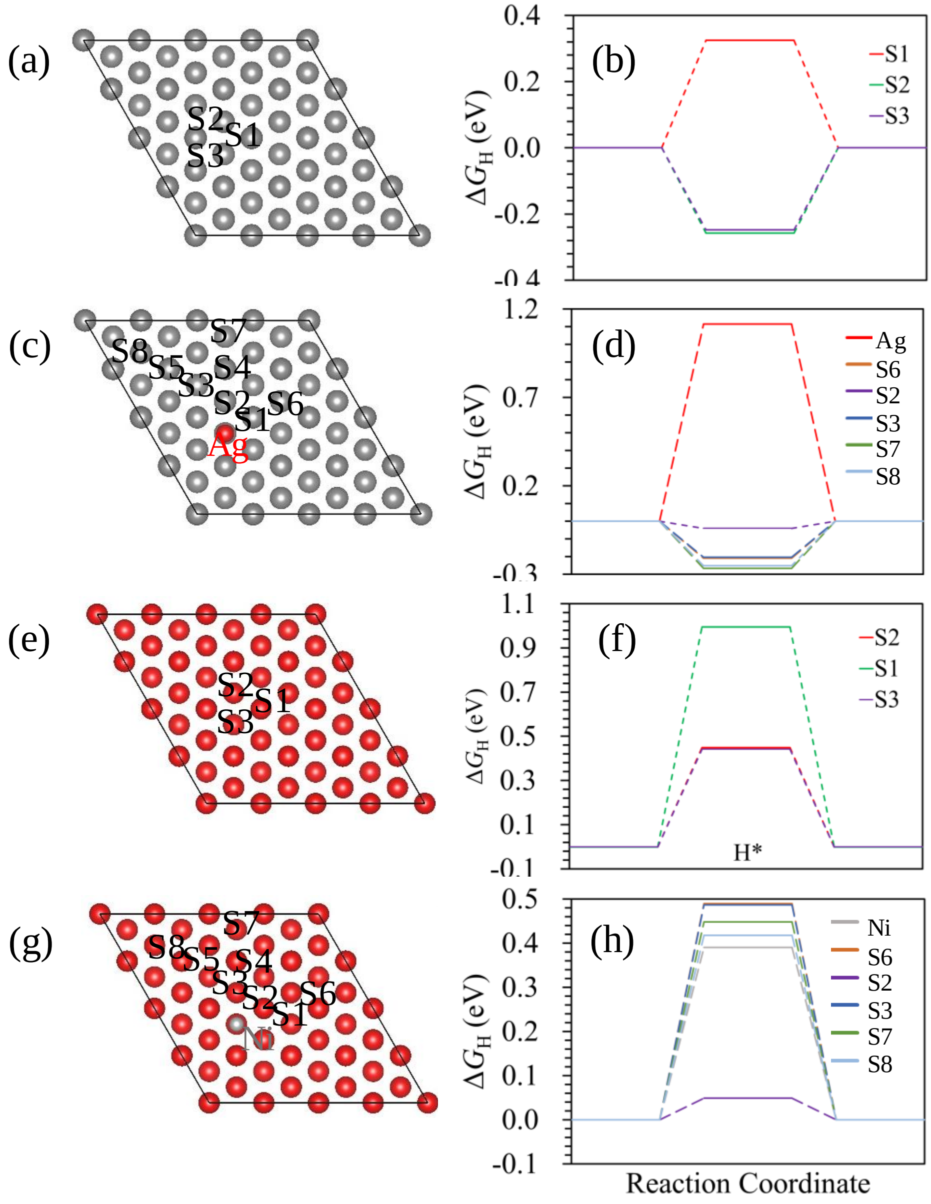

Figure 4.12 The top view with adsorption sites and free energy diagram for H atoms adsorbed on the (a/b) pristine Ni (111) surface and (c/d) the Ag/Ni (111) surface; the top view with adsorption sites and free energy diagram for H atoms adsorbed on (e/f) the pristine Ag (111) surface and (g/h) the Ni/Ag (111) surface.

In the case of pristine Ag (111) surface and Ni/Ag (111) interface, the ΔG_H values (Figure 4.12(e-h)) exhibit a similar trend. For the pristine Ag (111), ΔG_H are 0.995 eV (S1), 0.446 eV (S2), and 0.441 eV (S3) (Figure 4.12f). In contrast, the calculated $\triangle G_H$ for the S2 site is 0.05

eV, which is close to the optimum value (0 eV). The ΔG_H for S3 and S6 sites are ~0.49 eV, which is larger than pristine Ag. The ΔG_H for Ni site, S7, and S8 sites are 0.39 eV, 0.45 eV, and 0.42 eV, respectively. Thus, the Ni adsorption on Ag (111) surface alters the $\triangle G_H$ of the adjacent S2 site close to zero, while the remoter S3, S6, S7, and S8 sites are minimally affected. The H adsorption on S1, S4, and S5 sites was found to be not stable where the H atom moves to S6, S7, and S8 sites, respectively after relaxation. Thus, both Ag/Ni (111) interface and Ni/Ag (111) interface exhibit near zero $\triangle G_H$ values as revealed from the DFT study. Hence, from theoretical calculations, we can infer that Ni-Ag interface promotes hydrogen evolution.

The plot of the exchange current density (j_0) vs. Gibbs energy of hydrogen adsorption (ΔG_H) for different metals and compounds gives an array of points in the shape of a volcano. Popularly known as the volcano plot, this plot has catalysts with ΔG_H near to zero at the top with high exchange current densities (j_0) and the catalysts with large positive and negative ΔG_H exhibiting lower exchange current density on either side of the volcano peak. The position of a catalyst in the volcano plot provides key information about its activity. In this study, we calculated the j_0 for $NiAg_{0.4}$ 3DPNC by using the Tafel plot. The estimated j_0 for the $NiAg_{0.4}$ catalyst is equal to $5.10 * 10^{-5}$ A $cm^{-2}{}_{(ECSA)}$. The j_0 vs. ΔG_H plot for Ni, Ag, and $NiAg_{0.4}$ 3DPNC is shown in Figure 4.13a. The $NiAg_{0.4}$ 3DPNC has a higher exchange current density compared to Ni and Ag and lower Gibbs energy of adsorption (-0.04 eV) and reasonably fits in the volcano plot with its position closer to the volcano peak.

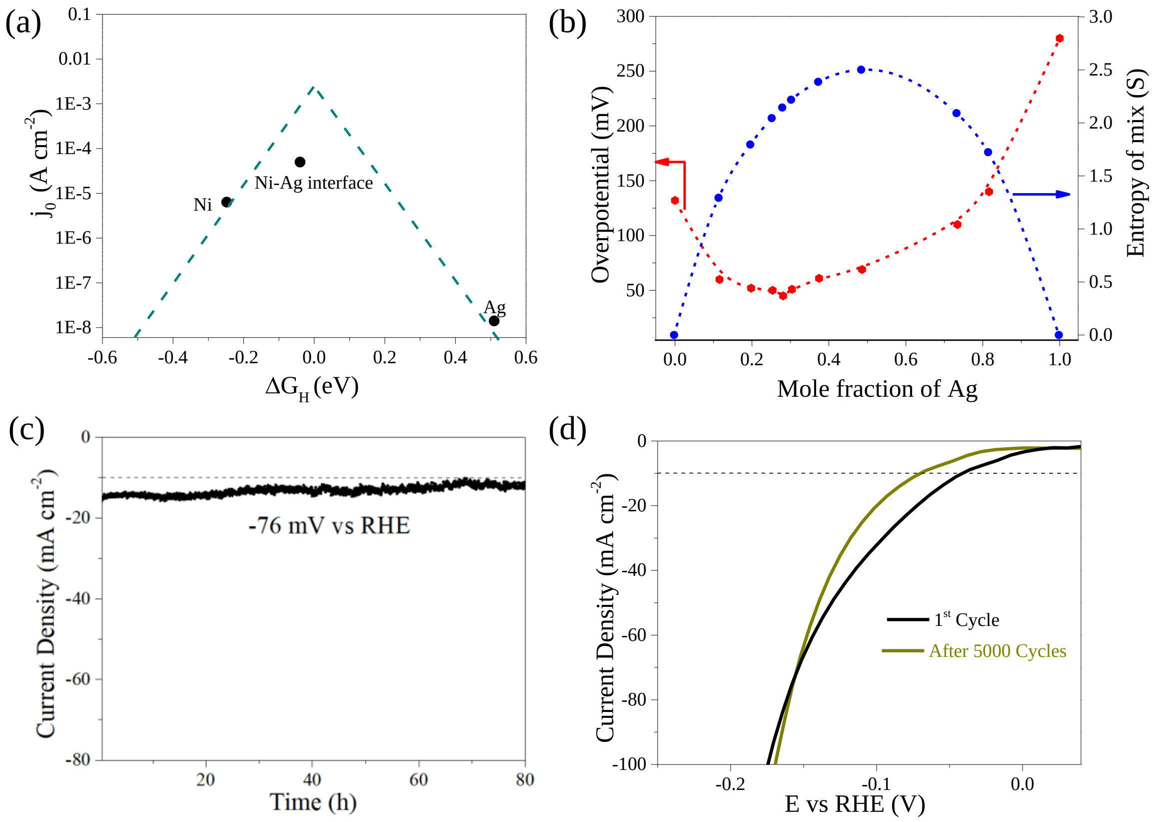

Figure 4.13 (a) The plot of exchange current density vs. Gibbs energy of hydrogen adsorption for pristine Ni, pristine Ag, and Ni-Ag interface. The ΔG_H and j_0 values of Ni and Ag are taken from ref.16. (b) Plot illustrating the relationship between the overpotential and entropy of mix (approximate estimate of interface surface area) with the increasing mole fraction of Ag. (c) Chronoamperometry test of $NiAg_{0.4}$ 3DPNC at -1 V vs Hg/HgO (76 mV overpotential) for 80 hours, (d) Comparison of HER polarization curves of $NiAg_{0.4}$ 3DPNC before and after 5000 CV cycles.

Thus, the epitaxial interface created between Ni (the element with a negative ΔG_H) and Ag (the element with a positive ΔG_H) exhibits higher exchange current density as observed from the experimental results, which is in line with a lower ΔG_H obtained from the theoretical calculations. Also, rationally a larger interface area between Ni and Ag is expected to drastically improve HER activity. For instance, if the surface area of Ni and Ag both are large, the interface area will be large (assuming Ni and Ag are homogeneously distributed throughout the structure) resulting in a higher HER activity. In contrast, if only one of the Ni or Ag surface areas is high, the interface area will be relatively low resulting in lower HER activity. Herein, we used the entropy of mix for two elements as a measure of interface area. The entropy of mix was calculated based on the mathematical formula for the entropy of the mix for a binary solid solution.[127] Although our samples do not represent solid solutions, nonetheless, the entropy of mix closely relates to the degree of the interface between Ni and Ag. In Figure 4.13b, the variation of overpotential vs. mole fraction of Ag is plotted alongside the variation of theoretical entropy of mix vs. mole fraction of Ag. The entropy of mix is low at both the lower and higher mole fractions of Ag and reaches a maximum at the mole fraction of 0.5. Thus, a higher interface area (hence a lower overpotential) is expected for the samples with a mole fraction of Ag near to 0.5. As expected, the overpotential reduces with the increase in the mole fraction of Ag; reaches a minimum at the mole fraction of 0.28; gradually increases till mole fraction of 0.724, and increases steeply thereafter. We want to bring to reader’s notice that, the interfacing of Ag and Ni throughout the nanocluster may not be perfect due to limitations of the synthesis process. Therefore, the variation of overpotential with the increase in mole fraction of Ag does not perfectly concur with the variation of the entropy of mix. Nevertheless, the variation of overpotential follows a trend similar to that of the entropy of mix to a reasonable extent, thus confirming the origin of the HER activity from the Ni-Ag epitaxial interface.

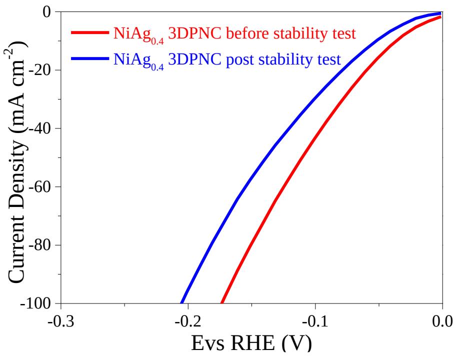

Figure 4.14 Comparison of HER polarization curve of $NiAg_{0.4}$ 3DPNC before and after 80 hours chronoamperometry test.

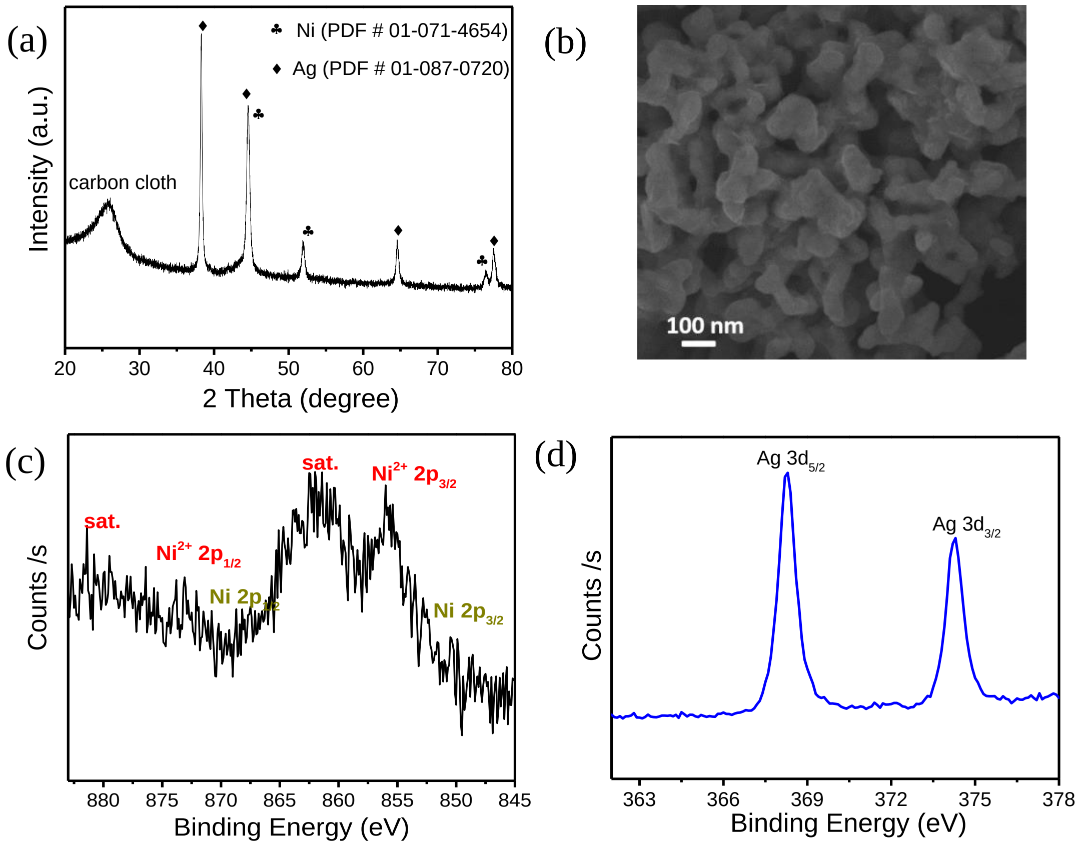

Figure 4.15 (a) XRD pattern of $NiAg_{0.4}$ 3DPNC after 80 hours chronoamperometry test. (b) FESEM image of the $NiAg_{0.4}$ 3DPNC after chronoamperometry test. XPS spectra of $NiAg_{0.4}$ 3DPNC after 80 hours chronoamperometry test in the (c) Ni 2p region, (d) Ag 3d region.

Since the commercial application of the catalyst necessitates higher activity as well as long-term durability, the chronoamperometry test was carried out at -1 V vs. Hg/HgO electrode (76 mV overpotential) for 80 hours. As revealed in Figure 4.13c, the $NiAg_{0.4}$ 3DPNC exhibits a current density of more than 10 mA cm^{-2} even after 80 hours of operation. Further, the HER polarization curves measured after the stability test reveals a marginal loss in the performance with η_{10} equal to 68 mV (Figure 4.14). Also, $NiAg_{0.4}$ 3DPNC was cycled for 5000 cyclic voltammetry (CV) cycles to further inspect the durability of the catalyst. The η_{10} increased to 70 mV after CV sweeps revealing slight degradation in the activity. However, HER activity of $NiAg_{0.4}$ 3DPNC at higher voltages remained the same as the as-synthesized catalyst (Figure 4.13d) revealing the modest durability of the catalyst. The phase, morphology, chemical state, and chemical composition of the $NiAg_{0.4}$ 3DPNC after the chronoamperometry test were investigated to detect any possible transformations in the sample. The phase of the catalyst remained the same as the synthesized sample after 80 hours chronoamperometry test as observed from the XRD patterns (Figure 4.15a). Furthermore, the SEM images of the sample after the chronoamperometry test revealed a similar 3D porous structure as of the synthesized sample demonstrating the excellent morphological stability of the catalyst (Figure 4.15b). XPS spectra of the sample after the chronoamperometry test are shown in Figure 4.15(c-d). Peaks at 852.7 eV (Ni $2p_{3/2}$) and 867.5 eV (Ni $2p_{1/2}$) correspond to the Ni (0) oxidation state, while the peaks at 856 eV (Ni^{2+} $2p_{3/2}$) and 873.1 eV (Ni^{2+} $2p_{1/2}$) alongside satellite peaks at 862 eV and 879.4 eV are the characteristic peaks of the oxidized nickel (Ni^{2+}), which is identical to the synthesized catalysts. However, the intensity of peaks at 856 eV (Ni^{2+} $2p_{3/2}$) and 873.1 eV (Ni^{2+} $2p_{1/2}$) ascribed to the oxidized nickel was higher in the tested sample revealing surface oxidation of nickel.

Table 4.4 HER activity of the $NiAg_{0.4}$ 3DPNC in comparison with other recently reported catalysts with good activity.

Catalyst	HER overpotential ($mV@mA\ cm^{-2}$)	Tafel slope ($mV\ dec^{-1}$)	Electrolyte	Stability	Reference
Boron doped RhFe alloy	25 mV @ 10 $mA\ cm^{-2}$	32	0.5 M H_2SO_4	8 hours	73
$Ni_{20}Fe_{20}Mo_{10}Co_{35}Cr_{15}$ high entropy alloy	172 mV @ 10 $mA\ cm^{-2}$	41	1 M KOH	8 hours	90
Pt_3Ni_3 NWs	70 mV @ 19.8 $mA\ cm^{-2}$	NA	1 M KOH	3 hours	71
Micro-nano MoS_2 spheres	214 mV @ 10 $mA\ cm^{-2}$	74	0.5 M H_2SO_4	24 hours	91
Pt_3Co nanoparticles	32.6 mV @ 10 $mA\ cm^{-2}$	28.6	0.5 M H_2SO_4	5000 CV cycles	72
np-CoP_3 on Ti mesh	76 mV @ 10 $mA\ cm^{-2}$	50	1 M KOH	60 hours	93
PtCo–Co/TiM	70 mV @ 46.5 $mA\ cm^{-2}$	35	1 M KOH	50 hours	94
$Fe_{1.89}Mo_{4.11}O_7/MoO_2$	197 mV @10 $mA\ cm^{-2}$	79	1 M KOH	1000 CV cycles	95
V-doped Ni_3S_2 Nanowires on Ni foam	68 mV @ 10 $mA\ cm^{-2}$	112	1 M KOH	7000 cycles	128
FeP nanoparticles	154 mV @ 10 $mA\ cm^{-2}$	65	0.5 M H_2SO_4	1.66 hours	98
IrAg nanotubes	20 mV @ 10 $mA\ cm^{-2}$	61.1	0.5 M H_2SO_4	6 hours	115
$NiAg_{0.4}$ 3DPNC	**40 mV @ 10 $mA\ cm^{-2}$**	**39.1**	**1 M KOH**	**80 hours and 5000 CV cycles**	**This work**

Further, the XPS spectrum in the Ag 3d region (Figure 4.15d) revealed peaks at 368.1 eV and 374.1 eV corresponding to Ag $3d_{5/2}$ and $3d_{3/2}$ with a spin-orbital splitting of 6 eV confirming unchanged Ag (0) oxidation of state of silver as present in the synthesized catalyst. Thus, from the XPS analysis, we argue that surface oxidation of nickel may have caused a marginal loss in the HER activity during the chronoamperometry test. In conclusion, $NiAg_{0.4}$ 3DPNC exhibits modest durability and activity and is superior to many of the recently reported catalysts (Table 4.3).

4.4 Conclusions

The electrocatalytic activity of Ni was remarkably improved by alloying with Ag. In depth, characterizations revealed the formation of heterogeneous Ni-Ag alloy with abundant interfaces between Ni and Ag throughout the 3D porous nanoclusters. The role of the Ni-Ag interface for the excellent activity of $NiAg_{0.4}$ was revealed from experimental results and the DFT calculation data. The specific activity of the catalyst approaches that of state-of-the-art Pt/C catalyst, which is in approval of near-zero (-0.04 eV) Gibbs energy of hydrogen adsorption computed from DFT studies. The catalyst showed exceptional stability and is a potential substitute for Pt/C catalyst for water splitting. In conclusion, alloying of metal with positive ΔG_H (Ag) with metal with negative ΔG_H (Ni) brought about an interface that is highly active for hydrogen evolution reaction. Thus, this work further verified our hypothesis of catalyst design as discussed before.

4.5 Outlook to next chapter

So far, we focused on the design and synthesis of new alloy systems which are active for electrolysis of water. We used conventional methods of synthesis for both the catalysts which come with inherent disadvantages. To address this issue, we developed a novel additive manufacturing process that can fabricate electrodes coated with various metal alloys and oxides in a single step. The details of the same will be discussed in the following chapter.

Chapter 5 Femtosecond Laser Direct Writing of High Entropy Alloy and Multi-metal Oxide Nanoparticles

In this chapter, we describe the development of a novel additive manufacturing process, which can be used to in-situ synthesize and coat multi-metal oxides and alloys on a variety of substrates. The ink formulation to carry out the femtosecond laser direct writing process is developed. Further, the effect of various laser parameters on the synthesis process is investigated. By detailed material characterization, the successful synthesis of a large family of oxides and alloys is established. Also, the application of fabricated electrodes for efficient electrocatalysis of water is testified. In the end, micropatterns of various shapes are fabricated using the same process to demonstrate the versatility of the method for multi-material additive manufacturing.

5.1 Introduction

Transition metal compounds such as alloys, oxides, hydroxides, sulfides, selenides, etc. are ubiquitous materials for energy storage, energy conversion, metrology, sensing, and monitoring. Consequently, the synthesis routes and fabrication methods of these devices are of enormous significance. Through the intelligent design of the synthesis process, the cost of the products can be significantly reduced for economic sustainability, while at the same time being eco-friendly. In the conventional processes, these compounds are synthesized through a variety of routes such as solvothermal process, arc melting, chemical vapor deposition, ball milling, and solid-state reaction. Unfortunately, these processes typically require a highly controlled environment and consume excess quantities of solvent and energy. Often, synthesis of these materials occurs in multiple steps and involves the use of solvents and chemicals which are unsafe to the environment. Further, the assembly of the electrochemical devices using these materials requires the use of binders to form a slurry, followed by the deposition of active material on the conductive substrate via a variety of coating or printing techniques. Unfortunately, the presence of binder and lack of close electrical contact between the active material, the conductive filler, and the electrode results in higher charge transfer resistance for electrochemical applications. Besides, the mechanical stability and durability of active material when used with the binder is often inadequate. To address this, the active material is often directly synthesized on the conductive substrates such as metal foams, carbon cloth, carbon fiber paper, etc. to produce binder-free[129-130] electrodes. However, since the conductive substrate is necessary to be inert, the choice of conductive substrates for various chemical systems is limited and all the chemical processes are not conducive to this approach. Also, for flexible/stretchable devices[131-133] comprising supercapacitors, batteries, and sensors the active material should be present on flexible/stretchable polymer substrates. Such applications involve multiple tedious steps including synthesis of materials, deposition, and assembling of the components. For the aforementioned reasons, combining the synthesis of materials and device fabrication into a single step can facilitate the fabrication of various types of devices (e.g. flexible and stretchable) and at the same time contribute to a significant reduction in consumption resources such as solvents and chemicals and energy. Laser-based synthesis can be a viable option to address the above problems. Laser-based ablation process[61, 134-135] is well known for producing metal nanoparticles in the aqueous medium. The process is versatile and can be used to synthesize a variety of metal-based nanoparticles. However, the process involves laser irradiation in the solvent medium followed by the filtration of the products similar to solvothermal processes.

To overcome these important problems, we advocate the laser direct writing method to fabricate binder-free electrodes coated with metal alloys or metal oxides. Laser-direct writing (LDW) is a simple, versatile, and low-cost process for producing devices with complex shape. It can process different types of materials depending on the wavelength of the laser source used. In the past, LDW is typically carried out using continuous-wave CO_2 lasers.[136-137] Besides, the interest in short-pulse lasers[138-139] for laser direct writing is been growing in recent years. Herein, we report the synthesis of multi-metal oxides and high entropy alloy micro and nanoparticles using femtosecond laser direct writing (FsLDW). The process involves a single step laser writing on the dried precursor ink on a substrate to produce a variety of metal alloys and oxides. The ink consists of a metal salt solution mixed with carboxymethyl cellulose (CMC) binder and citric acid. Through suitable modifications to the ink (choice of metal salt, the concentration of citric acid) the desired products can be achieved. The following section describes the process development for laser writing.

5.2 Materials and methods

5.2.1 Chemicals

Nickel nitrate tetrahydrate ($Ni(NO_3)_2.6H_2O$), cobalt nitrate hexahydrate ($Co(NO_3)_2.6H_2O$), silver nitrate solution (0.1 M), aluminum nitrate nonahydrate ($Al(NO_3)_3$. $9H_2O$), tin sulfate ($SnSO_4$), indium acetate ($(CH_3CO_2)_3In_3$), chromium acetate hydroxide ($(CH_3CO_2)_7Cr_3(OH)_2$), iron nitrate nonahydrate ($Fe(NO_3)_3.9H_2O$), zinc nitrate ($Zn(NO_3)_2.6H_2O$), cupric nitrate hemipentahydrate ($Cu(NO_3)_2.2.5H_2O$, gold chloride trihydrate ($HAuCl_4.3H_2O$), H_4PtCl_6, citric acid, and carboxymethyl cellulose (CMC) were used without further treatment.

5.2.2 Synthesis of the precursor ink

The constituents of the ink were tailored according to the choice of the final product. In a typical process, the metal salt solution was dissolved in deionized (DI) water. The molar concentration ranged from 0.1 M to 0.5 M. To this solution citric acid and carboxymethyl cellulose was added and stirred for 15 minutes. The composition of the ink is given as follows:

Desired end product	Ink composition
Oxides	Metal nitrate solution + CMC + citric acid (5% molar)
Metal/ alloys	Metal nitrate solution + CMC + citric acid (metal salt: citric acid ratio is 1:1)

5.2.3 Femtosecond direct laser writing (FsLDW) system

The precursor ink was drop cast on the stainless-steel plate/glass slide (typical quantity - 25 µl/cm^2) and dried on an electric hotplate at 60℃ for 5-10 minutes. The ink formed a uniform film over the substrate. The fabrication and patterning of transition metal alloy compounds were done through a FsLDW platform. A Yb-doped fiber laser (Amplitude Systèmes, Satsuma HP) as the pulsed laser source with a set of angle scanning Galvano mirror to guide the laser during laser writing. Ultraviolet (UV) femtosecond pulse laser (350 nm) with a repetition rate of 500 kHz and a pulse duration of 220 fs was used. The laser average power (200 mW - 700 mW) and laser writing speed (10 mm s^{-1} - 100 mm s^{-1}) were varied to investigate the effect of laser power and writing speed on the properties of the FsLDW pattern. The laser writing pitch was kept constant at 10 µm for all the samples. For printing of concentric circular patterns with three elements (Ni, Cu, and Ag) the laser writing was done in three steps. In the first step, ink containing silver precursor was drop cast, dried and laser writing was done. The glass slide was rinsed in water and dried. In the second step ink containing Cu, the precursor was drop cast on the previous pattern and dried and laser writing was carried out. In the third step, the Ni pattern was fabricated similar to the Cu pattern. For preparing a binder-free electrode for electrocatalysis, the ink was drop cast on a carbon fiber paper and dried for 10 minutes on the hotplate. Later, the carbon fiber paper with the dried ink was irradiated with Fs laser to synthesize the $NiCoCuFeCr_{0.5}$ HEA alloy.

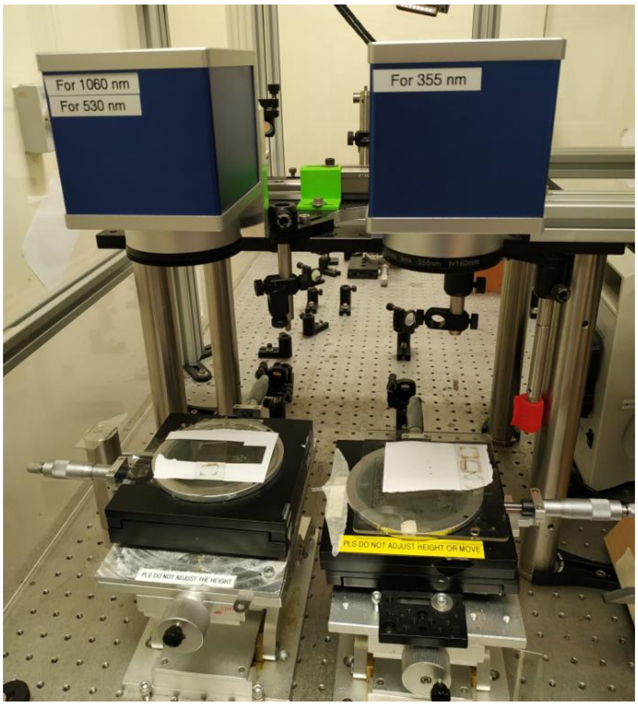

Figure 5.1 Picture showing the femtosecond laser setup used for laser direct writing.

5.2.4 Characterization

X-ray diffraction test was conducted on the Bruker D8 Advanced X-ray diffractometer with Cu K_α radiation ($\lambda = 1.5406$ Å) to identify the phase of the synthesized samples. The morphology of the samples was characterized using field emission scanning electron microscopy (FESEM, JEOL, 7600F) and transmission electron microscopy (TEM, JEOL, JEM-2100F). For the transmission electron microscopy testing, the samples from the stainless-steel foil were scrapped and dispersed in ethanol and dropped on the TEM grid for testing. To investigate the distribution of individual elements the energy-dispersive X-ray spectroscopy (EDS), elemental mapping, and bright field scanning transmission electron microscopy (BF-STEM) were performed by TEM (JEOL JEM 2100, 200 kV). The composition of the synthesized samples was tested by inductively coupled plasma-optical emission spectroscopy. Fourier transformed infrared (FTIR) spectroscopy was conducted using the Attenuated total reflectance accessory on FTIR Spectrometer (PerkinElmer - Frontier) to qualitatively assess polymer content remaining in the sintered sample.

5.2.5 Electrochemical characterization

The electrochemical measurements were done using Autolab PGSTAT302 (Eco Chemie, Netherlands) potentiostat. Testing for electrocatalysis was conducted in a typical 3 electrode cell comprising of Hg/HgO as the reference electrode, Pt electrode as a counter electrode in 1 M KOH and the laser patterned stainless steel foil/carbon fiber paper as the working electrode. The OER performance was measured by linear sweep voltammetry (LSV) at a scan rate of 2 mV s^{-1} from 0 V to 1 V vs. Hg/HgO reference electrode. The measured potential was converted to potential vs. reversible hydrogen electrode (RHE) by using the relation $E_{\mathrm{vsRHE}} = E_{\mathrm{vsHg/HgO}} + 0.098 + 0.059 * \mathrm{pH}$. The durability of the catalyst was tested by chronoamperometry test by applying a constant current of 10 mA cm^{-2} for 50 hours and measuring the voltage during the process.

CV scans were carried out from 0.3 V to 0.4 V vs Hg/HgO reference electrode at various scan rates from 5 mV/s to 60 mV/s. The difference in the current density ($j_{\mathrm{anodic}} - j_{\mathrm{cathodic}}$) was plotted against the scan rate. The slope of the plot equals twice the double-layer capacitance (C_{dl}). The electrochemical active surface area (ECSA) was calculated by dividing the C_{dl} by specific capacitance (assumed as 40 µF cm^{-2}). The ECSA normalized current was obtained by dividing the current density corresponding to the geometric area by the calculated ECSA.

5.3 Results and Discussion

The femtosecond laser direct writing fabrication of multi-metal oxides and alloys allows for a one-step fabrication of electrodes. Figure 5.2 succinctly summarizes the advantages of the femtosecond laser direct process over the conventional methods of synthesis. In the conventional process, nanoparticles are synthesized through different methods such as ball milling, hydrothermal process, solid-state reaction, solvothermal process, arc melting, sol-gel method, etc. The process is then followed by washing and drying of the powder and also thermal annealing in a furnace in the presence of inert gases like Ar/N_2 or reducing atmospheres like H_2/CO. Later the catalyst in the powder form is mixed with conductive fillers (e.g. Super Pure carbon), binder (Nafion, PVDF, CMC, etc.) and dispersed in a solvent (isopropyl alcohol, DMF, ethanol, etc.) to make the catalyst slurry. The slurry is coated on the conductive substrates like carbon fiber paper, carbon cloth, or metal foils and dried to be used as an electrode for energy storage, catalysis, or sensing. As described, the whole fabrication process involves multiple steps leading to downtime. The processes are often carried out at high temperature and pressure, use a large quantity of solvent, and are energy-intensive. In contrast, the femtosecond laser writing process is a single-step rapid process. It employs aqueous-based ink, with low usage of water and minute concentrations of the binder. Furthermore, the FsLDW is a cold process conducted at room temperature. The substrate remains at room temperature during and after the laser irradiation. Further, with the suitable tuning of the composition of the ink and the additives the final product of the synthesis can be determined viz. metal oxide and alloys. The process is carried out in an open atmosphere and does not need the presence of any gas such as Ar, N_2, or H_2. In the following section, we will discuss the details of the ink formulation.

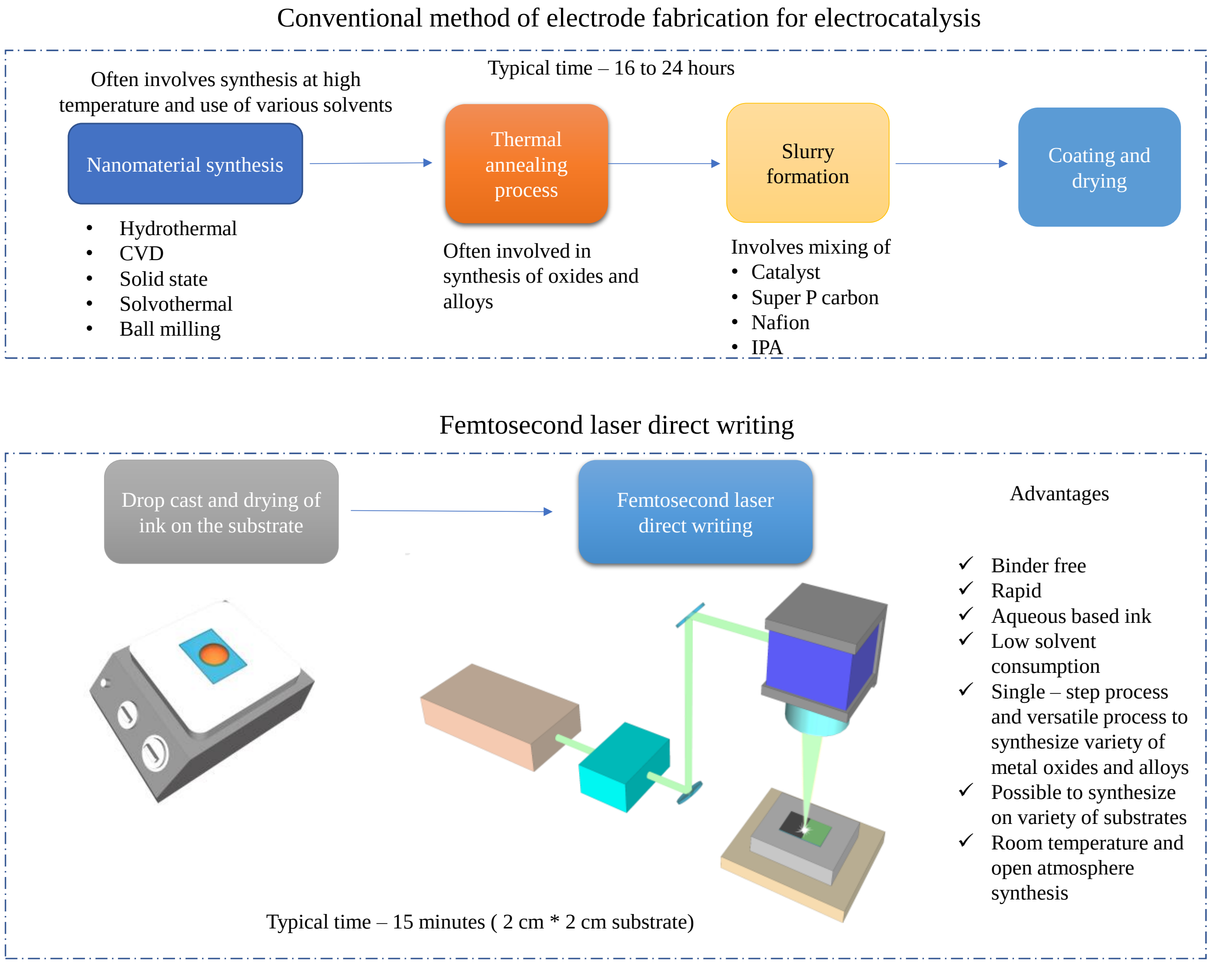

Figure 5.2 Comparison of conventional processes of electrode fabrication versus the femtosecond laser direct writing method.

5.3.1 Ink formulation and laser parameter optimization

As discussed previously the ink consists of metal salt solution mixed with CMC binder and citric acid. The metal salt acts as a feedstock for laser processing. The role of the CMC binder is to form a uniform thin film during the drying process. Citric acid plays the role of a surfactant, where the citric acid molecules behave like emulsifiers and stop the coagulation of metal salt solution with CMC. Figure 5.3a shows the coagulation of the CMC binder in Fe precursor ink in the absence of citric acid. In the metal alloy precursor ink, the citric acid concentration is equal to the salt concentration where it acts as a reducing agent. Interestingly citric acid is a mild reducing agent that does not react with metal ions under ambient conditions. The use of any strong reducing agents such as $NaBH_4$ will cause immediate precipitation. Owing to this unique property, our ink facilitates the formation of thin-film with all the constituents of the ink in their original state. Images of different precursor inks are shown in Figure 5.3b. The concentration of the salt solution was varied to examine the formation of a stable ink. It was observed that ink forms a stable solution up to 0.5 M concentration of the salt solution. For the concentrations above 0.5 M, agglomerates formed between the polymer and solution owing to the high salt concentrations. Therefore, solution concentration was kept below 0.5 M in all the inks. Further, CMC concentration greater than 0.2 mg/ml was required to form a uniform dried thin film free from any crystallized salt.

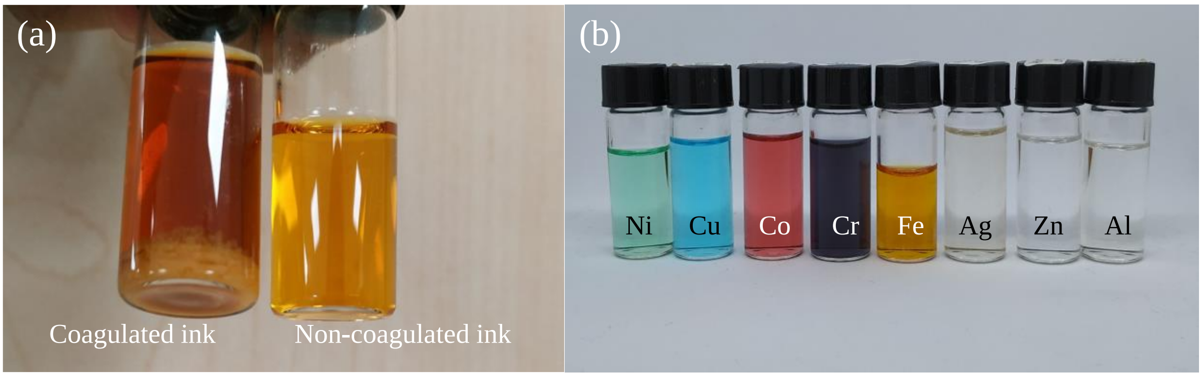

Figure 5.3 (a) Images showing coagulation of the Fe precursor ink in the absence of citric acid, (b) Picture of various precursors inks used for FsLDW..

The FESEM images in Figure 5.4a depict the micro-patterns formed by laser direct writing on the stainless-steel (SS) foil. On the right is the micro-patterns formed on SS foil with ink

(Figure 5.4b). As seen from FESEM images, micro-nano particles formed during the laser irradiation are strongly bonded to the SS foil. The process is versatile and can be repeated on a variety of substrates such as glass, carbon fiber paper, Zn foil, Cu foil, Ni foil, etc. Further, the ink formulation and the laser writing parameters are expected to have a significant effect on the nature of the product formed.

In the first step, we investigated the effect of ink formulation on the products formed. FESEM images (Figure 5.5(a-e)) reveal the type of product formed for inks with different salt concentrations. For low salt concentrations (0.01 M to 0.05 M) the quantity of nano-microparticles formed is extremely low and the SEM images show micropatterns similar to the bare SS foil. In contrast, the well-bonded nano-micro particles are seen for laser patterned inks with salt concentrations from 0.1 M to 0.5 M. The cross section FESEM images in Figure 5.6 and Figure 5.7 reveal further characteristics of impact of salt concentration. At low concentration of 0.01 M and 0.05 M, the ink is not dried uniformly on the substrate, and as a result the formed particles are not coated uniformly. However, for salt concentrations above 0.2 M the coating is relatively uniform. Since, higher mass loading of active material is always desired for electrochemical applications, 0.5 M salt concentration was used for all the inks in the future studies.

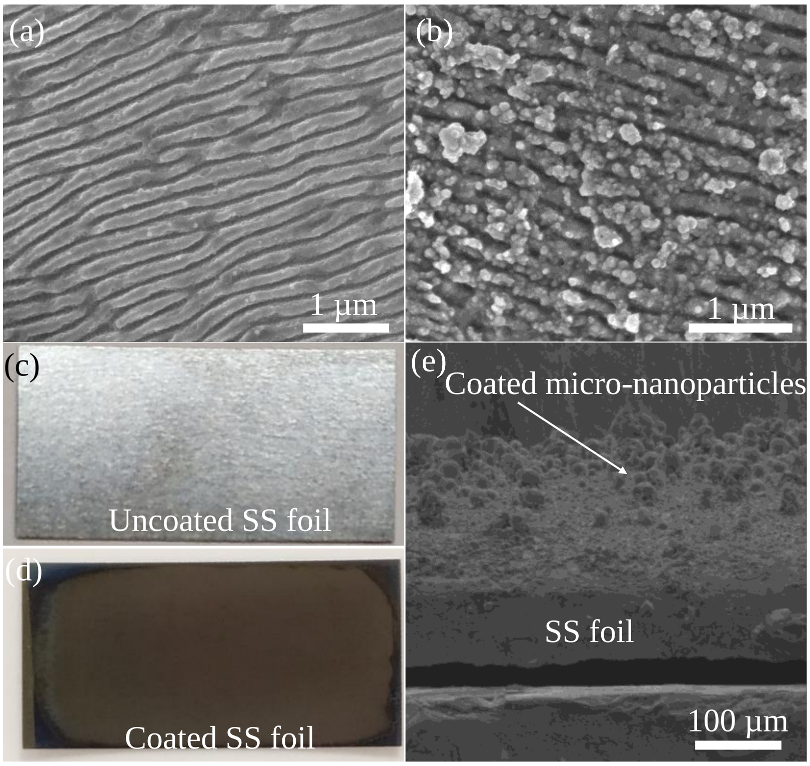

Figure 5.4 FESEM images of FsLDW pattern on (a) stainless steel foil without ink, (b) stainless steel foil with ink. Pictures of (c) bare SS foil, (d) SS foil coated with Ni. (e) Cross-section FESEM view of the SS foil coated with Ni using FsLDW.

In the next step CMC concentration was varied from 0.2 mg/ml to 1 mg/ml. As seen from Figure 5.5(f-j) the nature of the nano-microparticles during the laser writing process is not significantly affected by the CMC concentration. Since the presence of polymer is not suitable for electrochemical applications like electrolysis, it is advisable to use lower polymer concentrations. Therefore, in the subsequent experiments, the lower possible polymer concentration of 0.4 mg/ml was used. The ink with 0.2 mg/ml CMC concentration was not used, as the film formed upon drying on the hotplate was not uniform and promoted partial crystallization of salt.

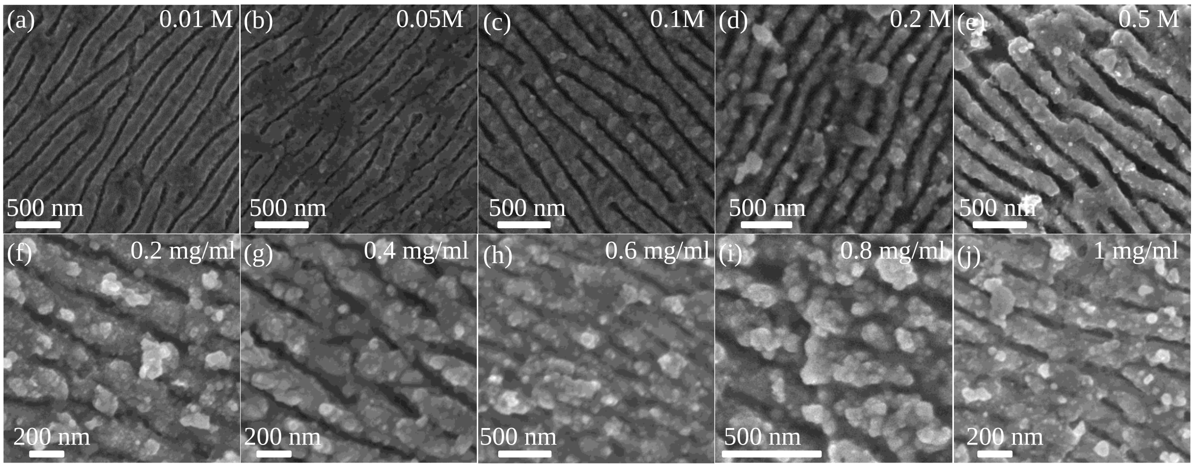

Figure 5.5 Field emission scanning electron microscope images of FsLDW patterns of Cu (a-e) for different salt concentrations from 0.01 M to 0.5 M, (f-j) for different polymer concentration from 0.2 mg/ml to 1 mg/ml.

The parameter, which primarily determines the extent of laser-material interaction is the laser fluence which is defined as the optical energy delivered per unit area. In the case of laser direct writing, the laser fluence can be tuned by varying laser power, writing speed, and the frequency. In our study, we have used the maximum frequency of 500 kHz that is available with the device to utilize the maximum power from the laser. Herein, we investigated the effect of laser power and laser writing speed on the nature of the product formed. When the laser power was low (200 mW to 400 mW) the ink was not sufficiently sintered as observed from Figure 5.8(a-c) and Figure 5.9(a-c)The FESEM images show dark regions and no visible formation of micro-nano particles. In contrast, at sufficiently higher powers from 500 mW to 700 mW finger-like patterns along with micro and nanoparticles were formed revealing the complete sintering of the ink as seen from FESEM images (Figure 5.8(d-f)). Further, the cross section FESEM images (Figure 5.9) also reveal uniform sintering and coating of synthesized particles for higher laser powers (500 mW – 600 mW). Based on these observations we chose 600 mW laser power for further tests.

Further probe into the effects of varying the lase writing speed gave interesting insights. As shown in Figure 5.10(a-f), on reducing the scan speed from 100 mm s^{-1} to 10 mm s^{-1} the sintering of the sample was enhanced, and the finger-like micropatterns vanished. The micro size line patterns may be attributed to the fast-scanning speed. At low scan speeds of 10 mm s^{-1}, there were no observed finger-like patterns (Figure 5.10f), and only uniformly dispersed nanoparticles were observed. Since, we desire sufficient sintering of samples, as well as fast fabrication speeds for practical application on the industrial scale we consider a scan speed of 40-60 mm s^{-1} to be sufficient to synthesize fully sintered nanoparticles.

Furthermore, we investigated the phase of the product formed for various laser writing speed and laser powers for Cu precursor ink. As seen from Figure 5.11a laser direct writing produces Cu as the product for the whole range of laser power from 300 mW to 600mW at a scan speed of 50 mm s^{-1}. At 200 mW the ink was not fully sintered hence no Cu was formed. In the next step, laser writing speed was varied to find the product formed. The FsLDW produces Cu as the product for laser writing speeds from 100 mm s^{-1} to 50 mm s^{-1}. When the speed was further reduced to 25 mm s^{-1} the XRD spectrum revealed the peaks of Cu and Cu_2O indicative of the partial oxidation of the Cu (Figure 5.11b). Further, when the scanning speed was 10 mm s^{-1} the XRD spectrum showed only Cu_2O peaks implying complete oxidation of Cu to Cu^+. This is not desirable for the formation of alloys. From these observations, the laser power of 600 mW and the scanning speed of 50 mm s^{-1} appears to be a suitable choice for the synthesis of oxides and alloys.

We also investigated the extent of sintering of CMC polymer during laser direct writing. It is desirable to have a lesser quantity of polymer after laser direct writing to prevent it from interfering with catalyst electrolyte interaction. Fourier transform infrared spectroscopy study was conducted for the samples synthesized on SS foil. Attenuated total reflectance (ATR) accessory was used during the testing and the absorbance of the sample was measured. As revealed in Figure 5.12, when the laser power is low there is residual CMC left in the samples. The stretched peaks at 3242.5 cm^{-1} is a characteristic peak for -OH stretching corresponds to hydroxyl bonds[140-141] of CMC. Also, peaks at 1629.5 cm^{-1} and 1324.8 cm^{-1} correspond to the carboxyl group, while the smaller peak at 1043.7 cm^{-1} is a characteristic of C-O-C.[142] Notably, the intensity of these peaks reduce at higher laser power and lower laser writing speeds. At laser power of 600 mW and writing speeds lesser than 50 mm/s the peaks are negligibly small revealing near-complete burnout of CMC during laser writing. Thus, laser power of 600 mW and 50 mm/s seems to be adequate for FsLDW from FTIR studies too. Even though lower writing speeds of 20 mm/s would support better removal of CMC, the alloys are oxidized at higher laser fluence. Hence, for all our studies we chose 600 mW laser power and 50 mm/s laser writing speed for FsLDW of oxides and alloys.

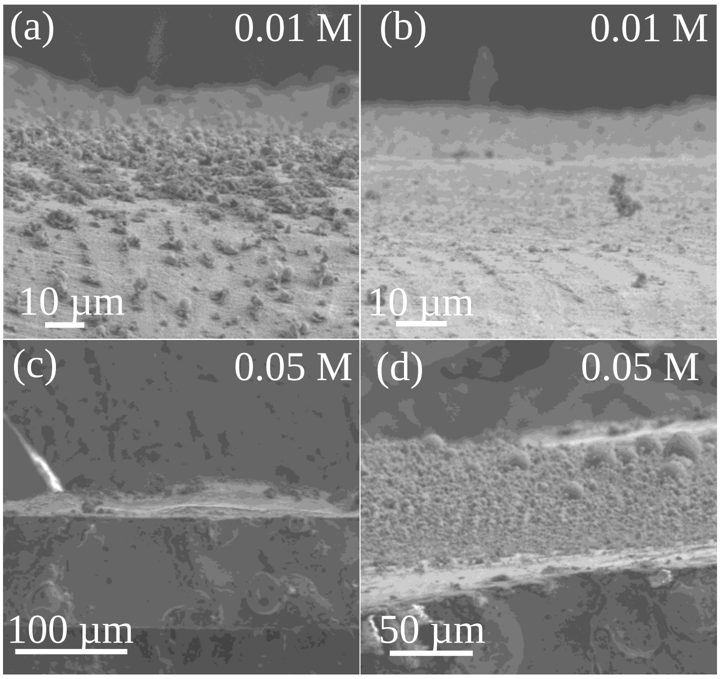

Figure 5.6 (a-d) Cross section FESEM images of FsLDW patterns of Cu for different salt concentrations from 0.01 M to 0.05 M.

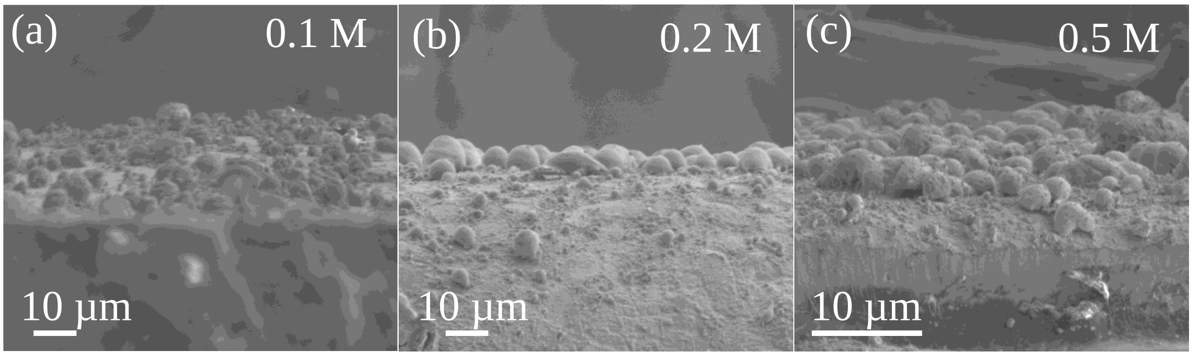

Figure 5.7 (a-c) Cross section FESEM images of FsLDW patterns of Cu for different salt concentrations from 0.1 M to 0.5 M.

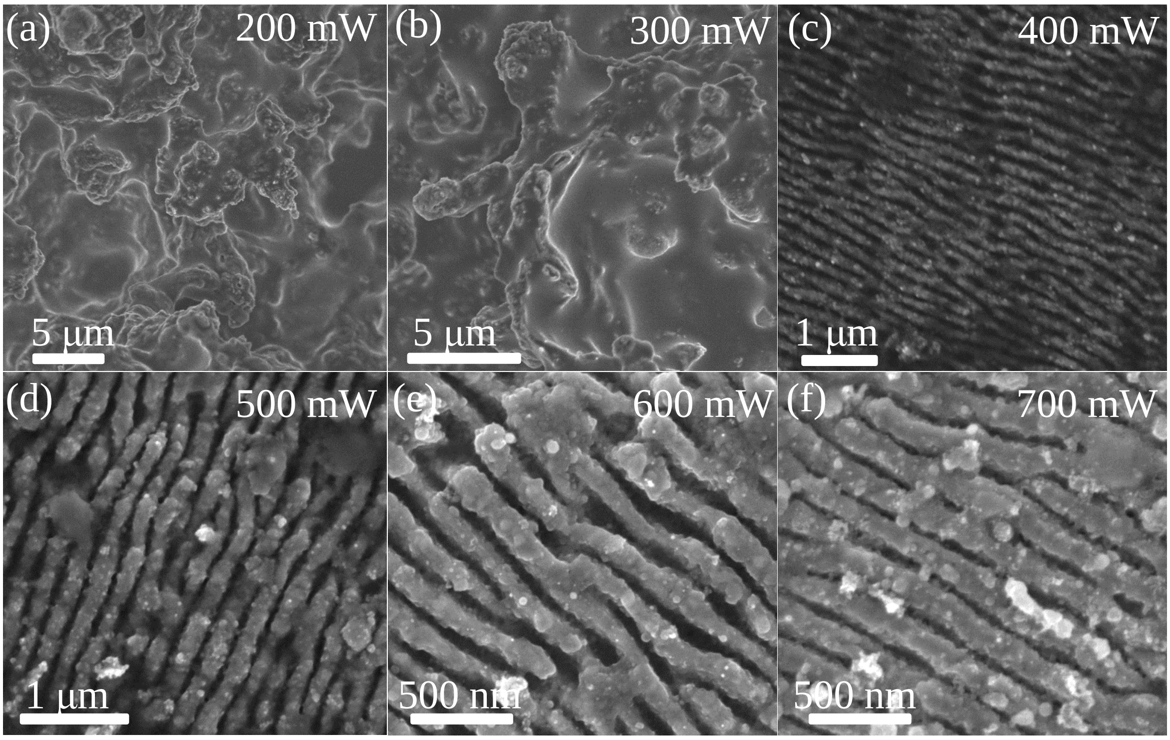

Figure 5.8 (a-f) Field emission scanning electron microscope images of FsLDW patterns of Cu for varying laser power from 200 mW to 700 mW.

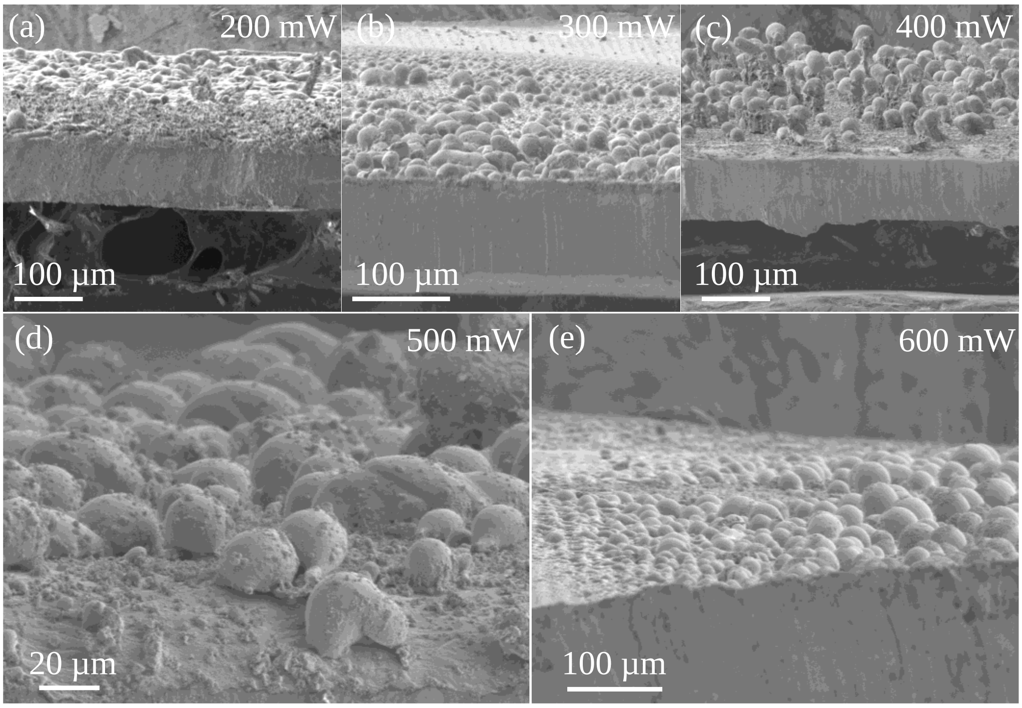

Figure 5.9 (a-f) Cross section FESEM images of FsLDW patterns of Cu for varying laser power from 200 mW to 600 mW.

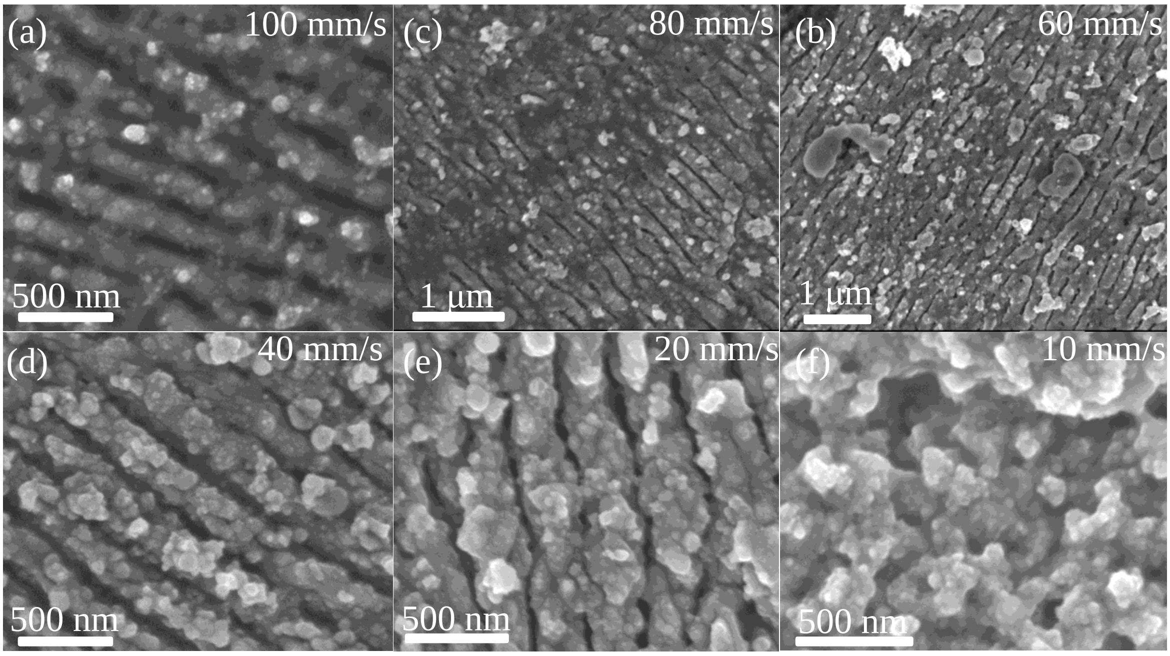

Figure 5.10 (a-f) Field emission scanning electron microscope images of FsLDW patterns of Cu for varying laser scan speed from 10 mm/s to 100 mm/s.

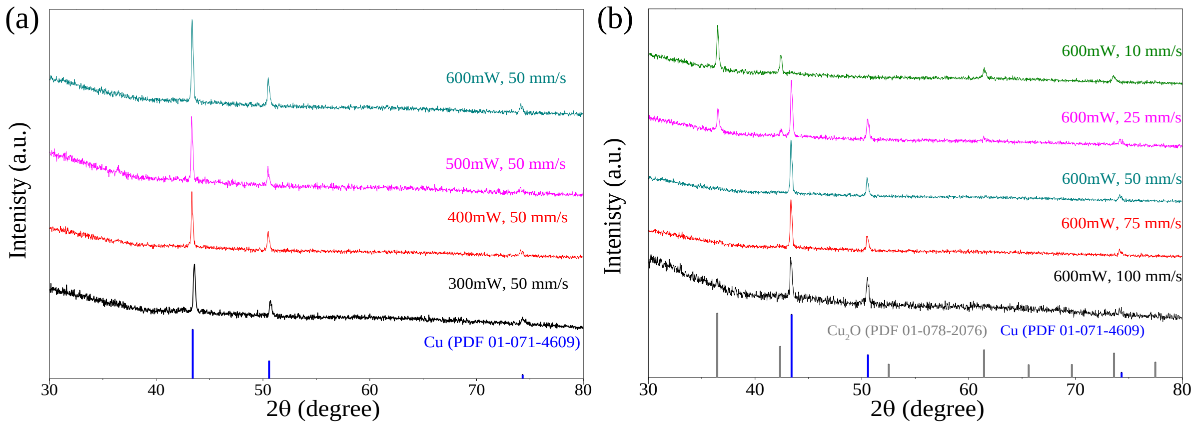

Figure 5.11 XRD spectra of Cu synthesized by femtosecond laser writing for (a) different laser power, (b) different laser writing speed.

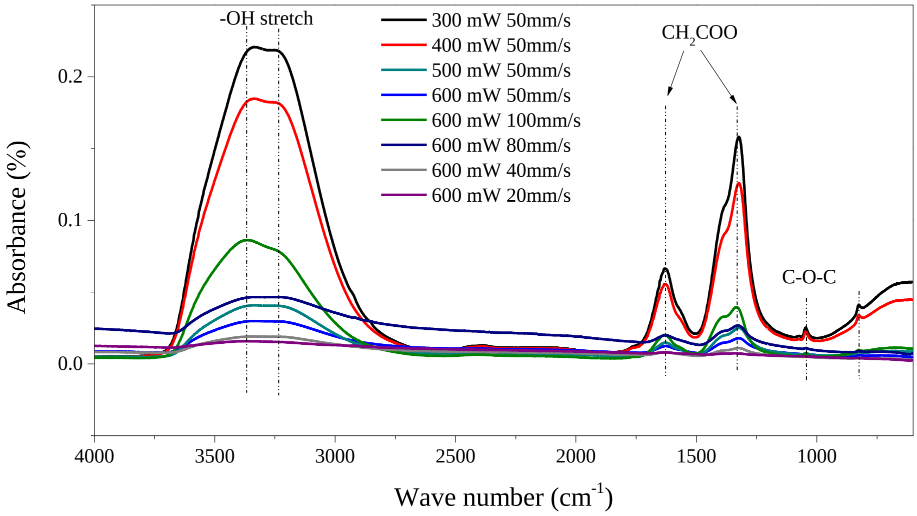

Figure 5.12 FTIR spectra of Cu samples for various laser power and writing speeds.

5.3.2 Synthesis of high entropy alloys and multi-metal oxides

The electrochemical applications often involve multi-element compounds which exhibit enhanced functionality towards catalysis, energy storage, and sensing. This is because doping, alloying, and interface engineering of multi-element compounds can achieve interesting electronic structures that is not present in single metals and oxides. Therefore, in this study, an attempt was made to synthesize alloys and multi-metal oxides using the FsDLW technique. The ink formulation is critical in determining the type of final product in this process. The metal oxide precursor ink consists of metal salt solution (typically 0.5 M solution of metal nitrate) mixed with CMC and citric acid (5% molar concentration of metal salt). The CMC polymer functions as a binder that plays an important role in forming a uniform thin film of ink after drying. Citric acid functions as a surfactant that helps in uniform mixing of metal salts with a CMC binder. The precursor ink is transformed into metal alloy or oxides by laser irradiation. The interesting aspect of a femtosecond laser is its extremely short pulse duration which in this case is 220 femtoseconds. When the laser is emitted, the high energy pulse excites the electrons in the target material during the pulse duration. The energy from the excited electrons is later transmitted to lattice in the time scale of few microseconds. Owing to this, the laser energy transferred to the substrate in those short time intervals can reach up to 5 MJ/s which is difficult to achieve in continuous-wave lasers. Despite, transfer of such high energy pulses, the temperature of the substrate remains at room temperature as the pulse duration is in femtoseconds. Consequently, the metal salt is transformed into metal oxide according to the following equation:

$$M(NO_3)_x + \text{citric acid (5\% molar)} + CMC \rightarrow M_xO_y + NO_z + CO_2 + C \qquad (5.1)$$

In the case of acetates, the product is CO_2 and metal oxides. The citric acid and CMC polymer are either burnt or are converted into carbon. In contrast, in the metal alloy precursor ink, the concentration of citric acid is equal to the molar concentration of metal salt. By so doing, the citric acid acts as a reducing agent by reducing the metal nitrates to metal according to the following chemical equation:

$$M(NO_3)_x + \text{citric acid} \rightarrow M + NO_z + CO_2 + C \qquad (5.2)$$

Going further, when the ink contains multiple metal salts, we can achieve the formation of multi-metal oxides and alloys as per the following equations:

$M_1(NO_3)_x + M_2(NO_3)_a + \ldots + M_n(NO_3)_b$ + citric acid (5% molar) + CMC $\rightarrow M_1M_{2\ldots.}M_nO_y + NO_z + CO_2 + C$ (5.3)

$M_1(NO_3)_x + M_2(NO_3)_a + \ldots. + M_n(NO_3)_b$ + citric acid + CMC $\rightarrow M_1M_{2\ldots.}M_n + NO_z + CO_2 + C$, where M_1, M_2,……,M_n are various metals. (5.4)

In our approach, preparing ink precursor for mixed metal compounds is extremely simplified. What is more, the concentration of each metal in the final product can be tuned by control of the respective salt concentration in the ink. The conventional method of laser ablation method would require different metal alloy plates for every composition of alloy for the synthesis of alloy and multi-metal oxide nanoparticles. Without a doubt, that approach is troublesome, especially for the synthesis of materials on a small scale. On the contrary, in our approach, any quantity of material ranging from milligrams to grams can be easily synthesized and the raw materials required are the same for all composition of alloys and oxides.

The products synthesized through FsLDW were first tested by XRD measurement to investigate the phase of the compounds formed. Metal alloys and oxides were synthesized on a glass substrate and used as it is for the testing. The XRD spectra of the synthesized oxides are shown in Figure 5.13, Figure 5.14, and Figure 5.16. Table 5.1 shows the list of oxides synthesized and the matching JCPDS files from the International center for diffraction data (ICCD) database. As evidenced, a large group of multi-metal oxides comprising Ni, Co, Cu, Fe, Cr, Mn, Zn, In, and Sn can be synthesized with this approach. Further, the EDS elemental mapping images in Figure 5.15, Figure 5.17, Figure 5.18, and Figure 5.19 reveal the homogeneous distribution of these metals and oxygen in the multi-metal oxides. Thus, the formation of multi-metal oxides is confirmed from XRD spectra and the EDS maps.

Table 5.1 List of multi-metal oxides synthesized by FsLDW process and the corresponding matching JCPDS files from the ICCD database.

Sl. No.	Synthesized oxide	Matching compound (JCPDS No.)	Sl. No.	Synthesized oxide	Matching compound (JCPDS No.)
1	NiO	Cubic NiO (01-071-4750)	18	FeCo oxide	Cubic $Fe_{0.1}Co_{0.9}O$ (04-019-5918), cubic Fe_2CoO_4 (00-066-0244)
2	CoO	Cubic CoO (01-076-3828)	19	$NiCu_{0.1}O$	Cubic $Ni_{0.9}Cu_{0.1}O$ (04-013-8956)
3	CuO/Cu_2O	Cubic Cu_2O (01-078-2076), monoclinic CuO (00-048-1548)	20	$ZnCu_{0.1}O$	Hexagonal $ZnCu_{0.1}O$ (04-019-3566)
4	ZnO	Hexagonal ZnO (04-009-7657)	21	ITO	Cubic $In_{1.826}Sn_{0.174}O_{3.09}$ (04-023-7387)
5	Cr_2O_3	Cr_2O_3 (96-901-5001)	22	NiFeCr oxide	Cubic $CrFe_2O_4$ (04-008-0778), cubic $Fe_{0.25}Ni_{0.75}O_4$ (04-002-4790)
6	Fe_2O_3/Fe_3O_4	Trigonal Fe_2O_3 (96-210-1169) / cubic Fe_3O_4 (96-900-2318)	23	NiCoCu oxide	Cubic $Co_{0.5}Ni_{0.5}O$ (04-019-6384), cubic $Cu_{0.36}Ni_{0.64}O$ (04-006-4881)
7	SnO_2	Tetragonal SnO_2 (00-041-1445)	24	NiCoCr oxide	Cubic NiO (01-071-4750)
8	MnO/Mn_3O_4	Cubic MnO (04-002-8344) / tetragonal Mn_3O_4 (01-085-6754)	25	CoFeCr oxide	Cubic $CrFeCoO_4$ (04-006-6585)
9	Al_2O_3	Trigonal Al_2O_3 (96-100-0060)	26	NiCoFe oxide	Cubic $Co_{0.5}Ni_{0.5}Fe_2O_4$ (00-066-0246)

10	CoNi oxide	Cubic $Co_{0.5}Ni_{0.5}O$ (04-019-6384)	27	NiCuCoCr oxide	Cubic $Co_{0.5}Ni_{0.5}O$ (04-019-6384), cubic $Cu_{0.36}Ni_{0.64}O$ (04-006-4881)
11	NiMn oxide	Cubic $(NiO)_{0.75}(MnO)_{0.25}$ (01-0778-0425	28	NiCoCuFe oxide	Cubic $Cu_{0.36}Ni_{0.64}O$ (04-006-4881), Cubic $Co_{0.5}Ni_{0.5}O$ (04-019-6384)
12	CoCr oxide	Cubic $Cr_{1.55}Co_{1.45}O_4$ (04-001-8686), cubic Cr_2CoO_4 (04-022-4700)	29	NiCoFeCr oxide	Cubic $Cr_{0.5}Fe_{1.5}Co_{0.5}Ni_{0.5}O_4$ (04-020-6842)
13	CoCu oxide	Cubic $Cu_{0.4}Co_{0.6}O$ (04-021-6819)	30	CoCuFeCr oxide	Cubic $Cu_{0.23}Cr_{0.76}Fe_{2.01}O_4$ (01-083-4280), Cubic $CrFeCoO_4$ (04-006-6585)
14	CuFe oxide	Cubic $CuFe_2O_4$ (04-001-7821)	31	NiCuFeCr oxide	Cubic $Cu_{0.7}Cr_{0.3}Fe_{1.7}Ni_{0.3}O_4$ (04-014-9685)
15	CrFe oxide	Cubic $CrFe_2O_4$ (04-008-0779)	32	NiCoCuFeCr oxide	Cubic $Cu_{0.4}Fe_{1.4}Co_{0.8}Ni_{0.2}O_{3.938}$ (04-021-6462)
16	NiFe oxide	Cubic $Fe_{1.7}Ni_{1.43}O_4$ (96-100-6117)	33	$Ni_{0.25}Co_{0.25}Cu_{0.25}Cr_{0.25}Fe_2O_4$	Cubic $Cr_{0.15}Fe_{1.85}Co_{0.8}Ni_{0.2}O_{3.938}$ (04-021-6459), cubic $Cu_{0.5}Fe_2Ni_{0.5}O_4$ (04-005-7634)
17	NiCr oxide	Cubic NiO (96-900-8694)			

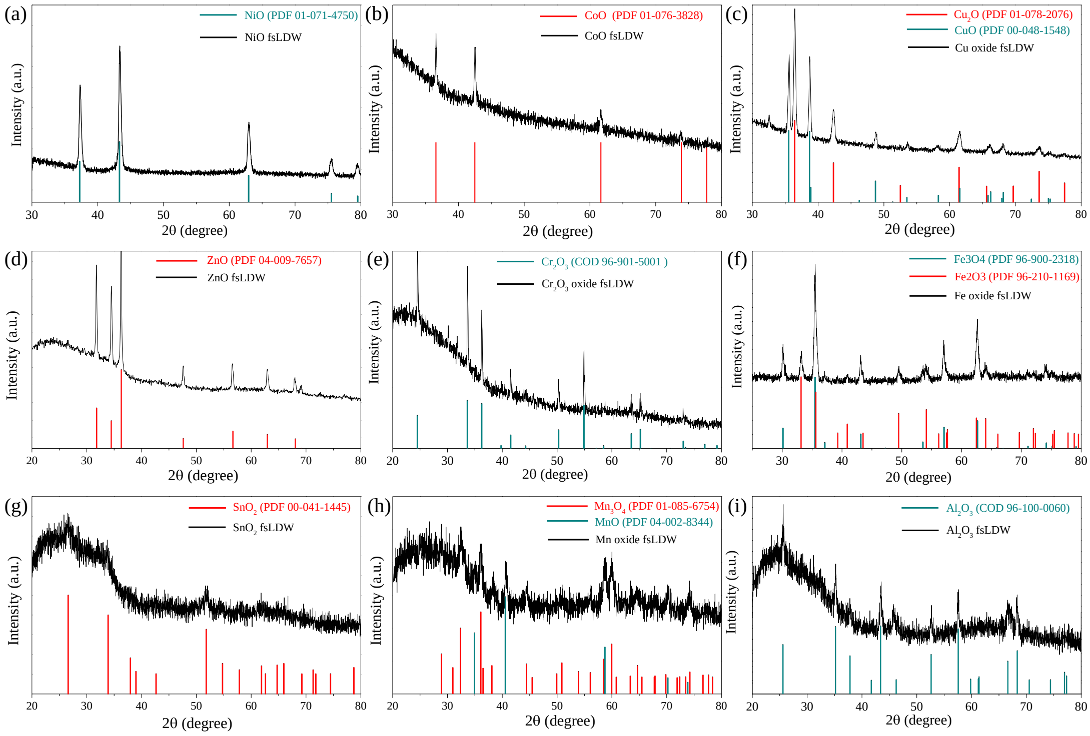

Figure 5.13 XRD spectra of (a) NiO, (b) CoO, (c) CuO/Cu_2O, (d) ZnO, (e) Cr_2O_3, (f) Fe_2O_3/Fe_3O_4, (g) SnO_2, (h) MnO/Mn_3O_4, (i) Al_2O_3 synthesized by femtosecond laser direct writing.

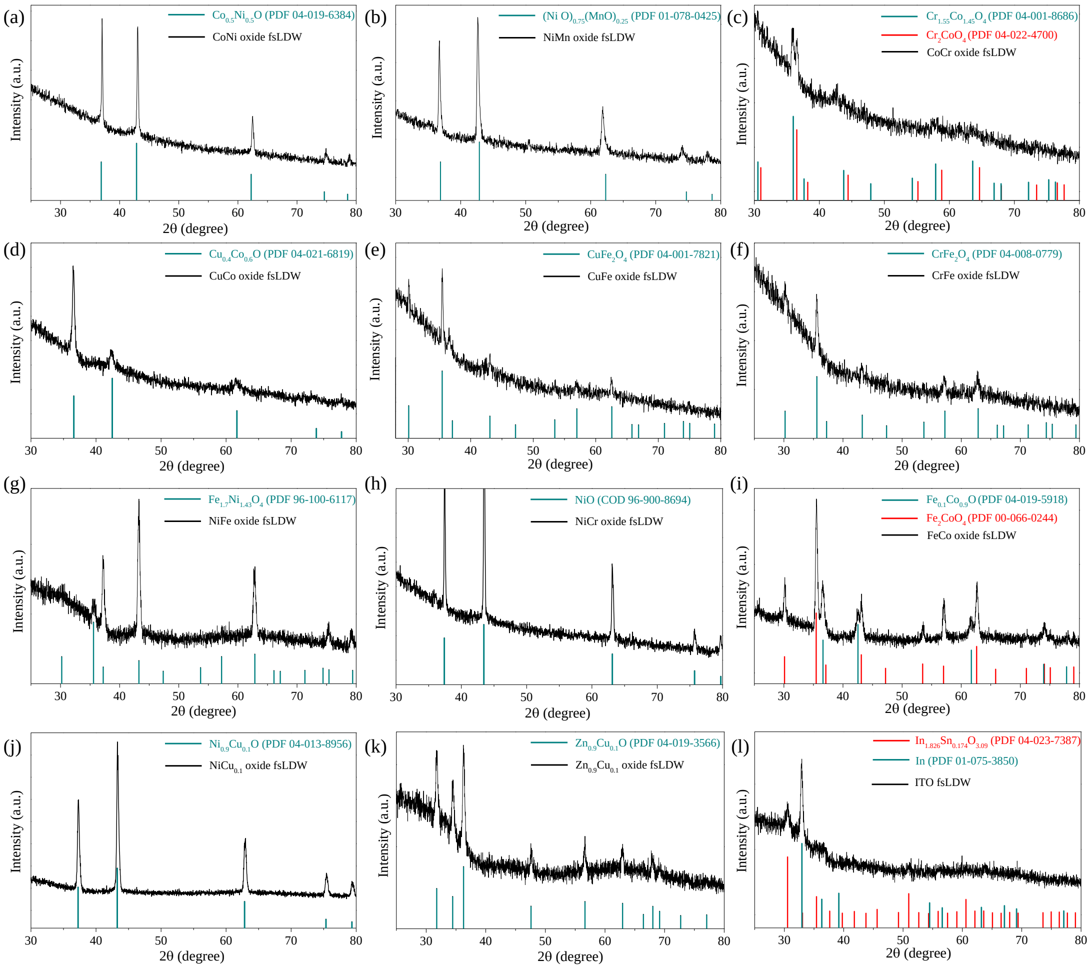

Figure 5.14 XRD spectra of (a) CoNi oxide, (b) NiMn oxide, (c) CoCr oxide, (d) CuCo oxide, (e) CuFe oxide, (f) CrFe oxide, (g) NiFe oxide, (h) NiCr oxide, (i) FeCo oxide, (j) $NiCu_{0.1}$ oxide, (k) $ZnCu_{0.1}$ oxide, (l) Indium tin oxide synthesized by femtosecond laser direct writing.

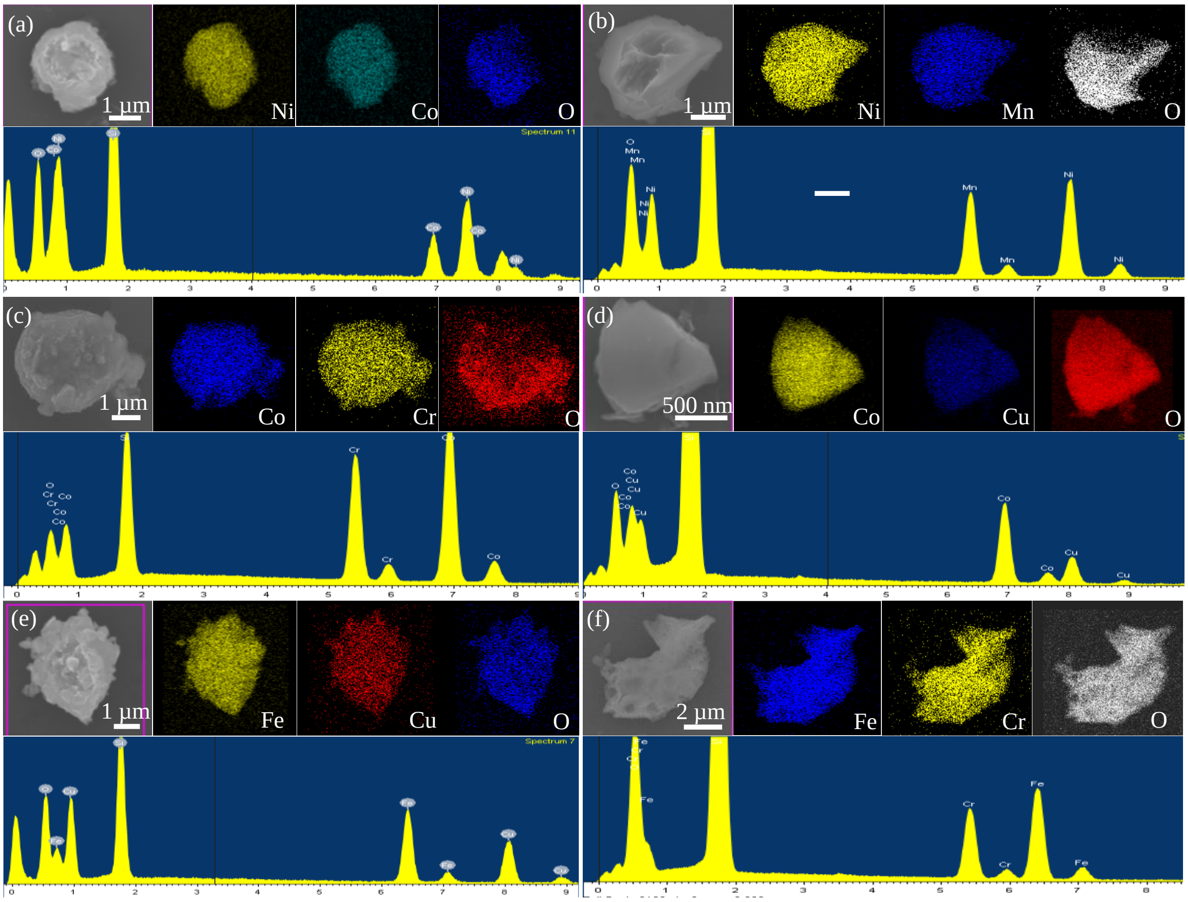

Figure 5.15 FESEM EDS elemental mapping and corresponding EDS spectra for Femtosecond laser synthesized (a) NiCo oxide, (b) NiMn oxide, (c) CoCr oxide, (d) CoCu oxide, (e) FeCu oxide, (f) FeCr oxide.

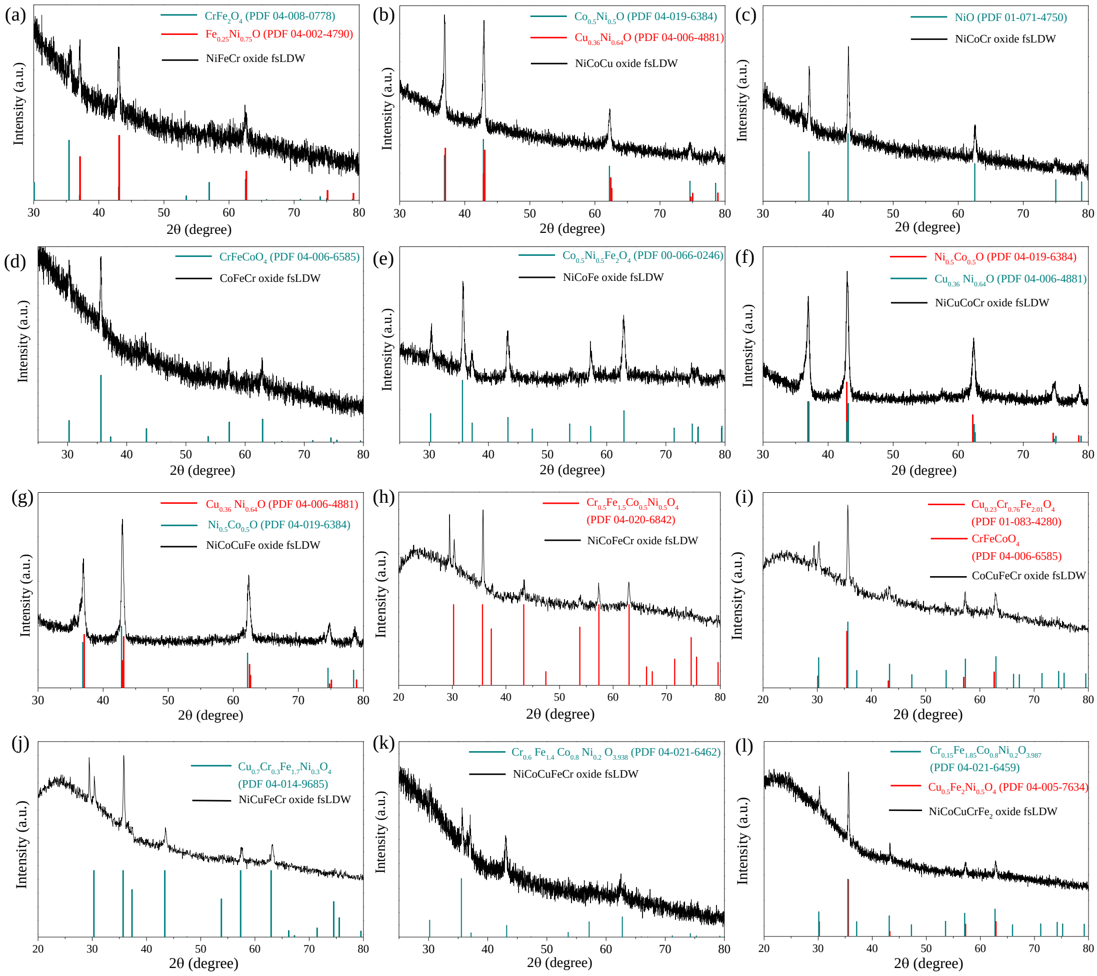

Figure 5.16 XRD spectra of (a) NiFeCr oxide, (b) NiCoCu oxide, (c) NiCoCr oxide, (d) CoFeCr oxide, (e) NiCoFe oxide, (f) NiCuCoCr oxide, (g) NiCoCuFe oxide, (h) $Ni_{0.5}Co_{0.5}Fe_2Cr_{0.5}$ oxide, (i) $Co_{0.5}Cu_{0.5}Fe_2Cr_{0.5}$ oxide, (j) $Ni_{0.5}Cu_{0.5}Fe_2Cr_{0.5}$ oxide, (k) NiCoCuFeCr oxide, (l) $Ni_{0.25}Co_{0.25}Cu_{0.25}Cr_{0.25}Fe_2$ oxide synthesized by femtosecond laser direct writing.

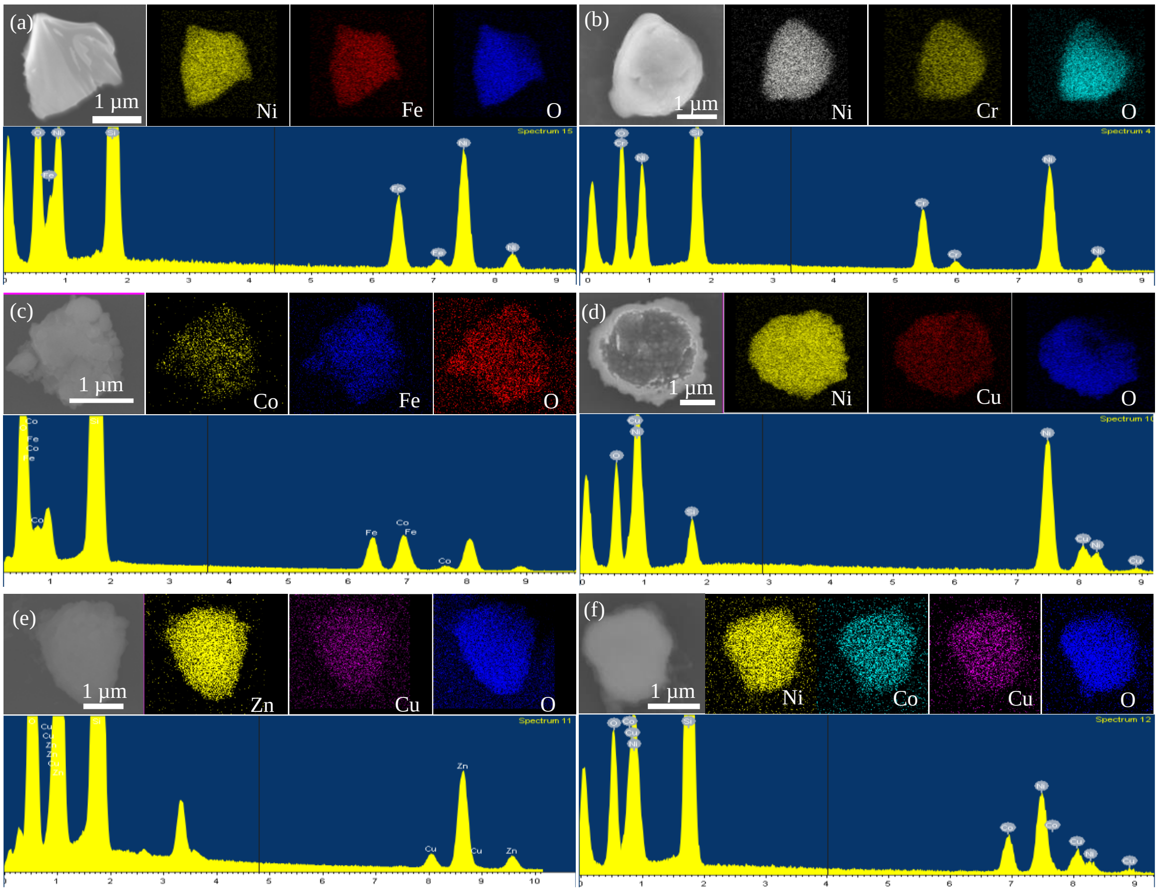

Figure 5.17 FESEM EDS elemental mapping and corresponding EDS spectra for Femtosecond laser synthesized (a) NiFe oxide, (b) NiCr oxide, (c) CoFe oxide, (d) $NiCu_{0.1}$ oxide, (e) $ZnCu_{0.1}$ oxide, (f) NiCoCu oxide.

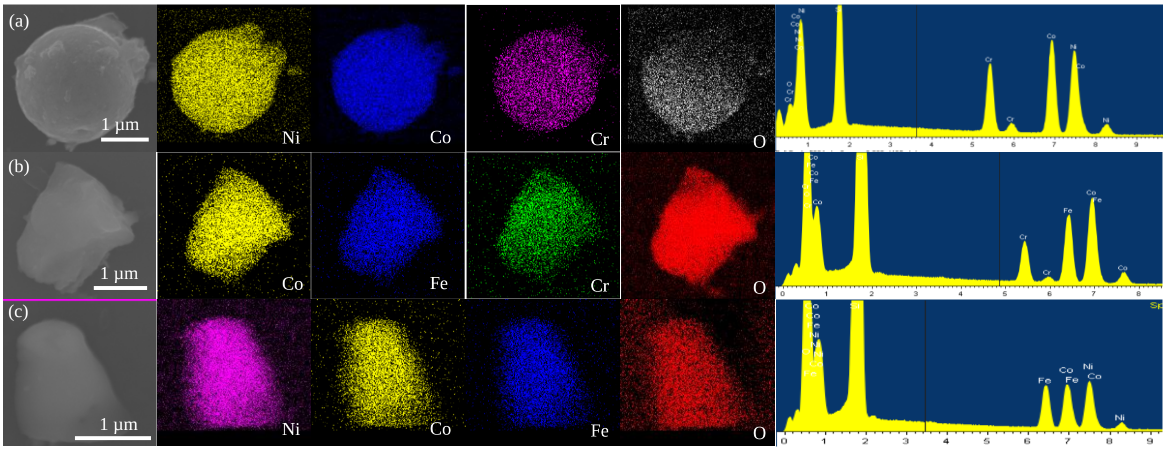

Figure 5.18 FESEM EDS elemental mapping and corresponding EDS spectra for Femtosecond laser synthesized (a) NiCoCr oxide, (b) CoFeCr oxide, (c) NiCoFe oxide.

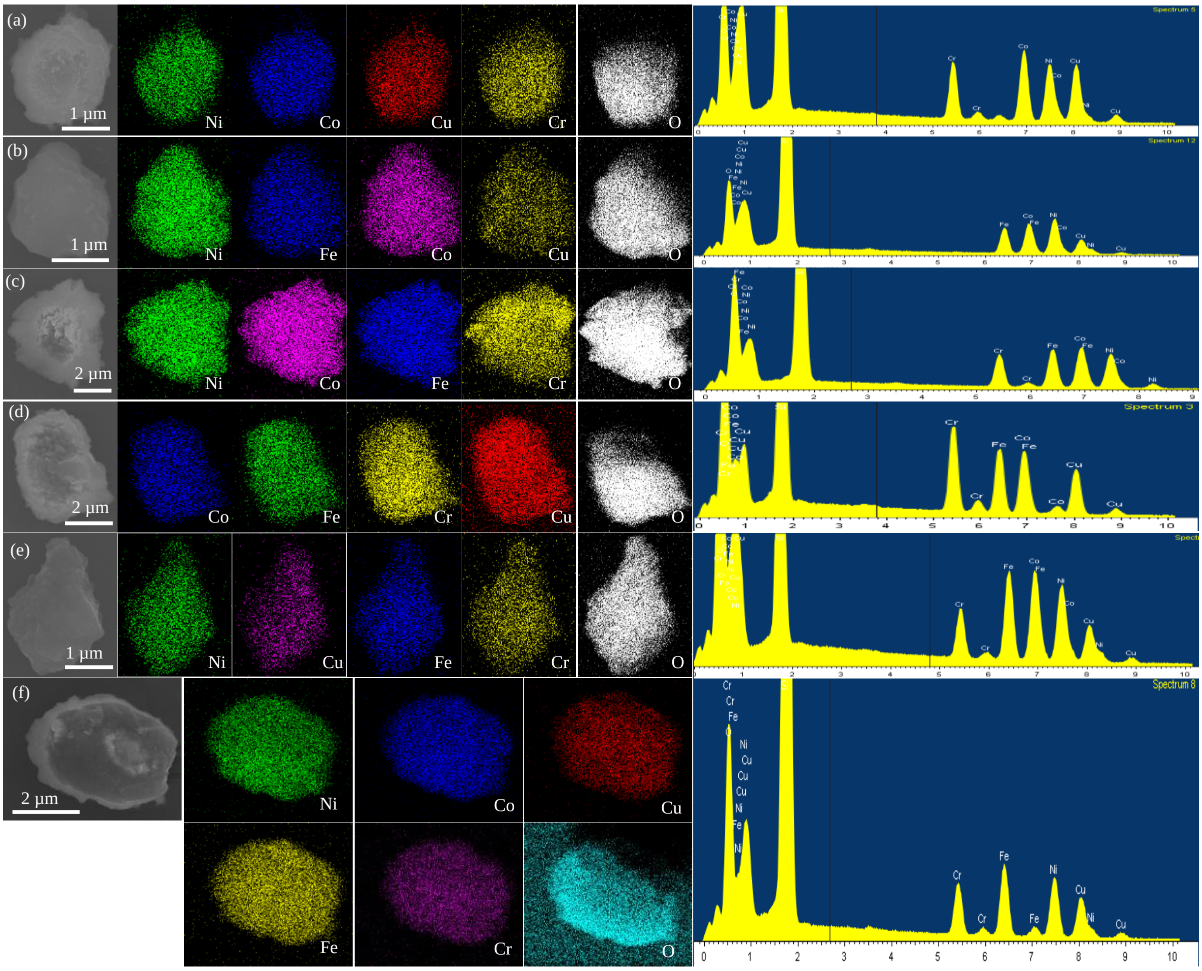

Figure 5.19 FESEM EDS elemental mapping and corresponding EDS spectra for Femtosecond laser synthesized (a) NiCoCuCr oxide, (b) NiCoCuFe oxide, (c) NiCoFeCr oxide, (d) CoCuFeCr oxide, (e) $Ni_{0.5}Cu_{0.5}Fe_2Cr_{0.5}$ oxide, (f) NiCoCuFeCr oxide.

Along the same lines, we synthesized a variety of metal alloys using the same laser parameters. Unlike the previous case, the concentration of the citric acid in the metal alloy precursor is equal to the concentration of the metal salt. Figure 5.20 and Figure 5.22 depict the XRD spectra of a large family of metal alloys. The matching PDF files from the ICCD database along with the synthesized alloys are listed in Table 5.2. The EDX elemental mapping images in Figure 5.21, Figure 5.23, and Figure 5.24 further reveal the homogeneous distribution of constitute elements thus confirming the formation of homogeneous alloys. Evidently, various metal alloys comprising Ni, Co, Cu, Fe, Cr, and individual metals viz. Au, Pt, Ag, and In can be synthesized through FsLDW. To probe further, transmission electron microscope imaging of NiCoCuFeCr high entropy alloy was conducted. TEM image (Figure 5.25b) and FESEM image (Figure 5.25a) reveal high entropy alloy nanoparticles with a particle size of 10 nm – 100nm. The STEM-EDX elemental mapping images (Figure 5.25c) show homogeneous distribution of the constituent metals in nanoparticles as small as ~50 nm. Therefore, we can convincingly conclude that these nanoparticles are indeed the high-entropy alloy nanoparticles i.e., alloys with 4 or more metals with a homogeneous distribution of atoms. Furthermore, the HRTEM image (Figure 5.25d) and the fast Fourier transform analyzed HRTEM image (Figure 5.25e) reveal a d-spacing of 0.210 nm corresponding to (111) plane of NiCoCuFeCr HEA which closely matches the d-spacing from the XRD spectrum i.e., 0.208 nm.

Table 5.2 List of alloys synthesized by the FsLDW process and the corresponding matching JCPDS files from the ICCD database.

Sl. No.	Synthesized alloy	Matching compound (JCPDS No.)	Sl. No.	Synthesized alloy	Matching compound (JCPDS No.)
1	Pt	Cubic Pt (01-070-2057)	13	FeCu	Cubic $Fe_{0.7}Co_{0.3}$ (04-002-1913)
2	Au	Cubic Au (03-065-8601)	14	NiCoCu	Cubic $Co_{0.35}Ni_{0.65}$ (04-002-1075), cubic $Cu_{0.5}Ni_{0.5}$ (04-005-6651)
3	Ag	Cubic Ag (04-002-1171)	15	NiCoCr	Cubic $Cr_{0.404}Co_{0.245}Ni_{0.351}$ (04-002-6636)
4	Cu	Cubic Cu (01-071-4609)	16	CoFeCu	Cubic $Cu_{0.6}Ni_{0.4}$ (04-002-8855), cubic $Cu_{0.5}Co_{0.5}$ (04-020-2827)
5	Ni	Cubic Ni (01-078-7533)	17	NiCoFe	Cubic NiCo (01-085-6754), cubic NiFe (00-047-1417)
6	Co	Cubic Co (01-071-4238)	18	NiCuCr	Cubic $Cu_{0.5}Ni_{0.5}$ (04-001-8686), cubic $Cr_{0.5}Ni_{0.5}$ (04-004-8469)

7	In	Tetragonal In (01-075-3850)	19	NiFeCuCr	Cubic $Cr_{0.1}Fe_{0.65}Ni_{0.25}$ (04-019-2390), cubic $Cu_{0.5}Ni_{0.5}$ (04-006-6385), cubic NiFe (00-047-1417)
8	NiCo	Cubic $Co_{0.35}Ni_{0.65}$ (04-002-1075)	20	NiCoFeCr	Cubic $Cr_{0.25}Fe_{0.25}Co_{0.25}Ni_{0.25}$ (04-022-2301)
9	NiCu	Cubic CuNi (96-152-4233)	21	NiCoCuFe	Cubic $Cu_{0.35}Fe_{0.35}Ni_{0.30}$ (04-019-8584)
10	NiFe	Cubic FeNi (00-047-1417)	22	NiCoCuCr	Cubic $Cr_{0.404}Co_{0.245}Ni_{0.351}$ (04-022-6636), cubic $Cu_{0.5}Ni_{0.5}$ (04-002-1345)
11	FeCo	Cubic $Fe_{0.05}Co_{0.95}$ (04-006-6434), cubic $Fe_{0.5}Co_{0.5}$ (04-004-9066)	23	CoCuFeCr	Cubic $Cr_{0.293}Fe_{0.468}Co_{0.239}$ (04-021-2007)
12	CoCu	Cubic $Cu_{0.5}Co_{0.5}$ (04-020-2827)	24	NiCoCuFeCr	Cubic $Cu_{0.112}Cr_{0.222}Fe_{0.222}Co_{0.222}Ni_{0.222}$ (04-022-2302)

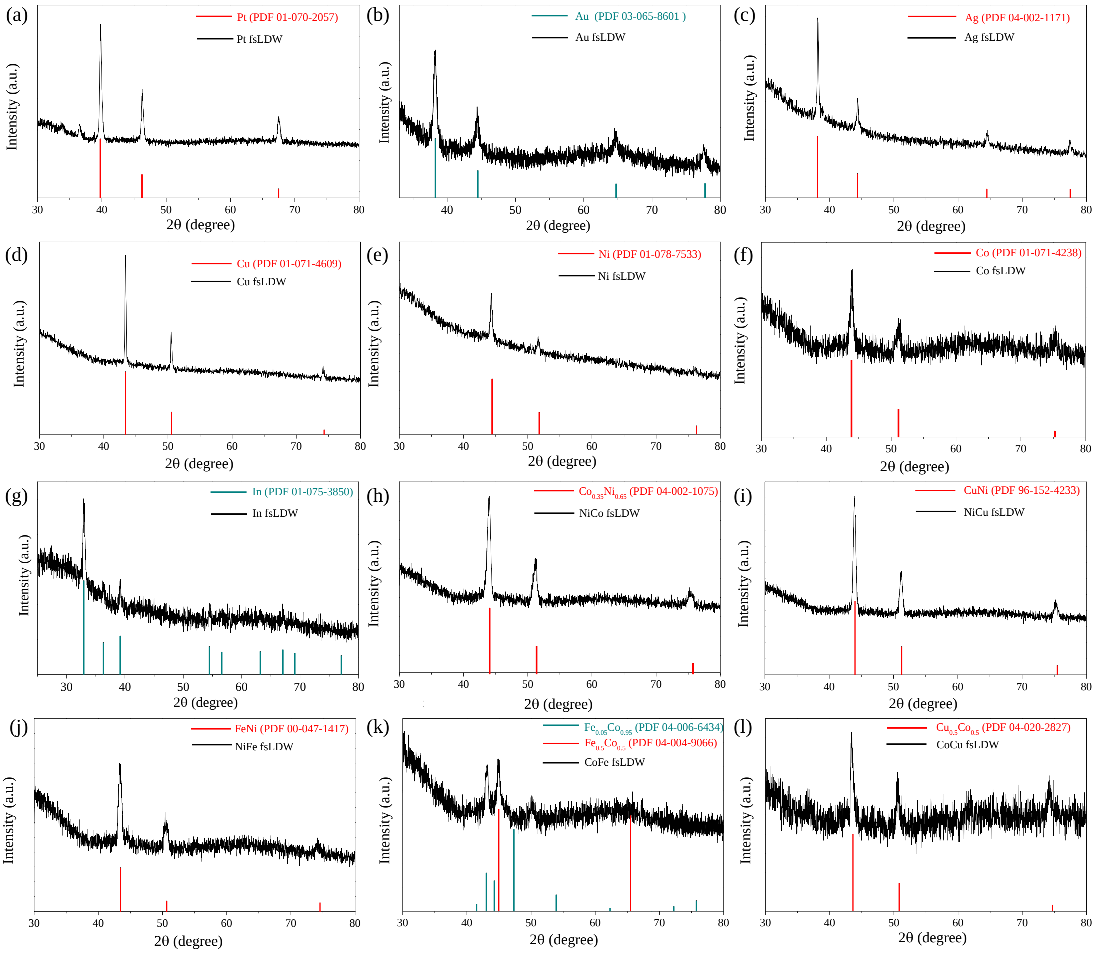

Figure 5.20 XRD spectra of (a) Pt, (b) Au, (c) Ag, (d) Cu, (e) Ni, (f) Co, (g) In, (h) NiCo, (i) NiCu, (j) NiFe, (k) CoFe, (l) CoCu synthesized by femtosecond laser direct writing.

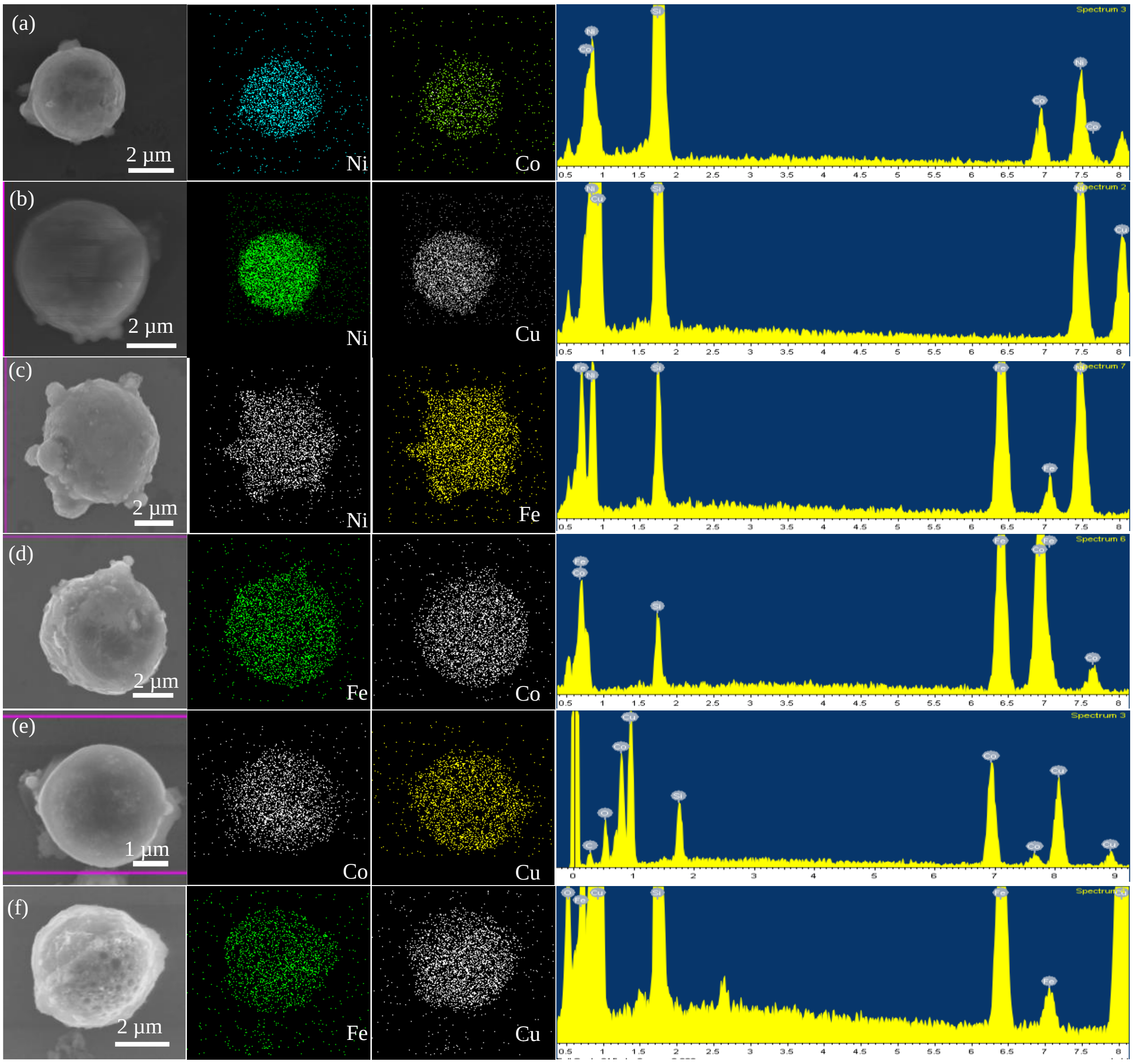

Figure 5.21 FESEM EDS elemental mapping and corresponding EDS spectra for Femtosecond laser synthesized (a) NiCo, (b) NiCu, (c) NiFe, (d) CoFe, (e) CoCu, (f) FeCu alloys.

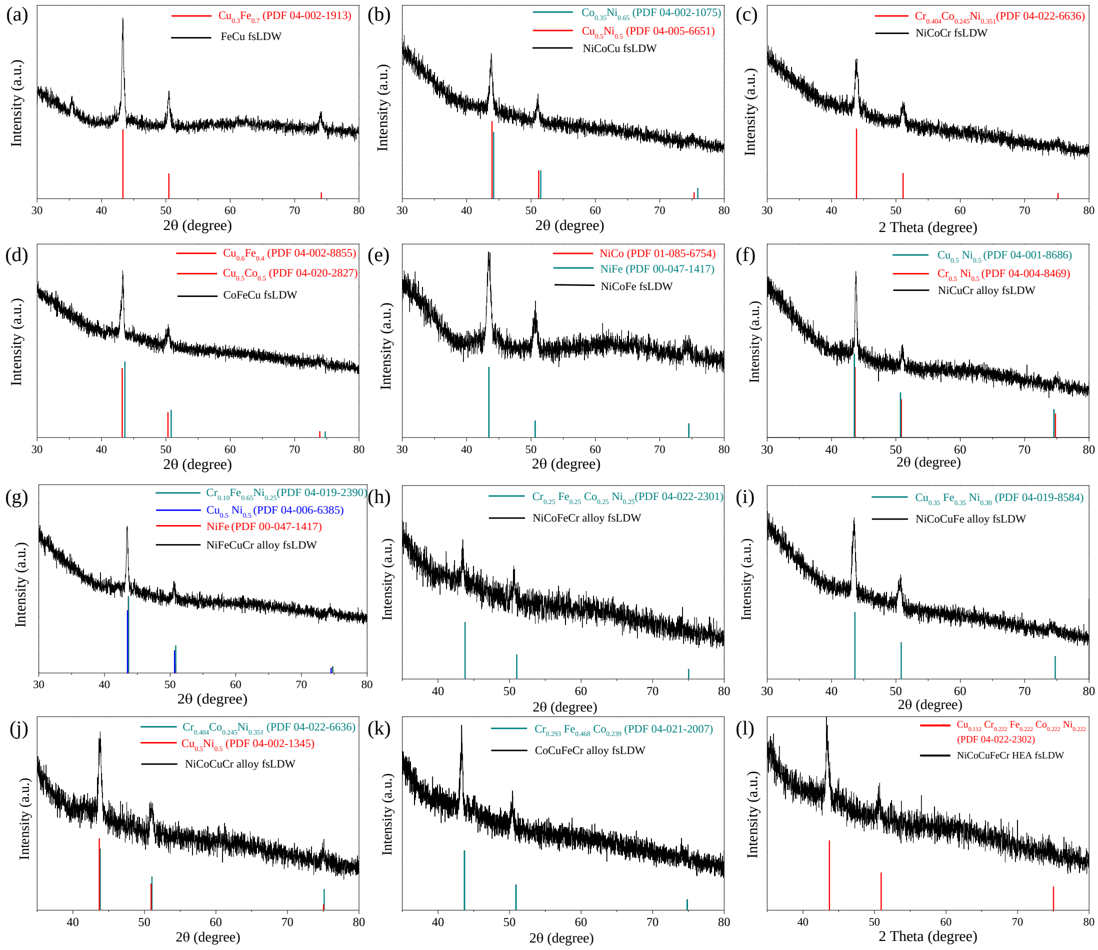

Figure 5.22 XRD spectra of (a) FeCu, (b) NiCoCu, (c) NiCoCr, (d) CoFeCu, (e) NiCoFe, (f) NiCuCr, (g) NiFeCuCr, (h) NiCoFeCr, (i) NiCoCuFe, (j) NiCoCuCr, (k) CoCuFeCr, (l) NiCoCuFeCr alloys synthesized by femtosecond laser direct writing.

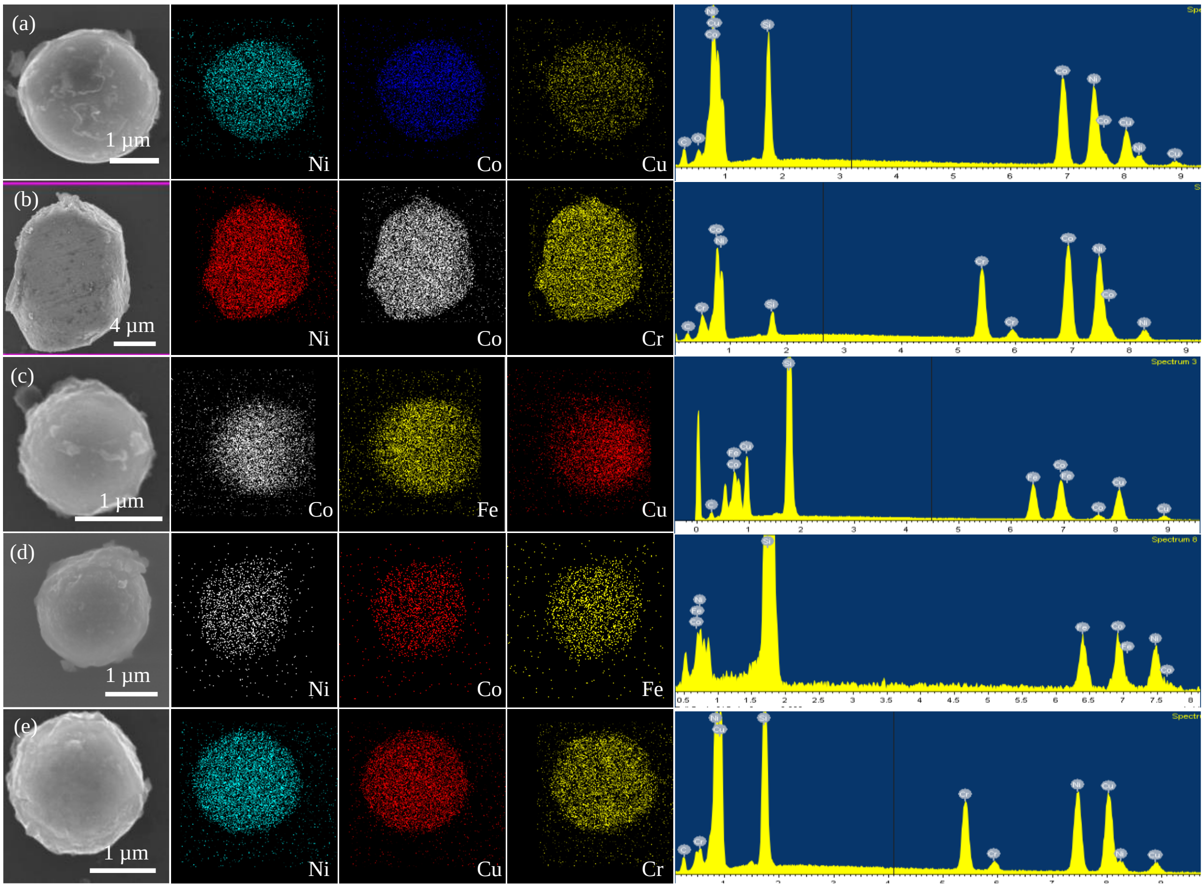

Figure 5.23 FESEM EDS elemental mapping and corresponding EDS spectra for Femtosecond laser synthesized (a) NiCoCu, (b) NiCoCr, (c) CoFeCu, (d) NiCoFe, (e) NiCuCr alloys.

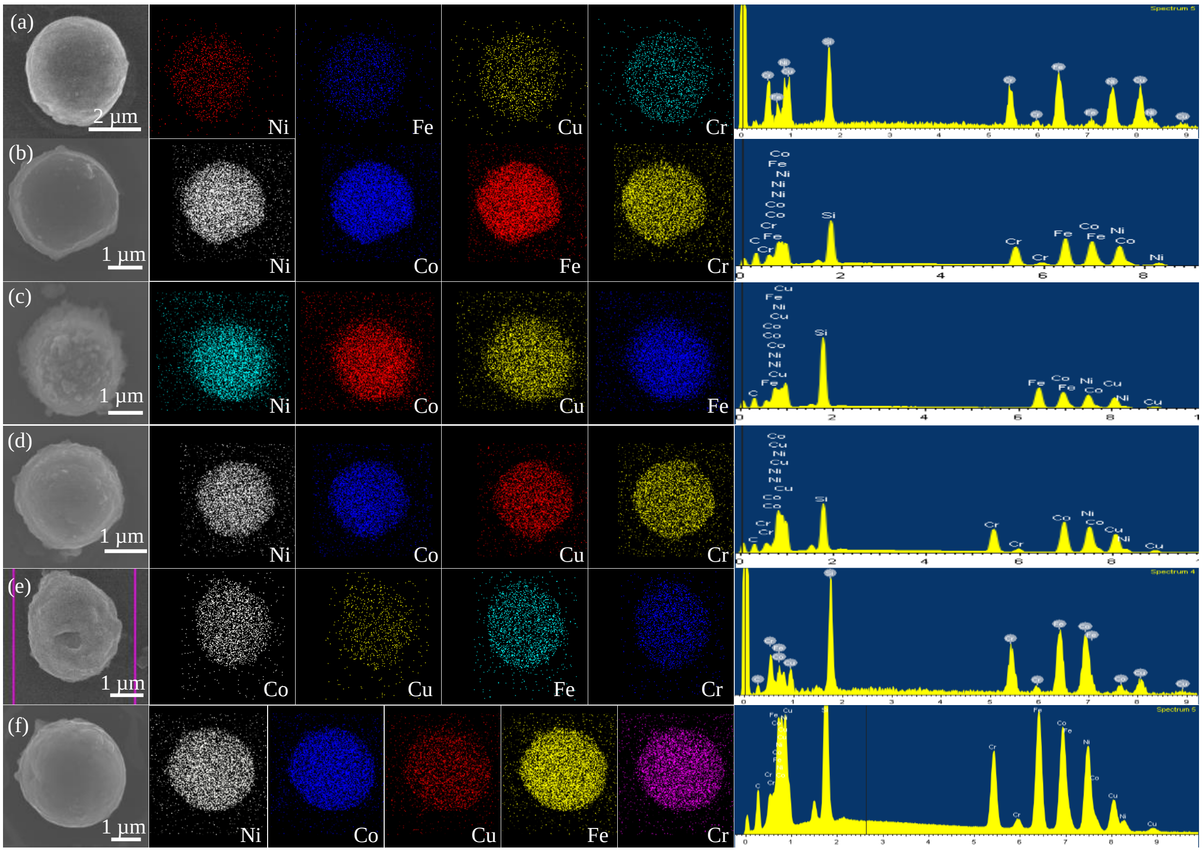

Figure 5.24 FESEM EDS elemental mapping and corresponding EDS spectra for Femtosecond laser synthesized (a) NiFeCuCr, (b) NiCoFeCr, (c) NiCoCuFe, (d) NiCoCuCr, (e) CoCuFeCr (f) NiCoCuFeCr alloys.

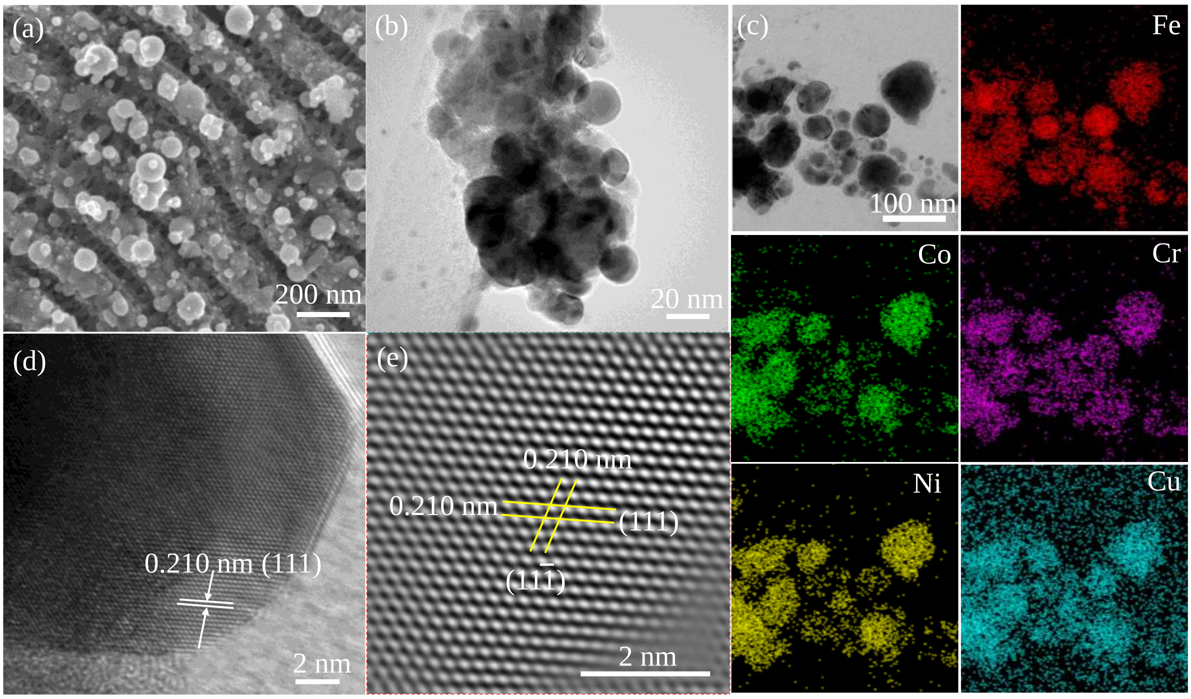

Figure 5.25 (a) FESEM image, (b) TEM image, (c) BF-STEM image and corresponding STEM-EDX elemental mapping images of Ni, Co, Cu, Fe, and Cr, (d) HRTEM image and corresponding (e) fast Fourier transform analyzed image, of femtosecond laser synthesized NiCoCuFeCr high entropy alloy.

ICP-OES tests were conducted to estimate the concentration of each element in the synthesized alloys. ICP-OES results for the 6 alloy systems and their corresponding ink precursors are listed in Table 5.3. The composition of the elements in the synthesized alloys are close to their respective concentrations in the precursor ink. Notably, the concentration of Fe and Cr in the alloys are lesser than the concentration in precursor ink. Nonetheless, the composition of each element is nearly equal and therefore we can reasonably term these alloy systems as high entropy alloys. To probe further into the surface oxidation state of high entropy alloys XPS tests were conducted. Samples were synthesized on a glass surface and used as it is for testing. As revealed in Figure 5.26 the high-resolution XPS spectra of NiCoCuFeCr alloy reveals characteristic peaks of Ni 2p, Cu 2p, Fe 2p, Cr 2p, Co 2p, and O 1s. The minor peaks at 870.5

eV and 852.8 eV show the presence of Ni in Ni (0) oxidation[143] state (Figure 5.26a). Further, the peaks at 856.2 eV and 873.3 eV with satellite peaks at 881.5 eV and 862.2 eV reveal the oxidized Ni^{2+} present in the sample. Similarly, in the case of Co 2p region, minor peaks at 778.9 eV and 791.2 eV correspond to Co[144] (0) state, while the peaks at 781.2 eV and 797.7 eV accompanied by satellite peaks of 802.5 eV and 787.5 eV show the presence of oxidized cobalt (Co^{2+}) in the sample. For Cu 2p XPS spectra, significantly visible peaks at 933.4 eV and 952.3 eV reveal the existence of Cu (0),[145] while the peaks at 935 eV and 954.5 eV accompanied by satellite peaks at 963.1 eV and 944.5 eV show the existence of oxidized copper (Cu^{2+}). Also, in case of Fe 2p spectrum, the presence of Fe (0)[146-147] (minor peaks at 707.5 eV and 717.8eV) and oxidized iron (Fe^{2+}/Fe^{3+}) (peaks at 711.8 eV and 724.5 eV) are revealed. Finally for Cr 2p region, peak at 573.4 eV shows presence of Cr(0)[148] and oxidized[149] Cr^{2+}/Cr^{3+} assigned for peak at 576.8 eV. It should be noted that synthesized samples are susceptible to surface oxidation[150] which probably is the reason for the majority of peaks corresponding to oxidized metal atoms. To probe further we also investigated O 1s spectrum of the synthesized alloy. The O 1s spectrum shows a peak at 532.7 eV, which is the characteristic of adsorbed oxygen (O_{ads})[151] and oxygen from the hydroxyl group (O_{hyd}). The O_{hyd} is probably originating from the residual CMC/citric acid present in the sample which is also revealed from the FTIR study discussed previously. The O 1s spectrum shows no peaks near to 529 eV which is the characteristic of lattice oxygen[152] present in oxides. Thus, it is clear that the synthesized material is a high entropy alloy and the oxidation of metal is limited to surface oxidation. Hence, through in-depth chemical characterizations comprising XRD, FESEM, TEM, XPS, ICP-OES, and EDS tests we have established the successful synthesis of multi-metal oxide and alloy micro-nano particles through femtosecond laser direct writing. In the next section, the activity of one of the synthesized catalysts for OER will be discussed.

Table 5.3 Inductively coupled optical emission spectroscopy results for the precursor ink and the corresponding synthesized alloys.

Alloy	Ni %	Co %	Cu %	Fe %	Cr %
CoCuFeCr ink	NA	25.88	26.05	24.72	23.35
CoCuFeCr alloy	NA	28.78	31.2	19.78	20.32
NiCoFeCr ink	24.98	27.07	NA	24.55	23.4
NiCoFeCr alloy	32.21	30.11	NA	21.08	16.6
NiCoCuCr ink	24.38	26.49	25.47	NA	23.66
NiCoCuCr alloy	27.26	27	24.28	NA	21.46
NiCoCuFe ink	24	25.19	26.10	24.71	NA
NiCoCuFe alloy	23.55	26.76	24.16	25.53	NA
NiCuFeCr ink	24.67	NA	26.83	25.12	23.38
NiCuFeCr alloy	32.71	NA	34.3	16.8	16.19
NiCoCuFeCr ink	19.58	21.34	21.05	19.36	18.67
NiCoCuFeCr alloy	24.22	22.80	23.75	14.69	14.56

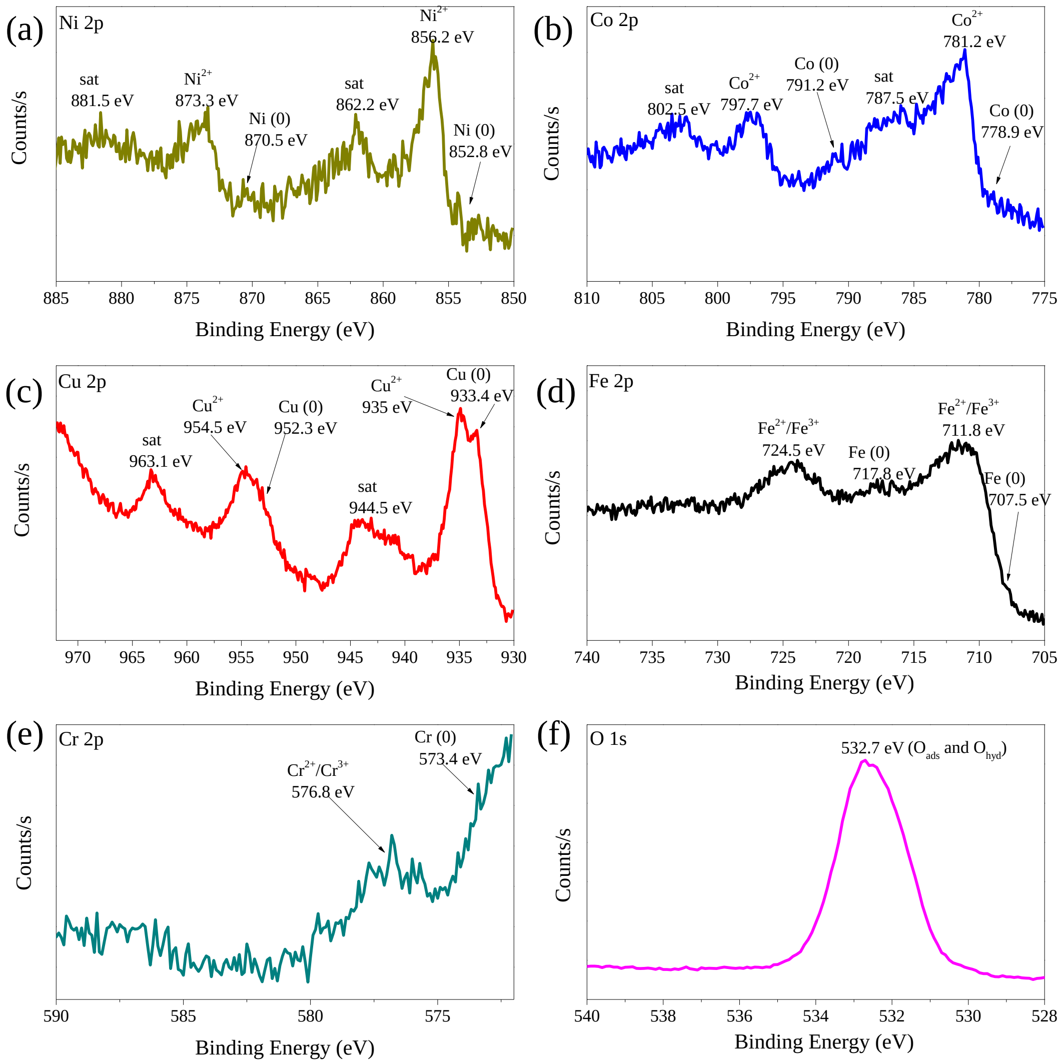

Figure 5.26 High resolution XPS spectra of NiCoCuFeCr HEA in the (a) Ni 2p region, (b) Co 2p region, (c) Cu 2p region, (d) Fe 2p region, (e) Cr 2p region, and (f) O 1s region.

5.3.3 Catalytic performance for water splitting

To investigate the feasible application of the synthesized products in the electrochemical applications, one of the synthesized catalysts was employed as a catalyst for water splitting. The precursor ink was drop cast on the stainless-steel foil and the carbon fiber paper and dried. The FsLDW was carried out as described previously to form an electrode to be directly used for electrocatalysis. The SS@NiCoCuFeCr$_{0.5}$ HEA catalyst was tested for its activity for OER in 1 M KOH solution. As shown in Figure 5.27a the catalyst exhibits a low η_{10} of 213 mV. Further, a low Tafel slope of 56.3 mV dec^{-1}, reveals higher reaction kinetics for water splitting. Since the stainless-steel substrate itself is reasonably active for OER, we also tested the $NiCoCuFeCr_{0.5}$ synthesized on carbon fiber paper substrate. As seen from Figure 5.27a the CFP@$NiCoCuFeCr_{0.5}$ exhibits excellent activity showing a low η_{10} of 232 mV. Furthermore, the catalyst achieves a high current density of 100 mA cm^{-2} for overpotential as low as 357 mV. In contrast, the bare carbon fiber paper reveals high η_{10} of 350 thus clearly showing the excellent activity of the catalyst. Since Ni and Fe based alloys and oxides are known to exhibit high activity for OER, we also tested the activity for CFP@NiFe catalyst to compare the activity of NiFe alloy against $NiCoCuFeCr_{0.5}$ HEA. The activity of CFP@NiFe stands at η_{10} of 265.5 mV and η_{100} of 420 mV. The activity of CFP@NiFe is similar to the previously reported NiFe alloy[86] and NiFe LDHs.[153] Evidently, the activity of CFP@NiFe is lesser compared to CFP@$NiCoCuFeCr_{0.5}$ as observed from LSV curves and Tafel plots from Figure 5.27(a-b). Hence, we can infer that the high entropy alloying of Ni, Co, Cu, Fe, and Cr produces a catalyst with a very high OER activity. We also compared the specific activity of $NiAg_{0.4}$ 3DPNC and $NiCu_{0.05}Fe_{0.025}$ PNW catalysts against the SS@$NiAg_{0.4}$ and SS@$NiCu_{0.05}Fe_{0.025}$ synthesized by femtosecond laser. As seen from Figure 5.27(c-d) the femtosecond laser synthesized catalysts show similar activity as of the conventionally synthesized catalysts. It's worth noting that that conventional synthesized catalyst was tested on a glassy carbon electrode whereas the laser synthesized catalyst was tested on stainless steel foil which might explain the slight difference in the activity. Nonetheless, it is safe to conclude that the femtosecond laser fabricated electrodes can easily replace the electrodes fabricated through conventional methods. In addition, the activity of the catalyst in itself does not attract the commercial application. The long-term durability of the catalyst is an important aspect to consider. We investigated the durability and stability of the CFP@$NiCoCuFeCr_{0.5}$ by conducting chronopotentiometry test for 50 hours. As seen from Figure 5.27e the catalyst exhibited excellent stability with no visible increase in the overpotential when operated for 50 hours. The overpotential at the end of 50 hours was 222 mV which is even less than the 232 mV measured by the linear sweep voltammetry method. In conclusion, the binder-free and single-step fabricated electrodes from FsLDW exhibit excellent electrocatalytic activity as well as durability. To further check the robustness of the synthesized catalyst on SS foil, the SS coated with $NiCoCuFeCr_{0.5}$ was ultrasonicated in DI water for 1 hour. Figure 5.28 shows the pictures before and after the ultrasonication. Very clearly, the ultrasonication has no significant effect on the coated the SS foil since the $NiCoCuFeCr_{0.5}$ coating remains strongly bonded to the SS foil. Thus, the process of FsLDW works akin to laser cladding in which the metal powder is welded to the substrate.

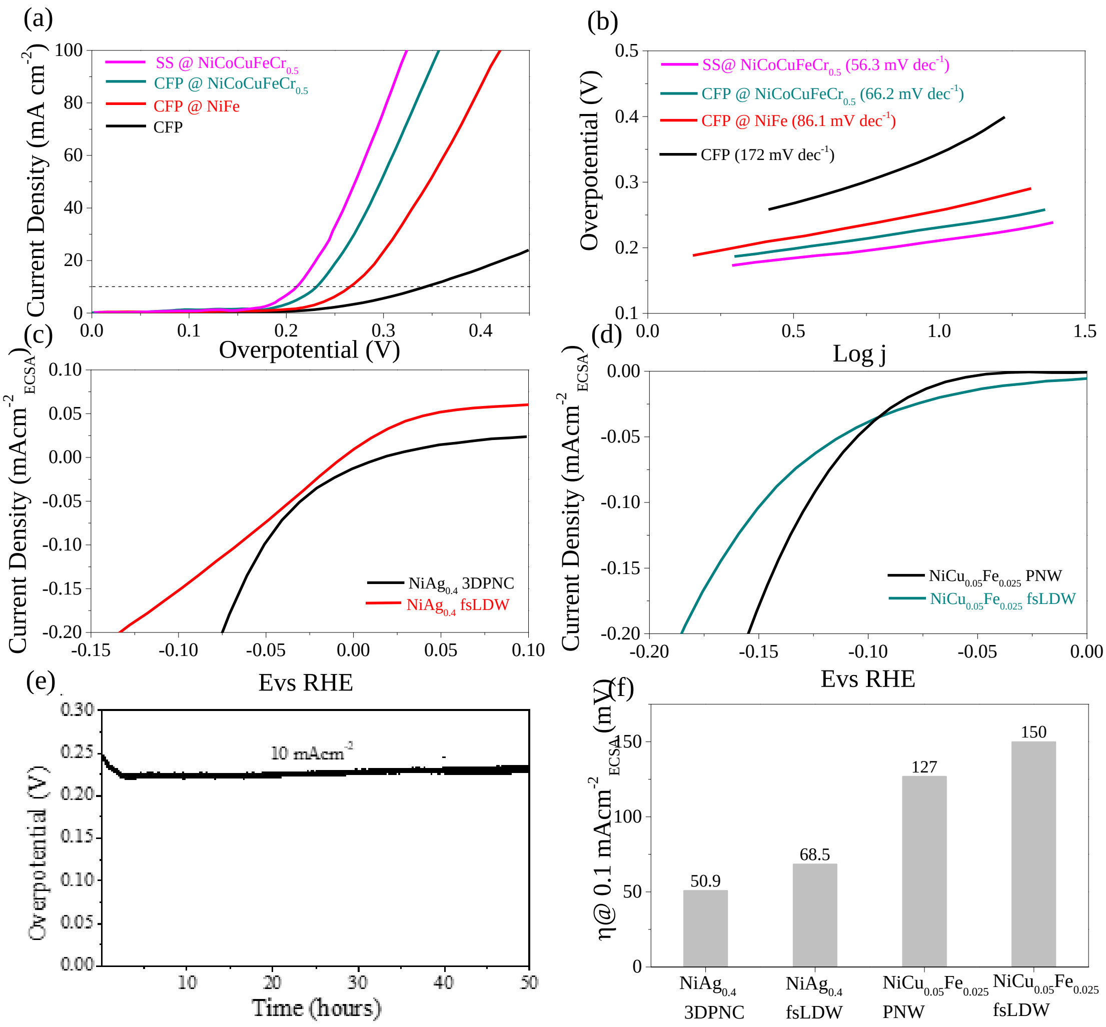

Figure 5.27 (a) Comparison of OER activity of $NiCoCuFeCr_{0.5}$ HEA alloy with NiFe alloy and pristine carbon fiber paper, and (b) corresponding Tafel slopes, and comparison of specific activity for hydrogen evolution of (c) femtosecond laser synthesized $NiAg_{0.4}$ vs. $NiAg_{0.4}$ 3DPNC synthesized by hydrothermal process, (d) femtosecond laser synthesized $NiCu_{0.05}Fe_{0.025}$ vs. $NiCu_{0.05}Fe_{0.025}$ PNW synthesized by hydrothermal process, (e) chronopotentiometry testing to investigate the stability of CFP@ $NiCoCuFeCr_{0.5}$ HEA at a constant current density of 10 mA cm^{-2}, (f) comparison of the specific activity of the catalysts synthesized by conventional processes against the femtosecond laser process at 0.1 mA $cm^{-2}{}_{(ECSA)}$.

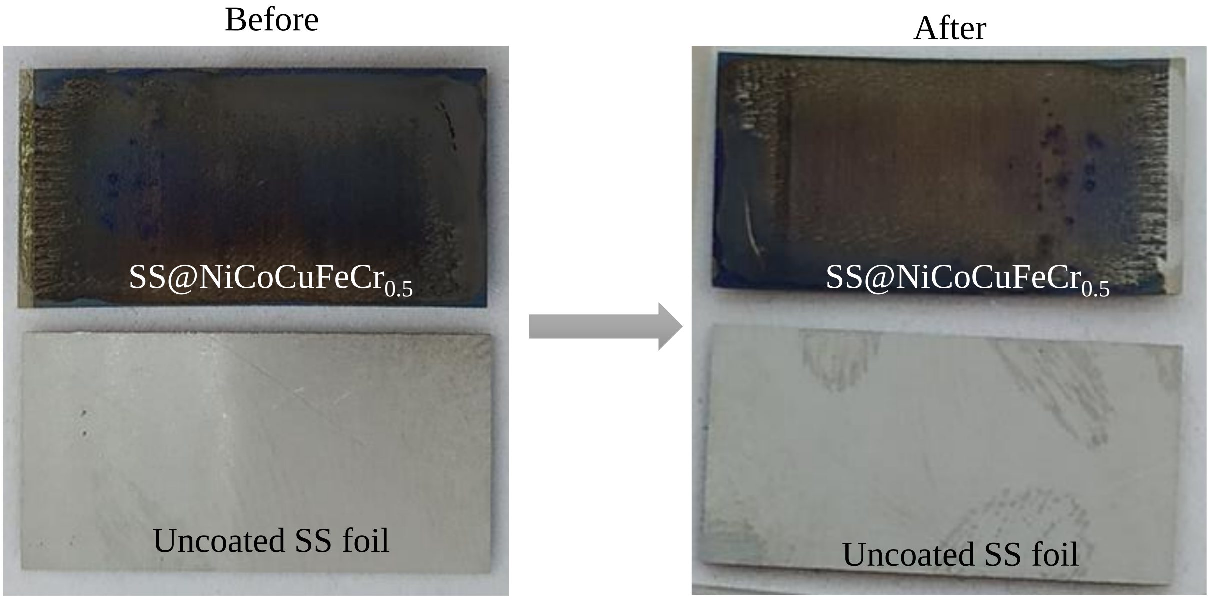

Figure 5.28 Pictures of SS@NiCoCuFeCr$_{0.5}$ before and after 1-hour ultrasonication in DI water. Uncoated SS foil is shown for reference to compare the coated SS foil with the bare SS foil.

5.3.4 FsLDW for Microfabrication of metal structures

Till now we have discussed the application of laser synthesized metal oxides and alloys for electrocatalysis. However, the applications can go beyond electrocatalysis and the same method can be used to create micro-patterns of oxides and alloys for interesting applications like sensing, energy storage, etc. Thus, to demonstrate the extent of micro-fabrication which is achievable by this process we printed concentric squares and circles using a femtosecond laser. As seen from Figure 5.29(a-b) the laser forms crisp patterns with excellent dimensional accuracy. The unsintered parts were removed by rinsing in water and ultrasonication for 20 seconds. Evidently, the sintered parts remain bonded to the substrate when the unsintered ink is removed. Furthermore, we also designed the logo of NTU Singapore using the process. The EDX elemental mapping (Figure 5.29d) shows the deposition of Cu in the NTU Singapore logo with an excellent representation of details. Also, to take a step further we fabricated concentric circles of three different metals i.e., Ni, Cu, and Ag in three consecutive steps. Firstly, Ag was deposited using Ag ink and the un-sintered part was removed by rinsing in water. Secondly, the Cu ink was drop cast on the previously patterned Ag, and the Cu patterning was done using a laser. The same steps were repeated for Ni. The Optical microscope image (Figure 5.29e) shows distinct circles of Ni, Cu, and Ag which is further revealed from the FESEM-EDS line scan image in Figure 5.29f. Based on these successful fabrications, we foresee the application of FsLDW for creating microstructures of oxides and alloys of a variety of metals.

Dimensional accuracy is critical to micro-fabrication. Hence, we investigated the effect of laser writing speed and the laser power on the dimensional accuracy of the laser fabricated lines. Lines with a dimension of 50 μm were fabricated using the femtosecond laser. The optical microscope images of the FsLDW patterns are shown in Figure 5.30(b-e). From the images, we can see that for laser speeds larger than 80 mm s^{-1} the energy is not sufficient for accurate patterning, while the laser writing speeds lower than 50 mm s^{-1} result in thicker patterns. At lower speeds the laser fluence is higher, leading to sintering of larger surface area. To quantitatively assess the laser patterned lines we introduce a new quantity “thickness ratio”, which is defined as

Thickness ratio = Patterned thickness/ designed thickness. (5.5)

When the thickness ratio is near to 1 the patterned shapes have the highest dimensional accuracy. The plot of the thickness ratio for various writing speeds and laser power is shown in Figure 5.30a. The central region hosts laser parameters for which the thickness ratio is near to 1. Upon assessing the plot, we suggest the use of laser writing speed of 50-60 mm/s and laser power of 500 mW – 600mW for accurate micro-fabrication.

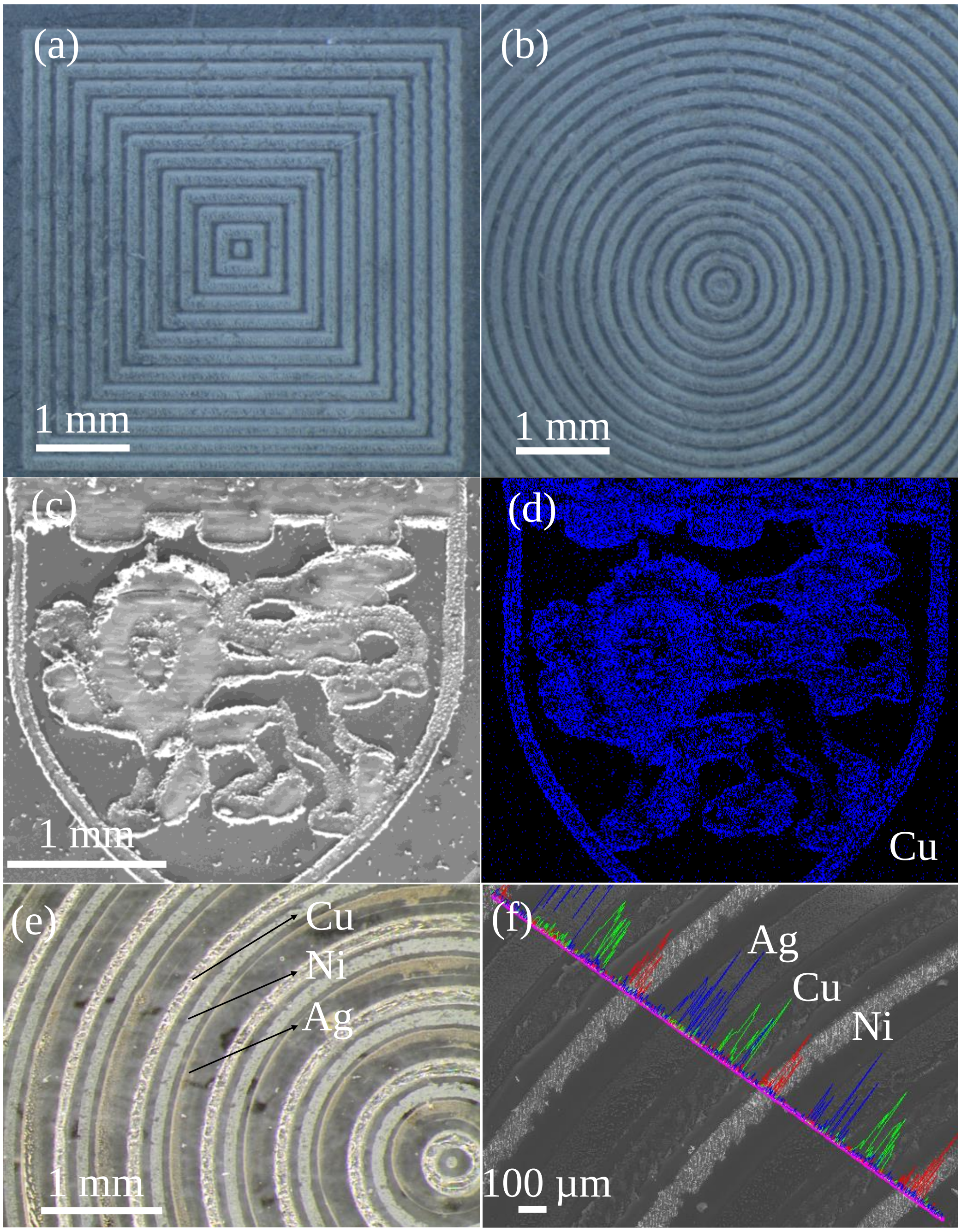

Figure 5.29 (a) Concentric squares, (b) concentric circles of NiO fabricated by femtosecond laser direct writing, (c) micropatterning of the logo of Nanyang Technological university by femtosecond laser and corresponding (d) EDS elemental mapping image, (e) Concentric circles of Ni, Cu and Ag patterned by femtosecond laser direct writing in 3 consecutive steps and the corresponding (f) EDS line scan spectra.

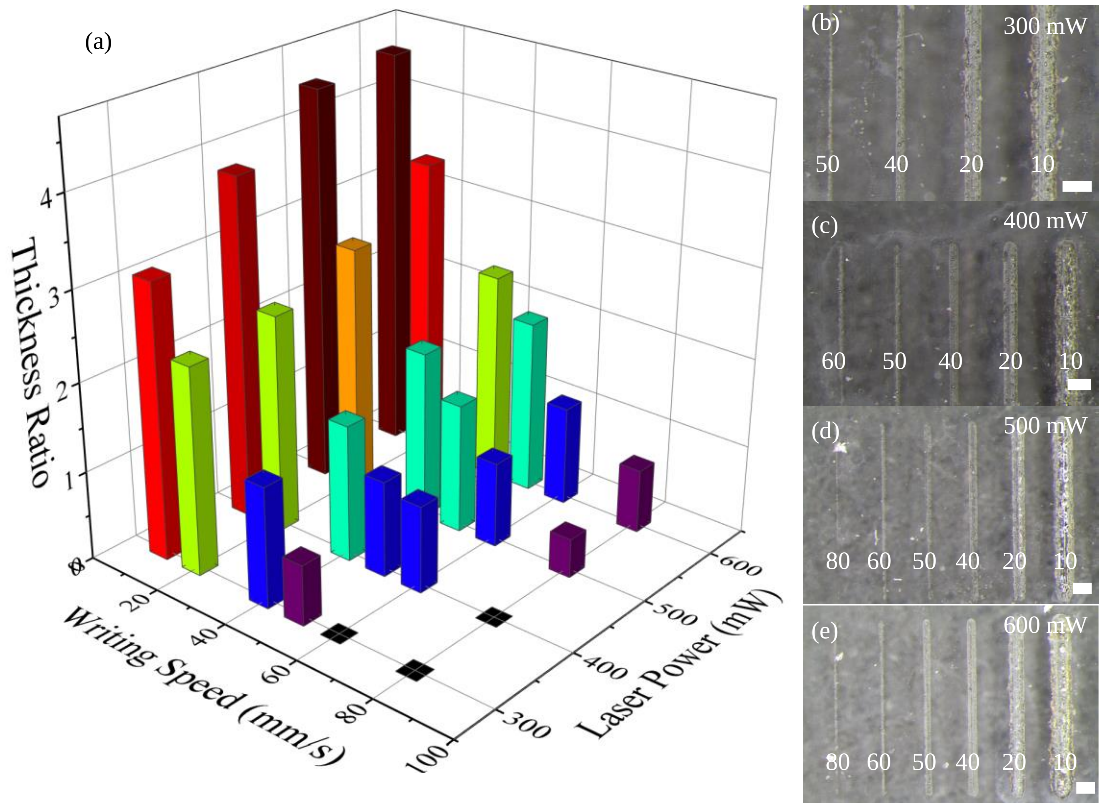

Figure 5.30 (a) Thickness ratio (printed thickness / designed thickness) of the femtosecond laser writing patterns for different writing speed and the laser power, and (b-e) corresponding optical microscope images of the fabricated patterns for varying laser power. (Scale – 50 µm)

5.3.5 Limitations of this process

We have demonstrated successful synthesis and deposition of a large group of metal oxides and alloys in this work. Nonetheless, the process comes with certain limitations. The substrate that needs to be coated should be inert to the precursor ink. For instance: Ag precursor ink cannot be used for coating on more reactive metal surfaces such as Cu and Ni as the metal can react with $AgNO_3$ present in the ink. Furthermore, the equipment currently used supports the highest laser power of 600 mW, which limits the laser writing speed resulting in a longer fabrication time. If the laser power is raised, then the fabrication times can be reduced by manyfold which is essential to realize laser patterning of large-area structures. Unfortunately, high-power femtosecond laser systems are very expensive currently. But we expect a drastic reduction in the price of lasers similar to CO_2 and other continuous-wave lasers. Also, our attempts to synthesize alloys based on Al, Zn, and other metals have not been successful and further studies are required in achieving the same. So far, the nitrates have worked the best for ink formulation, but further research into any other form of metal salts which might work better for the process is needed. Despite all the limitations we strongly believe that this thesis has been instrumental in introducing a new method of electrode fabrication coated with multi-metal oxides and alloys. Building upon this work we expect further research developments to synthesize many other oxide and alloy systems.

5.4 Conclusions

Herein, we demonstrate a novel method to in-situ synthesize as well as coat high entropy alloy and multi-metal oxide nano-microparticles using a one-step femtosecond laser direct writing process. FsLDW process is helpful to fabricate binder-free electrodes at room temperature and in an open atmosphere. Investigations on the ink formulation and laser parameters were carried out to identify the optimized parameters for successful laser direct writing. In detail material characterizations comprising XRD, FESEM, TEM studies confirm the formation of high entropy alloys and multi-metal oxides. One of the synthesized high entropy alloy catalysts, i.e. CFP@$NiCoCuFeCr_{0.5}$ showed excellent activity and stability towards OER. Towards the end of this chapter, we also illustrated the micro-fabrication achieved by FsLDW. In conclusion, the FsLDW process developed here shows promising results for the fabrication of electrodes for electrochemical applications. In the next chapter, we will address some of the limitations of this process by introducing a new hybrid additive manufacturing process, which simplifies the multi-material additive manufacturing of metal oxides and alloys.

Chapter 6 Development of Hybrid Additive Manufacturing Process to Synthesize Thin Films: Aerosol Jet Printing + Femtosecond Laser Direct Writing

In this chapter, we describe the development of a novel hybrid additive manufacturing process that combines aerosol jet printing and femtosecond laser direct writing. Using the same ink formulation which was used for the femtosecond laser direct writing, required patterns are printed using aerosol jet printing. The effects of various printing parameters on the quality of the print are investigated. The printed ink is irradiated with a femtosecond laser to transform the ink into metal oxide or alloy thin films. The advantages of this process over conventional device fabrication are briefly described and also the multitudes of feasible applications using this process are discussed.

6.1 Introduction

In the previous chapter, we discussed the development of a novel process to simultaneously synthesize and coat the substrates with high entropy alloys and multi-metal oxides. The process is versatile and can be easily applied for the fabrication of electrodes for electrocatalysis, energy storage, and sensing applications. However, in the previous process, the control over the shape and thickness of the thin film ink is relatively difficult. Also, in the case of micropatterns, the un-sintered parts need to be removed by rinsing in deionized water. This necessitates the subsequent drying of the fabricated patterns in the oven. Also, for the fabrication of multiple materials, the process has to be carried out in a step-by-step manner. But the material synthesized needs to be inert to the ink used in the subsequent step. For instance, Ag ink cannot be dried over more reactive metal patterns such as Ni, Cu, Fe, etc., because the printed pattern will dissolve in the ink. Thus, the FsLDW process lacks the freedom of the sequence of fabrication when printing multi-materials. Because of this, for the patterns that involve complex patterns and multiple materials, the FsLDW process is only limited to a few materials.

Alternatively, if the dried film of ink with the desired shape and thickness is fabricated, the laser can be subsequently used to transform the ink into alloys and oxides. Conventional printing methods such as inkjet printing and freeform extrusion are one of the few ways to print an aqueous-based ink. Since the ink used in this process is extremely low viscous akin to water, the freeform fabrication does not appeal. Inkjet printing is probably feasible, however, the immediate drying of the ink upon printing needs a heated plate which is often not available in most commercial printers. As a matter of choice aerosol jet printing is an attractive proposition to print inks of viscosity between 1 cP (centipoise) to 1000 cP. Further, aerosol jet printers allow for customization of the ink owing to simplified parts of the printer, viz. the tubing system for ink transport, the vial for ink storage, and the replaceable nozzle head and nozzle tips. Thus, printing custom-made ink in an aerosol jet printer is far easier than other commercial printers. Furthermore, the aerosol jet printer allows for the customization of nozzle diameters from 100 µm to 500 µm and allows for high printing speeds up to 100 mm/s allowing for rapid fabrication. The printer also supports the heating of the substrate up to 120℃ which is sufficient to evaporate most of the solvents within the ink. The aerosol jet printing works on the principle of formation of aerosols by ultrasonication of the ink to form nano-microdroplets of ink, which are carried by an inert gas such as nitrogen or argon to the nozzle. At the nozzle, another stream of inert gas (sheath gas) envelops the gas carrying aerosols to streamline the aerosols into a narrow stream. Consequently, at the nozzle, the aerosols are jetted at high velocities in a narrow stream. The solvent in the ink is usually volatile which evaporates on contact with the substrate which is often assisted by heating of the substrate. With proper control of sheath gas flow, ultrasonication energy, and the carrier gas flow, the desired linewidth of the printed patterns can be achieved.

The majority of the previous reports of aerosol jet printing[133, 154-156] has focused on printing commercially available inks which consist of metal and metal oxide nanoparticles dispersed in a solvent with suitable surfactants and binder. The solvent evaporates upon printing and the binder is often removed by thermal annealing after the printing. Silver nanoparticles are often printed using this method and later heat cured in an oven at 200℃ for 2 hours to facilitate sintering of Ag nanoparticles and binder removal. The challenge with the approach is the requirement of nanoparticles with uniform size distribution. Besides, the dispersion of metal and metal oxide nanoparticles is a challenge and often involves hazardous solvents and surfactants. The shelf life of these inks is limited as sediments are often observed in the ink when stored for a long time. Moreover, the ink is extremely expensive owing to the presence of nanoparticles. Figure 6.1 gives a fair idea of the increase in the cost of the nanoparticles compared to the bulk material. Furthermore, the environmental impacts[157] of nanomaterial synthesis and health concerns[158] of handling nanomaterials is a serious concern.

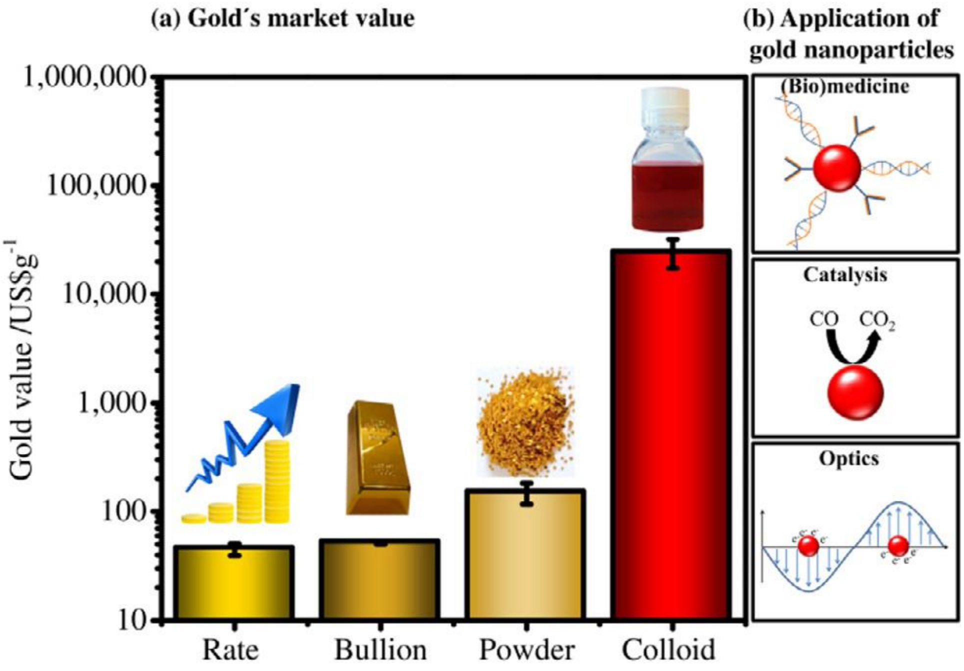

Figure 6.1 Price of different forms of gold (note that Y-axis is logarithmic).[159]

Herein, we suggest an alternate approach to thin-film fabrication in which instead of using nanoparticle-based inks, we use the solution-based ink for printing. The metal salt solution-based ink is aerosol jet printed to form a dried thin film. By appropriate adjustment of printing parameters, the desired thickness of the film can be achieved. Further, any complex 2D shape can be printed by this process. The printed pattern is instantly dried due to the heated substrate and is ready for further processing. The printed pattern is irradiated with femtosecond laser where the printed ink is transformed into metal alloy or metal oxide thin films based on the ink formulation. In the following section, we will discuss the detailed experimental setup and the procedure to synthesize these thin films.

6.2 Materials and methods

6.2.1 Ink formulation for the aerosol jet printing

The ink formulation for the aerosol jet printing is the same as the one used for the FsLDW process discussed in the previous chapter. Therefore, only a brief description is given as follows: the metal salt (typically nitrates or acetates) solution was dissolved in DI water to form a 0.5 M solution. In the next step citric acid (5% molar concentration) and carboxymethyl cellulose were mixed to form a homogeneous ink. The concentration of CMC in the final ink is 0.4 mg/ml. For the synthesis of metal alloy thin films, the citric acid concentration was kept at an equal molar concentration as the metal salt.

6.2.2 Aerosol jet printing (AJP) process

The prepared ink was loaded into the glass vial of the aerosol jet printer and ultrasonicated to generate aerosols. The carrier gas and the sheath gas pressure were adjusted to allow for uniform jetting of the aerosols to facilitate uniform printing. Nitrogen was used as the sheath gas and the carrier gas in this setup. The printer platform was heated to 80℃ to assist the rapid drying of the printed ink. A constant pitch of 50 µm and nozzle with a diameter of 300 µm was used for printing all the samples. The samples were printed at a fixed speed of 3 mm/s for all the samples.

6.2.3 Femtosecond laser direct writing

The as printed patterns were laser irradiated with a high-power femtosecond laser. Yb-doped fiber laser (Amplitude Systèmes, Satsuma HP) was the pulsed laser source, and a set of angle scanning Galvano mirror was used to support fast laser beam writing. UV laser with a wavelength of 350 nm, a repetition rate of 500 kHz with a pulse duration of 220 fs were used. The average laser power used for the process was usually between 400 mW to 500 mW at the writing speed of 50 mm/s. The pitch for the laser writing was kept at 10 µm for all the samples.

6.2.4 Material characterization

The Olympus SZX7 optical microscope was used to capture the image of the printed samples. The phase of the synthesized materials was tested by Bruker D8 advance X-ray diffraction testing equipment with Cu Ka radiation operated at 40 kV and 40 mA. The morphology of the samples was investigated by JEOL-7600F field emission scanning electron microscope. The energy-dispersive X-ray spectroscopy was conducted using INCA – Xact fitted with the JEOL-7600F to investigate the elemental distribution within the sample.

6.3 Results and Discussion

6.3.1 Aerosol jet printing of precursor ink

Herein, we have developed a novel hybrid additive manufacturing process to fabricate a large family of metal alloy and oxide thin films using a combination of aerosol jet printing and laser direct writing. The schematic of hybrid additive manufacturing process is as shown in Figure 6.2. The ink containing metal salt solution mixed with CMC binder and citric acid was printed using an aerosol jet printer. The printed pattern was instantly dried as the solvent (DI water) evaporated on coming in contact with the heated plate. In the next step, the printed pattern was laser processed using a femtosecond laser to transform the printed ink to metal alloys or metal oxides. In the previous chapter, we discussed about the femtosecond laser direct writing process in which the ink was drop cast on a substrate and dried using a hotplate. Herein, however, the aerosol jet printing replaces the drop-casting and drying process. As a result, the deposition of the ink over the selected area of any shape can be achieved with ease. Furthermore, the thickness of the printed ink is uniform unlike the thin films achieved through the drop cast method. The printing parameters of the aerosol jet printing can be highly customized to precisely control the dimensions of the final print. In the aerosol jet printer aerosols formed by ultrasonication is transported by a carrier gas and jetted at high velocity by the sheath gas.

Consequently, the following three parameters determine the quantity of aerosol flowing through the nozzle: (a) the ultrasonication energy, (b) carrier gas pressure, (c) sheath gas pressure. With an increase in ultrasonication energy higher quantity of aerosols are produced, thus increasing the material jetting. Carrier gas also increases the transport of aerosols per second thus delivering a higher quantity of aerosols at the nozzle. However, with an increase in carrier gas pressure, the thickness of the aerosol jet coming out of the nozzle increases leading to a larger width of the printed lines. The sheath gas on the other hand reduces the quantity of aerosol coming out of the nozzle. Furthermore, since the sheath gas envelops the aerosols, the higher pressure of the sheath gas helps is streamlining the aerosol jet leading to a thinner aerosol jet. As a result, when higher sheath gas pressure is used the printed lines are thinner.

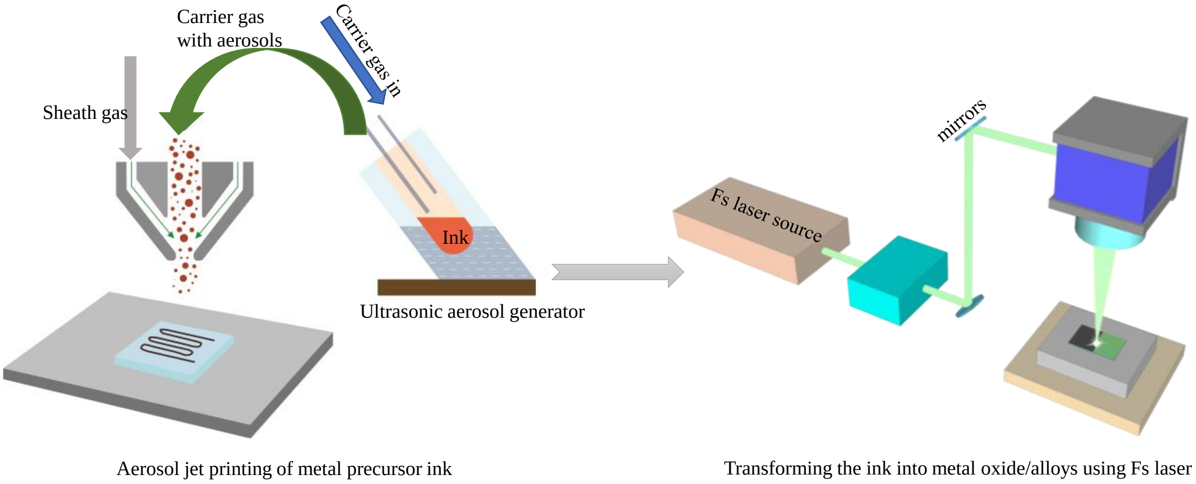

Figure 6.2 Schematic of the hybrid additive manufacturing process.

Owing to the above conditions of aerosol jet printing, it was essential to investigate the variation of printing width for different sheath gas pressure and carrier gas pressure. In all our experiments we have used a constant ultrasonic current of 0.5 A and aerosol jet printing was carried using a 300 µm diameter nozzle. From the preliminary experiments, we found that a minimum carrier gas flow of 25 sccm (standard cubic centimeters per minute) was needed for the reasonable jetting of the aerosols. Thus, we fixed the carrier gas flow at 25 sccm and varied the sheath gas flow from 15 sccm to 50 sccm to investigate the width of the printed lines. The width of the printed pattern was measured from the images captured using an optical microscope. The width of the printed reduced when the flow of the sheath gas is increased as observed from the plot (Figure 6.3 a) and as well as the optical microscope images (Figure 6.3 (j-p)). The sheath gas enveloping the aerosols reduces the aerosol outflow and also streamlines the aerosols into a narrow jet at higher pressure. It is worth to note that the printed lines fall within 200 µm to 140 µm width, which is lesser than the diameter of the nozzle. Figure 6.3b shows the variation of printed width for various carrier gas flow rates. The printed width increased from ~150 µm at 20 sccm to ~300 µm at 50 sccm flow rates of the carrier gas. As discussed previously the increased carrier gas flow results in the transport of larger amounts of aerosols thus leading to higher deposition rates. As the flow is increased beyond 35 sccm the printed pattern reveals zones of different thickness of the printed pattern. This is caused due to a high volume of aerosol deposition which results in delayed drying of the printed ink. Consequently, the printed ink remains in the liquid state for a few extra seconds, and due to delay in the drying process, the ink accumulation in a certain zone is larger than the others. Figure 6.3i distinctly reveals the larger patches of dried ink on certain regions. Therefore, the recommended printing parameters for the creation of a uniform thin film is (a) sheath gas pressure between 20 to 50 sccm and (b) carrier gas pressure between 25 to 35 sccm.

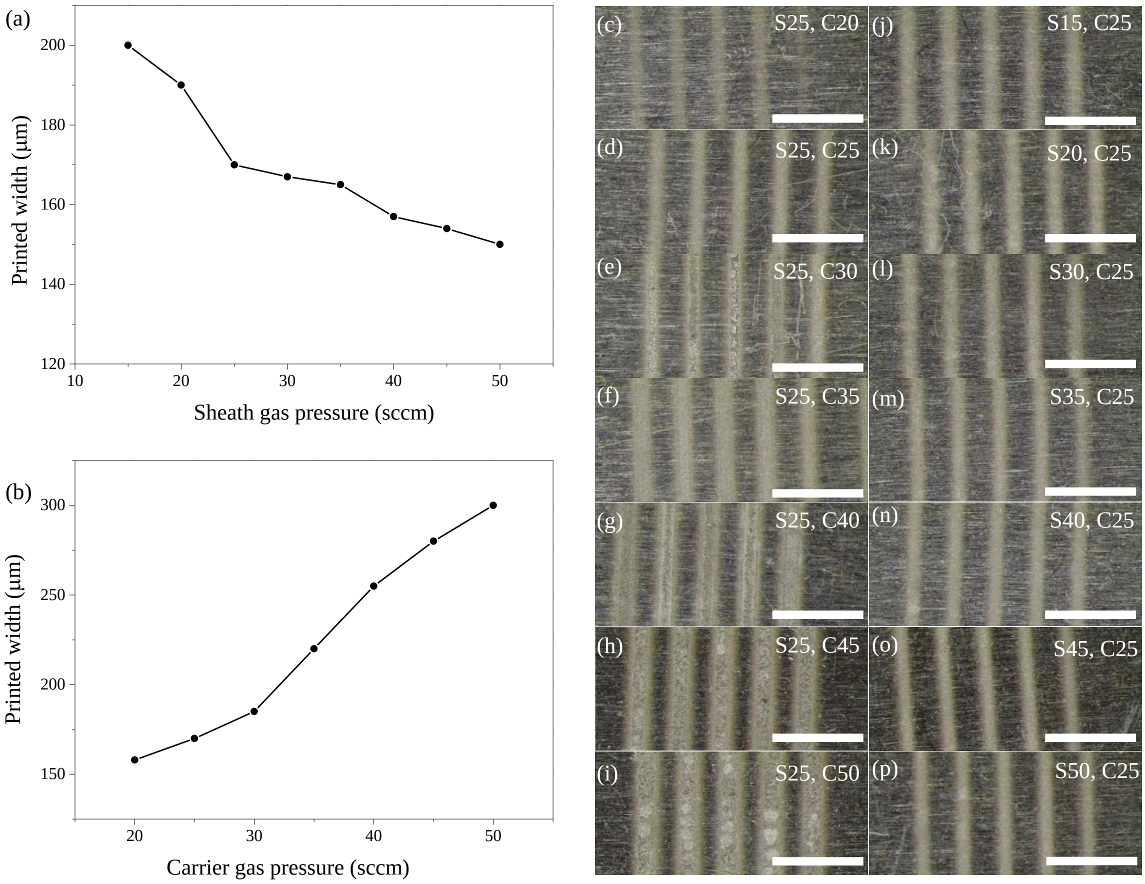

Figure 6.3 Variation of the thickness of the aerosol jet printed lines (a) for different sheath gas flow rates, (b) for different carrier gas flow rates, and corresponding (c) optical images of the printed lines for various sheath gas and carrier gas flow rates. (In the optical images, symbols S – sheath gas, C – carrier gas, the number following S and C correspond to gas flow rates in sccm) (scale 1 mm).

6.3.2 Femtosecond laser direct writing

The printed patterns were processed by femtosecond laser to transform the ink precursor to metal oxides or alloys. In principle, the aerosol jet printed ink is the same as the dried ink from the normal drop cast method, thus should result in the same product. However, as a proof of concept, we performed femtosecond laser direct writing for a few samples. To investigate the phase of the final product formed, the X-ray diffraction tests were carried out. Figure 6.4a shows the Ag XRD spectrum for the Ag thin film prepared by this method. The peaks match with the peaks of cubic silver (PDF 04-002-1171) showing that the $AgNO_3$ in the ink is completely transformed to Ag. Similarly, the femtosecond laser writing produces cubic Co (PDF 01-071-4238), cubic NiFe alloy (PDF 01-083-3765), cubic NiCr alloy (PDF 04-001-3422), hexagonal ZnO (PDF 04-009-7657), cubic CoO (PDF 01-076-3828), Cu_2O/CuO nanocomposite comprising cubic Cu_2O (PDF 01-078-2076) and monoclinic CuO (PDF 00-048-1548), Fe_3O_4/Fe_2O_3 nanocomposite comprising trigonal Fe_2O_3 (COD 96-210-1169) and cubic Fe_3O_4 (COD 96-900-2318) as shown in Figure 6.4 (b-h). We also synthesized $Fe_2Ni_{0.25}Co_{0.25}Cr_{0.25}Cu_{0.25}O_4$ whose peaks match with cubic $Cr_{0.15}Fe_{1.85}Co_{0.8}Ni_{0.2}O_{3.987}$ (PDF 04-021-6459) and cubic $Cu_{0.5}Fe_2Ni_{0.5}O_4$ (PDF 04-005-7634). Hence this hybrid AM process can also synthesize multi-metal oxides comprising up to 5 metals similar to the FsLDW process. The EDS spectra (Figure 6.5a) for the cross-section of the Zn@ $Fe_2Ni_{0.25}Co_{0.25}Cr_{0.25}Cu_{0.25}O_4$ fabricated through this method reveals the peaks corresponding to Ni, Co, Cu, Fe, and Cr confirming the formation of multi-metal oxide thin film. The EDS elemental mapping images for NiFe and NiCr alloy also shows a homogeneous distribution of Ni and Fe atoms for NiFe alloy, and Ni and Cr atoms for NiCr alloy confirming the formation of homogeneous alloy through the process. The Ag thin film formed after the laser direct writing process is ~ 1 – 10 µm thick as shown in Figure 6.6(a-b). The thickness of film produced using this hybrid AM is more uniform compared to FsLDW method reported in the previous chapter (Figure 5.9). Such thin films are very useful for sensing,[160] electrocatalysis,[161-162] and energy storage[163] applications. The FESEM image and EDS elemental mapping images for NiO and CuO thin films further demonstrate the formation of oxide thin films over the glass substrate (Figure 6.6(d-e)). Thus, this hybrid manufacturing process is versatile and can be used to synthesize a wide range of alloys and multi-metal oxides. Owing to the excessive time required for the synthesis of each of the alloy systems and oxides and further characterization by XRD and FESEM we have limited the fabrication to only these 9 metal alloys and oxides. However, since the process is exactly similar to the femtosecond laser direct writing of the dried ink precursor, we can safely conclude that this hybrid process can also synthesize all the range of alloys and oxides reported in the previous chapter.

The ink formulation for the process is highly simplified where the ink to synthesize a specific alloy or an oxide can be prepared by mixing the constitute metal salt solutions along with the CMC binder and citric acid. The CMC binder and citric acid combination work well with most of the salt solutions, hence simplifying the ink formulation. The concentration of metal to be incorporated in the alloy also can be tuned by tuning the concentration of metal salt in the ink. Thus, the process gives an excellent degree of freedom for the fabrication of a variety of oxides and alloys. If the same alloys and oxides were to be fabricated using nanoparticle-based ink, the ink formulation would be challenging. The ink would need a synthesis of every single metal oxide and alloy nanoparticles with uniform size distribution. Furthermore, the research development needed to choose the appropriate solvent and dispersant to formulate, and stable ink dispersion would be enormous.

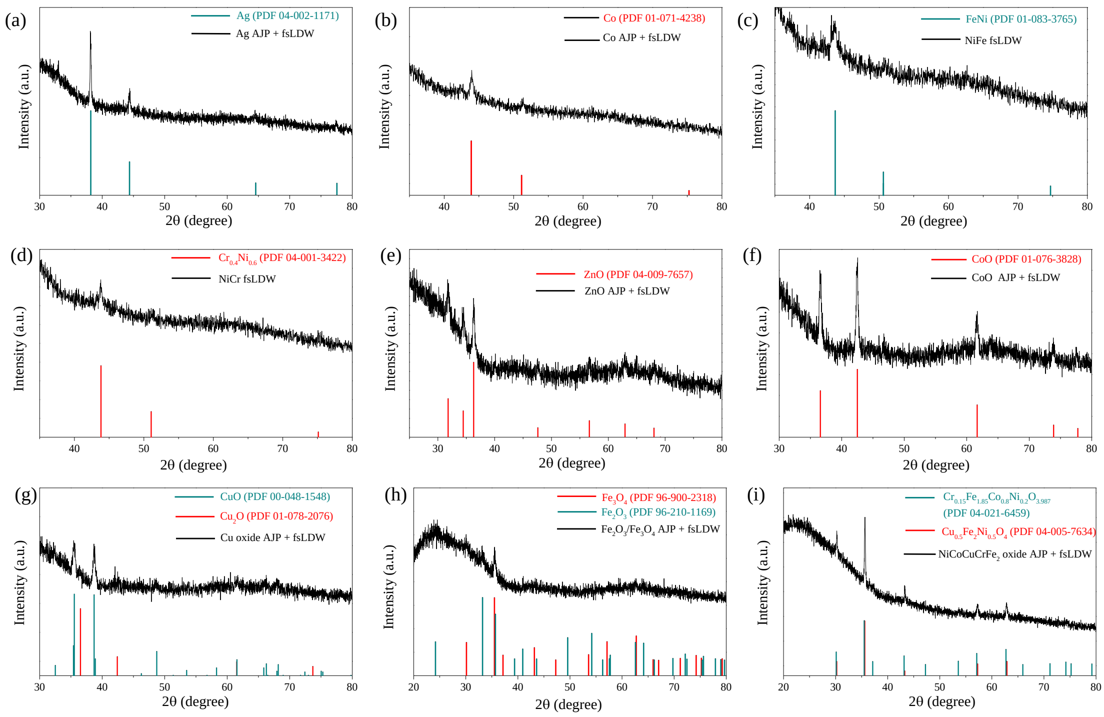

Figure 6.4 XRD spectra of aerosol jet printed + femtosecond laser direct writing processed (a) Ag, (b) Co, (c) NiFe alloy, (d) NiCr alloy, (e) ZnO, (f) CoO, (g) Cu_2O/CuO, (h) Fe_2O_3/Fe_3O_4, (i) $Fe_2Ni_{0.25}Co_{0.25}Cr_{0.25}Cu_{0.25}O_4$.

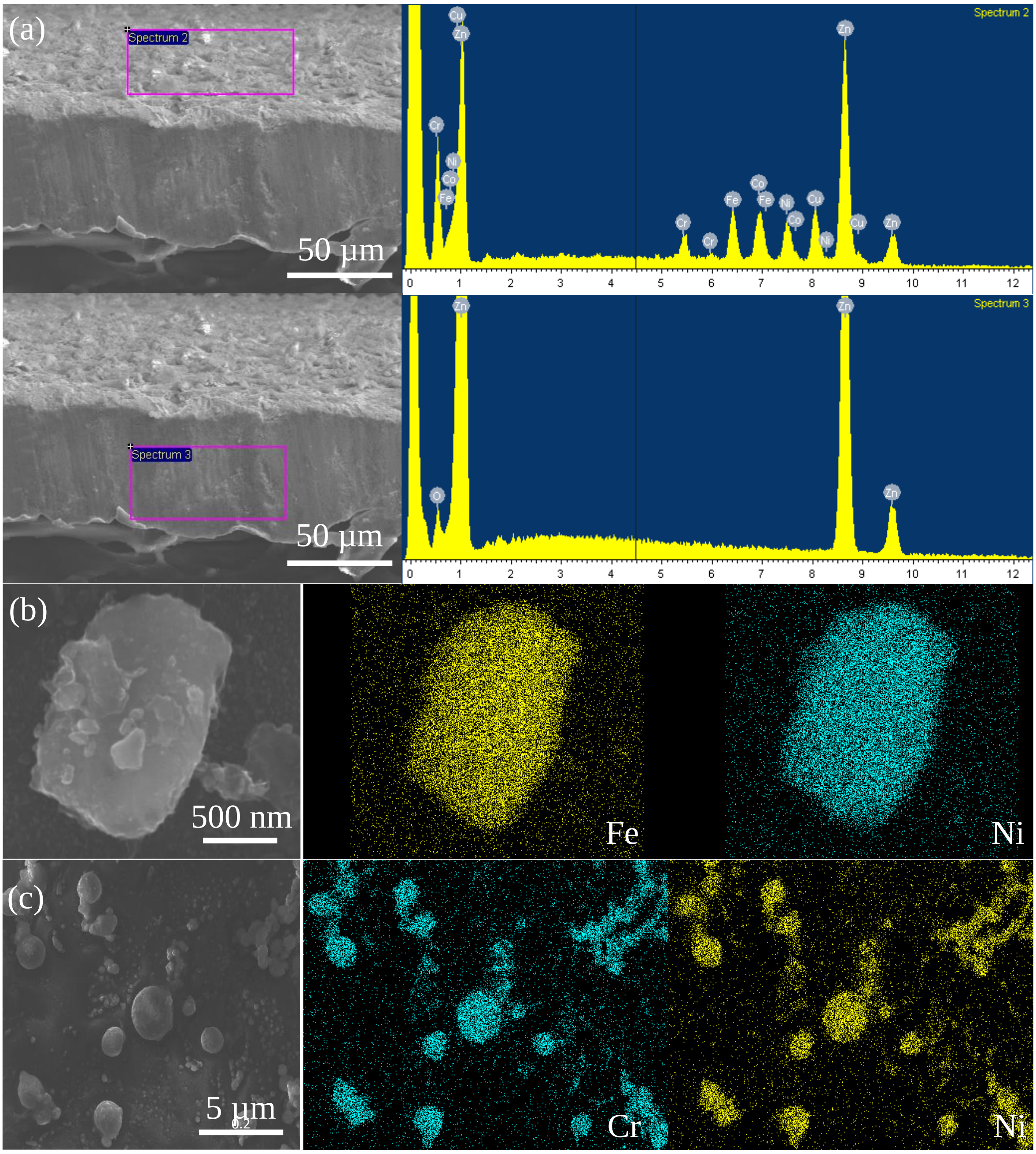

Figure 6.5 FESEM image and the corresponding EDS spectra of (a) Zn@Fe$_2$Ni$_{0.25}$Co$_{0.25}$Cr$_{0.25}$Cu$_{0.25}$O$_4$, (b) NiFe alloy, (c) NiCr alloy fabricated by AJP + fsLDW.

The hybrid additive manufacturing process has an added advantage. The precursor ink is deposited only where the material is required. Therefore, printing multiple materials on different locations on the substrate becomes much easier.

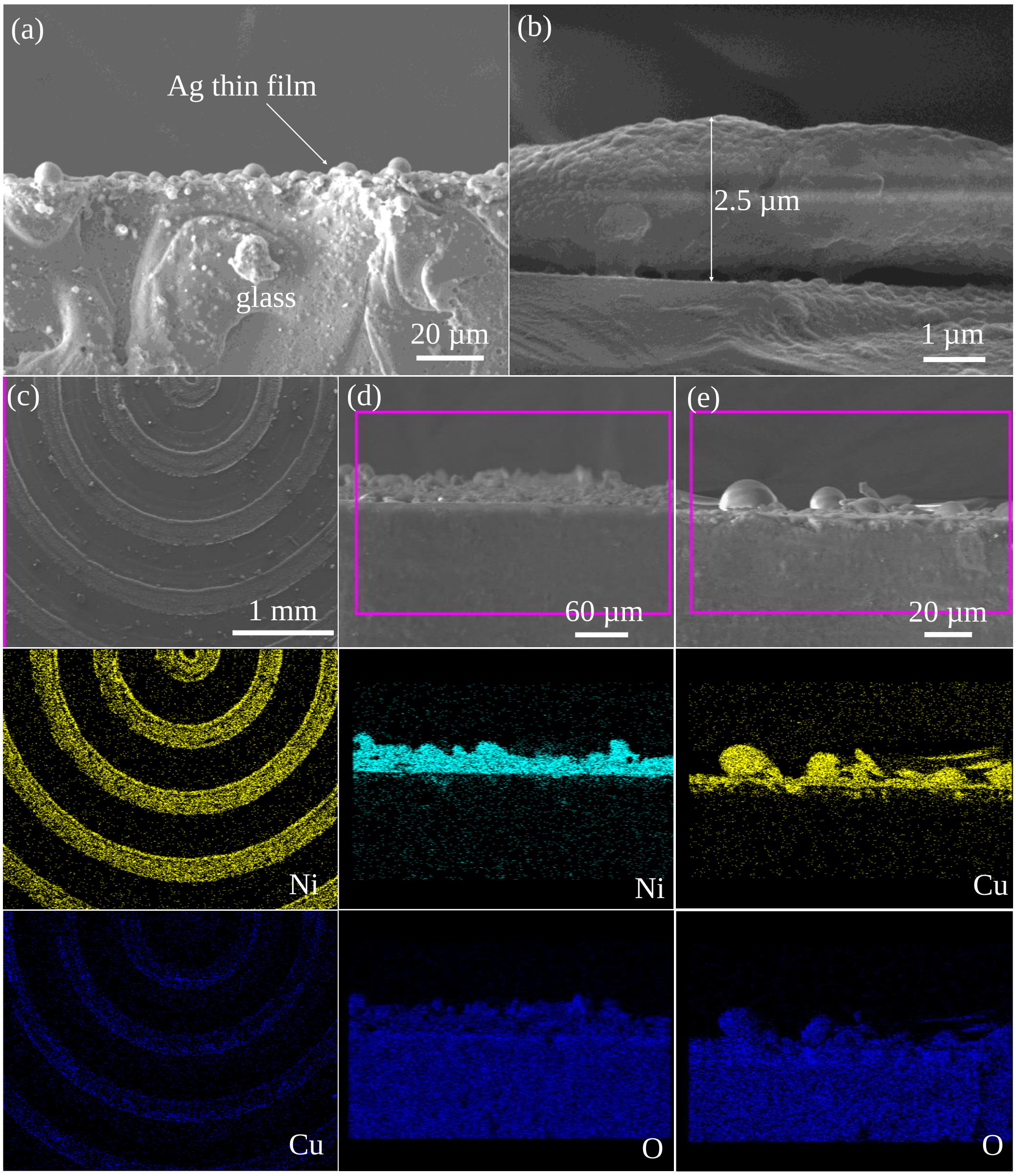

Figure 6.6 (a) FESEM image of the cross-section of glass@Ag fabricated by AJP + FsLDW, (b) FESEM cross-section revealing the thickness of the AJP + FsLDW printed patterns. FESEM image and corresponding EDS elemental mapping images of (c) Ni and Cu concentric circles, (d) cross-section of glass@NiO, and (e) cross-section of glass@CuO fabricated by AJP + FsLDW.

As a proof of concept, we printed Ni and Cu precursor ink in alternate concentric circles. Later, both the inks were simultaneously processed by a femtosecond laser transforming the ink into

Ni and Cu. The FESEM image and EDS elemental mapping images in Figure 6.6c show Ni and Cu concentric circular patterns formed with accurate shape and dimensional integrity. Without a doubt, the micro-patterns with complex shapes can be fabricated with great accuracy through the hybrid additive manufacturing process.

To take a step further in integrating the processing of different inks, we fabricated $Fe_2Ni_{0.25}Co_{0.25}Cr_{0.25}Cu_{0.25}O_4$ on Ag interdigitated electrode. As shown in Figure 6.7a, in the first step silver precursor ink was aerosol jet printed in the shape of an interdigitated electrode. Later $Fe_2Ni_{0.25}Co_{0.25}Cr_{0.25}Cu_{0.25}O_4$ precursor ink was printed on it. The printing shows remarkable accuracy of shape and dimensions. Later, both the inks were processed using a femtosecond laser to transform the inks into Ag interdigitated electrode and the $Fe_2Ni_{0.25}Co_{0.25}Cr_{0.25}Cu_{0.25}O_4$ rectangular pattern as shown in Figure 6.7b. It is worth noting that both the inks were processed in a single step. The same technique can be implemented to simultaneously process any number of materials, thus significantly reducing the number of steps involved in the fabrication. Various parts of sensors such as current collectors, electrodes, sensing material, etc. can be aerosol jet printed and processed with laser in one step to fabricate a fully functional sensor. The sensor designs such as this can find interesting applications in humidity sensing, UV light detection, micro-supercapacitors, batteries, and other electrochemical devices. Hence, the hybrid additive manufacturing process opens the door to the rapid and energy-efficient fabrication of multi-material components. We limit the discussion to multi-material fabrication in this thesis. The actual device fabrication and testing of the performance are beyond the scope of this thesis, as the primary focus of electrode fabrication in this work is for electrolysis of water. In the future, we hope to explore the application of this hybrid additive manufacturing process for the fabrication of devices such as sensors, micro-supercapacitors, and batteries.

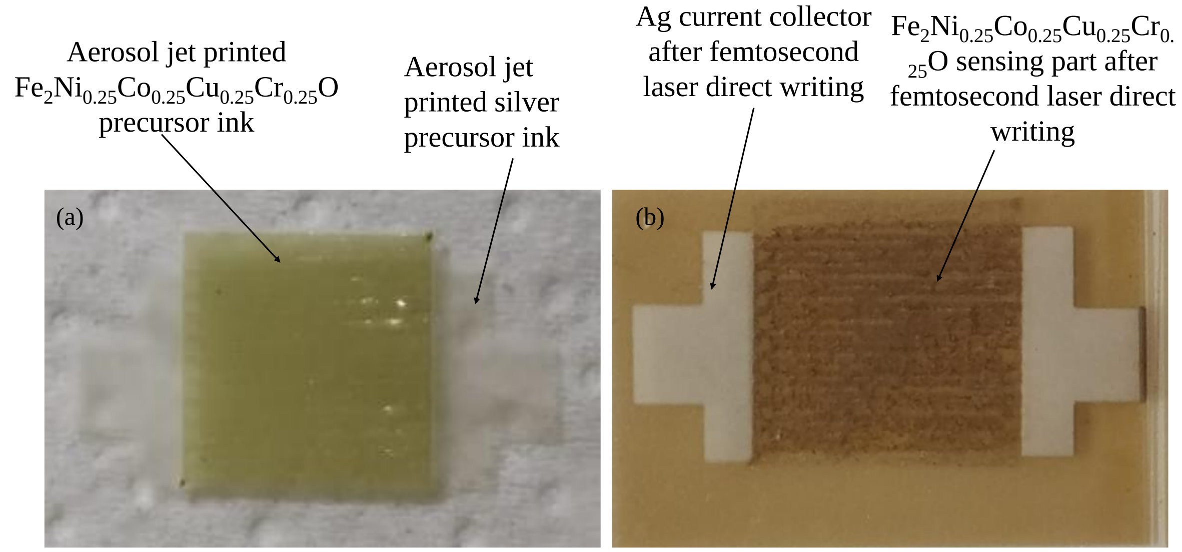

Figure 6.7 Optical images of the (a) aerosol jet printed silver precursor ink as inter-digited electrodes and $Fe_2Ni_{0.25}Co_{0.25}Cr_{0.25}Cu_{0.25}O_4$ precursor ink for the sensing part and the corresponding sensor (b) after processed using a femtosecond laser.

6.4 Conclusions

A novel hybrid additive manufacturing process for in-situ synthesis and coating of alloys and multi-metal oxides is developed. The combination of aerosol jet printing and femtosecond laser direct writing process allows for the fabrication of multi-metal oxide and alloy thin films. The process is versatile and adaptable for a large group of metal oxides and alloys. Process parameters suitable for aerosol jet printing of the precursor ink were investigated to arrive at the relationship between linewidth of the printed lines and the gas flow rates of carrier and sheath gas. In the end, as a proof of concept of multi-material fabrication Ag interdigitated electrodes in contact with $Fe_2Ni_{0.25}Co_{0.25}Cr_{0.25}Cu_{0.25}O_4$ were fabricated in just two steps. We foresee fabrications methods such as this to be further developed and extensively used in industries for device fabrications. In the next chapter key, the scientific contributions of this entire thesis are summarized and a brief recommendation for future work is discussed.

Chapter 7 Conclusions and Future outlook

In this chapter, we summarize the scientific contributions of this thesis and also highlight the novel fabrication processes developed as a part of the study. Taking the synthesis process as the basis we propose interesting research directions that can be pursued in the fabrication of single-atom catalysts and also aerosol jet printing of micropillars for sensing applications.

7.1 Conclusions

The research findings of this thesis demonstrate the additive manufacturing route to electrode fabrication for electrocatalysis. In the first part, we investigated new alloy systems that show superior activity for water splitting. In the later section, we developed an additive manufacturing process for the synthesis and coating of metal oxides and alloys. The following research findings succinctly outline the outcomes of this thesis:

1. Co-doping of Fe and Cu into Ni shifts the d-band energy of the Ni to a lower energy level and tunes the Gibbs energy of hydrogen adsorption to -0.131 eV. Consequently, the doped Ni exhibits enhanced catalytic activity compared to pristine Ni. Doping concentration affects the electrocatalytic activity. Further investigations reveal that Cu doping concentration of 5% and Fe doping concentration of 2.5% promote the best catalytic activity in Nickel. The intrinsic catalytic activity of the Ni is enhanced by co-doping of Cu and Fe which is revealed from the investigation into the specific activities of pristine and doped samples. Electron impedance spectroscopy studies reveal that doping enhanced the charge transfer kinetics of the Ni catalyst. The $NiCu_{0.05}Fe_{0.025}$ PNW catalyst is durable and stable when operated for an extended period.
2. NiAg heterogeneous alloy with epitaxial interfaces between Ni and Ag was prepared by thermal reduction of hydrothermally synthesized $Ag@Ni(OH)_2$. HRTEM images show the growth of Ag (200) planes on the Ni (111) planes creating abundant interfaces throughout the material. The density functional theory calculations estimate an extremely low Gibbs energy of hydrogen adsorption equal to -0.04 eV at the interface of Ni-Ag. Further, the alloying concentration of Ag exhibited a direct correlation with the interface area and therefore on the catalytic activity. Correspondingly, $NiAg_{0.4}$ 3DPNC with 28.57% Ag showed the best activity for HER exhibiting a low η_{10} of 40

mV. Furthermore, the specific activity of the $NiAg_{0.4}$ 3DPNC approaches that of state-of-the-art Pt/C catalyst. The catalyst continued to offer a current density of 10 mA cm^{-2} when operated at – 76 mV overpotential for more than 80 hours revealing its remarkable stability.

3. A novel additive manufacturing process for simultaneous in-situ synthesis and coating of multi-metal oxides and high entropy alloys is developed. The process involves a single step femtosecond laser processing of dried ink precursor, in which the ink is transformed into metal oxide or metal alloy depending on the ink formulation. A generic process for ink formulation is also developed in which the metal salt solution is mixed with CMC binder and citric acid to form a stable ink. XRD, XPS, ICP-OES, HRTEM, and FESEM imaging along with EDS tests confirm the formation of multi-metal oxide and high entropy alloys using the FsLDW process. The versatility of the process is demonstrated by fabricating a large group of 57 metal oxides and alloys. The coated metal alloys and oxides are strongly bonded to the substrate and can be directly utilized for electrocatalysis as binder-free electrodes. The method requires an extremely low quantity of solvents, energy, and fabrication time is significantly low compared to the conventional methods. The specific activity of $SS@NiAg_{0.4}$ and $SS@NiCu_{0.05}Fe_{0.025}$ fabricated using laser direct writing show similar activity as the hydrothermally synthesized samples. Furthermore, $CFP@NiCoCuFeCr_{0.5}$ HEA prepared through the FsLDW process exhibits excellent activity for OER with a very low η_{10} of 232 mV. The fabricated electrode is robust and shows no degradation of activity when operated for 50 hours at 10 mA cm^{-2}.
4. A novel hybrid manufacturing process combining aerosol jet printing and laser direct writing is developed to fabricate metal oxide and alloy thin films. The metal precursor ink is printed using an aerosol jet printer and later irradiated with a femtosecond laser

to transform the ink to metal oxides or alloys. The process is helpful to selectively deposit different materials in complex patterns which are common in the fabrication of sensors and other electrochemical devices. As a proof of concept Ag inter-digited electrodes with $Fe_2Ni_{0.25}Co_{0.25}Cr_{0.25}Cu_{0.25}O_4$ sensing element is fabricated successfully using the hybrid AM process.

7.2 Future outlook

In this work, we successfully demonstrated the synthesis and coating of metal alloys and oxides through laser direct writing and aerosol jet printing. However, the materials for electrocatalysis are not limited to alloys and oxides. Accordingly, we expect this fabrication method to be developed further for the synthesis of other classes of compounds as well. In addition, a hybrid additive manufacturing process could be used to create materials beyond thin films. In this light, we make the following recommendations for future research in this space:

7.2.1 Femtosecond laser direct writing of single-atom catalysts

In addition to alloys and oxides, there is an interesting class of materials known as single-atom catalysts. In these single atoms are bonded to substrates like reduced graphene,[164] C_3N_4, carbon,[165] MXenes, etc. Furthermore, there is another class of single-atom catalysts called single atom alloys[166] in which single atoms of a particular element are dispersed in the lattice of the host metal. Both of these catalyst systems possess interesting catalytic properties owing to their electronic structure. The unique advantage of these materials comes from a very low mass loading of metal atoms while maintaining excellent catalytic properties. As a result, the cost of the catalyst system can be significantly low and also environmentally benign owing to the low concentration of metal atoms. However, currently, the general method of synthesis of these single-atom catalysts involves processes such as ball milling, thermal annealing, hydrothermal process, etc. which are energy-intensive. In this light, the femtosecond laser process can be an appealing alternative to fabricate a variety of single-atom catalysts similar to the synthesis of metal alloys and oxides.

7.2.2 Aerosol jet printing of high aspect ratio metal oxide and metal alloy structures

Aerosol jet printing is an interesting additive manufacturing process that supports the printing of a wide variety of low viscosity inks. So far in this work, we printed thin films of metal precursors inks to be processed under laser later. To take it forward, with appropriate changes in the ink formulation and the process of printing, three-dimensional structures can be created which find interesting applications in sensing and energy storage. In our preliminary trials, we have successfully printed micropillars of CoO precursor ink (Figure 7.1a) and micro-walls of Ag precursor ink (Figure 7.1b) using aerosol jet printing. In the subsequent steps, we plan to transform the precursor ink to metal oxide and alloy high aspect ratio structures. The process parameters are yet to be optimized for printing perfectly aligned micropillars and micro-walls. Such high aspect ratios structures are very useful in sensing,[167] drug delivery,[168], and energy storage[169] applications. Hence, we foresee great opportunities and research development in these areas of microfabrication.

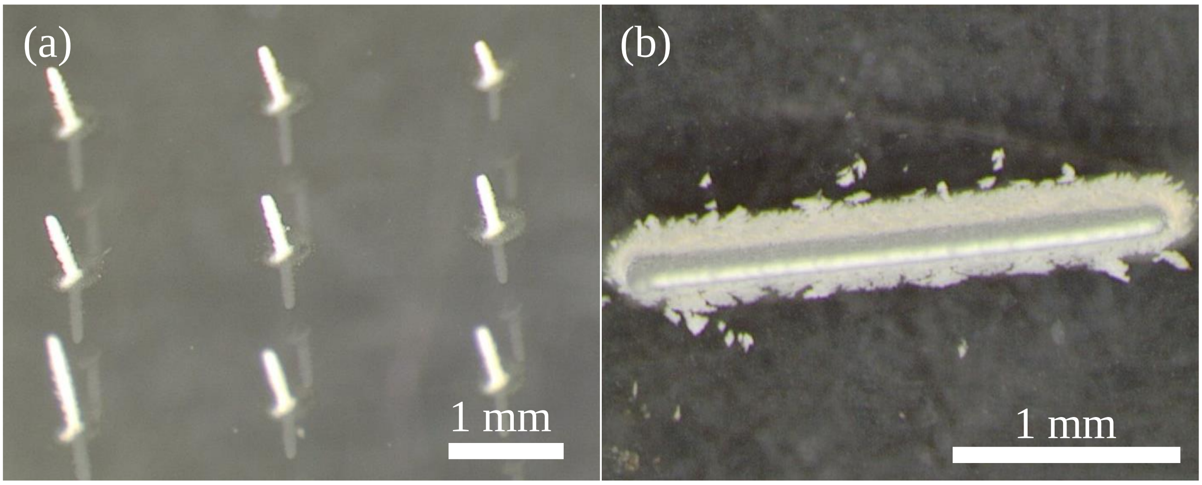

Figure 7.1 (a) $CoSO_4$ micropillars, (b) $AgNO_3$ micro-walls printed by aerosol jet printing on the glass surface.

References

(1) Seh, Z. W.; Kibsgaard, J.; Dickens, C. F.; Chorkendorff, I.; Norskov, J. K.; Jaramillo, T. F. Combining Theory and Experiment in Electrocatalysis: Insights into Materials Design. *Science* **2017,** *355* (6321).

(2) Xiong, B.; Chen, L.; Shi, J. Anion-Containing Noble-Metal-Free Bifunctional Electrocatalysts for Overall Water Splitting. *ACS Catalysis* **2018**.

(3) Carmo, M.; Fritz, D. L.; Mergel, J.; Stolten, D. A Comprehensive Review on Pem Water Electrolysis. *International Journal of Hydrogen Energy* **2013,** *38* (12), 4901-4934.

(4) Lu, F.; Zhou, M.; Zhou, Y.; Zeng, X. First-Row Transition Metal Based Catalysts for the Oxygen Evolution Reaction under Alkaline Conditions: Basic Principles and Recent Advances. *Small* **2017,** *13* (45).

(5) Jiao, Y.; Zheng, Y.; Jaroniec, M.; Qiao, S. Z. Design of Electrocatalysts for Oxygen- and Hydrogen-Involving Energy Conversion Reactions. *Chemical Society reviews* **2015,** *44* (8), 2060-2086.

(6) Vij, V.; Sultan, S.; Harzandi, A. M.; Meena, A.; Tiwari, J. N.; Lee, W.-G.; Yoon, T.; Kim, K. S. Nickel-Based Electrocatalysts for Energy-Related Applications: Oxygen Reduction, Oxygen Evolution, and Hydrogen Evolution Reactions. *ACS Catalysis* **2017,** *7* (10), 7196-7225.

(7) Medford, A. J.; Vojvodic, A.; Hummelshøj, J. S.; Voss, J.; Abild-Pedersen, F.; Studt, F.; Bligaard, T.; Nilsson, A.; Nørskov, J. K. From the Sabatier Principle to a Predictive Theory of Transition-Metal Heterogeneous Catalysis. *Journal of Catalysis* **2015,** *328*, 36-42.

(8) Gong, M.; Li, Y.; Wang, H.; Liang, Y.; Wu, J. Z.; Zhou, J.; Wang, J.; Regier, T.; Wei, F.; Dai, H. An Advanced Ni-Fe Layered Double Hydroxide Electrocatalyst for Water Oxidation. *Journal of the American Chemical Society* **2013,** *135* (23), 8452-8455.

(9) Lu, Y.; Jiang, B.; Fang, L.; Ling, F.; Wu, F.; Hu, B.; Meng, F.; Niu, K.; Lin, F.; Zheng, H. An Investigation of Ultrathin Nickel-Iron Layered Double Hydroxide Nanosheets Grown on Nickel Foam for High-Performance Supercapacitor Electrodes. *J Alloy Compd* **2017,** *714*, 63-70.

(10) Dutta, S.; Indra, A.; Feng, Y.; Song, T.; Paik, U. Self-Supported Nickel Iron Layered Double Hydroxide-Nickel Selenide Electrocatalyst for Superior Water Splitting Activity. *ACS applied materials & interfaces* **2017,** *9* (39), 33766-33774.

(11) Zhu, W.; Liu, L.; Yue, Z.; Zhang, W.; Yue, X.; Wang, J.; Yu, S.; Wang, L.; Wang, J. Au Promoted Nickel-Iron Layered Double Hydroxide Nanoarrays: A Modular Catalyst Enabling High-Performance Oxygen Evolution. *ACS applied materials & interfaces* **2017,** *9* (23), 19807-19814.

(12) Han, N.; Zhao, F.; Li, Y. Ultrathin Nickel–Iron Layered Double Hydroxide Nanosheets Intercalated with Molybdate Anions for Electrocatalytic Water Oxidation. *Journal of Materials Chemistry A* **2015,** *3* (31), 16348-16353.

(13) Dinh, K. N.; Zheng, P.; Dai, Z.; Zhang, Y.; Dangol, R.; Zheng, Y.; Li, B.; Zong, Y.; Yan, Q. Ultrathin Porous Nifev Ternary Layer Hydroxide Nanosheets as a Highly Efficient Bifunctional Electrocatalyst for Overall Water Splitting. *Small* **2017**.

(14) Bo Zhang, 2* Xueli Zheng,1,3* Oleksandr Voznyy,1* Riccardo Comin,1 Michal Bajdich,4,5; Max García-Melchor, 5 Lili Han,3,6 Jixian Xu,1 Min Liu,1 Lirong Zheng,7; F. Pelayo García de Arquer, C. T. D., 1 Fengjia Fan,1 Mingjian Yuan,1; Emre Yassitepe, N. C., 8 Tom Regier,8 Pengfei Liu,9 Yuhang Li,9 Phil De Luna,1; Alyf Janmohamed, H. L. X., 6 Huagui Yang,9; Aleksandra Vojvodic, 5† Edward H. Sargent1†. Homogeneously Dispersed Multimetal Oxygen Evolving Catalysts. *Science* **2016,** *352* (6283), 333-337.

(15) Shen, Y.; Zhou, Y.; Wang, D.; Wu, X.; Li, J.; Xi, J. Nickel-Copper Alloy Encapsulated in Graphitic Carbon Shells as Electrocatalysts for Hydrogen Evolution Reaction. *Advanced Energy Materials* **2018,** *8* (2), 1701759.

(16) Kuang, M.; Wang, Q.; Han, P.; Zheng, G. Cu, Co-Embedded N-Enriched Mesoporous Carbon for Efficient Oxygen Reduction and Hydrogen Evolution Reactions. *Advanced Energy Materials* **2017,** *7* (17), 1700193.

(17) Zou, X.; Huang, X.; Goswami, A.; Silva, R.; Sathe, B. R.; Mikmekova, E.; Asefa, T. Cobalt-Embedded Nitrogen-Rich Carbon Nanotubes Efficiently Catalyze Hydrogen Evolution Reaction at All Ph Values. *Angewandte Chemie* **2014,** *53* (17), 4372-4376.

(18) Zhang, L.; Gong, H. Unravelling the Correlation between Nickel to Copper Ratio of Binary Oxides and Their Superior Supercapacitor Performance. *Electrochimica Acta* **2017,** *234*, 82-92.

(19) Zhang, J.; Xiao, B.; Liu, X.; Liu, P.; Xi, P.; Xiao, W.; Ding, J.; Gao, D.; Xue, D. Copper Dopants Improved the Hydrogen Evolution Activity of Earth-Abundant Cobalt Pyrite Catalysts by Activating the Electrocatalytically Inert Sulfur Sites. *Journal of Materials Chemistry A* **2017,** *5* (33), 17601-17608.

(20) Wang, Y.; Zhou, T.; Jiang, K.; Da, P.; Peng, Z.; Tang, J.; Kong, B.; Cai, W.-B.; Yang, Z.; Zheng, G. Reduced Mesoporous Co3o4nanowires as Efficient Water Oxidation Electrocatalysts and Supercapacitor Electrodes. *Advanced Energy Materials* **2014,** *4* (16), 1400696.

(21) Xu, L.; Jiang, Q.; Xiao, Z.; Li, X.; Huo, J.; Wang, S.; Dai, L. Plasma-Engraved Co3 O4 Nanosheets with Oxygen Vacancies and High Surface Area for the Oxygen Evolution Reaction. *Angewandte Chemie* **2016,** *55* (17), 5277-5281.

(22) Bao, J.; Zhang, X.; Fan, B.; Zhang, J.; Zhou, M.; Yang, W.; Hu, X.; Wang, H.; Pan, B.; Xie, Y. Ultrathin Spinel-Structured Nanosheets Rich in Oxygen Deficiencies for Enhanced Electrocatalytic Water Oxidation. *Angewandte Chemie* **2015,** *54* (25), 7399-7404.

(23) Liu, Y.; Cheng, H.; Lyu, M.; Fan, S.; Liu, Q.; Zhang, W.; Zhi, Y.; Wang, C.; Xiao, C.; Wei, S.; Ye, B.; Xie, Y. Low Overpotential in Vacancy-Rich Ultrathin Cose2 Nanosheets for Water Oxidation. *Journal of the American Chemical Society* **2014,** *136* (44), 15670-15675.

(24) Zhang, T.; Wu, M.-Y.; Yan, D.-Y.; Mao, J.; Liu, H.; Hu, W.-B.; Du, X.-W.; Ling, T.; Qiao, S.-Z. Engineering Oxygen Vacancy on Nio Nanorod Arrays for Alkaline Hydrogen Evolution. *Nano Energy* **2018,** *43*, 103-109.

(25) Deng, D.; Novoselov, K. S.; Fu, Q.; Zheng, N.; Tian, Z.; Bao, X. Catalysis with Two-Dimensional Materials and Their Heterostructures. *Nature nanotechnology* **2016,** *11* (3), 218-230.

(26) Cui, X.; Ren, P.; Deng, D.; Deng, J.; Bao, X. Single Layer Graphene Encapsulating Non-Precious Metals as High-Performance Electrocatalysts for Water Oxidation. *Energy & Environmental Science* **2016,** *9* (1), 123-129.

(27) Ren, X.; Wu, D.; Ge, R.; Sun, X.; Ma, H.; Yan, T.; Zhang, Y.; Du, B.; Wei, Q.; Chen, L. Self-Supported Comos4 Nanosheet Array as an Efficient Catalyst for Hydrogen Evolution Reaction at Neutral Ph. *Nano Research* **2018,** *11* (4), 2024-2033.

(28) Wang, R.; Han, J.; Zhang, X.; Song, B. Synergistic Modulation in Mx2 (Where m = Mo or W or V, and X = S or Se) for an Enhanced Hydrogen Evolution Reaction. *Journal of Materials Chemistry A* **2018,** *6* (44), 21847-21858.

(29) Wang, Q.; Zhao, Z. L.; Dong, S.; He, D.; Lawrence, M. J.; Han, S.; Cai, C.; Xiang, S.; Rodriguez, P.; Xiang, B.; Wang, Z.; Liang, Y.; Gu, M. Design of Active Nickel Single-Atom Decorated Mos2 as a Ph-Universal Catalyst for Hydrogen Evolution Reaction. *Nano Energy* **2018,** *53*, 458-467.

(30) Wu, H.; Lu, X.; Zheng, G.; Ho, G. W. Topotactic Engineering of Ultrathin 2d Nonlayered Nickel Selenides for Full Water Electrolysis. *Advanced Energy Materials* **2018,** *8* (14).

(31) Chen, Y.; Yu, J.; Jia, J.; Liu, F.; Zhang, Y.; Xiong, G.; Zhang, R.; Yang, R.; Sun, D.; Liu, H.; Zhou, W. Metallic Ni3mo3n Porous Microrods with Abundant Catalytic Sites as Efficient Electrocatalyst for Large Current Density and Superstability of Hydrogen Evolution Reaction and Water Splitting. *Applied Catalysis B: Environmental* **2020,** *272*.

(32) Xu, K.; Chen, P.; Li, X.; Tong, Y.; Ding, H.; Wu, X.; Chu, W.; Peng, Z.; Wu, C.; Xie, Y. Metallic Nickel Nitride Nanosheets Realizing Enhanced Electrochemical Water Oxidation. *J Am Chem Soc* **2015,** *137* (12), 4119-4125.

(33) Laursen, A. B.; Wexler, R. B.; Whitaker, M. J.; Izett, E. J.; Calvinho, K. U. D.; Hwang, S.; Rucker, R.; Wang, H.; Li, J.; Garfunkel, E.; Greenblatt, M.; Rappe, A. M.; Dismukes, G. C. Climbing the Volcano of Electrocatalytic Activity While Avoiding Catalyst Corrosion: Ni3p, a Hydrogen Evolution Electrocatalyst Stable in Both Acid and Alkali. *ACS Catalysis* **2018,** *8* (5), 4408-4419.

(34) Zhou, M.; Weng, Q.; Zhang, X.; Wang, X.; Xue, Y.; Zeng, X.; Bando, Y.; Golberg, D. In Situ Electrochemical Formation of Core–Shell Nickel–Iron Disulfide and Oxyhydroxide Heterostructured Catalysts for a Stable Oxygen Evolution Reaction and the Associated Mechanisms. *Journal of Materials Chemistry A* **2017,** *5* (9), 4335-4342.

(35) Wang, Y.; Ni, Y.; Liu, B.; Shang, S.; Yang, S.; Cao, M.; Hu, C. Vertically Oriented Coo@Feooh Nanowire Arrays Anchored on Carbon Cloth as a Highly Efficient Electrode for Oxygen Evolution Reaction. *Electrochimica Acta* **2017,** *257*, 356-363.

(36) Han, X.; Tong, X.; Wu, G.; Yang, N.; Guo, X.-Y. Carbon Fibers Supported Nise Nanowire Arrays as Efficient and Flexible Electrocatalysts for the Oxygen Evolution Reaction. *Carbon* **2018,** *129*, 245-251.

(37) Chi, J.-Q.; Yan, K.-L.; Xiao, Z.; Dong, B.; Shang, X.; Gao, W.-K.; Li, X.; Chai, Y.-M.; Liu, C.-G. Trimetallic Ni Fe Co Selenides Nanoparticles Supported on Carbon Fiber Cloth as Efficient Electrocatalyst for Oxygen Evolution Reaction. *International Journal of Hydrogen Energy* **2017,** *42* (32), 20599-20607.

(38) Zhang, D.; Shao, Y.; Kong, X.; Jiang, M.; Lei, D.; Lei, X. Facile Fabrication of Large-Area Hybrid Ni-Co Hydroxide/Cu(Oh) 2 /Copper Foam Composites. *Electrochimica Acta* **2016,** *218*, 294-302.

(39) Zhang, Y.; Zang, J.; Han, C.; Jia, S.; Tian, P.; Gao, H.; Wang, Y. Molybdenum Oxide and Molybdenum Carbide Coated Carbon Black as an Electrocatalyst for Hydrogen Evolution Reaction in Acidic Media. *International Journal of Hydrogen Energy* **2017,** *42* (44), 26985-26994.

(40) Guo, J.; Wang, J.; Xuan, C.; Wu, Z.; Lei, W.; Zhu, J.; Xiao, W.; Wang, D. Molybdenum Carbides Embedded on Carbon Nanotubes for Efficient Hydrogen Evolution Reaction. *Journal of Electroanalytical Chemistry* **2017,** *801*, 7-13.

(41) Zhou, W.; Wu, X.-J.; Cao, X.; Huang, X.; Tan, C.; Tian, J.; Liu, H.; Wang, J.; Zhang, H. Ni3s2 Nanorods/Ni Foam Composite Electrode with Low Overpotential for Electrocatalytic Oxygen Evolution. *Energy & Environmental Science* **2013,** *6* (10), 2921.

(42) Nsanzimana, J. M. V.; Peng, Y.; Xu, Y. Y.; Thia, L.; Wang, C.; Xia, B. Y.; Wang, X. An Efficient and Earth-Abundant Oxygen-Evolving Electrocatalyst Based on Amorphous Metal Borides. *Advanced Energy Materials* **2018,** *8* (1), 1701475.

(43) Li, D.; Baydoun, H.; Verani, C. N.; Brock, S. L. Efficient Water Oxidation Using Comnp Nanoparticles. *Journal of the American Chemical Society* **2016,** *138* (12), 4006-4009.

(44) Xing, Z.; Gan, L.; Wang, J.; Yang, X. Experimental and Theoretical Insights into Sustained Water Splitting with an Electrodeposited Nanoporous Nickel Hydroxide@Nickel Film as an Electrocatalyst. *Journal of Materials Chemistry A* **2017,** *5* (17), 7744-7748.

(45) Yu, J.; Cheng, G.; Luo, W. Ternary Nickel–Iron Sulfide Microflowers as a Robust Electrocatalyst for Bifunctional Water Splitting. *Journal of Materials Chemistry A* **2017,** *5* (30), 15838-15844.

(46) Xu, Y.-Z.; Yuan, C.-Z.; Liu, Z.-W.; Chen, X.-P. In Situ Synthesis of Nise@Cop Core–Shell Nanowire Arrays on Nickel Foam as a Highly Efficient and Robust Electrode for Electrochemical Hydrogen Generation in Both Alkaline and Acidic Media. *Catalysis Science & Technology* **2018,** *8* (1), 128-133.

(47) Xuehui Gao+, H. Z., Quanguo Li, Xuegong Yu, Zhanglian Hong, Xingwang Zhang,*; Chengdu Liang, a. Z. L. Hierarchical Nico2o4 Hollow Microcuboids as Bifunctional Electrocatalysts for Overall Water Splitting. *Angewandte Chemie* **2016,** (55), 6290-6294.

(48) Ma, Y.; He, Z.; Wu, Z.; Zhang, B.; Zhang, Y.; Ding, S.; Xiao, C. Galvanic-Replacement Mediated Synthesis of Copper–Nickel Nitrides as Electrocatalyst for Hydrogen Evolution Reaction. *Journal of Materials Chemistry A* **2017,** *5* (47), 24850-24858.

(49) Chen, S.; Kang, Z.; Zhang, X.; Xie, J.; Wang, H.; Shao, W.; Zheng, X.; Yan, W.; Pan, B.; Xie, Y. Highly Active Fe Sites in Ultrathin Pyrrhotite Fe7s8 Nanosheets Realizing Efficient Electrocatalytic Oxygen Evolution. *ACS central science* **2017,** *3* (11), 1221-1227.

(50) Dangol, R.; Dai, Z.; Chaturvedi, A.; Zheng, Y.; Zhang, Y.; Dinh, K. N.; Li, B.; Zong, Y.; Yan, Q. Few-Layer Nips3 Nanosheets as Bifunctional Materials for Li-Ion Storage and Oxygen Evolution Reaction. *Nanoscale* **2018,** *10* (10), 4890-4896.

(51) Greeley, J.; Jaramillo, T. F.; Bonde, J.; Chorkendorff, I.; Nørskov, J. K. Computational High-Throughput Screening of Electrocatalytic Materials for Hydrogen Evolution. *Nature materials* **2006,** *5* (11), 909-913.

(52) Wei, C.; Xu, Z. J. The Comprehensive Understanding of 10 Ma Cmgeo−2 as an Evaluation Parameter for Electrochemical Water Splitting. *Small Methods* **2018,** *2* (11).

(53) Wang, Z.; Wang, J.; Li, M.; Sun, K.; Liu, C. J. Three-Dimensional Printed Acrylonitrile Butadiene Styrene Framework Coated with Cu-Btc Metal-Organic Frameworks for the Removal of Methylene Blue. *Scientific reports* **2014,** *4*, 5939.

(54) Michorczyk, P.; Hędrzak, E.; Węgrzyniak, A. Preparation of Monolithic Catalysts Using 3d Printed Templates for Oxidative Coupling of Methane. *Journal of Materials Chemistry A* **2016,** *4* (48), 18753-18756.

(55) Ambrosi, A.; Moo, J. G. S.; Pumera, M. Helical 3d-Printed Metal Electrodes as Custom-Shaped 3d Platform for Electrochemical Devices. *Advanced Functional Materials* **2016,** *26* (5), 698-703.

(56) Jakus, A. E.; Taylor, S. L.; Geisendorfer, N. R.; Dunand, D. C.; Shah, R. N. Metallic Architectures from 3d-Printed Powder-Based Liquid Inks. *Advanced Functional Materials* **2015,** *25* (45), 6985-6995.

(57) Taylor, S. L.; Jakus, A. E.; Shah, R. N.; Dunand, D. C. Iron and Nickel Cellular Structures by Sintering of 3d-Printed Oxide or Metallic Particle Inks *Adv Eng Mater* **2016**.

(58) Taylor, S. L.; Shah, R. N.; Dunand, D. C. Ni-Mn-Ga Micro-Trusses Via Sintering of 3d-Printed Inks Containing Elemental Powders. *Acta Materialia* **2018,** *143*, 20-29.

(59) Sha, J.; Li, Y.; Villegas Salvatierra, R.; Wang, T.; Dong, P.; Ji, Y.; Lee, S. K.; Zhang, C.; Zhang, J.; Smith, R. H.; Ajayan, P. M.; Lou, J.; Zhao, N.; Tour, J. M. Three-Dimensional Printed Graphene Foams. *ACS nano* **2017,** *11* (7), 6860-6867.

(60) Deng, H.; Zhang, C.; Xie, Y.; Tumlin, T.; Giri, L.; Karna, S. P.; Lin, J. Laser Induced Mos2/Carbon Hybrids for Hydrogen Evolution Reaction Catalysts. *Journal of Materials Chemistry A* **2016,** *4* (18), 6824-6830.

(61) Jin Zhang, J. W., Stephane De´nomme´e, Christopher Kingston, Zygmunt J. Jakubek,; Yves Deslandes, M. P., and Benoit Simard. Synthesis of Metal Alloy Nanoaprticles I Solution by Laser Irradiation of a Metal Powder Suspension. *J. Phys. Chem. B* **2003,** *107*, 6920-6923.

(62) Zarzar, L. D.; Swartzentruber, B. S.; Donovan, B. F.; Hopkins, P. E.; Kaehr, B. Using Laser-Induced Thermal Voxels to Pattern Diverse Materials at the Solid-Liquid Interface. *ACS Appl Mater Interfaces* **2016,** *8* (33), 21134-21139.

(63) Kindle, C.; Castonguay, A.; McGee, S.; Tomko, J. A.; Hopkins, P. E.; Zarzar, L. D. Direct Laser Writing from Aqueous Precursors for Nano to Microscale Topographical Control, Integration, and Synthesis of Nanocrystalline Mixed Metal Oxides. *ACS Applied Nano Materials* **2019,** *2* (5), 2581-2586.

(64) Ruquan Ye, Z. P., Tuo Wang, Yunong Xu, Jibo Zhang, Yilun Li, Lizanne G. Nilewski,; Jian Lin; Tour, a. J. M. In Situ Formation of Metal Oxide Nanocrystals Embedded in Laser Induced Graphene. *ACS Nano* **2015,** *9* (9), 9244-9251.

(65) Jiang, N.; You, B.; Sheng, M.; Sun, Y. Electrodeposited Cobalt-Phosphorous-Derived Films as Competent Bifunctional Catalysts for Overall Water Splitting. *Angewandte Chemie* **2015,** *54* (21), 6251-6254.

(66) Lu, B.; Guo, L.; Wu, F.; Peng, Y.; Lu, J. E.; Smart, T. J.; Wang, N.; Finfrock, Y. Z.; Morris, D.; Zhang, P.; Li, N.; Gao, P.; Ping, Y.; Chen, S. Ruthenium Atomically Dispersed in Carbon Outperforms Platinum toward Hydrogen Evolution in Alkaline Media. *Nature communications* **2019,** *10* (1), 631.

(67) Burke, M. S.; Enman, L. J.; Batchellor, A. S.; Zou, S.; Boettcher, S. W. Oxygen Evolution Reaction Electrocatalysis on Transition Metal Oxides and (Oxy)Hydroxides: Activity Trends and Design Principles. *Chemistry of Materials* **2015,** *27* (22), 7549-7558.

(68) Dinh, K. N.; Liang, Q.; Du, C.-F.; Zhao, J.; Tok, A. I. Y.; Mao, H.; Yan, Q. Nanostructured Metallic Transition Metal Carbides, Nitrides, Phosphides, and Borides for Energy Storage and Conversion. *Nano Today* **2019,** *25*, 99-121.

(69) Durst, J.; Siebel, A.; Simon, C.; Hasché, F.; Herranz, J.; Gasteiger, H. A. New Insights into the Electrochemical Hydrogen Oxidation and Evolution Reaction Mechanism. *Energy Environ. Sci.* **2014,** *7* (7), 2255-2260.

(70) Oh, A.; Sa, Y. J.; Hwang, H.; Baik, H.; Kim, J.; Kim, B.; Joo, S. H.; Lee, K. Rational Design of Pt-Ni-Co Ternary Alloy Nanoframe Crystals as Highly Efficient Catalysts toward the Alkaline Hydrogen Evolution Reaction. *Nanoscale* **2016,** *8* (36), 16379-16386.

(71) Wang, P.; Jiang, K.; Wang, G.; Yao, J.; Huang, X. Phase and Interface Engineering of Platinum-Nickel Nanowires for Efficient Electrochemical Hydrogen Evolution. *Angewandte Chemie* **2016,** *55* (41), 12859-12863.

(72) Cheng, Z.; Geng, X.; Chen, L.; Zhang, C.; Huang, H.; Tang, S.; Du, Y. In Situ Synthesis of Chemically Ordered Primitive Cubic Pt3co Nanoparticles by a Spray Paint Drying Method for Hydrogen Evolution Reaction. *Journal of Materials Science* **2018,** *53* (17), 12399-12406.

(73) Zhang, L.; Lu, J.; Yin, S.; Luo, L.; Jing, S.; Brouzgou, A.; Chen, J.; Shen, P. K.; Tsiakaras, P. One-Pot Synthesized Boron-Doped Rhfe Alloy with Enhanced Catalytic Performance for Hydrogen Evolution Reaction. *Applied Catalysis B: Environmental* **2018,** *230*, 58-64.

(74) Kuang, M.; Huang, W.; Hegde, C.; Fang, W.; Tan, X.; Liu, C.; Ma, J.; Yan, Q. Interface Engineering in Transition Metal Carbides for Electrocatalytic Hydrogen Generation and Nitrogen Fixation. *Materials Horizons* **2019**.

(75) Norskov, J. K.; Bligaard, T.; Rossmeisl, J.; Christensen, C. H. Towards the Computational Design of Solid Catalysts. *Nature chemistry* **2009,** *1* (1), 37-46.

(76) Liang, Q.; Zhong, L.; Du, C.; Luo, Y.; Zhao, J.; Zheng, Y.; Xu, J.; Ma, J.; Liu, C.; Li, S.; Yan, Q. Interfacing Epitaxial Dinickel Phosphide to 2d Nickel Thiophosphate Nanosheets for Boosting Electrocatalytic Water Splitting. *ACS nano* **2019,** *13* (7), 7975-7984.

(77) Luo, X.; Shao, Q.; Pi, Y.; Huang, X. Trimetallic Molybdate Nanobelts as Active and Stable Electrocatalysts for the Oxygen Evolution Reaction. *ACS Catalysis* **2018,** *9* (2), 1013-1018.

(78) Nørskov, J. K.; Bligaard, T.; Logadottir, A.; Kitchin, J. R.; Chen, J. G.; Pandelov, S.; Stimming, U. Trends in the Exchange Current for Hydrogen Evolution. *Journal of The Electrochemical Society* **2005,** *152* (3), J23-J26.

(79) Long, X.; Li, G.; Wang, Z.; Zhu, H.; Zhang, T.; Xiao, S.; Guo, W.; Yang, S. Metallic Iron-Nickel Sulfide Ultrathin Nanosheets as a Highly Active Electrocatalyst for Hydrogen Evolution Reaction in Acidic Media. *Journal of the American Chemical Society* **2015,** *137* (37), 11900-11903.

(80) McCrory, C. C.; Jung, S.; Peters, J. C.; Jaramillo, T. F. Benchmarking Heterogeneous Electrocatalysts for the Oxygen Evolution Reaction. *Journal of the American Chemical Society* **2013,** *135* (45), 16977-16987.

(81) Kresse, G. Efficient Iterative Schemes for Ab Initio Total-Energy Calculations Using a Plane-Wave Basis Set. *PHYSICAL REVIEW B* **1996,** *54*, 11169e11186.

(82) Furthmu¨ller, G. K. J. Efficient Iterative Schemes for Ab Initio Total-Energy Calculations Using a Plane-Wave Basis Set. *PHYSICAL REVIEW B* **1999,** *54*, 11169-11186.

(83) Chris G. Van de Walle a, Jonathan P. Goss b. Energetics and Vibrational Frequencies of Interstitial H2 Molecules in Semiconductors. *Materials Science and Engineering B* **1999,** *58*, 17-23.

(84) David M. Bishop, S. M. C. Calculation of the Fundamental Vibrational Frequencies and Intensities of Hz, D2, and N2 in the Presence of Li+ or Na+. *Chemical Physics Letters* **1994,** *230*, 177-181.

(85) Voiry, D.; Yamaguchi, H.; Li, J.; Silva, R.; Alves, D. C.; Fujita, T.; Chen, M.; Asefa, T.; Shenoy, V. B.; Eda, G.; Chhowalla, M. Enhanced Catalytic Activity in Strained Chemically Exfoliated Ws(2) Nanosheets for Hydrogen Evolution. *Nature materials* **2013,** *12* (9), 850-855.

(86) Changhong Wang, H. Y., Yejun Zhang and Qiangbin Wang. Nife Alloy Nanoparticle with Hcp Structure Stimulates Superior Oer. *Angewandte Chemie International Edition* **2019,** *58*, 6099-6103.

(87) Fan, K.; Chen, H.; Ji, Y.; Huang, H.; Claesson, P. M.; Daniel, Q.; Philippe, B.; Rensmo, H.; Li, F.; Luo, Y.; Sun, L. Nickel-Vanadium Monolayer Double Hydroxide for Efficient Electrochemical Water Oxidation. *Nat Commun* **2016,** *7*, 11981.

(88) Jin, Z.; Liu, C.; Qi, K.; Cui, X. Photo-Reduced Cu/Cuo Nanoclusters on Tio2 Nanotube Arrays as Highly Efficient and Reusable Catalyst. *Scientific reports* **2017,** *7*, 39695.

(89) Guo, Y.; Shang, C.; Wang, E. An Efficient Cos2/Cose2 Hybrid Catalyst for Electrocatalytic Hydrogen Evolution. *Journal of Materials Chemistry A* **2017,** *5* (6), 2504-2507.

(90) Zhang, G.; Ming, K.; Kang, J.; Huang, Q.; Zhang, Z.; Zheng, X.; Bi, X. High Entropy Alloy as a Highly Active and Stable Electrocatalyst for Hydrogen Evolution Reaction. *Electrochimica Acta* **2018,** *279*, 19-23.

(91) Guo, B.; Yu, K.; Li, H.; Song, H.; Zhang, Y.; Lei, X.; Fu, H.; Tan, Y.; Zhu, Z. Hollow Structured Micro/Nano Mos(2) Spheres for High Electrocatalytic Activity Hydrogen Evolution Reaction. *ACS Appl Mater Interfaces* **2016,** *8* (8), 5517-5525.

(92) Zhang, X.; Ji, J.; Yang, Q.; Zhao, L.; Yuan, Q.; Hao, Y.; Jin, P.; Feng, L. Phosphate Doped Ultrathin Fep Nanosheets as Efficient Electrocatalysts for the Hydrogen Evolution Reaction in Acid Media. *ChemCatChem* **2019,** *11* (10), 2484-2489.

(93) Ji, Y.; Yang, L.; Ren, X.; Cui, G.; Xiong, X.; Sun, X. Nanoporous Cop3 Nanowire Array: Acid Etching Preparation and Application as a Highly Active Electrocatalyst for the Hydrogen Evolution Reaction in Alkaline Solution. *ACS Sustainable Chemistry & Engineering* **2018,** *6* (9), 11186-11189.

(94) Wang, Z.; Ren, X.; Luo, Y.; Wang, L.; Cui, G.; Xie, F.; Wang, H.; Xie, Y.; Sun, X. An Ultrafine Platinum-Cobalt Alloy Decorated Cobalt Nanowire Array with Superb Activity toward Alkaline Hydrogen Evolution. *Nanoscale* **2018,** *10* (26), 12302-12307.

(95) Hao, Z.; Yang, S.; Niu, J.; Fang, Z.; Liu, L.; Dong, Q.; Song, S.; Zhao, Y. A Bimetallic Oxide Fe1.89mo4.11o7 Electrocatalyst with Highly Efficient Hydrogen Evolution Reaction Activity in Alkaline and Acidic Media. *Chemical science* **2018,** *9* (25), 5640-5645.

(96) Chen, L.; Zhang, J.; Ren, X.; Ge, R.; Teng, W.; Sun, X.; Li, X. A Ni(Oh)2-Cos2 Hybrid Nanowire Array: A Superior Non-Noble-Metal Catalyst toward the Hydrogen Evolution Reaction in Alkaline Media. *Nanoscale* **2017**.

(97) Dinh, C.-T.; Jain, A.; de Arquer, F. P. G.; De Luna, P.; Li, J.; Wang, N.; Zheng, X.; Cai, J.; Gregory, B. Z.; Voznyy, O.; Zhang, B.; Liu, M.; Sinton, D.; Crumlin, E. J.; Sargent, E. H. Multi-Site Electrocatalysts for Hydrogen Evolution in Neutral Media by Destabilization of Water Molecules. *Nature Energy* **2018,** *4* (2), 107-114.

(98) Tian, L.; Yan, X.; Chen, X. Electrochemical Activity of Iron Phosphide Nanoparticles in Hydrogen Evolution Reaction. *ACS Catalysis* **2016,** *6* (8), 5441-5448.

(99) Xue Feng Lu, L. Y., Xiong Wen (David) Lou*. Highly Crystalline Ni Doped Fep Carbon Holow Nanorods as All Ph Efficient and Durable Her. *Science Advances* **2019**.

(100) Norskov, J. K.; Abild-Pedersen, F.; Studt, F.; Bligaard, T. Density Functional Theory in Surface Chemistry and Catalysis. *Proc Natl Acad Sci U S A* **2011,** *108* (3), 937-943.

(101) Hwang, S. J.; Kim, S.-K.; Lee, J.-G.; Lee, S.-C.; Jang, J. H.; Kim, P.; Lim, T.-H.; Sung, Y.-E.; Yoo, S. J. Role of Electronic Perturbation in Stability and Activity of Pt-Based Alloy Nanocatalysts for Oxygen Reduction. *Journal of the American Chemical Society* **2012,** *134* (48), 19508-19511.

(102) Tsai, C.; Chan, K.; Abild-Pedersen, F.; Norskov, J. K. Active Edge Sites in Mose2 and Wse2 Catalysts for the Hydrogen Evolution Reaction: A Density Functional Study. *Physical chemistry chemical physics : PCCP* **2014,** *16* (26), 13156-13164.

(103) Ouyang, Y.; Ling, C.; Chen, Q.; Wang, Z.; Shi, L.; Wang, J. Activating Inert Basal Planes of Mos2 for Hydrogen Evolution Reaction through the Formation of Different Intrinsic Defects. *Chemistry of Materials* **2016,** *28* (12), 4390-4396.

(104) Friebel, D.; Louie, M. W.; Bajdich, M.; Sanwald, K. E.; Cai, Y.; Wise, A. M.; Cheng, M. J.; Sokaras, D.; Weng, T. C.; Alonso-Mori, R.; Davis, R. C.; Bargar, J. R.; Norskov, J. K.; Nilsson, A.; Bell, A. T. Identification of Highly Active Fe Sites in (Ni,Fe)Ooh for Electrocatalytic Water Splitting. *Journal of the American Chemical Society* **2015,** *137* (3), 1305-1313.

(105) Chen, Y.; Xu, S.; Zhu, S.; Jacob, R. J.; Pastel, G.; Wang, Y.; Li, Y.; Dai, J.; Chen, F.; Xie, H.; Liu, B.; Yao, Y.; Salamanca-Riba, L. G.; Zachariah, M. R.; Li, T.; Hu, L. Millisecond Synthesis of Cos Nanoparticles for Highly Efficient Overall Water Splitting. *Nano Research* **2019,** *12* (9), 2259-2267.

(106) Yu, F.; Zhou, H.; Huang, Y.; Sun, J.; Qin, F.; Bao, J.; Goddard, W. A., 3rd; Chen, S.; Ren, Z. High-Performance Bifunctional Porous Non-Noble Metal Phosphide Catalyst for Overall Water Splitting. *Nature communications* **2018,** *9* (1), 2551.

(107) Dong, J.; Zhang, F.-Q.; Yang, Y.; Zhang, Y.-B.; He, H.; Huang, X.; Fan, X.; Zhang, X.-M. (003)-Facet-Exposed Ni3s2 Nanoporous Thin Films on Nickel Foil for Efficient Water Splitting. *Applied Catalysis B: Environmental* **2019,** *243*, 693-702.

(108) Fan, X.; Liu, Y.; Chen, S.; Shi, J.; Wang, J.; Fan, A.; Zan, W.; Li, S.; Goddard, W. A., 3rd; Zhang, X. M. Defect-Enriched Iron Fluoride-Oxide Nanoporous Thin Films Bifunctional Catalyst for Water Splitting. *Nat Commun* **2018,** *9* (1), 1809.

(109) Wang, Y.; Sun, Y.; Yan, F.; Zhu, C.; Gao, P.; Zhang, X.; Chen, Y. Self-Supported Nimo-Based Nanowire Arrays as Bifunctional Electrocatalysts for Full Water Splitting. *Journal of Materials Chemistry A* **2018,** *6* (18), 8479-8487.

(110) Guo, P.; Wu, J.; Li, X.-B.; Luo, J.; Lau, W.-M.; Liu, H.; Sun, X.-L.; Liu, L.-M. A Highly Stable Bifunctional Catalyst Based on 3d Co(Oh)2@Ncnts@Nf Towards Overall Water-Splitting. *Nano Energy* **2018,** *47*, 96-104.

(111) Mohammed-Ibrahim, J.; Xiaoming, S. Recent Progress on Earth Abundant Electrocatalysts for Hydrogen Evolution Reaction (Her) in Alkaline Medium to Achieve Efficient Water Splitting – a Review. *Journal of Energy Chemistry* **2019,** *34*, 111-160.

(112) Liu, K.-H.; Zhong, H.-X.; Li, S.-J.; Duan, Y.-X.; Shi, M.-M.; Zhang, X.-B.; Yan, J.-M.; Jiang, Q. Advanced Catalysts for Sustainable Hydrogen Generation and Storage Via Hydrogen Evolution and Carbon Dioxide/Nitrogen Reduction Reactions. *Progress in Materials Science* **2018,** *92*, 64-111.

(113) Danilovic, N.; Subbaraman, R.; Strmcnik, D.; Chang, K. C.; Paulikas, A. P.; Stamenkovic, V. R.; Markovic, N. M. Enhancing the Alkaline Hydrogen Evolution Reaction Activity through the Bifunctionality of Ni(Oh)2/Metal Catalysts. *Angewandte Chemie* **2012,** *51* (50), 12495-12498.

(114) Ito, Y.; Ohto, T.; Hojo, D.; Wakisaka, M.; Nagata, Y.; Chen, L.; Hu, K.; Izumi, M.; Fujita, J.-i.; Adschiri, T. Cooperation between Holey Graphene and Nimo Alloy for Hydrogen Evolution in an Acidic Electrolyte. *ACS Catalysis* **2018,** *8* (4), 3579-3586.

(115) Zhu, M.; Shao, Q.; Qian, Y.; Huang, X. Superior Overall Water Splitting Electrocatalysis in Acidic Conditions Enabled by Bimetallic Ir-Ag Nanotubes. *Nano Energy* **2019,** *56*, 330-337.

(116) Feng, X.; Bo, X.; Guo, L. Com(M=Fe,Cu,Ni)-Embedded Nitrogen-Enriched Porous Carbon Framework for Efficient Oxygen and Hydrogen Evolution Reactions. *Journal of Power Sources* **2018,** *389*, 249-259.

(117) Tang, M. H.; Hahn, C.; Klobuchar, A. J.; Ng, J. W.; Wellendorff, J.; Bligaard, T.; Jaramillo, T. F. Nickel-Silver Alloy Electrocatalysts for Hydrogen Evolution and Oxidation in an Alkaline Electrolyte. *Physical chemistry chemical physics : PCCP* **2014,** *16* (36), 19250-19257.

(118) Nilsson, A.; Pettersson, L. G. M.; Hammer, B.; Bligaard, T.; Christensen, C. H.; Norskov, J. K. The Electronic Structure Effect in Heterogeneous Catalysis. *Catalysis Letters* **2005,** *100* (3-4), 111-114.

(119) Zaera, F. Nanostructured Materials for Applications in Heterogeneous Catalysis. *Chemical Society reviews* **2013,** *42* (7), 2746-2762.

(120) Kuang, M.; Huang, W.; Hegde, C.; Fang, W.; Tan, X.; Liu, C.; Ma, J.; Yan, Q. Interface Engineering in Transition Metal Carbides for Electrocatalytic Hydrogen Generation and Nitrogen Fixation. *Materials Horizons* **2020,** *7* (1), 32-53.

(121) Hegde, C.; Sun, X.; Dinh, K. N.; Huang, A.; Ren, H.; Li, B.; Dangol, R.; Liu, C.; Wang, Z.; Yan, Q.; Li, H. Cu- and Fe-Codoped Ni Porous Networks as an Active Electrocatalyst for Hydrogen Evolution in Alkaline Medium. *ACS applied materials & interfaces* **2020,** *12*, 2380−2389.

(122) Zhenyuan Zhang, T. M. N., *,† Jian Yu Huang,‡ Donald T. Berry,§ and; Provencio, P. P. Room Temperature Synthesis of Thermal Immiscible Ag Ni Nanoalloys. *J. Phys. Chem. C* **2009,** *113* (4), 1155-1159.

(123) Yu, A.; Lee, C.; Lee, N. S.; Kim, M. H.; Lee, Y. Highly Efficient Silver-Cobalt Composite Nanotube Electrocatalysts for Favorable Oxygen Reduction Reaction. *ACS Appl Mater Interfaces* **2016,** *8* (48), 32833-32841.

(124) Li, Y.; Wang, H.; Xie, L.; Liang, Y.; Hong, G.; Dai, H. Mos2 Nanoparticles Grown on Graphene: An Advanced Catalyst for the Hydrogen Evolution Reaction. *J Am Chem Soc* **2011,** *133* (19), 7296-7299.

(125) Wei, C.; Sun, S.; Mandler, D.; Wang, X.; Qiao, S. Z.; Xu, Z. J. Approaches for Measuring the Surface Areas of Metal Oxide Electrocatalysts for Determining Their Intrinsic Electrocatalytic Activity. *Chemical Society reviews* **2019,** *48* (9), 2518-2534.

(126) Lohmann-Richters, F. P.; Abel, B.; Varga, Á. In Situ Determination of the Electrochemically Active Platinum Surface Area: Key to Improvement of Solid Acid Fuel Cells. *Journal of Materials Chemistry A* **2018,** *6* (6), 2700-2707.

(127) Denbig, K. The Principles of Chemical Equilibrium 4thed. *Cambridge university press* **1971**, 432.

(128) Qu, Y.; Yang, M.; Chai, J.; Tang, Z.; Shao, M.; Kwok, C. T.; Yang, M.; Wang, Z.; Chua, D.; Wang, S.; Lu, Z.; Pan, H. Facile Synthesis of Vanadium-Doped Ni3s2 Nanowire Arrays as Active Electrocatalyst for Hydrogen Evolution Reaction. *ACS Appl Mater Interfaces* **2017,** *9* (7), 5959-5967.

(129) Sankar, K. V.; Lee, S. C.; Seo, Y.; Ray, C.; Liu, S.; Kundu, A.; Jun, S. C. Binder-Free Cobalt Phosphate One-Dimensional Nanograsses as Ultrahigh-Performance Cathode Material for Hybrid Supercapacitor Applications. *Journal of Power Sources* **2018,** *373*, 211-219.

(130) Zhu, X.; Wu, Y.; Wan, W.; Yan, Y.; Wang, Y.; He, X.; Lü, Z. Cnf-Grafted Carbon Fibers as a Binder-Free Cathode for Lithium Oxygen Batteries with a Superior Performance. *International Journal of Hydrogen Energy* **2018,** *43* (2), 739-747.

(131) Lee, D.; Seol, M. L.; Motilal, G.; Kim, B.; Moon, D. I.; Han, J. W.; Meyyappan, M. All 3d-Printed Flexible Zno Uv Photodetector on an Ultraflat Substrate. *ACS Sens* **2020,** *5* (4), 1028-1032.

(132) Meng, C.; Liu, C.; Chen, L.; Hu, C.; Fan, S. Highly Flexible and All-Solid-State Paperlike Polymer Supercapacitors. *Nano Lett* **2010,** *10* (10), 4025-4031.

(133) Jabari, E.; Toyserkani, E. Aerosol-Jet Printing of Highly Flexible and Conductive Graphene/Silver Patterns. *Materials Letters* **2016,** *174*, 40-43.

(134) Marzun, G.; Levish, A.; Mackert, V.; Kallio, T.; Barcikowski, S.; Wagener, P. Laser Synthesis, Structure and Chemical Properties of Colloidal Nickel-Molybdenum Nanoparticles for the Substitution of Noble Metals in Heterogeneous Catalysis. *J Colloid Interface Sci* **2017,** *489*, 57-67.

(135) Mansoureh, G.; Parisa, V., Synthesis of Metal Nanoparticles Using Laser Ablation Technique. In *Emerging Applications of Nanoparticles and Architecture Nanostructures*, 2018; pp 575-596.

(136) Ye, R.; Chyan, Y.; Zhang, J.; Li, Y.; Han, X.; Kittrell, C.; Tour, J. M. Laser-Induced Graphene Formation on Wood. *Adv Mater* **2017,** *29* (37).

(137) Li, Y.; Luong, D. X.; Zhang, J.; Tarkunde, Y. R.; Kittrell, C.; Sargunaraj, F.; Ji, Y.; Arnusch, C. J.; Tour, J. M. Laser-Induced Graphene in Controlled Atmospheres: From Superhydrophilic to Superhydrophobic Surfaces. *Adv Mater* **2017,** *29* (27).

(138) Sugioka, K.; Cheng, Y. Femtosecond Laser Three-Dimensional Micro- and Nanofabrication. *Applied Physics Reviews* **2014,** *1* (4).

(139) Le, T. S. D.; Park, S.; An, J.; Lee, P. S.; Kim, Y. J. Ultrafast Laser Pulses Enable One-Step Graphene Patterning on Woods and Leaves for Green Electronics. *Advanced Functional Materials* **2019,** *29* (33).

(140) Ghazali, S. R.; Kubulat, K.; Isa, M. I. N.; Samsudin, A. S.; Khairul, W. M. Contribution of Methyl Substituent on the Conductivity Properties and Behaviour of Cmc-Alkoxy Thiourea Polymer Electrolyte. *Molecular Crystals and Liquid Crystals* **2014,** *604* (1), 126-141.

(141) Tan, J.; Xie, S.; Wang, G.; Yu, C. W.; Zeng, T.; Cai, P.; Huang, H. Fabrication and Optimization of the Thermo-Sensitive Hydrogel Carboxymethyl Cellulose/Poly(N-Isopropylacrylamide-Co-Acrylic Acid) for U(Vi) Removal from Aqueous Solution. *Polymers (Basel)* **2020,** *12* (1).

(142) Gayathri, D.; Jayakumari, L. S. Evaluation of Commercial Arrowroot Starch/Cmc Film for Buccal Drug Delivery of Glipizide. *Polímeros* **2019,** *29* (4).

(143) Payne, B. P.; Biesinger, M. C.; McIntyre, N. S. Use of Oxygen/Nickel Ratios in the Xps Characterisation of Oxide Phases on Nickel Metal and Nickel Alloy Surfaces. *Journal of Electron Spectroscopy and Related Phenomena* **2012,** *185* (5-7), 159-166.

(144) Bazylewski, P.; Boukhvalov, D. W.; Kukharenko, A. I.; Kurmaev, E. Z.; Hunt, A.; Moewes, A.; Lee, Y. H.; Cholakh, S. O.; Chang, G. S. The Characterization of Co-Nanoparticles Supported on Graphene. *RSC Advances* **2015,** *5* (92), 75600-75606.

(145) Sun, L.; Deng, Y.; Yang, Y.; Xu, Z.; Xie, K.; Liao, L. Preparation and Catalytic Activity of Magnetic Bimetallic Nickel/Copper Nanowires. *RSC Advances* **2017,** *7* (29), 17781-17787.

(146) Wang, C.; Yang, H.; Zhang, Y.; Wang, Q. Nife Alloy Nanoparticles with Hcp Crystal Structure Stimulate Superior Oxygen Evolution Reaction Electrocatalytic Activity. *Angew Chem Int Ed Engl* **2019,** *58* (18), 6099-6103.

(147) Hegde, C.; Sun, X.; Dinh, K. N.; Huang, A.; Ren, H.; Li, B.; Dangol, R.; Liu, C.; Wang, Z.; Yan, Q.; Li, H. Cu- and Fe-Codoped Ni Porous Networks as an Active Electrocatalyst for Hydrogen Evolution in Alkaline Medium. *ACS Appl Mater Interfaces* **2020,** *12* (2), 2380-2389.

(148) Hedberg, Y.; Karlsson, M. E.; Wei, Z.; Žnidaršič, M.; Odnevall Wallinder, I.; Hedberg, J. Interaction of Albumin and Fibrinogen with Stainless Steel: Influence of Sequential Exposure and Protein Aggregation on Metal Release and Corrosion Resistance. *Corrosion* **2017,** *73* (12), 1423-1436.

(149) Wright, K.; Barron, A. Catalyst Residue and Oxygen Species Inhibition of the Formation of Hexahapto-Metal Complexes of Group 6 Metals on Single-Walled Carbon Nanotubes. *C* **2017,** *3* (4).

(150) Gao, S.; Hao, S.; Huang, Z.; Yuan, Y.; Han, S.; Lei, L.; Zhang, X.; Shahbazian-Yassar, R.; Lu, J. Synthesis of High-Entropy Alloy Nanoparticles on Supports by the Fast Moving Bed Pyrolysis. *Nat Commun* **2020,** *11* (1), 2016.

(151) Yang, X.; Sun, H.; Zhang, L.; Zhao, L.; Lian, J.; Jiang, Q. High Efficient Photo-Fenton Catalyst of Alpha-Fe2o3/Mos2 Hierarchical Nanoheterostructures: Reutilization for Supercapacitors. *Sci Rep* **2016,** *6*, 31591.

(152) Wu, L. Q.; Li, Y. C.; Li, S. Q.; Li, Z. Z.; Tang, G. D.; Qi, W. H.; Xue, L. C.; Ge, X. S.; Ding, L. L. Method for Estimating Ionicities of Oxides Using O1s Photoelectron Spectra. *AIP Advances* **2015,** *5* (9).

(153) Dinh, K. N.; Zheng, P.; Dai, Z.; Zhang, Y.; Dangol, R.; Zheng, Y.; Li, B.; Zong, Y.; Yan, Q. Ultrathin Porous Nifev Ternary Layer Hydroxide Nanosheets as a Highly Efficient Bifunctional Electrocatalyst for Overall Water Splitting. *Small* **2018,** *14* (8).

(154) Agarwala, S.; Goh, G. L.; Dinh Le, T. S.; An, J.; Peh, Z. K.; Yeong, W. Y.; Kim, Y. J. Wearable Bandage-Based Strain Sensor for Home Healthcare: Combining 3d Aerosol Jet Printing and Laser Sintering. *ACS Sens* **2019,** *4* (1), 218-226.

(155) Deiner, L. J.; Jenkins, T.; Howell, T.; Rottmayer, M. Aerosol Jet Printed Polymer Composite Electrolytes for Solid-State Li-Ion Batteries. *Advanced Engineering Materials* **2019,** *21* (12).

(156) Saleh, M. S.; Li, J.; Park, J.; Panat, R. 3d Printed Hierarchically-Porous Microlattice Electrode Materials for Exceptionally High Specific Capacity and Areal Capacity Lithium Ion Batteries. *Additive Manufacturing* **2018,** *23*, 70-78.

(157) Ray, P. C.; Yu, H.; Fu, P. P. Toxicity and Environmental Risks of Nanomaterials: Challenges and Future Needs. *J Environ Sci Health C Environ Carcinog Ecotoxicol Rev* **2009,** *27* (1), 1-35.

(158) Hoet, P. H.; Bruske-Hohlfeld, I.; Salata, O. V. Nanoparticles - Known and Unknown Health Risks. *J Nanobiotechnology* **2004,** *2* (1), 12.

(159) Jendrzej, S.; Gokce, B.; Epple, M.; Barcikowski, S. How Size Determines the Value of Gold: Economic Aspects of Wet Chemical and Laser-Based Metal Colloid Synthesis. *Chemphyschem* **2017,** *18* (9), 1012-1019.

(160) Rydosz, A.; Brudnik, A.; Staszek, K. Metal Oxide Thin Films Prepared by Magnetron Sputtering Technology for Volatile Organic Compound Detection in the Microwave Frequency Range. *Materials (Basel)* **2019,** *12* (6).

(161) Louie, M. W.; Bell, A. T. An Investigation of Thin-Film Ni-Fe Oxide Catalysts for the Electrochemical Evolution of Oxygen. *J Am Chem Soc* **2013,** *135* (33), 12329-12337.

(162) Trotochaud, L.; Ranney, J. K.; Williams, K. N.; Boettcher, S. W. Solution-Cast Metal Oxide Thin Film Electrocatalysts for Oxygen Evolution. *J Am Chem Soc* **2012,** *134* (41), 17253-17261.

(163) Martti Kaempgen, C. K. C., J. Ma, Yi Cui, and George Gruner. Printable Thin Film Supercaps Using Single Walled Cnt. *Nano Letters* **2009,** *9* (5), 1872-1876.

(164) Han, G.; Zheng, Y.; Zhang, X.; Wang, Z.; Gong, Y.; Du, C.; Banis, M. N.; Yiu, Y.-M.; Sham, T.-K.; Gu, L.; Sun, Y.; Wang, Y.; Wang, J.; Gao, Y.; Yin, G.; Sun, X. High Loading Single-Atom Cu Dispersed on Graphene for Efficient Oxygen Reduction Reaction. *Nano Energy* **2019,** *66*.

(165) Yao, Y.; Huang, Z.; Xie, P.; Wu, L.; Ma, L.; Li, T.; Pang, Z.; Jiao, M.; Liang, Z.; Gao, J.; He, Y.; Kline, D. J.; Zachariah, M. R.; Wang, C.; Lu, J.; Wu, T.; Li, T.; Wang, C.; Shahbazian-Yassar, R.; Hu, L. High Temperature Shockwave Stabilized Single Atoms. *Nat Nanotechnol* **2019,** *14* (9), 851-857.

(166) Hannagan, R. T.; Giannakakis, G.; Flytzani-Stephanopoulos, M.; Sykes, E. C. H. Single-Atom Alloy Catalysis. *Chem Rev* **2020**.

(167) Ali, M. A.; Hu, C.; Jahan, S.; Yuan, B.; Saleh, M. S.; Ju, E.; Gao, S.-J.; Panat, R. P. Sensing of Covid-19 Antibodies in Seconds. **2020**.

(168) Zips, S.; Grob, L.; Rinklin, P.; Terkan, K.; Adly, N. Y.; Weiss, L. J. K.; Mayer, D.; Wolfrum, B. Fully Printed Mu-Needle Electrode Array from Conductive Polymer Ink for Bioelectronic Applications. *ACS Appl Mater Interfaces* **2019,** *11* (36), 32778-32786.

(169) Hao, Z.; Xu, L.; Liu, Q.; Yang, W.; Liao, X.; Meng, J.; Hong, X.; He, L.; Mai, L. On-Chip Ni–Zn Microbattery Based on Hierarchical Ordered Porous Ni@Ni(Oh)2 Microelectrode with Ultrafast Ion and Electron Transport Kinetics. *Advanced Functional Materials* **2019,** *29* (16).

List of patents, publications, and conferences

The scientific contribution of the additive manufacturing process in the chapter 5 is in the process of patent application:

1. **Hegde, C**; Lim, J; Li, H; In-situ Synthesis and Deposition of High Entropy Alloy and Multi Metal Oxide Nano/Micro particles by Femtosecond Laser Direct Writing. [US patent application number 63092710]

The scientific contributions of this thesis are published (or in preparation) in the following journals:

1. **Hegde, C**.; Sun, X.; Dinh, K. N.; Huang, A.; Ren, H.; Li, B.; Dangol, R.; Liu, C.; Wang, Z.; Yan, Q.; Li, H. Cu- and Fe- Co-doped Ni Porous Networks as an Active Electrocatalyst for Hydrogen Evolution in Alkaline Medium. ***ACS Appl. Mater. Interfaces*** **2020,** *12* (2), 2380-2389.
2. **Hegde, C**.; Sun, X.; Ren, H.; Huang, A.; Liu, D.; Li, B.; Dangol, R.; Liu, C.; Li, S.; Li, H.; Yan, Q. $NiAg_{0.4}$ 3D Porous Nanoclusters with Epitaxial Interfaces Exhibiting Pt Like Activity Towards Hydrogen Evolution in Alkaline Medium. ***Nanoscale*** **2020,** *12* (15), 8432-8442.
3. **Hegde, C**. *et al*, In-situ Synthesis and Coating of High Entropy Alloy and Multi-metal Oxide Nanoparticles by Femtosecond Laser Direct Writing Under Ambient Conditions. [Manuscript in preparation]
4. **Hegde, C.** *et al*, Rapid and Low Energy Fabrication of metal oxide and alloy thin films by Hybrid Additive Manufacturing Process: Aerosol Jet Printing + Laser Direct Writing. [Manuscript in preparation]
5. Kuang, M.; Huang, W.; **Hegde, C**.; Fang, W.; Tan, X.; Liu, C.; Ma, J.; Yan, Q. Interface Engineering in Transition Metal Carbides for Electrocatalytic Hydrogen Generation and Nitrogen Fixation. ***Materials Horizons*** **2020,** *7* (1), 32-53.

A part of the work of this thesis was also presented at the following conferences:

1. **Hegde, C**.; Yan, Q.; Li, H. 3D Printing Electro-Catalysts for Hydrogen Production. *Proceedings of the* ***3rd International Conference on Progress in Additive Manufacturing (Pro-AM 2018)*** **2018**, 625-630.
2. **Hegde, C**.; Li, H. 3D Printing of Barium Titanate. ***9th International Conference on Materials for Advanced Technologies -2017***. [Oral presentation]
3. **Hegde, C**.; Li, H.; Yan, Q., CoCu Nanowires as a Bifunctional Electrocatalyst for Water Splitting. ***10th International Conference on Materials for Advanced Technologies -2019***. [Oral presentation]